

**SURFACE - SENSITIVE  
SPECTROSCOPY**

**OF THE CATALYTIC  
HYDROGENATION OF**

**CO AND CO<sub>2</sub>**

**IRIS C. TEN HAVE**

ten Have, Iris Chloë

Title: Surface-Sensitive Spectroscopy of the Catalytic Hydrogenation of CO and CO<sub>2</sub>

Printing: Gildeprint Enschede, [gildeprint.nl](http://gildeprint.nl)

Layout and design: Erwin Timmerman, [persoonlijkproefschrift.nl](http://persoonlijkproefschrift.nl)

Cover design: Canva, [canva.com](http://canva.com)

ISBN: 978-94-6419-648-1

DOI: <https://doi.org/10.33540/1581>

The work described in this thesis was carried out at the Faculty of Science, Inorganic Chemistry and Catalysis group, Utrecht University, The Netherlands.

Copyright © 2022 by Iris C. ten Have. All rights reserved. Any unauthorized reprint or use of this material is prohibited. No part of this thesis may be reproduced, stored or transmitted in any form or by any means, without written permission of the author or, when appropriate, of the publishers of the publications.

Printing: Gildeprint Enschede, [gildeprint.nl](http://gildeprint.nl)

Layout and design: Erwin Timmerman, [persoonlijkproefschrift.nl](http://persoonlijkproefschrift.nl)

**Surface-Sensitive Spectroscopy of the  
Catalytic Hydrogenation of CO and CO<sub>2</sub>**

**Oppervlaktegevoelige Spectroscopie van de  
Katalytische Hydrogenering van CO en CO<sub>2</sub>**  
(met een samenvatting in het Nederlands)

**Proefschrift**

ter verkrijging van de graad van doctor aan de  
Universiteit Utrecht  
op gezag van de  
rector magnificus, prof.dr. H.R.B.M. Kummeling,  
ingevolge het besluit van het college voor promoties  
in het openbaar te verdedigen op

woensdag 14 december 2022 des ochtends te 10.15 uur

door

**Iris Chloë ten Have**

geboren op 5 november 1993  
te Amsterdam

**Promotor:**

Prof. dr. ir. B.M. Weckhuysen (Utrecht University)

**Copromotor:**

Dr. F. Meirer (Utrecht University)

**Beoordelingscommissie:**

Prof. dr. E.T.C. Vogt (Utrecht University)

Dr. M. Monai (Utrecht University)

Prof. dr. N. Kruse (Washington State University)

Prof. dr. M. Rønning (Norwegian University of Science and Technology)

Prof. dr. M Saeys (Ghent University)

Dit proefschrift werd (mede) mogelijk gemaakt met financiële steun van de Nederlandse Organisatie voor Wetenschappelijk Onderzoek (NWO) in het kader van een Technology Area (TA) beurs van het Innovation Fund Chemistry (no. 731016201) en in samenwerking met Shell, DSM Resolve, en Leiden Probe Microscopy.

## Table of Contents

1	General Introduction	7
2	Applications of Nanoscale Spectroscopy: from Materials Science to Environmental Science and Heterogeneous Catalysis	67
3	Through the Lens of <i>Operando</i> Spectroscopy: Mechanistic Insights in the Fischer-Tropsch Synthesis	95
4	The Reaction Mechanism behind CoO as Active Phase for the Catalytic Hydrogenation of CO <sub>2</sub>	141
5	Potassium Promoter Effects in Cobalt-based Catalytic Hydrogenation of CO and CO <sub>2</sub>	183
6	Using Biomass Gasification Mineral Residue as Hydrogenation Catalyst to Produce Light Olefins from CO, CO <sub>2</sub> , and H <sub>2</sub> Mixtures	205
7	Summary, Conclusions, and Future Perspectives	241
8	Summary in Dutch and Information about the Author	259
	List of Abbreviations	265
	Acknowledgements	272



# **CHAPTER I**

## **GENERAL INTRODUCTION**







## 1.1 Spectroscopy

Spectroscopy is the study of the interaction between light and matter. The terminology originates from the Latin word *spectrum*, which means “image” or “appearance”,<sup>1</sup> and the Greek word σκοπεῖν, which means “to look at”.<sup>2</sup> This fundamental tool covers a variety of applications ranging from chemical identification of materials to detecting methane gas on the planet Mars.<sup>3-7</sup> Light consists of photons that propagate as electromagnetic waves and the amount of energy a photon carries, dictates the wavelength. The higher the energy per photon, the shorter the wavelength. The nature of the interaction between photons and matter distinguishes the different types of spectroscopy. Infrared (IR) absorption spectroscopy is a particularly common method in the toolbox of analytical chemists. In a broader context, scientists started using IR spectroscopy in the 1930s to identify compounds and investigate their molecular structure.<sup>8</sup> Molecules absorb specific frequencies of the IR light, corresponding to the vibrational frequencies of their chemical bonds. Hence, every IR absorption spectrum is a unique fingerprint containing the chemical identity of a particular compound. Another common spectroscopic technique that probes molecular vibrations is Raman spectroscopy. This technique is for example used by airport security to screen the contents of cabin baggage.<sup>9</sup> The principle of Raman spectroscopy relies on scattering of monochromatic light, which is usually a laser in the visible light range of the electromagnetic spectrum.<sup>10,11</sup> The incoming laser light interacts with molecular vibrations. This results in outgoing photons with lower or higher energy, providing characteristic information about a compound. IR and Raman spectroscopy both probe molecular vibrations, but have different selection rules and are thus complementary. Besides these so-called vibrational spectroscopic techniques, X-ray spectroscopic techniques are also used to gain insights into the local geometric and/or electronic structure of matter.<sup>12,13</sup>

## 1.2 Micro-spectroscopy

Spatially resolved chemical information can be obtained when spectroscopy is combined with microscopy. This is referred to as micro-spectroscopy and defines all methods in which spectroscopic analyses are combined with imaging techniques.<sup>14</sup> These methods are vital to enable chemical identification and localization of particular compounds in fields like forensics, medicine, biology, chemistry, and geology.<sup>15-19</sup> The spatial resolution of the imaging technique is an important parameter, as it determines how sharply we see an object. For example, when comparing satellite images of the Delta Works in the Netherlands (**Figure 1.1**) with 320 and 13.2 m spatial resolution, it is clear that one could easily miss essential details if the spatial resolution is not sufficient. The same principle applies to imaging materials on the micrometer scale, such as human

cells, and the nanometer scale, such as metal nanoparticles that are for example applied in the biomedical field and in chemical sciences, including the field of catalysis.<sup>20</sup>

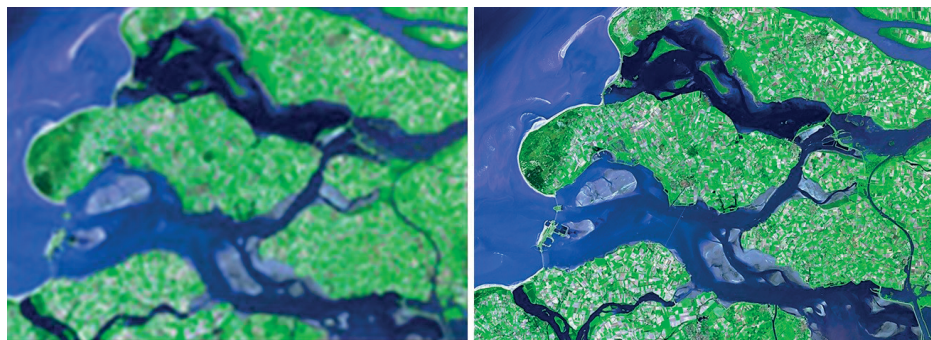


**Figure 1.1.** Satellite images of the Delta Works the Netherlands recorded with 320 m (left) and 13.2 m spatial resolution (right). Images adapted from <https://visibleearth.nasa.gov/>.

### 1.3 *In Situ* and *Operando* (Micro-)Spectroscopy

Scientists have been using IR spectroscopy to identify compounds and investigate their molecular structure in a static fashion since the 1930s.<sup>8</sup> However, studying dynamic processes, such as chemical reactions, requires more advanced analytical methods. The term "*in situ*" describes the study of phenomena exactly in the place where they occur and in their natural state.<sup>4</sup> An example can be found in the biomedical field, where spectroscopy and imaging techniques are used as diagnostics for many different diseases without having to remove tissue.<sup>15</sup> While it is relatively straightforward to assess whether or not an animal or human is in its natural state, *i.e.* alive, certain research fields require additional tools to proof the natural state of a phenomenon. The term "*operando*" emerged from the catalysis field in the early 2000s and describes the study of phenomena, while providing proof of realistic catalytic performance.<sup>4,21-24</sup> The latter can be done by installing next to the spectrometer also a device, such as a gas chromatograph (GC) or mass spectrometer (MS) to measure online the performance of the catalyst material under study. A graphical representation of the concept *operando* spectroscopy in the field of catalysis is displayed in **Figure 1.2**.

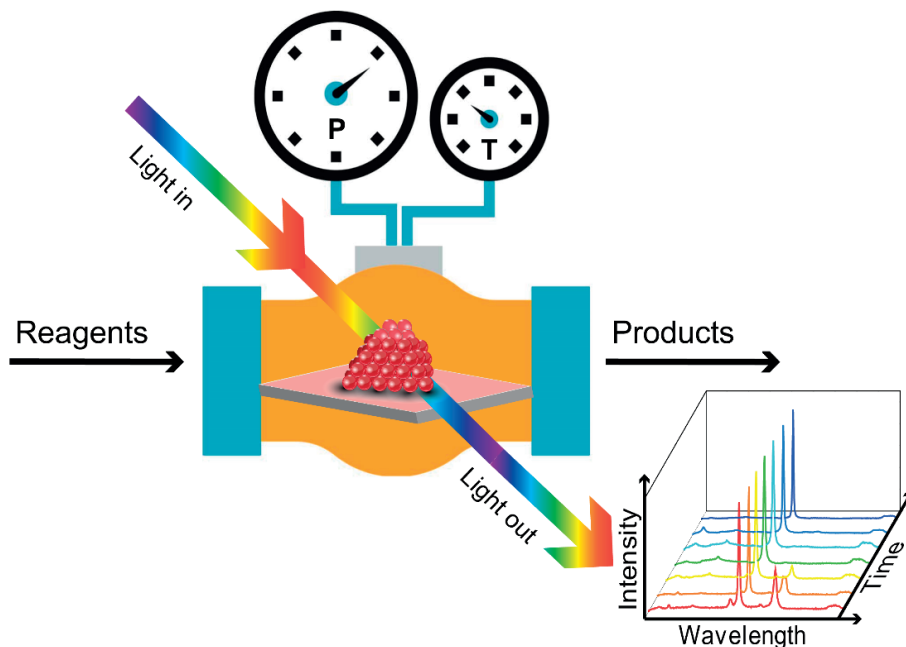


**Figure 1.2.** The concept of *operando* spectroscopy, which arose from the field of catalysis in the early 2000s. A catalyst is converting reagents into products under realistic reaction conditions, *i.e.* at elevated pressure (P) and temperature (T). Spectroscopic information is obtained, while the catalytic performance is monitored with gas chromatography (GC) and/or mass spectrometry (MS).

#### 1.4 The Origin of *Operando* Spectroscopy

The term *operando* first appeared in the open literature in early 2002, in a feature article that described the possibilities and limitations of *in situ* spectroscopy.<sup>25</sup> *In situ* spectroscopy had existed for a while already, but was only loosely defined as mimicking one or more reaction conditions during a spectroscopic investigation. This definition did, however, not fully appreciate the complexity and dynamics of catalytic systems, as assessing the catalytic performance was not included. Consequently, it was postulated that proof of activity and selectivity should be given in spectroscopic studies of catalysts under realistic reaction conditions and that an alternative name for such a complete approach would be appropriate.<sup>25</sup> Though, before appearing in the open literature, the term *operando* had already been suggested verbally at an international scientific conference. In August 2000, Miguel Bañares, Eric Gaigneaux, Gerhard Mestl, and Bert Weckhuysen proposed the new name during a lively discussion at the 220<sup>th</sup> American Chemical Society (ACS) National Meeting in Washington, DC (USA).<sup>23</sup> The term *operando* is based on the Latin gerund, meaning operating or working, and thus fully

covers the wholesome approach of spectroscopic investigation under realistic reaction conditions combined with on-line catalytic performance analysis.

Even though the distinction between *in situ* and *operando* spectroscopy was postulated and recognized only in the early 2000s, researchers had been doing *operando* spectroscopy already before using this term. **Figure 1.3** provides an overview of *in situ* spectroscopic studies conducted before 2001 that can be considered *operando* studies, because they were combined with catalytic performance analysis. The methodology was back then often described as *in situ* spectroscopy with on-line catalytic performance analysis using gas chromatography (GC) and/or mass spectrometry (MS).<sup>26-31</sup> In some cases, the catalytic performance was assessed indirectly by using the relevant peak areas or ratios from the acquired spectra for specific components.<sup>32-34</sup>

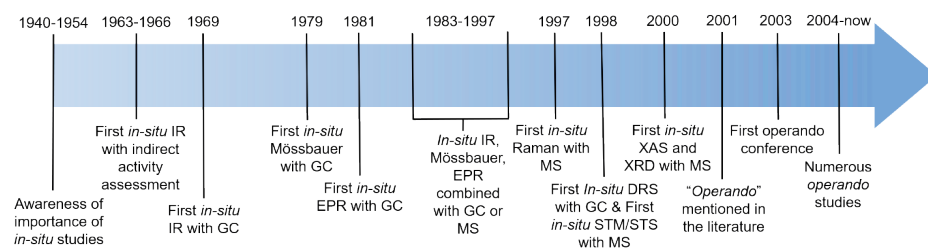


**Figure 1.3.** Timeline indicating moments in history when *in situ* spectroscopic studies could be considered "*operando*" before the term *operando* was formally proposed in the early 2000s.

In the 1930s, scientists started using IR spectroscopy to identify compounds and investigate their molecular structure.<sup>8</sup> However, both the available equipment as well as the knowledge were at that point still a far cry from applications that come close to *operando* spectroscopy. Nevertheless, the drive and the awareness existed already that relevant structure-composition performance relationships should be established to understand catalytic reactions in detail and to improve the functioning of catalytic materials.<sup>35</sup> By means of IR spectroscopy the first historical steps were taken towards *in situ* spectroscopy in the field of catalysis. In 1954, the Eischens group studied the interaction of CO with silica-supported Co, Pt, Pd, and Ni catalysts as well as the interaction of NH<sub>3</sub> with cracking catalysts *in situ*.<sup>21,36,37</sup> In the same period, there was also a Russian group that reported IR spectra of adsorbed molecules on siliceous materials.<sup>38-40</sup> These materials were however not yet considered as catalytic solids.<sup>21</sup>

In the 1960s, the first spectroscopic studies on catalytic systems combined with catalytic performance analysis appeared.<sup>41-43</sup> Some studies were using calibration lines

derived from IR spectra<sup>42</sup> or spectral intensity<sup>43</sup> to determine catalytic performance. These studies represent the start of *operando* in its most rudimentary form; reliable structure-performance relationships should be quantitative with minimal error margins. For example, when spectral intensity is used as a tool to assess catalytic performance, it becomes difficult to compare results obtained with different equipment and/or by different researchers. In 1969, Wood *et al.* investigated  $\text{Cu}_2\text{O}$  catalysts for propylene oxidation with IR reflectance spectroscopy, while analyzing the catalytic performance with GC<sup>44</sup>. This was one of the first real *operando* studies; the type of Cu species was assessed simultaneously with quantitative catalytic performance. In their research paper, they included a schematic drawing of the setup used (Figure 1.4).

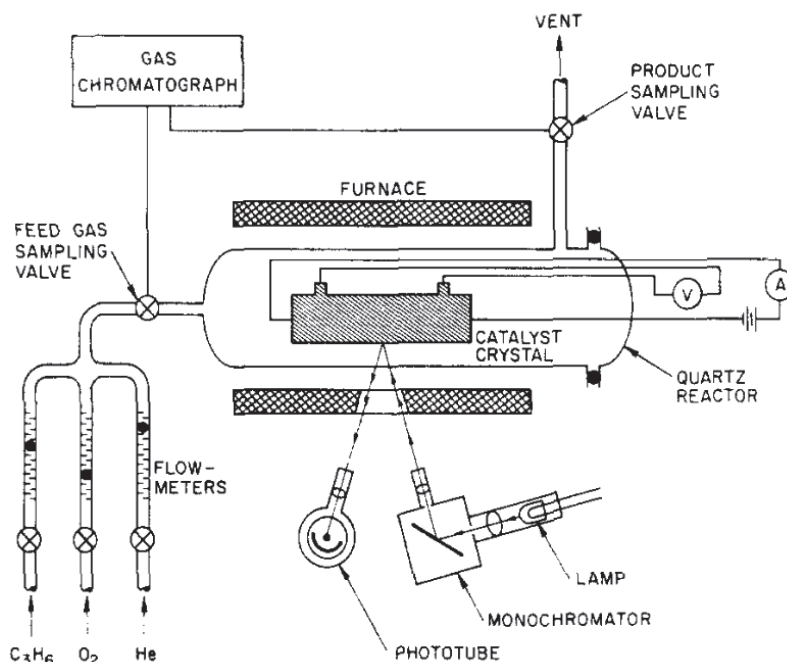


**Figure 1.4.** Schematic drawing of setup used by Wood *et al.* in 1969 to investigate  $\text{Cu}_2\text{O}$  crystals during the propylene oxidation reaction. Reprinted from reference /sup(44) with permission from Elsevier.

Up until the 1980s, the *operando*-like studies were mostly using IR spectroscopy.<sup>45,46</sup> In the 1980s, researchers started using Mössbauer spectroscopy<sup>47</sup> and electron paramagnetic resonance (EPR)<sup>48</sup> for *in situ* studies with simultaneous catalytic performance analysis as well. For example, iron carbide formation in iron-based catalysts for the Fischer-Tropsch Synthesis (FTS) reaction, the conversion of  $\text{CO}$  and  $\text{H}_2$  into fuels or

chemical building blocks, was investigated with Mössbauer spectroscopy during that time period.<sup>49-51</sup> IR spectroscopy was still widely used in the 1980s too. For example, by Mochida *et al.* to investigate the active species on a Rh/TiO<sub>2</sub> catalyst during the FTS reaction, while at the same time analyzing the reaction products formed with MS.<sup>52</sup>

The beginning of the 1990s was marked by the appearance of multiple EPR<sup>53-56</sup> and IR<sup>57-59</sup> spectroscopy studies combined with either MS or GC to assess the performance of the catalytic materials under study. In the second half of the 1990s, the repertoire of spectroscopy techniques that were combined with performance analysis was clearly expanded. In 1997, a study appeared that analyzed vanadium oxide catalysts with *in situ* Raman spectroscopy, while using online MS to analyze the product output.<sup>60</sup> In 1998, supported chromium oxide catalysts were studied with *in situ* diffuse reflectance spectroscopy (DRS), while analyzing the products with online GC.<sup>61</sup> In the same year, the nanoparticle size effect of gold model clusters supported on thin film titania in the CO oxidation reaction were studied with *in situ* scanning tunneling microscopy/spectroscopy (STM/STS), while monitoring activity with MS.<sup>62,63</sup> Even though this investigation and its results represent an important step in the *operando* history, it must be noted that the model catalysts used in this study were significantly different compared to industrially relevant materials. Nevertheless, although not meant as a complete overview, these selected showcase examples illustrate the increased use of online catalytic performance measurements to relate spectroscopic features of a catalyst with its performance under more and more realistic operating conditions.

The beginning of a new century (2000s) was marked by the increasing use of X-ray techniques; these had been widely used for example in material characterization or in the medical field, but not yet really in an *operando* mode in the catalysis field. A noteworthy breakthrough was the development of low-energy *in situ* X-ray absorption spectroscopy (XAS) in Germany. The researchers presented a set-up that could measure at the carbon K-edge, oxygen K-edge and copper L-edge in gas atmospheres of 1-10 mbar while assessing the catalytic performance with online MS.<sup>64</sup> At the same time, high-energy *in situ* XAS was developed in the United Kingdom<sup>65</sup> and was for example used to investigate the vanadium oxide structure during CO oxidation, while measuring catalytic performance with online MS.<sup>66</sup> Another study by a Danish group that came out in the same year even combined two different X-ray techniques, X-ray diffraction (XRD) and X-ray absorption fine structure (XAFS), to analyze a Cu/ZnO catalyst for methanol synthesis, while monitoring the catalytic performance with online MS.<sup>67</sup> The group used a similar methodology to study alumina-supported rhodium catalysts for the partial oxidation of methane.<sup>68</sup> Besides, a vast number of research articles kept appearing for example using UV-Vis DRS,<sup>28,30,31</sup> Raman,<sup>69</sup> or IR<sup>32</sup> spectroscopy or even a combination

of multiple techniques<sup>70</sup>, while using online GC or MS to prove realistic catalytic performance of the systems under investigations.

The term *operando* first appeared in the open literature as an attractive alternative name for *in situ* in a 2002 feature article that described the possibilities and limitations of *in situ* spectroscopy.<sup>25</sup> This article was based on a keynote lecture presented at the 5<sup>th</sup> European Congress on Catalysis (Europacat, Limerick, Ireland, 2001). In 2002, Bañares and coworkers were the first to use the suggested term *operando* in a research article in the catalysis field called “*Operando* Raman study of alumina-supported Sb-V-O catalyst during propane ammoxidation to acrylonitrile with on-line activity measurement”.<sup>71</sup> They investigated the propane ammoxidation reaction<sup>71-73</sup> with a combination of Raman spectroscopy and MS and found out that the process requires both surface mono-oxo vanadium oxide species and SbVO<sub>4</sub> phases.<sup>72</sup>

Since then, *operando* spectroscopy research has gained pace, especially since the technical advances made in terms of cell design, time resolution, and signal-to-noise have increased the applicability of the *operando* methodology. Over the past 20 years, the number of publications has increased exponentially (Figure 1.5). Given the constant improvement of spectroscopic techniques and methodologies, this trend is expected to continue.<sup>13</sup> Table 1.1 provides an overview of relevant (*operando*) spectroscopy techniques in catalysis research and lists the advantages, disadvantages, and some contemporary variations.

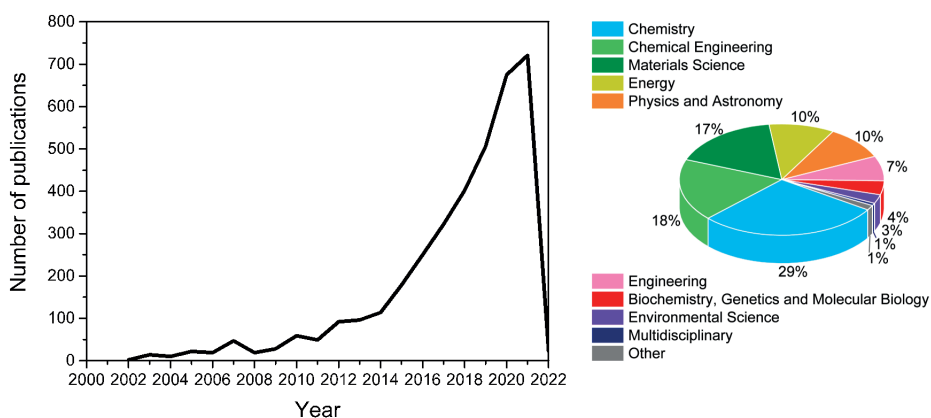


**Figure 1.5. Operando spectroscopy literature data analysis.** The search was done on Scopus on December 3<sup>rd</sup> 2021 with input *operando* spectroscopy or *operando* microscopy or *operando* characterization in the title, abstract, or keywords of publications. The number of publications per year is displayed on the left. The distribution of these publications amongst various fields is displayed on the right.

**Table 1.1.** Overview of relevant (*operando*) spectroscopy techniques in catalysis research, advantages, disadvantages, and contemporary variations.

<b>Class of spectroscopy</b>	<b>Technique</b>	<b>Advantages</b>	<b>Disadvantages</b>	<b>Contemporary variations</b>
Vibrational	Infrared (IR)	+ Reaction intermediates + Adsorbates + Metal-reactant bonds	- Water interference - Does not assess catalyst composition	Microscopy, surface-sensitive (PM)-IRRAS), surface-enhanced (SEIRAS), tip-enhanced (SNOM), atomic force microscopy (AFM)-IR, photo-induced force microscopy (PIFM) <sup>6,74,77</sup>
	Raman	+ Carbon deposition + Reaction intermediates + Metal-reactant bonds + No water interference + Assesses catalyst composition to some extent	- Low signal intensity - Fluorescence interference - Laser damage	Microscopy, shell-isolated nanoparticle-enhanced (SHINERS), tip-enhanced (TERS), surface-enhanced (SERS) <sup>74,78</sup>
X-ray	X-ray absorption spectroscopy (XAS)	+ Element-specific + Chemical state + Bond lengths + Active site characterization	- Reaction intermediates typically not assessed	XANES, EXAFS, Microscopy (TXM, STXM), XRS <sup>14,79,81</sup>
	X-ray diffraction (XRD)	+ Crystallographic structure + Crystallite size + Structural periodicity	- Does not work well with amorphous compounds	Grazing incidence-XRD, SAXS, WAXS <sup>3</sup>
	X-ray emission spectroscopy (XES)	+ Element specific + Site specific + Electronic properties	- Reaction intermediates typically not assessed	XRF, RIXS <sup>3</sup>
	Energy dispersive X-ray (EDX)	+ Element specific + Chemical mapping	- Does not assess chemical structure	(S)TEM-EDX, SEM-EDX

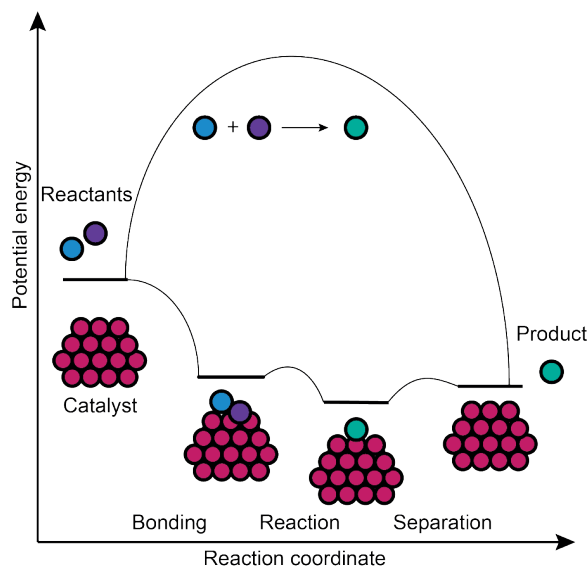


Table 1.1. (Continued)

Class of spectroscopy	Technique	Advantages	Disadvantages	Contemporary variations
Electron	X-ray photoelectron spectroscopy (XPS)	+ Element specific + Surface-sensitive + Chemical state	- Typically done in vacuum	AP-XPS, HP-XPS <sup>82</sup>
	Electron energy loss spectroscopy (EELS)	+ Element specific + Chemical mapping + High spatial resolution	- Limited sample thickness	(S)TEM-EELS <sup>80</sup>
Electronic	Ultraviolet-visible (UV-Vis)	+ Carbon deposition + Reaction intermediates	- Not very selective - Broad spectral lines	Microscopy <sup>83</sup>
Nuclear/spin	Electron paramagnetic resonance (EPR)	+ Molecular structure + Site quantification	- Paramagnetic sample required	
	Nuclear magnetic resonance (NMR)	+ Selective + Local chemical environment	- Low sensitivity	Solid-state NMR, magic angle spinning <sup>84</sup>
	Mössbauer	+ Chemical environment of nucleus	- Solid sample required	

## 1.5 Catalysis

Catalysis is everywhere: numerous products ranging from disinfectants and detergents to food ingredients and packaging have been created using catalytic processes.<sup>85</sup> Many of the chemical reactions required to manufacture commodity products can only proceed by overcoming an energy barrier. This barrier is often too high for the reaction to occur spontaneously. However, catalysts facilitate chemical reactions by lowering the energy barriers and/or opening up alternative pathways that are energetically more favorable. The catalyst achieves this by forming bonds with the reacting molecules and transforming them into the products. The products detach from the catalyst surface leaving it unaltered and ready for a new catalytic cycle. The catalyst itself is utilized, but not consumed during the reaction and therefore only a small amount of catalytic material is generally required. A conceptual overview, illustrating the difference between a catalyzed and an uncatalyzed reaction, is displayed in **Figure 1.6**. The overall performance of a catalyst is typically expressed using the parameters activity, selectivity, and stability. Activity describes the total amount of reactants, commonly in percentages, that is converted by the catalyst, while selectivity indicates the percentage of a certain desired product in the total amount of products formed. Stability is used to describe the changes in catalytic performance over prolonged reaction time. It is not uncommon that the performance deteriorates over time; this is called catalyst deactivation and can be caused by various phenomena, including fouling, poisoning, and decomposition.

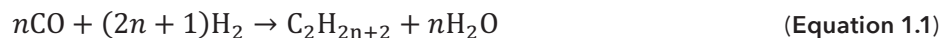


**Figure 1.6.** Potential energy diagram of a catalytic reaction. The reactants must overcome an energy barrier to form the product(s). The catalyst typically lowers the energy barrier and/or facilitates alternative pathways.

The numerous catalysts known today are commonly divided into three groups based on their composition and the state of aggregation in which they act: homogeneous, bio, and heterogeneous. Homogeneous catalysis describes processes where the catalyst, reactants, and products reside in the same, often liquid, phase. The catalyst itself typically consists of a transition metal atom stabilized by (organic) ligands. Homogeneous catalysts occupy only an estimated market share of 10-15% in the total catalysis market.<sup>85</sup> Biocatalysts, also known as enzymes, are remarkably efficient due to complex enzymatic/catalytic centers that are precisely tailored to facilitate a specific reaction. Although the downsides of biocatalysts include often high costs and sensitivity to deactivation as well as the high volume of reactor space needed to achieve sufficient product yields, their importance is predicted to increase mainly due to process developments in enzymatic biofuel production as well as genetic and metabolic engineering approaches.<sup>86</sup> Heterogeneous catalysis is by far the most common industrial catalysis form. In such processes, the reactants and reaction products reside in a different phase, liquid or gas, than the solid catalyst. One of the biggest advantages of this is the facile separation of the catalyst from the products. The heterogeneous catalyst itself typically consists of metal (oxide) nanoparticles that are stabilized by a support material. The metal (oxide) nanoparticles differ from the bulk phase in various ways; the most important difference being increased reactivity of nanoparticles due to higher surface area and thus surface energy. In the previous section we already saw a couple of examples of heterogeneous catalysis in the chemical industry, such as methanol synthesis using copper-based catalysts. Another interesting and historical example is the Haber-Bosch process, which synthesizes ammonia from nitrogen and hydrogen using amongst others iron-based catalysts.<sup>85,87</sup> Ammonia is used as fertilizer on a global scale and has transformed our world tremendously since the invention of the Haber-Bosch process in the early 1900s.<sup>87</sup> Another relevant catalytic process was invented in the 1920s by Franz Fischer and Hans Tropsch. They found out that carbon monoxide (CO) and hydrogen (H<sub>2</sub>) could be converted into long-chain hydrocarbons, which could be used as fuel.<sup>88,89</sup> Nowadays, the so-called the Fischer-Tropsch Synthesis (FTS) offers an elegant solution to enrich energy supplies, mitigate carbon dioxide (CO<sub>2</sub>) emissions, and minimize waste streams. Understanding how the catalytically active phase arises and leads to the formation of a certain product is essential to maximize the catalyst performance. This PhD Thesis is mainly focused on cobalt-based catalysts for the conversion of CO and CO<sub>2</sub> to hydrocarbons by using hydrogen as reductant. In what follows, we present an overview of the active and inactive phases in the cobalt-based FTS and encourage to connect fundamental insights with real industrial catalysis.<sup>90</sup> Only then can we transition to a more circular and sustainable society.

### 1.5.1 Fischer-Tropsch Synthesis

FTS is a collective name for chemical reactions that convert a mixture of carbon monoxide and hydrogen, coined synthesis gas or syngas, into long-chain hydrocarbons.<sup>91,92</sup> The most common overall reactions yield linear alkanes (**Equation 1.1**) or alkenes (**Equation 1.2**), although oxygenates, such as alcohols, can also be produced.<sup>93</sup>



This technology dates back to the 1920s<sup>89,94</sup> and initially coal was used as a feedstock to produce synthesis gas (**Figure 1.7a**). Later, natural gas and biomass were used, as synthesis gas can virtually be produced from any (hydro)carbon feedstock. In the light of climate change and sustainability, CO<sub>2</sub> seems an attractive renewable feedstock for future purposes.<sup>95-97</sup> Cobalt, iron, nickel, and ruthenium are all catalytically active in the FTS reaction. However, nickel is highly selective towards methane, while ruthenium is scarce and expensive. Generally, FTS is commercially conducted with cobalt- and iron-based heterogeneous catalysts. A conceptual representation of the FTS can be found in **Figure 1.7b**. Cobalt mainly yields linear paraffins and operates at 200-250°C. Iron, on the other hand, can operate in a wider temperature range (200-350°C) and generally produces more olefins and oxygenates, especially at the higher end of the temperature range (320-350°C).<sup>91,92</sup> Water and CO<sub>2</sub> are byproducts of the FTS due to the water-gas shift (WGS) reaction (**Equation 1.3**):



Cobalt has a relatively low WGS activity<sup>91</sup> and is therefore more suitable for feedstocks with H<sub>2</sub>/CO<sub>2</sub>≈2, such as natural gas. Iron, on the other hand, possesses a higher WGS activity and is often used for feedstocks with H<sub>2</sub>/CO<sub>2</sub>≈1, such as coal and biomass.<sup>98</sup> Maximizing the output of desired products remains an ongoing quest in heterogeneous catalysis research and there are many ways to do this; for example by, investigating catalyst deactivation,<sup>79,81,91,99-101</sup> reaction mechanisms,<sup>102-107</sup> and active phases.<sup>79,81,99,100,108-111</sup>

Catalyst deactivation is a major challenge in both cobalt- and iron-based FTS. The large industrial and academic interests in this subject are not surprising. Replacing a catalyst regularly is very unfavorable from a commercial point of view and understanding the pathways responsible for the complex deactivation behavior of catalytic systems is interesting from an academic perspective. Even though significant research efforts have been made over the past years,<sup>79,81,91,98-100</sup> deactivation remains a topic of debate in the open literature.<sup>91</sup> Many different processes are at interplay simultaneously, of which sintering,<sup>112,113</sup> re-oxidation,<sup>91,108</sup> metal-support reactions,<sup>108,113,114</sup> and carbon deposition<sup>99</sup> are just a few examples.

Understanding which reaction mechanisms are responsible for the formation of certain products, is another way to maximize the desired output. For the FTS, the C-O bond scission and C-C coupling mechanisms are particularly interesting. Promoting these pathways would enhance the activity and selectivity during the reaction. Various mechanisms have been proposed for CO dissociation and chain growth. Although not unquestioned, direct dissociation of CO followed by C hydrogenation and polymerization of  $\text{CH}_x$  is advocated by most researchers.<sup>102-105</sup> The most widely accepted alternative is the H-assisted C-O scission and chain growth by CO insertion.<sup>102,103,106,107</sup> Reaction mechanisms remain a controversial topic, as conclusive experimental evidence is rather scarce. The FTS reaction mechanisms will be summarized in **Section 1.5.2**.

Identifying the active phase(s) in the catalyst under reaction conditions is a promising approach to maximize the FTS product yield. FTS catalysts typically consist of metal oxide nanoparticles before the reaction, *i.e.*,  $\text{Co}_3\text{O}_4$  in the case of cobalt and  $\text{Fe}_2\text{O}_3$  in the case of iron. To convert the catalyst to the active form, it is treated with  $\text{H}_2$ , or potentially CO/synthesis gas for iron. In general, it is recognized that metallic and oxidic species coexist after activation and during FTS. For iron carbidic species may exist if the catalyst was activated in CO/synthesis gas, which are believed to be the active phase in iron-based FTS. For cobalt, on the other hand, the metallic form is considered the active phase. This difference (*i.e.*, carbide vs. metal) is quite remarkable and underlines the complexity of identifying the active phase(s), as the two metals catalyze an almost identical chemical process with presumably comparable reaction mechanisms.

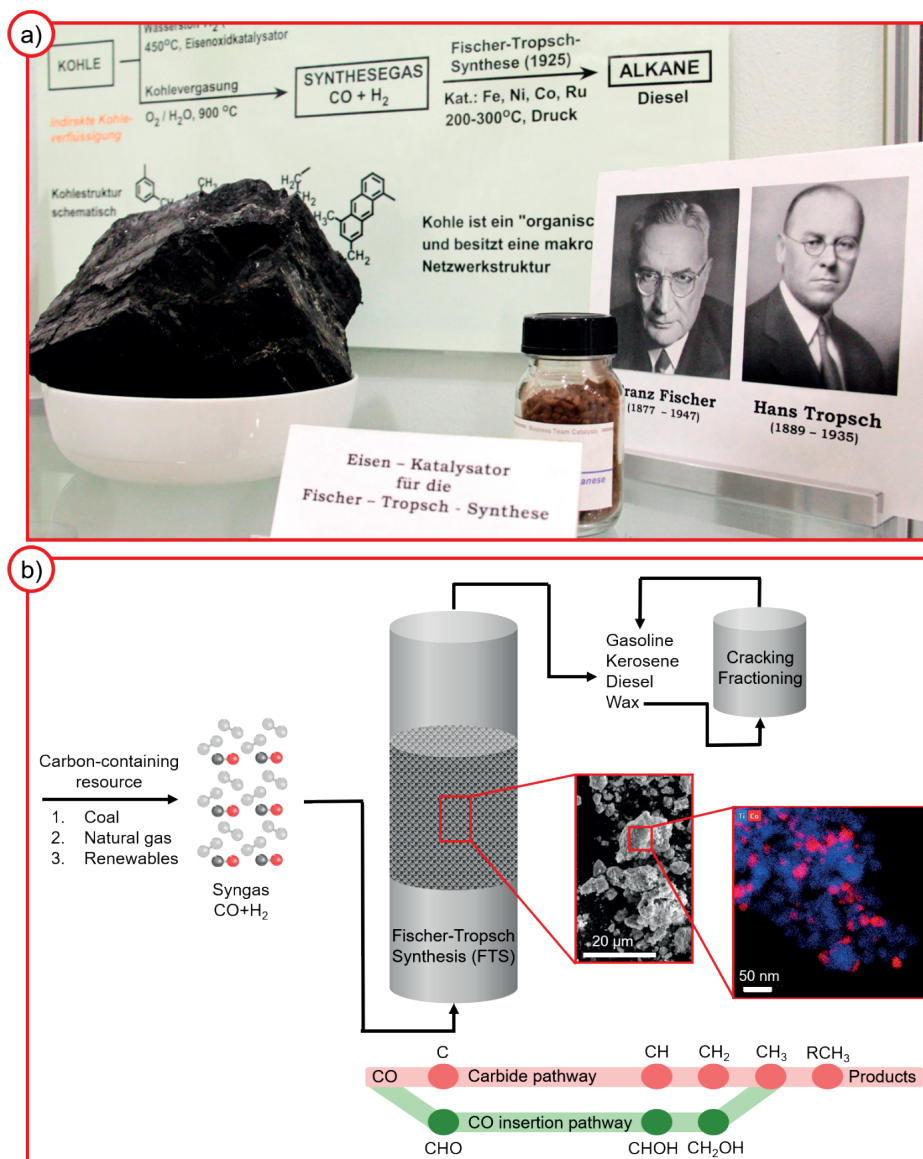


**Figure 1.7. Overview of the Fischer-Tropsch Synthesis (FTS) process.** **a)** Photograph taken at the Max-Planck-Institut für Kohlenforschung (Mülheim, Germany) displaying the first *Eisen* (iron) catalyst for FTS and the inventors Franz Fischer and Hans Tropsch. **b)** Conceptual overview of FTS: Syngas, *i.e.*,  $\text{CO}$  and  $\text{H}_2$ , can be produced from virtually any carbon-containing resource. When FTS was invented in the 1920s, coal was used. Later, natural gas and nowadays more renewable resources, such as biomass,  $\text{CO}_2$ , and eventually perhaps municipal waste can be used. The syngas is led over a solid heterogeneous catalyst material, containing iron or cobalt nanoparticles as the active component. The right side of panel (B) displays an electron microscopy image and X-ray elemental analysis of a typical FTS catalyst, namely cobalt nanoparticles (red) on a titania support (blue).

### 1.5.2 Reaction Mechanisms in Fischer-Tropsch Synthesis

The FTS reaction mechanism has been a topic of debate ever since the first papers were published by Franz Fischer and Hans Tropsch (**Figure 1.7a**).<sup>88,89</sup> The development of surface science tools,<sup>102,107,115-121</sup> as well as *in situ* and *operando* studies<sup>79,81,100-102,122,123</sup> have significantly increased our understanding. Nevertheless, the dispute around reaction mechanisms in FTS is still ongoing. Generally, all the relevant mechanisms can be divided into three elementary steps:<sup>124</sup>

1. Chain initiation
2. Chain growth
3. Chain termination

These steps are accurately described by the Anderson-Schulz-Flory (ASF) model.<sup>125,126</sup> This model presumes the FTS reaction as an ideal polymerization reaction with a single chain growth probability factor  $\alpha$ , which determines the hydrocarbon chain length  $n$  (**Figure 1.8**). The optimal value for  $\alpha$  depends on the application. For small chemical building blocks, like ethylene and propylene, a low  $\alpha$  value is desirable, whereas for longer molecules, for example transportation fuels such as  $C_{12}$ - $C_{18}$  diesel, a higher value is required (**Figure 1.8**). The three main reaction mechanisms proposed for FTS are described below and depicted in **Figure 1.9**.

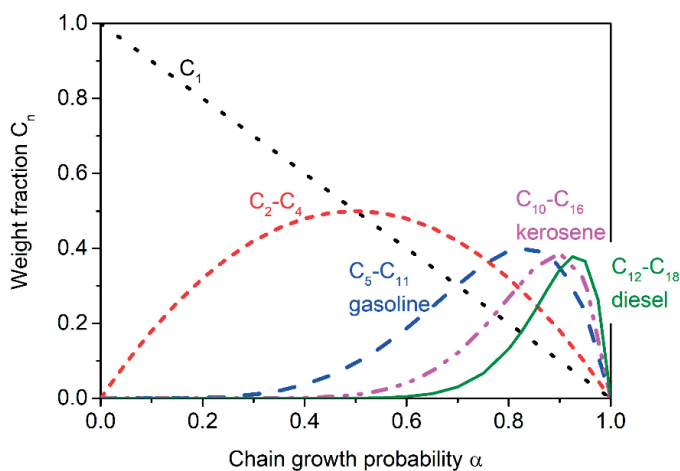


**Figure 1.8. Hydrocarbon product distribution** Weight fraction  $C_n$  with chain length  $n$  plotted as a function of the chain growth probability factor  $\alpha$ .

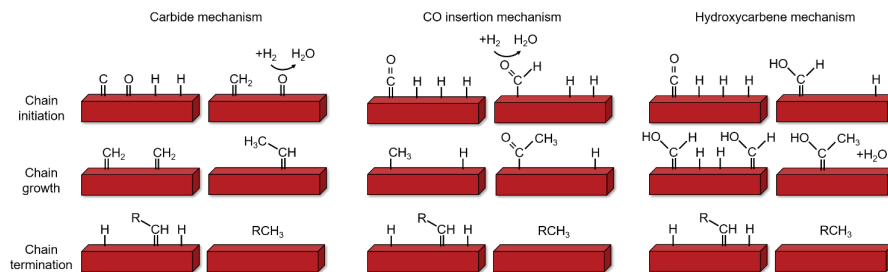


**Figure 1.9. Schematic of the three main mechanisms in Fischer-Tropsch Synthesis** Representations of the carbide, CO insertion, and hydroxycarbene mechanism. The three elementary steps chain initiation, growth, and termination are depicted from top to bottom.

**Carbide mechanism.** The first<sup>88,89</sup> and most widely accepted mechanism<sup>102-105,127</sup> in cobalt-based FTS is the carbide mechanism. This mechanism presumes direct dissociation of CO and H<sub>2</sub>, followed by hydrogenation of C atoms, and polymerization of CH<sub>x</sub>. Chain termination takes place either by abstraction or addition of a H atom from or to the chain.

**CO insertion mechanism.** The second mechanism proposes the adsorption of CO, followed by a reaction with H atoms on the surface to an aldehyde functionality (COH).<sup>102,103,106,107</sup> Chain growth takes place by insertion of CO and chain termination by hydrogenation. For flat cobalt terrace sites, it has been established that this mechanism has a lower energy barrier than the direct dissociation of CO.<sup>103,106,107,127</sup> It is therefore not unthinkable that multiple reaction mechanisms occur simultaneously during the FTS.<sup>128</sup>

**Hydroxycarbene mechanism.** A third mechanism proposes the adsorption of CO, followed by a reaction with H atoms on the surface to a hydroxycarbene group (CHOH).<sup>104,124</sup> Chain growth of these species can take place by condensation polymerization, losing H<sub>2</sub>O, or the individual hydroxycarbene groups can first be hydrogenated and then undergo condensation polymerization. Chain termination occurs via hydrogenation. For this mechanism there are, however, no strong experimental indications for realistic FTS catalysts.<sup>104</sup>

Apart from the reaction mechanism, the rate-determining step is also still under debate. CO dissociation,<sup>129,130</sup> C hydrogenation,<sup>129,131</sup> O removal,<sup>104,129,132</sup> and chain termination<sup>104,131,133</sup> have all been mentioned before as rate-controlling steps. Reaching a consensus on this is difficult, as parameters like temperature and H availability influence the rate-determining step too.<sup>104</sup> It has for example been reported that CO dissociation is the dominant rate-controlling step at low temperatures, while hydrogenation becomes more



rate-controlling at higher temperatures.<sup>134</sup> Besides, the cobalt phases present under reaction conditions are of paramount importance for the resulting activity and selectivity.

### 1.5.3 Origin of Cobalt and Cobalt Phases in Fischer-Tropsch Synthesis

Cobalt occurs naturally in the Earth's crust in the form of ores, chemically combined with other elements. The name cobalt is derived from the German word *Kobold*, which means "goblin" or "evil spirit".<sup>135,136</sup> This refers to the challenging mining process, in which arsenic and sulfur fumes were released while isolating cobalt from the ores. Cobalt also occurs naturally as an organometallic complex in vitamin B12, which is produced by microbes in soil and the marine environment.<sup>137</sup> Today, cobalt has applications in for example the paint industry, lithium-ion batteries, gas sensors, and catalysis.<sup>136</sup> Cobalt-based FTS catalysts are typically synthesized from a metal salt precursor and the fresh cobalt catalyst, containing cobalt oxides (**Figure 1.10**), is obtained by applying a calcination procedure. The catalyst is then activated in H<sub>2</sub> at elevated temperatures, as metallic cobalt is generally postulated as the active phase.<sup>92,108</sup> However, metallic cobalt is most often not the only phase present under reaction conditions (**Figure 1.10**) and it has been mentioned before that cobalt oxides,<sup>109,124,138</sup> cobalt carbide,<sup>81,139-141</sup> cobalt with carbon deposition<sup>79,118</sup>, and cobalt-support interfaces,<sup>109,122,138</sup> are catalytically active as well. The debate around the cobalt active phase in FTS dates back to the 1920s and in the coming section we will elaborate on the history of the dispute about the active phase.

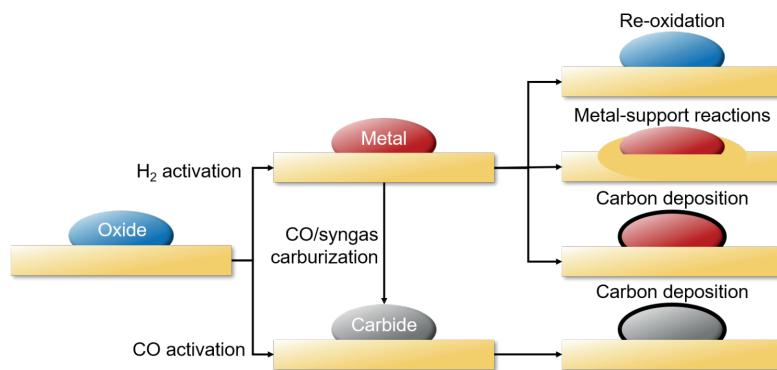


**Figure 1.10. Schematic of various proposed (in)active phases in Fischer-Tropsch Synthesis** The fresh catalyst typically consists of supported metal oxide nanoparticles (left). After activation in H<sub>2</sub> or CO the catalyst contains a metal or carbide, respectively (middle). Besides, the metallic catalyst can be converted to a carbide with CO or syngas. Re-oxidation, metal-support reactions, and carbon deposition may occur under reaction conditions (right).

### 1.5.4 The History of the Disputed Active Phases in Cobalt Fischer-Tropsch Synthesis

In 1902, Sabatier and Senderens first published results of synthesis gas conversion into methane over nickel and cobalt catalysts.<sup>142</sup> In the 1920s Fischer and Tropsch found out that synthesis gas could also be converted into long-chain hydrocarbons, which could be used as fuel.<sup>88,89</sup> In their first patent in 1925 they described the use of cobalt- and iron-based catalysts at atmospheric pressure below 300°C.<sup>143</sup> Different claims have been made over the past century regarding the (de)active phase(s) and (in)active sites in cobalt-based FTS catalysts. A chronological overview of these claims is presented in **Figure 1.11**.

In 1930, Fischer and Tropsch specifically mentioned the “metallic catalyzer” cobalt as active component in their patent.<sup>144</sup> However, multiple studies from 1931 till 1945<sup>145-148</sup> described  $\text{Co}_2\text{C}$  as an “unstable intermediate” in the FTS reaction. For example, Herington and Woodward proposed in 1939 that cobalt carbide was responsible for the formation of  $\text{CH}_2$  groups and polymerization into long-chain hydrocarbons, while metallic cobalt was considered responsible for chain termination by hydrogenation.<sup>147</sup> Hofer and Peebles reported in 1947 using X-ray diffraction (XRD) that face-centered cubic (FCC) cobalt is formed upon reduction of  $\text{Co}/\text{SiO}_2$  in  $\text{H}_2$  at 400°C. They then carburized the catalyst to  $\text{Co}_2\text{C}$  and reduced it again, which led to the formation of the more active hexagonal closest packed (HCP) cobalt.<sup>149</sup>

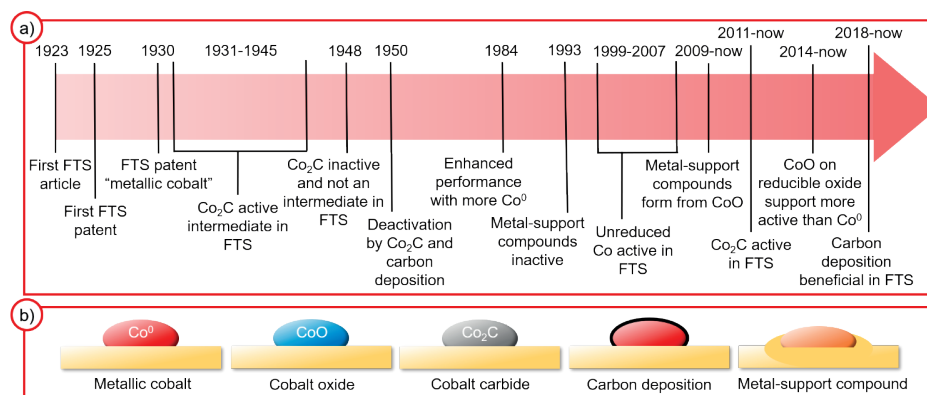


**Figure 1.11. Chronological overview of the proposed (in)active phases in the cobalt-based Fischer-Tropsch Synthesis** a) Varying claims have been made throughout the almost 100 years of Fischer-Tropsch Synthesis history. b) Schematic overview of the different (in)active cobalt phases.

The hypothesis that cobalt carbide was an active intermediate in the FTS reaction was invalidated by Weller *et al.* using XRD in 1948.<sup>150</sup> In the same year, Kummer *et al.* showed with <sup>14</sup>C as a tracer that only 10% of the hydrocarbon products were formed *via* a surface cobalt carbide.<sup>151</sup> Carbon deposition and cobalt carbide formation were mentioned as deactivation mechanisms in the cobalt-based FTS reaction in a patent by Mattox in 1950.<sup>152</sup> Cobalt carbide was still disregarded as a plausible intermediate in the FTS in 1959 and studies became increasingly focused on the FTS reaction mechanism.<sup>153</sup> However, in the 1960s, the interest in FTS decreased due to the large availability of crude oil.

In the 1970s and 1980s, the interest in FTS was renewed due to oil crises and the sanctions towards South Africa.<sup>92,98</sup> In this era, many studies were focused on unraveling the complicated and multifaceted FTS reaction mechanisms.<sup>154</sup> In 1984, Reuel and Bartholomew published a comprehensive study on support and dispersion effects in the cobalt-based FTS.<sup>155</sup> They mentioned, among others, that an increasing "extent of reduction", *i.e.* metallic cobalt, had a positive influence on the activity and selectivity towards long-chain hydrocarbons.<sup>155,156</sup> This claim was substantiated during the 1990s by multiple studies using catalytic testing, temperature programmed reduction (TPR),<sup>157-159</sup> and X-ray photoelectron spectroscopy (XPS).<sup>160</sup> These studies also postulated that metal-support compounds, such as cobalt aluminates and cobalt silicates, were inactive in the FTS reaction.<sup>157-160</sup> The development of *in situ* characterization methods, such as infrared (IR) spectroscopy and XRD, contributed to the finding that not only metallic cobalt was capable of adsorbing CO; cobalt oxide could do that as well.<sup>161</sup> These developments also brought to light that metallic cobalt and cobalt oxides almost always coexist under FTS reaction conditions.<sup>161</sup> In 1999, Ernst *et al.* concluded that a higher percentage of unreduced cobalt did not necessarily influence the activity, but shifted the selectivity from C<sub>22+</sub> (waxes) to C<sub>5</sub>-C<sub>13</sub> (gasoline).<sup>162</sup> This suggests that cobalt oxides are active in the FTS reaction as well. Interestingly, many important hypotheses around the active phase in cobalt-based FTS had already been formed during the first 75 years after the invention of FTS. However, the instrumentation required to prove or disprove these hypotheses had not yet fully been developed. The beginning of the 21<sup>st</sup> century marked a new and fruitful era for methodology development. For example, various surface science tools as well as *in situ* and *operando* studies have contributed to our increased understanding of the active phase in FTS.

In the 2000s, the FTS process was revived even more due to resource depletion and environmental concerns.<sup>163</sup> Many investigations were focused on the effect of cobalt nanoparticle size and it was found that smaller nanoparticles ( $\leq 6$  nm) are more difficult to reduce than larger ones.<sup>164-167</sup> From 2004 till 2007, Morales and Weckhuysen published multiple papers on the TiO<sub>2</sub> support and MnO promoter effects in cobalt

FTS.<sup>168-174</sup> One of the findings they reported was that MnO decreased the reducibility of cobalt, but enhanced both the FTS activity and selectivity towards C<sub>5+</sub> hydrocarbons.<sup>168,170</sup> This suggested again that cobalt oxides could be active in the FTS. However, it was also found that cobalt oxides resulting from re-oxidation by water could form inactive metal-support compounds more easily than metallic cobalt.<sup>91,108,163</sup> For metallic cobalt, it had already been established that the HCP crystal phase was more active in FTS than the FCC crystal phase.<sup>149,163</sup> Saib *et al.* reported for metallic cobalt the B<sub>5</sub> step-edge sites as the most active sites in FTS.<sup>175</sup> These B<sub>5</sub> sites were first introduced in the 1960s to describe the crystallite size effect on N<sub>2</sub> adsorption,<sup>176,177</sup> but they were not specifically linked to cobalt-based FTS until 2010.<sup>175</sup>

From 2011 till now, multiple studies have appeared reporting Co<sub>2</sub>C as a highly active phase in the cobalt-based FTS towards olefins<sup>139,178-180</sup> or oxygenates.<sup>140,178,181-184</sup> All these studies mentioned that Co<sub>2</sub>C was stabilized by and in synergy with an oxidic compound and/or an alkali promoter. Up till now, Co<sub>2</sub>C has also been reported as deactivating by studies that did not use oxidic compounds or alkali promoters.<sup>81,91,100,185-187</sup>

From 2014 till now, evidence has been presented that CoO supported on TiO<sub>2</sub> was more active in both FTS and CO<sub>2</sub> hydrogenation than its metallic cobalt variant.<sup>109,188</sup> Similarly for Co/Al<sub>2</sub>O<sub>3</sub>, an increased CO<sub>2</sub> hydrogenation to ethanol activity has been reported due to coexisting Co and CoO phases.<sup>189</sup> For MnO<sub>x</sub>/Co<sub>3</sub>O<sub>4</sub> as well; the cobalt oxide phase has been reported more active than metallic cobalt in the CO<sub>2</sub> hydrogenation towards methanol.<sup>138</sup> However, for Co/SiO<sub>2</sub> the opposite has been reported: the metallic variant was more active.<sup>109</sup> The presence of a (somewhat) reducible oxide seems thus vital for enhancing the FTS performance of cobalt oxides.

In 2018, two studies emerged reporting that carbon deposition was beneficial for generating an active FTS catalyst.<sup>79,190</sup> It was also reported that graphitic carbon species could particularly block methanation sites<sup>190</sup> and that a higher Co valence state could be correlated to the degree of saturation in the carbon deposits.<sup>79</sup> Research on this topic is still ongoing and the development of, among others, surface science tools is vital for our understanding.

## 1.5.5 Discussion of the Different Hypotheses on the Cobalt Active Phase

### 1.5.5.1 General properties of metallic cobalt and its role in Fischer-Tropsch Synthesis

Metallic cobalt is a solid with a silvery blue color and magnetic properties.<sup>135,136</sup> Metallic cobalt can exist in three different crystal phases: hexagonal closest packed (HCP, lattice parameter  $a=2.507 \text{ \AA}^{191}$ ), face-centered cubic (FCC,  $a=3.538 \text{ \AA}^{192,193}$ ), or cubic primitive (CP).<sup>124</sup> Under FTS reaction conditions the HCP and FCC crystal phases are the main allotropes reported for cobalt nanoparticles (**Figure 1.12**).<sup>122</sup>

In bulk cobalt the transition from FCC to HCP occurs around  $400^\circ\text{C}$ ,<sup>124</sup> but can occur already at temperatures  $\leq 300^\circ\text{C}$  for metal nanoparticles.<sup>194</sup> HCP cobalt nanoparticles have been reported to have a higher FTS activity compared to FCC cobalt.<sup>130,163,195</sup> Theoretical results indicated a higher CO dissociation rate on most HCP facets than on FCC facets and thus a higher intrinsic FTS activity on HCP cobalt.<sup>196</sup> Besides, theoretical calculations suggested that direct dissociation of CO is more favorable on HCP cobalt, while H-assisted CO dissociation is preferred on FCC cobalt. The higher intrinsic activity of HCP cobalt is related to the higher surface energy compared to FCC cobalt, caused by the lower coordination numbers of the surface atoms. Although this property may be beneficial for activity, it has a negative influence on the stability of the metallic cobalt phase under reaction conditions. HCP cobalt has been reported less resistant to water-induced re-oxidation<sup>108</sup> and to cobalt carbide<sup>81</sup> formation.

The size of the cobalt nanoparticles has an influence on the crystal phase and on the available surface sites under reaction conditions. It was found that as-synthesized cobalt nanoparticles  $\leq 20 \text{ nm}$  are pure FCC phase,  $\sim 30 \text{ nm}$  a mixture of FCC and HCP, and  $\geq 40 \text{ nm}$  almost pure HCP.<sup>194</sup> For the FTS reaction, the optimum cobalt nanoparticle size is established at  $6\text{--}8 \text{ nm}$  (**Figure 1.13a**).<sup>197,198</sup> For such a catalyst, one would thus expect the pure FCC phase. In practice, however, a (partial) phase transition to HCP may take place during the activation procedure and under FTS reaction conditions.<sup>81</sup> Below this optimum size, the catalyst produces more undesired methane and is more prone to re-oxidation.<sup>108</sup> Above this size, the turnover frequency is lower. This is related to the available surface sites. For small nanoparticles, the lower reactivity towards FTS is often ascribed to the lack of reactive  $B_5$  step-edge sites.<sup>199</sup> The term "B<sub>n</sub> site" was first used by van Hardeveld and Hartog in the 1960s to indicate an ensemble of  $n$  surface atoms that are in close contact with an adsorbed species (**Figure 1.13b**).<sup>176</sup>

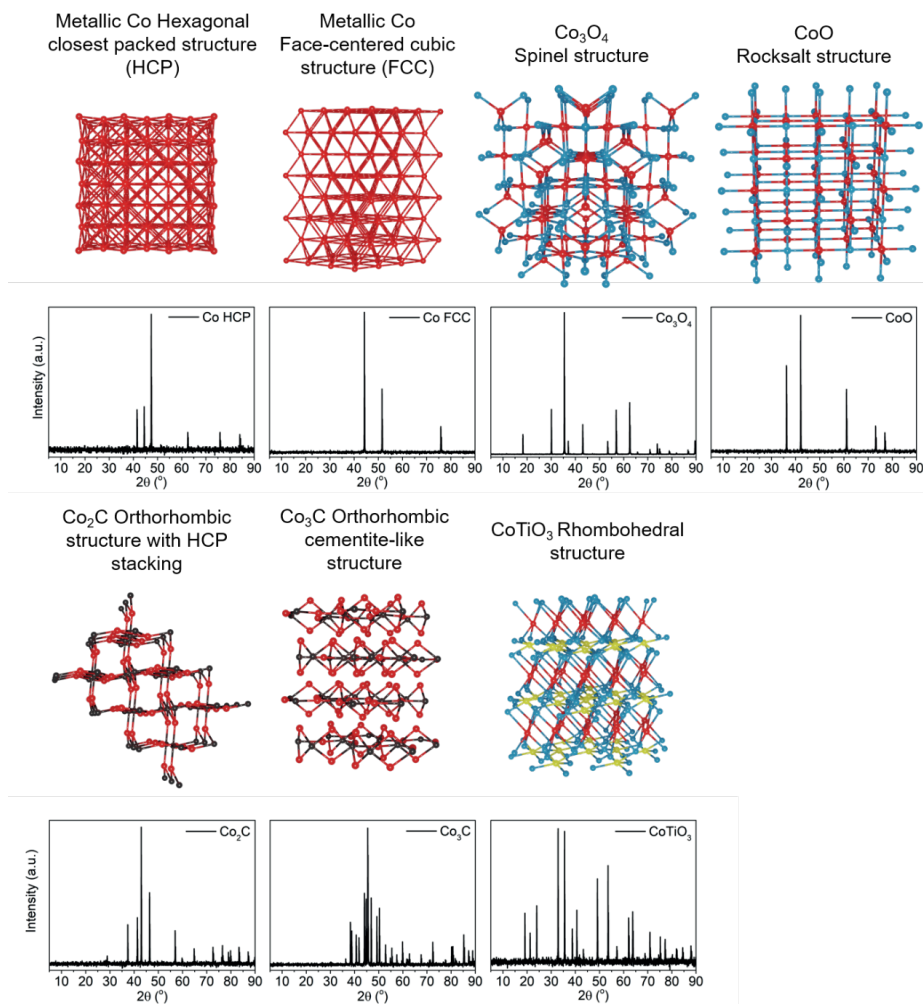


**Figure 1.12. Relevant cobalt crystal structures in Fischer-Tropsch synthesis** Crystal structures (top row from left to right) of HCP metallic cobalt, FCC metallic cobalt,  $\text{Co}_3\text{O}_4$  with spinel structure, CoO with rocksalt structure, (third row from left to right)  $\text{Co}_2\text{C}$  with orthorhombic structure and HCP stacking,  $\text{Co}_3\text{C}$  with orthorhombic cementite-like structure, and  $\text{CoTiO}_3$  with rhombohedral structure (representing metal-support compounds). The second and fourth row display simulated XRD patterns (Cu K $\alpha$  radiation) for each structure.

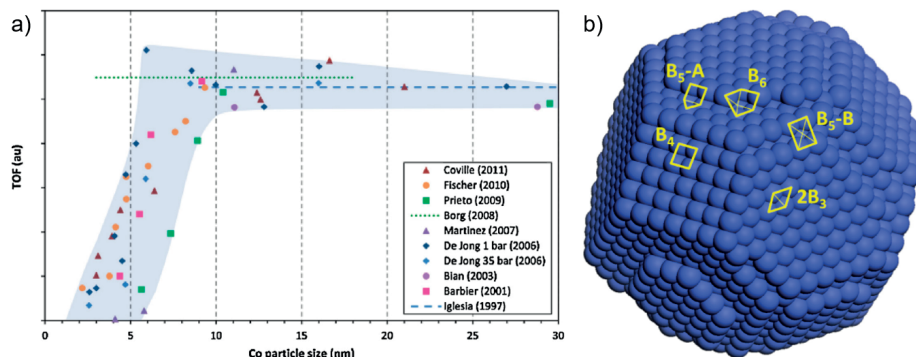


**Figure 1.13. The cobalt particle size effect in Fischer-Tropsch Synthesis** **a)** Size-dependent turnover frequency (TOF) in Fischer-Tropsch Synthesis as a function of the cobalt nanoparticle size. Reproduced from references <sup>92,192</sup> and includes references <sup>198,200-205</sup>. **b)** A 4 nm metallic cobalt nanoparticle (FCC) showing different B<sub>n</sub> sites, including two types of reactive B<sub>5</sub> sites. Reproduced from reference <sup>192</sup>.

### 1.5.5.2. General properties of cobalt oxides and their role in Fischer-Tropsch synthesis

Cobalt oxides are generally crystalline solids with a dark color. While three different cobalt oxides exist, only Co<sub>3</sub>O<sub>4</sub> and CoO have been well-characterized and are of potential importance in the FTS reaction. Cobalt (III) oxide, Co<sub>2</sub>O<sub>3</sub>, is a dark gray to black crystalline powder. The compound has been reported as metastable with a hexagonal HCP structure in the literature.<sup>206</sup> Co<sub>2</sub>O<sub>3</sub> is not as well characterized as other cobalt oxides; it is still uncertain whether or not it can exist as a stable solid crystal. Cobalt (II,III) oxide, Co<sub>3</sub>O<sub>4</sub>, is a black antiferromagnetic solid and one of the two well-characterized cobalt oxides.<sup>206</sup> It has applications in for example lithium-ion batteries, gas sensors, electrochemistry, and catalysis. Co<sub>3</sub>O<sub>4</sub> has a normal cubic spinel structure ( $a=8.020 \text{ \AA}^{206}$ ), as depicted in **Figure 1.12**, and is the thermodynamically favored cobalt oxide under ambient conditions. Cobalt (II) oxide, CoO, is an olive green or gray solid with applications as coloring agent in the ceramics industry, electrochemistry, and catalysis. It has a rock salt crystal structure ( $a=4.258 \text{ \AA}^{206}$ ) consisting of two interpenetrating FCC sublattices of Co<sup>2+</sup> and O<sup>2-</sup> (**Figure 1.12**).<sup>206</sup>

Typically, the fresh FTS catalyst material containing Co<sub>3</sub>O<sub>4</sub> is activated at elevated temperatures in H<sub>2</sub> via CoO to metallic cobalt. However, it is generally accepted that CoO and metallic cobalt coexist under FTS reaction conditions.<sup>79,80,122,207,208</sup> Small metallic cobalt nanoparticles can easily re-oxidize to CoO/Co<sub>3</sub>O<sub>4</sub> during FTS due to the production of water,<sup>108,209,210</sup> which has been considered as a deactivation mechanism.<sup>211</sup> Additionally, it has been reported that it is thermodynamically more likely that CoO

rather than metallic Co undergoes metal-support solid state reactions and form inactive metal-support compounds,<sup>108</sup> such as cobalt titanates ( $\text{CoTiO}_3$ ,  $a=5.485 \text{ \AA}$ <sup>212</sup>) or cobalt aluminates ( $\text{CoAl}_2\text{O}_4$ ,  $a=8.105 \text{ \AA}$ ).<sup>208,213</sup> There is a discrepancy between different studies regarding the role of cobalt oxides in FTS. To clarify this, we should take into account the cobalt nanoparticle size, support material, and reaction conditions.

Some studies report irreducibility and/or re-oxidation of 2-3 nm cobalt metal nanoparticles,<sup>213</sup> whereas others mention a re-oxidation threshold of 5.3 nm<sup>208</sup> or 7.5 nm.<sup>209</sup> A safe lower size limit would thus be ~8 nm to control and, if desired, avoid re-oxidation.

The support material seems to have a major influence on the performance of cobalt oxides in the FTS and  $\text{CO}_2$  hydrogenation reaction. Evidence has been presented that CoO supported on  $\text{TiO}_2$  was more active in both FTS and  $\text{CO}_2$  hydrogenation than its metallic cobalt variant.<sup>109,188</sup> Though, in the same study it was mentioned that on  $\text{SiO}_2$  support, metallic cobalt was more active. This effect was ascribed to a unique interface between CoO and the reducible  $\text{TiO}_2$  support.<sup>109</sup> In another study, it was found that Co/ $\text{Al}_2\text{O}_3$  converted  $\text{CO}_2$  into ethanol with high selectivity due to coexisting Co and CoO phases.<sup>189</sup> However, specific active sites for cobalt oxides have to our best knowledge not yet been reported in the open literature. Although, intuitively one could imagine that a stepped rather than a flat surface composes the active sites, as both FTS and  $\text{CO}_2$  hydrogenation are structure-sensitive reactions.<sup>214</sup> For example, for CoO with rock salt structure a plausible active site in terms of "B<sub>n</sub> site" could be  $\text{B}_5\text{O}_2$ , where B represents cobalt atoms, O represents oxygen atoms, and n denotes the number of atoms in close contact to an adsorbed species.

Reaction conditions are of paramount importance to the cobalt and/or support phases present in the catalyst material. At high conversion rates, when the water production is high, Co and/or CoO may more readily form inactive metal-support compounds.<sup>108</sup> Also the reaction temperature cannot be overlooked. While deactivating cobalt aluminates have been reported at high conversion rates and reaction temperatures of 220-250°C,<sup>208,209,213</sup> coexisting Co and CoO on  $\text{Al}_2\text{O}_3$  support were mentioned as active phase at 140-200°C.<sup>189</sup>

While metallic cobalt is generally accepted as active phase, cobalt oxides coexist under FTS reaction conditions. Cobalt oxides can be (part of) the active phase, provided that the support material is not  $\text{SiO}_2$  and that they do not form inactive metal-support compounds. Besides, it is important to mindfully design the catalyst synthesis procedure and to choose suitable reaction conditions.



### 1.5.5.3 General properties of cobalt carbide and its role in Fischer-Tropsch synthesis

Cobalt carbide is currently known to exist as  $\text{Co}_2\text{C}$  and  $\text{Co}_3\text{C}$  (Figure 1.12).  $\text{Co}_2\text{C}$  is a gray/black paramagnetic solid with noble metal-like properties<sup>182</sup> and an orthorhombic crystal structure ( $a=2.877 \text{ \AA}^{185}$ ), isomorphous to  $\eta\text{-Fe}_2\text{C}$ .  $\eta\text{-Fe}_2\text{C}$  is a C-rich iron carbide that is unstable under FTS reaction conditions without the presence of an alkali promoter.<sup>110</sup> It is thus likely that  $\text{Co}_2\text{C}$  needs to be stabilized by alkali metals too.  $\text{Co}_3\text{C}$  has an orthorhombic crystal structure as well ( $a=4.483 \text{ \AA}^{215}$ ), but has been characterized to a lesser extent than  $\text{Co}_2\text{C}$ . However,  $\text{Co}_3\text{C}$  has been mentioned before as isomorphous to  $\theta\text{-Fe}_3\text{C}$  (cementite).<sup>215,216</sup> The C-poor  $\theta\text{-Fe}_3\text{C}$  has been associated with deposition of deactivating carbon species on the catalyst surface and the carbide phase is not necessarily stabilized by alkali promoters.<sup>110</sup> In iron-based FTS,  $\chi\text{-Fe}_5\text{C}_2$  (Hägg carbide) has been postulated as the most stable active phase under reaction conditions. However, such an isomorph has not been mentioned before in cobalt-based FTS. Besides in catalysis, carbides have found applications in cutting tools, machinery, and ammunition for its hardness and mechanical strength.

While iron carbides are considered as active phase in FTS,<sup>110,111</sup> the formation of cobalt carbides and their role in the FTS reaction is a controversial topic. Carbon diffusion in iron (43.9-69.0 kJ/mol) occurs more easily than in cobalt (145 kJ/mol),<sup>217,218</sup> but the two metals have quite similar activation energies for the FTS reaction, 89.1 and 105 kJ/mol respectively.<sup>219</sup> Because of this, iron catalysts first go through an initiation period in which carbides are formed and at least 6 different types of carbides have been reported in iron-based FTS.<sup>98</sup> On the other hand, CO and  $\text{H}_2$  are readily converted into FTS products over cobalt catalysts. Cobalt carbides can however be formed under FTS conditions, particularly at low  $\text{H}_2/\text{CO}$  ratios.<sup>81,186</sup> Although only  $\text{Co}_2\text{C}$  and  $\text{Co}_3\text{C}$  have been reported thus far, more cobalt carbide polymorphs may exist. The formation of cobalt carbides is exothermic and they are less stable compared to iron carbides.<sup>186,220</sup> An underlying reason for their instability is the geometry of the crystal phase. The unit cells of hexagonal facets in HCP cobalt match well with hexagonal graphitic structures, whereas the predominantly body-centered cubic (BCC) iron facets do not present a good match for graphite.<sup>220</sup> Therefore, the formation of graphitic carbon on cobalt may be more favorable than the formation of cobalt carbides.<sup>81,186</sup>

Some studies correlate cobalt carbide formation to higher selectivity towards lower olefins,<sup>139,178-180,221-223</sup> or oxygenates,<sup>140,178,181-184,224-226</sup> while others relate its presence to catalyst deactivation.<sup>81,91,100,185-187</sup> The role of cobalt carbides in the FTS reaction is thus rather ambiguous and evokes further discussion. We should remind ourselves that cobalt-based FTS catalysts do not only contain cobalt, but also a support material and

often promoter elements. Interestingly, most studies that report an increased olefin or oxygenate selectivity upon cobalt carbide formation use catalysts containing an oxidic compound, like  $\text{MnO}$ <sup>139,178-180,183,225,227-230</sup> or  $\text{La}_2\text{O}_3$ ,<sup>181,231</sup> and/or an alkali promoter.<sup>140,178,232</sup> For iron-based catalysts it is well-established that the alkali promoters sodium<sup>110,111</sup> and potassium<sup>233,234</sup> act as structural stabilizers for iron carbide formation. As cobalt carbides are intrinsically less stable than iron carbides,<sup>235</sup> the presence of an alkali metal may even be more essential for stabilization of the cobalt carbide phase. Besides, synergistic effects at the interface of cobalt carbide and the oxidic compound,  $\text{MnO}$  or  $\text{La}_2\text{O}_3$ , seem to be responsible for the enhanced selectivity towards olefins or oxygenates.<sup>178</sup>

Similar to metallic cobalt, particle size effects were reported for cobalt carbides as well. The optimum cobalt carbide nanoparticle size was established at  $\sim 7$  nm.<sup>236</sup> Below that size, the turnover frequency was lower and the methane selectivity was higher. Above that size, the turnover frequency decreased again. The particle size effects for cobalt carbides were, similar as for metallic cobalt, linked to the available surface sites.<sup>184,229,236,237</sup> Small nanoparticles mainly exposed the  $\text{Co}_2\text{C}(111)$  surface, which favored methane formation.<sup>236,237</sup> The stepped  $\text{Co}_2\text{C}(101)$  and  $\text{Co}_2\text{C}(020)$  surfaces were responsible for olefin formation.<sup>236</sup> We would herein like to conform the active sites on cobalt carbide nanoparticles to the “ $\text{B}_n$  site” notation. B then represents cobalt atoms, C represents carbon atoms, and n denotes the number of atoms in close contact to an absorbed active species. The  $\text{Co}_2\text{C}(101)$  surface is then noted as  $\text{B}_7\text{C}_2$  and the  $\text{Co}_2\text{C}(020)$  surface as  $\text{B}_6\text{C}_1$ .

Even though metallic cobalt is generally accepted as the active phase, cobalt carbides may represent a hidden gem in FTS catalysis, provided that the cobalt carbide phase synergizes with an oxidic compound and/or an alkali promoter.

#### **1.5.5.4 General properties of carbon deposits and their role in Fischer-Tropsch Synthesis**

Carbon deposition is a rather broad collective term that can be confusing when not elaborated. It essentially describes all carbon on the catalyst surface, ranging from a single carbon atom to vast sheets of graphitic carbon. Some of them are intermediates in the FTS reaction, while others block certain active sites. Hence, it is indispensable to clarify the specific structure when describing carbon deposits, as they can either be advantageous or detrimental. When used sensibly, carbon deposition is a promising tool for tweaking selectivity in the FTS reaction.

Carbon deposits are generally gray or black solids that can either be crystalline or amorphous, depending on their structure. The most well-known crystalline carbon allotropes are diamond, with a cubic crystal structure, and graphite, with a hexagonal crystal structure. Diamond is applied in for example cutting tools and gemstones. Graphite is used in pencils and lubricants, as well as electronics for its high conductivity. Only graphite is formed as crystalline carbon deposition on catalyst surfaces.

Amorphous carbon could be any kind of carbon allotrope without crystalline structure. The properties of amorphous carbon are dependent on  $sp^2$  and  $sp^3$  ratios and can vary strongly. These types of carbon are for example applied as pigments, gas storage materials, or in catalysis.<sup>238</sup>

Similarly to cobalt carbides, the role of carbon deposits in cobalt-based FTS remains rather obscure. Some studies describe carbon deposition as deactivation mechanism,<sup>99</sup> while others argue that carbon deposition is beneficial for generating an active FTS catalyst.<sup>79,190</sup> To offer some clarification, we should first divide carbon deposits into atomic, amorphous aliphatic, amorphous (poly)aromatic, and crystalline. Finally, we will briefly describe subsurface carbon deposits. Atomic carbon is a single carbon atom on the cobalt surface resulting from C-O bond scission. These carbon atoms are considered the most reactive type of carbon deposition.<sup>118</sup> Amorphous carbon is a relatively reactive type of carbon deposition and can often be removed from the cobalt surface by hydrogenation.<sup>190</sup> Crystalline carbon represents a class of carbon materials with a highly-ordered structure. Graphite, a monolayer of  $sp^2$  carbon atoms arranged in a hexagonal lattice, is the most relevant type of crystalline carbon in the FTS reaction. Multiple layers of graphite stacked on top of each other is referred to as graphene. Subsurface carbon describes a location instead of a chemical phase and indicates carbon atoms at interstitial positions of a metal lattice.<sup>193</sup>

Atomic carbon has been reported to weaken the adsorption of CO and  $H_2$ .<sup>118</sup> However, it is also an intermediate in the FTS reaction and does not prevent the cobalt surface from adsorbing reactants. Therefore, atomic carbon is not considered a detrimental form of carbon deposition.

Amorphous aliphatic carbon deposits are relatively reactive and can easily be removed from the surface by hydrogenation at typical FTS reaction temperatures  $<260^\circ\text{C}$ .<sup>99,239</sup> Such deposits, for example a growing hydrocarbon chain, are generally intermediates in the FTS reaction and not considered detrimental to catalyst performance.

Amorphous (poly)aromatic carbon deposits are typically less reactive than the aliphatic version. It is known that (oxygenated) (poly)aromatic (hydro)carbon deposits form on cobalt-based catalysts during the FTS reaction.<sup>79,190</sup> These species are only considered detrimental if they cannot be removed from the surface by hydrogenation below 350°C.<sup>99,115</sup>

Crystalline (graphitic) carbon can arise from amorphous carbon structures on the catalyst surface and is known to kinetically, thermodynamically, and geometrically prefer flat cobalt terrace sites over step-edges.<sup>239</sup> When such species are irreversibly adsorbed on the catalyst surface, they are considered as deactivating. However, graphitic carbon has also been reported to selectively block methanation sites.<sup>190</sup> This could be interesting for FTS, as methane is an unwanted side product.

Subsurface carbon arises from diffusion of atomic carbon on the catalyst surface into the metal lattice. Some studies mentioned that subsurface carbon may decrease catalyst activity.<sup>91,99</sup> However, it has been reported before that carbon migration to subsurface cobalt layers is only energetically feasible at high carbon coverage and unlikely to occur to a significant extent under FTS conditions.<sup>193</sup> Subsurface carbon may precede and initiate the formation of bulk cobalt carbides.<sup>228</sup> Similarly to cobalt carbides, subsurface carbon may thus require the presence of oxidic surfaces and/or alkali promoters to be stabilized.

#### **1.5.5.5 General properties of cobalt-support interfaces and their role in Fischer-Tropsch Synthesis**

Transition metals, like cobalt, are known to interact with metal oxide supports and the strength of these metal-support interactions (MSIs) correlates with the reducibility of the support. The "strong metal-support interactions" (SMSIs) between transition metals and the reducible TiO<sub>2</sub> support, leading to reduced CO and H<sub>2</sub> chemisorption, were first described by Tauster *et al.* in 1978.<sup>240</sup> They explained that Ti<sup>4+</sup> can be reduced to Ti<sup>3+</sup>, which then transfers an electron to the supported metal atom. This would result in a strong ionic bond between Ti<sup>3+</sup> and the metal.<sup>241,242</sup>

Support materials used in heterogeneous catalysis are typically not inert and their interactions with metal nanoparticles may give rise to interfaces with special properties. Such interfaces have been reported to enhance catalytic performance in the cobalt-based FTS and CO<sub>2</sub> hydrogenation.<sup>242-245</sup> Over the past few decades, varying reasons for this behavior have been mentioned in the literature. Understanding these special interfaces is of great significance in rational catalyst design.

The two main factors contributing to MSIs are electronic and geometric. The electronic factor results from charge transfer between the support and the metal, while the geometric factor originates from a thin layer of reduced support oxide covering the metal.<sup>246</sup> The strength of MSIs depends on the reducibility of the support oxide. If MSIs are too strong, they are considered deleterious for catalyst performance.<sup>247</sup> In particular, when support oxide patches are covering active sites or when solid state reactions form an inactive metal-support compound.<sup>108,208,213</sup> However, when MSIs are too weak, they will not influence the catalytic performance at all and in order to benefit from MSIs it is thus essential to find the optimum interaction strength.

Theoretical and experimental evidence suggests that the interface between cobalt and reducible oxides, like  $\text{TiO}_2$ ,<sup>109,245</sup>  $\text{CeO}_2$ ,<sup>183,243</sup>  $\text{La}_2\text{O}_3$ ,<sup>181</sup> or  $\text{MnO}$ <sup>138,173,174</sup> offers a low-energy reaction pathway and thereby enhances FTS and  $\text{CO}_2$  hydrogenation activity. Various elemental steps have been mentioned to occur *via* these low-energy reaction pathways at cobalt-support interfaces. For FTS catalysts, CO dissociation<sup>248,249</sup> as well as C-C coupling<sup>250</sup> have been postulated as the facilitated elementary steps at the metal-support interface. More specifically for cobalt FTS catalysts, CO and  $\text{CO}_2$  dissociation have been mentioned for Co- $\text{TiO}_2$ ,<sup>109,245</sup> possibly due to electron transfer from Ti to cobalt. For Co- $\text{CeO}_2$ , CO and  $\text{CO}_2$  dissociation were the facilitated elementary steps as well, potentially due to the formation of oxygen vacancies in the  $\text{CeO}_2$  support.<sup>183,243</sup>

$\text{La}_2\text{O}_3$  and  $\text{MnO}$  are mostly used as promoters rather than support materials. However, they are widely used in FTS, so we will briefly discuss them here. Like the previously mentioned reducible oxides,  $\text{La}_2\text{O}_3$ <sup>251</sup> and  $\text{MnO}$ <sup>174</sup> facilitate electron transfer. But, instead of donating electrons, they both withdraw electrons from cobalt and decrease reducibility. For Co- $\text{La}_2\text{O}_3$ , theoretical evidence pointed to C-C coupling as the elemental step to occur *via* a low-energy reaction pathway.<sup>181</sup> This enhanced the selectivity to higher alcohols. With  $\text{MnO}$ , the lower reducibility of cobalt resulted in lower hydrogenation activity and less of the unwanted product methane.<sup>172,174</sup> Besides,  $\text{MnO}$  increases olefin/paraffin ratio and oxygenates,<sup>172,252</sup> likely due to its activity in the WGS reaction.<sup>138,174</sup> One could argue that the addition of  $\text{MnO}$  to a cobalt-based FTS catalyst makes the catalyst more similar to iron-based systems.

MSIs provide an opportunity to enhance the FTS activity and even to tweak the selectivity, when carefully orchestrated. They could create interfaces with special properties or simply alter the reducibility of the metal nanoparticles.

### 1.5.6 The Co/TiO<sub>2</sub> Showcase

As this PhD Thesis focusses on the Co/TiO<sub>2</sub> FTS catalyst, the active and deactivating phases of this material will be comprehensively discussed. Cobalt supported on TiO<sub>2</sub> is of great importance in FTS, both in academic and industrial settings. TiO<sub>2</sub> was first mentioned by Tauster *et al.* in the 1980s as an activity-enhancing support in the FTS reaction.<sup>241,242</sup> Since then, many scientists have been elucidating the underlying reasons for this behaviour. Our research group has contributed to the better understanding of the Co/TiO<sub>2</sub> system in FTS,<sup>80,100,168,170,171,173,174,207,253,254</sup> using advanced spectroscopic characterization techniques, such as XRD,<sup>100,255</sup> X-ray absorption spectroscopy (XAS),<sup>173,254-256</sup> Raman spectroscopy,<sup>100</sup> (scanning) transmission X-ray microscopy ((S)TXM),<sup>79,207</sup> and X-ray Raman scattering (XRS) spectroscopy,<sup>81</sup> under realistic reaction conditions.

The Co/TiO<sub>2</sub> catalyst is an intricate system. As briefly discussed before, TiO<sub>2</sub> is a reducible metal oxide that actively participates in the formation of the active phase under FTS reaction conditions. The three most common crystal phases of TiO<sub>2</sub> are: Anatase (tetragonal), brookite (orthorhombic), and rutile (tetragonal).<sup>257</sup> The phases can be distinguished for example with vibrational spectroscopy<sup>257</sup> or XRD.<sup>258</sup> Often mixtures of the two tetragonal crystal phases, such as P90 (90% anatase, 10% rutile),<sup>79,81</sup> are used in heterogeneous catalysis. Both anatase and rutile TiO<sub>2</sub> can already be reduced to TiO<sub>2-x</sub> suboxide species in H<sub>2</sub> at temperatures above 300°C.<sup>187</sup> These suboxides interact electronically with the cobalt nanoparticles, leading to the formation of interfaces with special properties, e.g. enhanced FTS activity.<sup>241,242</sup> However, if these MSIs are too strong, TiO<sub>2-x</sub> suboxide species may block active sites or cobalt titanate (CoTiO<sub>3</sub>) may be formed.<sup>108</sup> This inactive metal-support compound is more likely to be formed at high CO conversions and when cobalt oxides are present in the catalyst under reaction conditions. The latter is because positively charged Co<sup>2+</sup> more readily accepts an electron than Co<sup>0</sup>. With the Co/TiO<sub>2</sub> system, it is thus only a fine line between enhanced activity and deactivation.

The first step towards understanding these so-called unique interfaces (*i.e.* interfaces with enhanced catalytic properties) is detecting and characterizing them in detail, preferably under relevant reaction conditions. X-ray absorption spectroscopy is a promising technique, because it is element specific and sensitive to the direct surroundings of atoms (*i.e.*, local bonds and oxidation state). Nevertheless, experiments that aim to study low energy elements such as C and O with Co/TiO<sub>2</sub> can be challenging due to the relatively short attenuation length, which is element specific as well, of TiO<sub>2</sub> (**Figure 1.14a**). The intensity of the X-ray beam is reduced according to Beer-Lambert's law as it traverses through the material, mainly caused by strong absorption of photons by TiO<sub>2</sub>, which is the main component (80-90% by weight) of a typical Co/TiO<sub>2</sub> FTS catalyst. The X-ray intensity decrease is material dependent and typically quantified by the parameter

attenuation length, which describes the distance into a material where the X-ray intensity has dropped to 1/e of its original value.<sup>259</sup> The attenuation length below the Ti L-edge is  $\sim 600$  nm, while at the C K-edge, O K-edge, and Co L-edge it is only  $\sim 200$ -350 nm. At the Ti K-edge and Co K-edge it can reach up to  $\sim 9$  and 18  $\mu\text{m}$ , respectively. High resolution imaging methods based on X-ray absorption spectroscopy (XAS), such as STXM (**Figure 1.14b** and **1.15c**), are promising for detecting and characterizing interfaces. Such methods can, for example, be used to distinguish various cobalt oxidation states from each other (**Figure 1.14c**) or to analyze oxidation state variations at different locations in a catalyst particle (**Figure 1.14b**). However, sample thickness is an important feature to control when using an X-ray transmission imaging technique. Particularly when measuring in the soft X-ray regime (50-2000 eV<sup>14</sup>), the sample thickness is limited to 200-600 nm in order to obtain a decent signal-to-noise ratio. Working in the soft X-ray regime is, for example, inevitable when characterizing carbon deposition (C K-edge 270-350 eV) on a catalyst surface. The low energy X-rays used, attenuate to 1/e after a rather short distance (200-300 nm) (**Figure 1.14a**). Sample thickness is therefore an optimum in a rather narrow window. If the sample is too thick, the X-rays cannot travel through the material, but if the sample is too thin, there is not enough signal to draw any meaningful conclusions about e.g., the direct surroundings of the carbon atoms.

Besides, bulk characterization techniques do not suffice for detecting and characterizing interfaces. If interfaces are present in a catalyst material, their concentration is far lower compared to the bulk phases. A surface-sensitive or nanoscale chemical imaging technique, such as high resolution STXM<sup>14,79,80</sup> or TXM,<sup>80,207,260</sup> could offer an outcome when characterizing low concentration interfaces is the aim (**Figure 1.15c** and **d**).

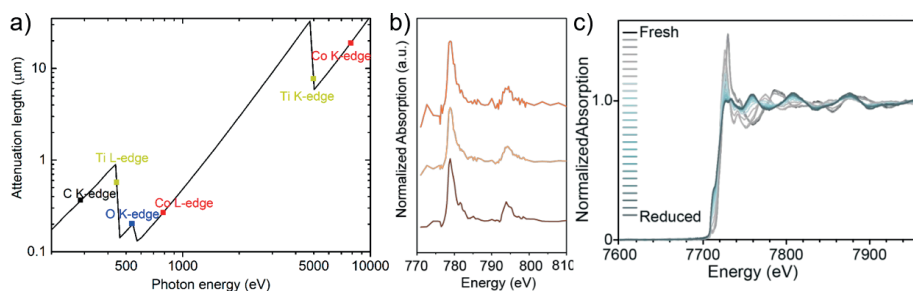


**Figure 1.14. X-ray spectroscopy characterization of Co/TiO<sub>2</sub>** **a**) X-ray attenuation length at the C K-, Ti L-, O K-, Co L-, Ti K-, and Co K-edge. The TiO<sub>2</sub> density was set at 3.9 g/cm<sup>3</sup> (anatase) and the beam incident angle at 90°. Calculated via<sup>259</sup>. **b**) Co L<sub>2,3</sub>-edge spectra of a 15 wt.% Co/TiO<sub>2</sub> catalyst particle after reduction in H<sub>2</sub> as measured with *in situ* STXM. Reprinted with permission from<sup>79</sup>. Copyright (2018) John Wiley and Sons. **c**) Co K-edge spectra of a 15 wt.% Co/TiO<sub>2</sub> catalyst during reduction in H<sub>2</sub> as measured with *in situ* XAS. Reprinted with permission from<sup>255</sup>. Copyright (2021) American Chemical Society.

Besides X-ray-based imaging techniques, electron-based imaging techniques are promising to characterize interfaces as well (**Table 1.1**). By themselves, electron-based techniques, such as transmission electron microscopy (TEM) are not necessarily element specific. However, when combined with energy dispersive X-ray (EDX) spectroscopy or electron energy loss spectroscopy (EELS), high resolution chemical mapping can be achieved (**Figure 1.15a**).<sup>80</sup> Similar to X-ray-based methods, TEM-EDX and TEM-EELS are limited by the effect of sample thickness too.<sup>261</sup>

Furthermore, the widely used vibrational spectroscopy techniques IR and Raman (micro) spectroscopy are promising tools to study carbon-containing species on Co and Co-TiO<sub>2</sub> interfaces. These techniques are based on the principle that molecules absorb or scatter specific frequencies of light that correspond to the vibrational frequencies of their unique bonds. However, those techniques can be complicated due to the strong absorption of IR and visible light by the black Co/TiO<sub>2</sub> system. Besides, the reduced TiO<sub>2</sub> suboxide species (TiO<sub>2-x</sub>) exhibit high IR and visible light absorption activity. This is beneficial for photocatalytic applications,<sup>262</sup> but becomes problematic during vibrational spectroscopy experiments under FTS reaction conditions. Moreover, the need for a surface-sensitive or nanoscale chemical imaging technique applies to vibrational spectroscopy as well. The spatial resolutions of both IR and Raman spectroscopy are limited by the wavelength. For Raman spectroscopy this is in the range of several hundreds of nanometers (e.g., 532 nm<sup>263</sup>), but for IR spectroscopy the wavelength ranges from 1 μm to 1000 μm. The diffraction limitations can be overcome by combining vibrational spectroscopy with scanning probe techniques, such as atomic force microscopy (AFM).<sup>75,76</sup> Examples of this include AFM-Raman, tip-enhanced Raman spectroscopy (TERS),<sup>10,264</sup> AFM-IR, and photo-induced force microscopy (PiFM).<sup>75,265</sup> Using such state-of-the-art methods under FTS reaction conditions is extremely challenging and although developments are ongoing,<sup>76,266</sup> we still have a long road ahead.

Apart from the unique interfaces between cobalt and TiO<sub>2</sub> (e.g., resulting in enhanced FTS activity<sup>241,242</sup>), carbide formation and carbon deposition are important to detect and characterize. Both cobalt carbide formation and carbon deposition are phenomena that start at the catalyst surface under FTS reaction conditions. Bulk characterization techniques may again be insufficient to detect these phenomena at an early stage. Soft X-ray spectroscopy techniques can detect carbon species by measuring at the C K-edge (~280 eV) and may offer a solution. Surface-sensitive techniques, such as XPS (**Figure 1.15b**),<sup>82,109,190</sup> and nanoscale chemical imaging techniques, such as STXM (**Figure 1.15c**),<sup>79</sup> allow analysis of carbon deposits even under FTS reaction conditions. STXM, however, has been able to operate at higher pressure (several bars) compared to XPS (mbar range).



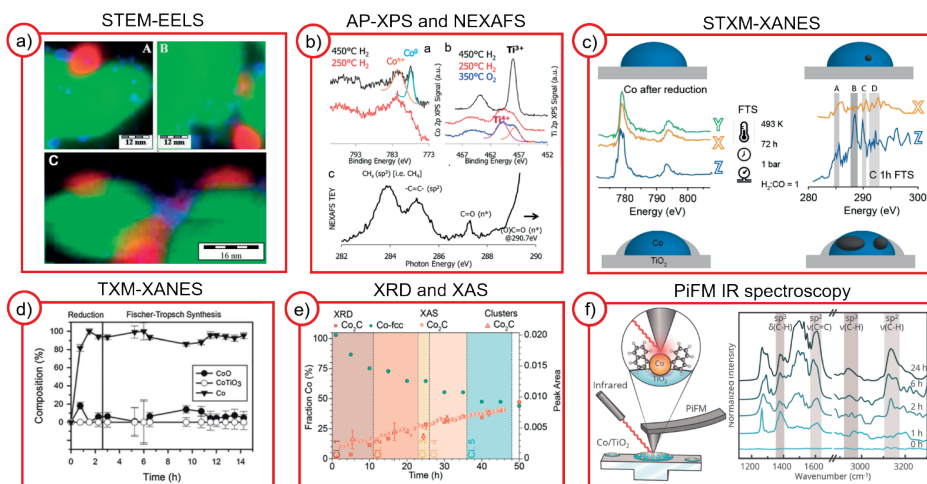


**Figure 1.15. Overview of promising techniques used and results obtained for Co/TiO<sub>2</sub> from different studies** **a)** STEM – electron energy loss spectroscopy (EELS) results on a reduced CoMn/TiO<sub>2</sub> catalyst, showing interfaces between cobalt and titania. Reproduced from reference <sup>170</sup> and from reference <sup>171</sup> with permission from the PCCP Owner Societies. **b)** Ambient pressure (AP) – XPS at (a) Co 2p and (b) Ti 2p core levels under the given conditions (T=250–450°C, P=100–150 mTorr), as well as (c) *in situ* near edge X-ray absorption fine edge structure (NEXAFS) results at the C K-edge under CO<sub>2</sub> hydrogenation conditions (T=250°C, P=1 bar, H<sub>2</sub>/CO<sub>2</sub>=3). Reprinted with permission from <sup>109</sup>. Copyright (2014) American Chemical Society. **c)** *Operando* STXM – XANES results on a Co/TiO<sub>2</sub> catalyst under FTS reaction conditions (T=220°C, P=1 bar, H<sub>2</sub>/CO=1). The Co L-edge (left) shows that particles X and Y contain metallic cobalt, whereas particle Z is slightly oxidized. As a result, particle Z forms more carbon deposits (C K-edge, right) compared to particles X and Y. Reprinted with permission from <sup>79</sup>. Copyright (2018) John Wiley and Sons. **d)** *In situ* TXM – X-ray absorption near edge structure (XANES) results indicating the cobalt phases present in a Co/TiO<sub>2</sub> catalyst particle under FTS reaction conditions (T=250°C, P=10 bar, H<sub>2</sub>/CO=2). Reproduced from reference <sup>207</sup> with permission from The Royal Society of Chemistry. **e)** *Operando* XRD and XAS results on a Co/TiO<sub>2</sub> catalyst indicating the cobalt phases present under FTS reaction conditions (T=220°C, P=16 bar, H<sub>2</sub>/CO=1). Reprinted with permission from <sup>255</sup>. Copyright (2021) American Chemical Society. **f)** Scanning probe vibrational spectroscopy: Photo-induced force microscopy (PiFM) IR spectroscopy to detect carbon species on a Co/TiO<sub>2</sub> FTS catalyst post FTS (T=220°C, P=1 bar, H<sub>2</sub>/CO=2), as will be discussed in **Chapter 3**.

Carbon deposition was linked to an increased selectivity towards the desired long-chain hydrocarbon products.<sup>190</sup> Scanning probe vibrational spectroscopy techniques (**Figure 1.15f**) are promising too for detecting surface carbides and carbon deposition, as will be demonstrated in this PhD Thesis. However, employing these techniques under realistic FTS conditions is challenging and still in its infancy.

Resolving the debate regarding the active and deactivating phases in cobalt-based FTS has been and still remains challenging. The main issues we need to address more clearly in the open literature are the catalyst synthesis procedure and the resulting

catalyst properties, such as cobalt nanoparticle size, the properties of the support material, and the reaction conditions. Besides, clarifying speculations regarding surface and/or interface phenomena, such as interfaces with enhanced catalytic properties between cobalt and  $\text{TiO}_2$ , requires surface-sensitive and/or nanoscale chemical imaging techniques under relevant FTS reaction conditions. Progress with X-ray-based techniques has certainly been made over the past few decades,<sup>79,207,209,261</sup> while for the field of scanning probe vibrational spectroscopy developments are still ongoing.<sup>76</sup> An overview highlighting promising characterization techniques and results obtained on  $\text{Co/TiO}_2$  can be found in **Figure 1.10**.

Nevertheless, based on the discussion above we can now briefly summarize some general findings regarding the active and deactivating phases in the  $\text{Co/TiO}_2$  FTS system. The catalytically active phases in the  $\text{Co/TiO}_2$  FTS catalyst are metallic cobalt,<sup>92,108</sup> the interface between metallic cobalt or cobalt oxide and  $\text{TiO}_2$ ,<sup>109</sup> and metallic cobalt with atomic or amorphous carbon deposition.<sup>79,118</sup> The deactivating phases are cobalt titanates<sup>108</sup> and metallic cobalt with graphitic carbon deposition, which specifically inhibits methane formation.<sup>190</sup> Cobalt carbides can be active in FTS and selective towards olefins and oxygenates, provided that they are stabilized by an oxidic compound<sup>139,178,179,181,183,227,231</sup> and/or alkali promoter.<sup>140,178</sup> The active cobalt phase under FTS reaction conditions is dependent on the composition of the syngas feed, which determines both the chemical potentials of carbon ( $\mu_c$ ) and oxygen ( $\mu_o$ ). When the chemical potentials are higher than the critical chemical potential ( $\mu_{\text{cri}}$ ), a phase transition can take place.<sup>184,267</sup> For example, when  $\mu_c > \mu_{\text{cri}}$  cobalt carbide will be formed and when  $\mu_o > \mu_{\text{cri}}$  cobalt oxide will be formed. In the classical cobalt-based FTS scenario, the syngas feed is produced from natural gas and has  $\text{H}_2/\text{CO}=2$  (**Figure 1.16a**). Metallic cobalt is the main active phases under such conditions, while some  $\text{CoO}$  and metal-support interfaces could be present as well. Linear paraffin products are then the output of the reaction. Under high  $\text{CO}$  conversion conditions, large amounts of water may deactivate the catalyst *via* e.g. sintering, oxidation, or the formation of inactive metal-support compounds.<sup>108</sup> If coal, plastic, and potentially municipal waste are used as feedstock, the syngas contains typically more  $\text{CO}$ , e.g.  $\text{H}_2/\text{CO} \leq 1$  (**Figure 1.16b**). Under such reaction conditions, carbon deposition is often formed and possibly surface and/or bulk cobalt carbide, as  $\mu_c > \mu_{\text{cri}}$ . The output then shifts to olefin and oxygenated products. Under these conditions, the  $\text{CO}_2$  content at the reactor exit may be significant enough to induce surface oxidation. Besides, water could again lead to deactivation at high conversion rates. Waste streams from metallurgy are generally a mixture of  $\text{H}_2/\text{CO}/\text{CO}_2$ , with  $[\text{CO}] > [\text{CO}_2]$ , and could also be used as syngas (**Figure 1.16c**). Metallic cobalt is again the main active phase under such conditions, while some  $\text{CoO}$  and metal-support interfaces could also be present and paraffin products are the output. Another waste stream that could be employed as

syngas comes from the steel industry. This is also a mixture of  $H_2/CO/CO_2$ , with  $[CO] < [CO_2]$  (Figure 1.16d).<sup>268</sup> This feed, as well as the feed from metallurgy, is slightly more oxidizing due to the presence of  $CO_2$ . The active phases under these conditions are metallic cobalt or CoO and potentially metal-support interfaces. The output are paraffin products and the amount of methane likely scales with the concentration of  $CO_2$  vs. CO. For both the feeds from metallurgy and the steel industry, it is expected that water may deactivate the catalyst at high conversion rates.

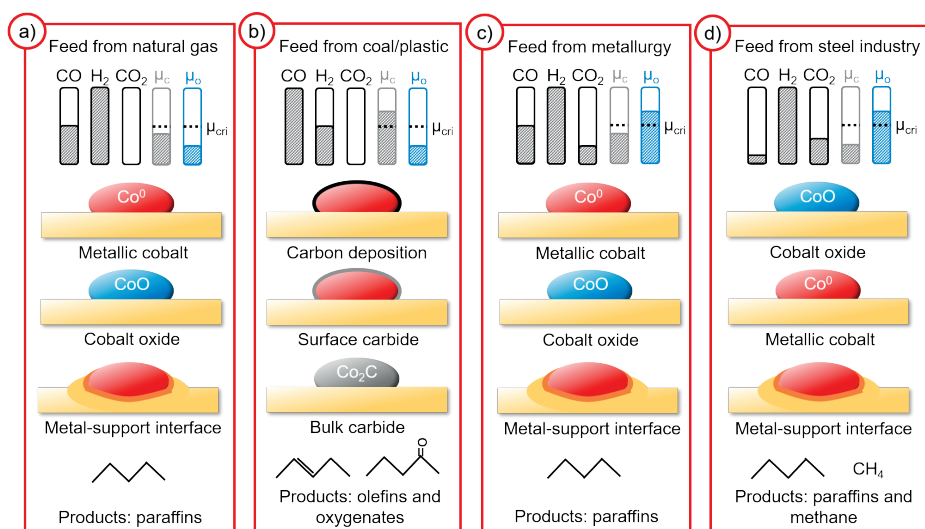


**Figure 1.16. Overview of the chemical potentials  $\mu_c$  and  $\mu_o$  under Fischer-Tropsch Synthesis conditions** The composition of syngas, which is dependent on the feedstock, determines the cobalt active phase under reaction conditions and the final products that are formed. Syngas prepared from: **a)** Natural gas ( $H_2/CO=2$ ); metallic cobalt is present under these conditions and potentially some CoO and/or metal-support interfaces. **b)** Coal, plastic, or municipal waste ( $H_2/CO \leq 1$ ); carbon deposition is likely formed under these conditions, as well as surface and/or bulk cobalt carbide. **c)** Metallurgy ( $H_2/CO/CO_2$  with  $[CO] > [CO_2]$ ); metallic cobalt, CoO, and potentially metal-support interfaces are present under these conditions (D) Steel production ( $H_2/CO/CO_2$  with  $[CO] < [CO_2]$ ); metallic cobalt, CoO, and potentially metal-support interfaces are present under these conditions.

## 1.6 Concluding Remarks

The discussed literature on the active and inactive phases of a cobalt-based Fischer-Tropsch Synthesis catalyst underlines that the reported opinions are divergent. Most often, multiple phases coexist under FTS reaction conditions, which makes it challenging to correlate one specific phase to e.g., enhanced performance or deactivation. Most researchers believe that metallic cobalt is the true active phase in FTS. However, cobalt

oxides, cobalt carbides, cobalt with carbon deposition, and cobalt-support interfaces have all been reported as active phases as well. This is summarized in **Table 1.2**. However, specific terms have to be met in order for the aforementioned cobalt phases to be active in FTS:

- Cobalt oxides have only been reported as active in FTS when supported on a reducible metal oxide support.
- Cobalt carbides have been reported active in FTS and selective to olefins and/or oxygenates, provided that they are stabilized by and in synergy with an oxidic compound and/or an alkali promoter.
- Cobalt with carbon deposition has only been considered an active phase if the carbon species are atomic or amorphous and can be removed from the surface by hydrogenation below 350°C.
- Cobalt-support interfaces have been reported to enhance the FTS activity, when the support was a reducible metal oxide and given that the interactions were not too strong. Oxidic promoter elements have also been reported to form interfaces with cobalt that display enhanced FTS activity.

**Table 1.2.** Proposed active and inactive phases in the cobalt-based Fischer-Tropsch Synthesis.

Phase	Short description	Active	Inactive
Metallic cobalt	Metallic cobalt is formed in the catalyst during reduction in H <sub>2</sub> and is the most widely accepted active phase in FTS.	92,105,108,122,124,130,187,25 2,269,270	n.a.
Cobalt oxides	Cobalt oxides often coexist with metallic cobalt in the catalyst under FTS reaction conditions. The presence of water promotes re-oxidation of small cobalt nanoparticles.	109,138,188,189	91,108,210,211
Cobalt carbides	Cobalt carbides can form under FTS reaction conditions, especially in CO-rich conditions and under high pressure. Typically, an alkali or oxidic compound is needed for stabilization.	139,140,178,181- 184,223,224,226,228- 230,236,255,271	81,91,100,185-187
Cobalt with carbon deposition	Carbon deposition is present on the catalyst under reaction conditions. This can be in atomic, amorphous aliphatic, amorphous (poly)aromatic, or graphitic form.	79,118,239	91,99,115
Metal-support interfaces	Metal-support interfaces can form readily on reducible supports during reduction or FTS.	109,138,173,174,181,183,241,247- 250	247
Metal-support compounds	Mixed-metal support compounds can form at high CO conversion conditions in the presence of water.	n.a.	91,108,208-210,213

If these terms are not met, the cobalt phases mentioned above are often reported as inactive or deactivating in FTS. Additionally, cobalt with irreversible carbon deposition and cobalt-support compounds have exclusively been reported as deactivating in FTS. Catalyst deactivation is a multifaceted process and under reaction conditions and it is likely that different mechanisms play a role in the overall deteriorating catalyst activity and selectivity. Over the past decade, progress has been made with surface-sensitive and nanoscale chemical imaging techniques under reaction conditions (*in situ*), while monitoring the activity and selectivity (*operando*). Besides, long-term deactivation studies, both with synchrotron and lab-based techniques, have been enabled by close collaborations between industry and academia. Examples of such collaborations are investigating actual commercial catalysts and designing reactors for spectroscopic studies under industrially-relevant reaction conditions. All of this has contributed tremendously to our understanding of the active and inactive phases in cobalt-based FTS. However, promising developments are still ongoing and will likely lead to new insights. For example, advances in scanning probe vibrational spectroscopy, which will be one of the topics of this PhD Thesis.

**1**

### 1.7 Scope and Outline of this PhD Thesis

Society as we know it has industrial catalysis at its core. For example, the well-known Haber-Bosch process has enabled large-scale ammonia synthesis and thus food production for the ceaselessly growing global population, while the so-called Fischer-Tropsch Synthesis (FTS) process has been contributing to fuel production since the 1920s. Currently, the latter process offers great future potential to enrich energy supplies, for example by recycling deleterious carbon-containing exhaust gases, such as CO<sub>2</sub>. Both industry and academia are constantly in pursuit of improvement when it comes to process efficiency and product yield. Facilitating this improvement starts with fundamentally understanding the catalytically active sites and the relevant reaction mechanisms. The goal of this PhD Thesis is two-fold: first, to provide insight into the active phase of cobalt-based catalysts for CO and CO<sub>2</sub> hydrogenation. Secondly, to uncover the reaction mechanisms at play during the formation of (un)desired reaction products and catalyst deactivation. To achieve these two goals, the capabilities and limitations of contemporary spectroscopy and microscopy techniques are explored.

**Chapter 2** discusses nanoscale spectroscopy and how this methodology can answer open questions in catalysis research. We will first introduce the nanoscale chemical imaging tool photo-induced force microscopy (PiFM), which records nanoscale infrared (IR) spectra with a very sharp tip. We will highlight some of its recent applications, including nano-sized plastic particle detection in environmental samples and catalytic

material characterization. Then, we will outline the barriers that have to be overcome to use so-called tip-based spectroscopy methods under realistic reaction conditions. To understand the fundamental phenomena that take place during catalytic processes, analytical techniques with nanoscale resolution should be employed under relevant reaction conditions (*i.e.*, at elevated temperature and pressures). However, tip-based spectroscopy tools used in academic research typically operate under vacuum or low pressure and with simplified model catalysts. These two chasms have to be crossed to make fundamental findings more relevant for industrial catalysis. To aid this process, a more realistic model catalyst system will be introduced in **Chapter 2**. The system consists of cobalt nanoparticles stabilized by ordered mesoporous titania micro-islands. We demonstrate that the intricacies of industrial catalysts are well-represented, while the model system is flat enough for analysis with photo-induced force microscopy, a surface-sensitive tool.

**Chapter 3** focuses on the reaction mechanisms involved in hydrocarbon product formation and carbon deposition onto the catalyst surface during the CO hydrogenation reaction with a Co/TiO<sub>2</sub> FTS catalyst. A multitude of unconventional spectroscopic techniques is required to decipher the myriad of reaction mechanisms that can occur during this reaction. Modulation excitation (ME) spectroscopy is used to increase the sensitivity of IR spectroscopy and to uncover active species and intermediates. Oxygen-containing species appear as active species on the Co/TiO<sub>2</sub> surface, indicating that C-O bond scission may be assisted by hydrogen atoms. Shell-isolated nanoparticle-enhanced Raman spectroscopy (SHINERS) is used during CO hydrogenation at elevated temperatures and pressures to enhance the spectroscopic sensitivity and to observe surface species. We observe evidence for direct C-O bond scission, without the aid of hydrogen atoms. Carbon deposition onto the catalyst surface, which is addressed with PiFM, Raman micro-spectroscopy, and scanning transmission X-ray microscopy (STXM), occurs via unsaturated carbonaceous species.

**Chapter 4** investigates the catalytically active phase and reaction mechanisms at play during CO<sub>2</sub> hydrogenation with cobalt-based catalysts. Various support oxide materials are used to stabilize the cobalt (oxide) nanoparticles. We find that cobalt oxide nanoparticles on a titania support perform best in terms of long-chain hydrocarbon production. This refutes the general consensus that metallic cobalt nanoparticles are the (only) active phase in cobalt-based catalysts. We use ME-IR spectroscopy to shed light on the reaction mechanisms at play and find that, independent of the support material, metallic cobalt and cobalt oxide follow different reaction pathways when forming hydrocarbon products from CO<sub>2</sub>.

**Chapter 5** evaluates the effects of promoter element potassium on cobalt-based CO and CO<sub>2</sub> hydrogenation. The addition of potassium to Co/TiO<sub>2</sub> shifts the product selectivity towards longer hydrocarbon chains with more unsaturated bonds. Kinetic parameters are studied at elevated temperatures and pressures to explain these phenomena. The addition of alkali elements, like potassium, to the catalyst formulation appears particularly interesting for CO<sub>2</sub> valorization purposes. The lower methane selectivity and longer hydrocarbon chain length is caused by two particular effects: Firstly, the addition of potassium leads to an increase in reverse water gas shift activity, forming the more reactive CO molecule and thereby increasing the overall CO<sub>2</sub> conversion. Secondly, a decrease in the amount of hydrogen on the catalyst surface increases the C-C coupling probability. The promoting effect exerted by potassium will be compared with the effects of manganese, a promoter element frequently used in industrial cobalt-based FTS processes, and the cobalt oxide phase, linking the results back to **Chapter 4**.

**Chapter 6** investigates the use of solid industrial mineral residue from biomass gasification as catalyst material. The iron-containing mineral residue converts a mixed gas stream of CO, CO<sub>2</sub>, H<sub>2</sub>, and N<sub>2</sub> into methane (57%) and C<sub>2</sub>-C<sub>5</sub> olefins (43%). We demonstrate with *operando* X-ray diffraction that the transformation of metallic iron into an iron carbide phase increases both the catalytic activity and selectivity towards the desired olefin reaction products. While the mineral residue would otherwise have been discarded as industrial waste, the findings in **Chapter 6** offer a new perspective on how waste streams can be utilized.

The PhD Thesis ends in **Chapter 7** with a summary, concluding remarks, and connecting the dots, thereby presenting some future perspectives. This includes an outlook on recent developments and possible experiments in future heterogeneous catalysis research. Additional information can be found in **Chapter 8**, which contains a Dutch summary, a list of abbreviations, a list of publications, conferences, awards, and outreach activities, acknowledgements, and a curriculum vitae of the author.

### 1.8 Author Contributions and Acknowledgements

This Chapter is based on the book chapter “ten Have, I. C., Vogt, C., Meirer, F., Weckhuysen, B. M. The History of *Operando* Spectroscopy. *In Preparation*. (2022).” and the manuscript: “ten Have, I. C. & Weckhuysen, B. M. (2021). The active phase in cobalt-based Fischer-Tropsch synthesis. *Chem Catalysis*, 1, 339-363.”

The original plans for the book chapter and review article were conceived by Bert Weckhuysen. The book chapter was further constructed by Iris ten Have under the supervision

of Bert Weckhuysen and with input from Charlotte Vogt and Florian Meirer. The review article was further constructed and written by Iris ten Have under the supervision of Bert Weckhuysen. Prof. Dr. E.T.C. Vogt is gratefully acknowledged for providing the crystal structures and XRD patterns in **Figure 1.12**.



## 1.9 References

1. Loyson, P. Influences from Latin on Chemical Terminology. *Journal of Chemical Education* **87**, 1303-1307 (2010).
2. Loyson, P. Influences of Ancient Greek on Chemical Terminology. *Journal of Chemical Education* **86**, 1195-1199 (2009).
3. Schoebrechts, J. P., Colery, J. C., Lunsford, J. H., Lunsford, J. H., Samanta, C., Jana, P. & Sciences, P. Strong Release of Methane on Mars in Northern Summer 2003. *Science* **323**, 1041-1046 (2009).
4. Weckhuysen, B. M. Snapshots of a working catalyst: Possibilities and limitations of in situ spectroscopy in the field of heterogeneous catalysis. *Chemical Communications* **2**, 97-110 (2002).
5. Coates, J. in *Encyclopedia of analytical chemistry: applications, theory and instrumentation* (ed. Meyers, R. A.) 10815-10837 (John Wiley & Sons, New York, 2006).
6. Nishikida, K. & Coates, J. in *Handbook of plastics analysis* (eds. Lobo, H. & Bonilla, J. V.) (CRC Press, Boca Raton, 2003).
7. Stuart, B. H. *Infrared Spectroscopy: Fundamentals and Applications. Infrared Spectroscopy: Fundamentals and Applications* **8**, (2005).
8. Barnes, R. B. & Bonner, L. G. The Early History and the Methods of Infrared Spectroscopy. *American Journal of Physics* **4**, 181-189 (1936).
9. Commissariat, T. Raman technique peers into cabin baggage. (2012). at <<https://physicsworld.com/a/raman-technique-peers-into-cabin-baggage/>>
10. Hartman, T., Wondergem, C. S., Kumar, N., van den Berg, A. & Weckhuysen, B. M. Surface- and Tip-Enhanced Raman Spectroscopy in Catalysis. *Journal of Physical Chemistry Letters* **7**, 1570-1584 (2016).
11. Ferrari, A. C. & Basko, D. M. Raman spectroscopy as a versatile tool for studying the properties of graphene. *Nature Nanotechnology* **8**, 235-246 (2013).
12. van Grieken, R. E. & Markowicz, A. A. Quantification in XRF analysis of intermediate-thickness samples in *Handbook of X-ray spectrometry* **235**, 407-435 (CRC press, Boca Raton, 2001).
13. Timoshenko, J. & Roldan Cuenya, B. In Situ/Operando Electrocatalyst Characterization by X-ray Absorption Spectroscopy. *Chemical Reviews* **121**, 882-961 (2021).
14. Hitchcock, A. P. Soft X-ray spectromicroscopy and ptychography. *Journal of Electron Spectroscopy and Related Phenomena* **200**, 49-63 (2015).
15. Preul, M. C., Caramanos, Z., Collins, D. L., Villemure, J.-G., LeBlanc, R., Olivier, A., Pokrupa, R. & Arnold, D. L. Accurate, noninvasive diagnosis of human brain tumors by using proton magnetic resonance spectroscopy. *Nature Medicine* **2**, 323-325 (1996).
16. Dazzi, A. & Prater, C. B. AFM-IR: Technology and applications in nanoscale infrared spectroscopy and chemical imaging. *Chemical Reviews* **117**, 5146-5173 (2017).
17. Huth, F., Govyadinov, A., Amarie, S., Nuansing, W., Keilmann, F. & Hillenbrand, R. Nano-FTIR absorption spectroscopy of molecular fingerprints at 20 nm spatial resolution. *Nano Letters* **12**, 3973-3978 (2012).
18. Ramer, G., Aksyuk, V. A. & Centrone, A. Quantitative Chemical Analysis at the Nanoscale Using the Photothermal Induced Resonance Technique. *Analytical Chemistry* **89**, 13524-13531 (2017).
19. Dazzi, A., Saunier, J., Kjoller, K. & Yagoubi, N. Resonance enhanced AFM-IR: A new powerful way to characterize blooming on polymers used in medical devices. *International Journal of Pharmaceutics* **484**, 109-114 (2015).

20. Bayda, S., Adeel, M., Tuccinardi, T., Cordani, M. & Rizzolio, F. The history of nanoscience and nanotechnology: From chemical-physical applications to nanomedicine. *Molecules* **25**, 1-15 (2020).
21. Weckhuysen, B. M. *In-situ Spectroscopy of Catalysts* (American Scientific Publishers, Stevenson Ranch, 2004).
22. Weckhuysen, B. M. Chemistry: Catalysts live and up close. *Nature* **439**, 548 (2006).
23. Weckhuysen, B. M. Determining the active site in a catalytic process: Operando spectroscopy is more than a buzzword. *Physical Chemistry Chemical Physics* **5**, 4351-4360 (2003).
24. Weckhuysen, B. M. Studying birth, life and death of catalytic solids with operando spectroscopy. *National Science Review* **2**, 147-149 (2015).
25. Weckhuysen, B. M. Snapshots of a working catalyst: Possibilities and limitations of in situ spectroscopy in the field of heterogeneous catalysis. *Chemical Communications* **2**, 97-110 (2002).
26. Weckhuysen, B. M. & Schoonheydt, R. A. Alkane dehydrogenation over supported chromium oxide catalysts. *Catalysis Today* **51**, 223-232 (1999).
27. Weckhuysen, B. M. & Schoonheydt, R. A. Recent progress in diffuse reflectance spectroscopy of supported metal oxide catalysts. *Catalysis Today* **49**, 441-451 (1999).
28. Weckhuysen, B. M., Verberckmoes, A. A., Debaere, J., Ooms, K., Langhans, I. & Schoonheydt, R. A. In situ UV-Vis diffuse reflectance spectroscopy - On line activity measurements of supported chromium oxide catalysts: Relating isobutane dehydrogenation activity with Cr-speciation via experimental design. *Journal of Molecular Catalysis A: Chemical* **151**, 115-131 (2000).
29. Weckhuysen, B. M., Voort, P. & Catana, G. *Spectroscopy of transition metal ions on surfaces*. (Leuven University Press, Leuven, 2000).
30. Puurunen, R. L., Beheydt, B. G. & Weckhuysen, B. M. Monitoring chromia/alumina catalysts in situ during propane dehydrogenation by optical fiber UV-visible diffuse reflectance spectroscopy. *Journal of Catalysis* **204**, 253-257 (2001).
31. Puurunen, R. L. & Weckhuysen, B. M. Spectroscopic study on the irreversible deactivation of chromia/alumina dehydrogenation catalysts. *Journal of Catalysis* **210**, 418-430 (2002).
32. Harrison, P. G. & Daniell, W. Catalytic activity, surface redox properties, and structural evolution during the thermal processing of chromium-promoted ceria oxidation catalysts. *Chemistry of Materials* **13**, 1708-1719 (2001).
33. Ishimori, M. & Tsuruta, T. Infrared studies on organometallic compounds as polymerization catalysts. I. Diethylzinc-alcohol system for epoxide polymerization. *Die Makromolekulare Chemie* **64**, 190-206 (1963).
34. Heyne, H. & Tompkins, F. C. Application of infrared spectroscopy and surface potential measurements in a study of the oxidation of carbon monoxide on platinum. *Proceedings of the Royal Society of London. Series A. Mathematical and Physical Sciences* **292**, 460-478 (1966).
35. Ipatieff, V. N. Mixed Catalysts. *Science* **91**, 605-608 (1940).
36. Eischens, R. P., Pliskin, W. A. & Francis, S. A. Infrared spectra of chemisorbed carbon monoxide. *The Journal of Chemical Physics* **22**, 1786-1787 (1954).
37. Mapes, J. E. & Eischens, R. P. The infrared spectra of ammonia chemisorbed on cracking catalysts. *The Journal of Physical Chemistry* **58**, 1059-1062 (1954).
38. Yaroslavskii, N. G. & Terenin, A. N. Infrazrasnye Spektry Pogloscheniya Adsorbirovannykh Molekul. *Doklady Akademii Nauk SSSR* **66**, 885-888 (1949).
39. Kurbatov, L. N., Nueimin, G. C. -. *Doklady Akademii Nauk SSSR* **68**, 341 (1949).
40. Yaroslavskii, N. G., Karayakin, A. V. -. *Doklady Akademii Nauk SSSR* **85**, 1103 (1952).

41. Wood, B. J., Wise, H. & Yolles, R. S. Selectivity and Stoichiometry of Copper Oxide in Propylene Oxidation. *Journal of Catalysis* **15**, 355-362 (1969).
42. Ishimori, M. & Tsuruta, T. Infrared studies on organometallic compounds as polymerization catalysts. I. Diethylzinc-alcohol system for epoxide polymerization. *Die Makromolekulare Chemie* **64**, 190-206 (1963).
43. Heyne, H. & Tompkins, F. C. Application of infrared spectroscopy and surface potential measurements in a study of the oxidation of carbon monoxide on platinum. *Proceedings of the Royal Society of London. Series A. Mathematical and Physical Sciences* **292**, 460-478 (1966).
44. Wood, B. J., Wise, H. & Yolles, R. S. Selectivity and Stoichiometry of Copper Oxide in Propylene Oxidation. *Journal of Catalysis* **15**, 355-362 (1969).
45. Chuang, T. T. & Dalla Lana, I. G. Catalytic Activity and Selectivity of NaOH-Doped  $\gamma$ -Aluminas. Dehydration and Dehydrogenation of 3-Pentanol. *Journal of the Chemical Society, Faraday Transactions 1: Physical Chemistry in Condensed Phases* **68**, 773-784 (1971).
46. Howe, R. F., Davidson, D. E. & Whan, D. A. Infrared spectra and catalytic activity of supported molybdenum hexacarbonyl. *Journal of the Chemical Society, Faraday Transactions 1: Physical Chemistry in Condensed Phases* **68**, 2266-2280 (1972).
47. Raupp, G. B. & Delgass, W. N. Mössbauer Investigation of Supported Fe Catalysts: III. In Situ Kinetics and Spectroscopy during Fischer-Tropsch Synthesis. *Journal of Catalysis* **58**, 361-369 (1979).
48. Niwa, M., Yagi, K. & Murakami, Y. A Magnetic Resonance Study of the  $\text{Fe}_{2\text{O}_3}/\text{Al}_2\text{O}_3$  Catalyst in a CO- $\text{N}_2\text{O}$  Reaction. *Bull Chem Soc Jpn* **54**, 975-979 (1981).
49. Bianchi, D., Borcar, S., Teule-Gay, F. & Bennett, C. O. Evolution of surface and bulk compositions of an iron catalyst in relation to catalytic activity for the Fischer-Tropsch reaction. *Journal of Catalysis* **82**, 442-456 (1983).
50. Vaishnav, P. P. & Montano, P. A.  $^{57}\text{Fe}$  Mössbauer Spectroscopic Study of the Geometrical Effects in the Catalytic Reactions with Intercalation Compounds. *MRS Online Proceedings Library (OPL)* **20**, 397-402 (1983).
51. Raupp, G. B. & Delgass, W. N. Mössbauer Investigation of Supported Fe Catalysts: III. In Situ Kinetics and Spectroscopy during Fischer-Tropsch Synthesis. *Journal of Catalysis* **58**, 361-369 (1979).
52. Mochida, I., Fujitsu, H. & Ikeyama, N. Infrared spectroscopic study of catalytic activity of Rh/ $\text{TiO}_2$  for the CO +  $\text{H}_2$  reaction. *Journal of the Chemical Society, Faraday Transactions 1: Physical Chemistry in Condensed Phases* **83**, 1427-1436 (1987).
53. Eriksen, K. M., Fehrmann, R. & Bjerrum, N. J. ESR investigations of sulfuric acid catalyst deactivation. *Journal of Catalysis* **132**, 263-265 (1991).
54. Eriksen, K. M., Karydis, D. A., Boghosian, S. & Fehrmann, R. Deactivation and Compound Formation in Sulfuric Acid Catalysts and Model Systems. *Journal of Catalysis* **155**, 32-42 (1995).
55. Masters, S. G., Chrissanthopoulos, A., Eriksen, K. M., Boghosian, S. & Fehrmann, R. Catalytic activity and deactivation of  $\text{SO}_2$  oxidation catalysts in simulated power plant flue gases. *Journal of Catalysis* **166**, 16-24 (1997).
56. Brückner, A., Radnik, J., Hoang, D. L. & Lieske, H. In situ investigation of active sites in zirconia-supported chromium oxide catalysts during the aromatization of n-octane. *Catalysis Letters* **60**, 183-189 (1999).
57. Topsøe, N. Y. & Topsøe, H. Combined in-situ FTIR and on-line activity studies: applications to vanadia-titania DeNOx catalyst. *Catalysis Today* **9**, 77-82 (1991).
58. Topsøe, N. Y., Topsøe, H. & Dumesic, J. A. Vanadia/Titania Catalysts for Selective Catalytic Reduction (SCR) of Nitric Oxide by Ammonia. *Journal of Catalysis* **151**, 226-240 (1995).

59. Topsøe, N. Y., Topsøe, H. & Dumesic, J. A. Vanadia/Titania Catalysts for Selective Catalytic Reduction of Nitric Oxide by Ammonia: II. Studies of Active Sites and Formulation of Catalytic Cycles. *Journal of Catalysis* **151**, 241-252 (1995).
60. Wachs, I. E., Jehng, J. M., Deo, G., Weckhuysen, B. M., Gulians, V. V., Benziger, J. B. & Sundaresan, S. Fundamental studies of butane oxidation over model-supported vanadium oxide catalysts: Molecular structure-reactivity relationships. *Journal of Catalysis* **170**, 75-88 (1997).
61. Weckhuysen, B. M., Bensalem, A., Schoonheydt, R. A. & Interfasciechemie, D. In situ UV - VIS diffuse reflectance spectroscopy - on-line activity measurements catalyzed by supported chromium oxide catalysts. *Journal of the Chemical Society, Faraday Transactions* **94**, 2011-2014 (1998).
62. Valden, M., Lai, X. & Goodman, D. W. Onset of catalytic activity of gold clusters on titania with the appearance of nonmetallic properties. *Science* **281**, 1647-1650 (1998).
63. Campbell, R. A. & Goodman, D. W. A new design for a multitechnique ultrahigh vacuum surface analysis chamber with high pressure capabilities. *Review of Scientific Instruments* **63**, 172-174 (1992).
64. Knop-Gericke, A., Hävecker, M., Schedel-Niedrig, T. & Schlögl, R. High-pressure low-energy XAS: A new tool for probing reacting surfaces of heterogeneous catalysts. *Topics in Catalysis* **10**, 187-198 (2000).
65. Thomas, J. M. & Sankar, G. The role of synchrotron-based studies in the elucidation and design of active sites in titanium - Silica epoxidation catalysts. *Accounts of Chemical Research* **34**, 571-581 (2001).
66. Ruitenbeek, M., van Dillen, A. J., de Groot, F. M. F., Wachs, I. E., Geus, J. W. & Koningsberger, D. C. The structure of vanadium oxide species on  $\gamma$ -alumina; an in situ X-ray absorption study during catalytic oxidation. *Topics in Catalysis* **10**, 241-254 (2000).
67. Grunwaldt, J. D., Molenbroek, A. M., Topsøe, N. Y., Topsøe, H. & Clausen, B. S. In situ investigations of structural changes in Cu/ZnO catalysts. *Journal of Catalysis* **194**, 452-460 (2000).
68. Grunwaldt, J. D., Basini, L. & Clausen, B. S. In situ EXAFS study of Rh/Al<sub>2</sub>O<sub>3</sub> catalysts for catalytic partial oxidation of methane. *Journal of Catalysis* **200**, 321-329 (2001).
69. Bulushev, D. A., Kiwi-Minsker, L., Zaikovskii, V. I. & Renken, A. Formation of active sites for selective toluene oxidation during catalyst synthesis via solid-state reaction of V<sub>2</sub>O<sub>5</sub> with TiO<sub>2</sub>. *Journal of Catalysis* **193**, 145-153 (2000).
70. Brückner, A. Simultaneous combination of in situ-EPR/UV-VIS/on line GC: A novel setup for investigating transition metal oxide catalysts under working conditions. *Chemical Communications* **1**, 2122-2123 (2001).
71. Guerrero-Pérez, M. O. & Banares, M. A. Operando Raman study of alumina-supported Sb-V-O catalyst during propane ammoxidation to acrylonitrile with on-line activity measurement. *Chemical Communications* **2**, 1292-1293 (2002).
72. Bañares, M. A., Guerrero-Pérez, M. O., Fierro, J. L. G. & Cortez, G. G. Raman spectroscopy during catalytic operations with on-line activity measurement (operando spectroscopy): A method for understanding the active centres of cations supported on porous materials. *Journal of Materials Chemistry* **12**, 3337-3342 (2002).
73. Bañares, M. A. & Wachs, I. E. Molecular structures of supported metal oxide catalysts under different environments. *Journal of Raman Spectroscopy* **33**, 359-380 (2002).
74. Jarzembski, A., Shaskey, C. & Park, K. Review: Tip-based vibrational spectroscopy for nanoscale analysis of emerging energy materials. *Frontiers in Energy* **12**, 43-71 (2018).

75. Nowak, D., Morrison, W., Wickramasinghe, H. K., Jahng, J., Potma, E., Wan, L., Ruiz, R., Albrecht, T. R., Schmidt, K., Frommer, J., Sanders, D. P. & Park, S. Nanoscale chemical imaging by photoinduced force microscopy. *Science Advances* **2**, e1501571 (2016).
76. Bechtel, H. A., Johnson, S. C., Khatib, O., Muller, E. A. & Raschke, M. B. Synchrotron infrared nano-spectroscopy and -imaging. *Surface Science Reports* **75**, 100493 (2020).
77. Jahng, J., Potma, E. O. & Lee, E. S. Nanoscale spectroscopic origins of photoinduced tip-sample force in the midinfrared. *Proceedings of the National Academy of Sciences of the United States of America* **116**, 26359–26366 (2019).
78. Li, J. F. & Tian, Z. Q. Shell-Isolated Nanoparticle-Enhanced Raman Spectroscopy (SHINERS). *Nature* **464**, 392–396 (2010).
79. van Ravenhorst, I. K., Vogt, C., Oosterbeek, H., Bossers, K. W., Moya-Cancino, J. G., van Bavel, A. P., van der Eerden, A. M. J., Vine, D., de Groot, F. M. F., Meirer, F. & Weckhuysen, B. M. Capturing the Genesis of an Active Fischer-Tropsch Synthesis Catalyst with Operando X-ray Nanospectroscopy. *Angewandte Chemie International Edition* **57**, 11957–11962 (2018).
80. Cats, K. H., Andrews, J. C., Stéphan, O., March, K., Karunakaran, C., Meirer, F., de Groot, F. M. F. & Weckhuysen, B. M. Active phase distribution changes within a catalyst particle during Fischer-Tropsch synthesis as revealed by multi-scale microscopy. *Catalysis Science & Technology* **6**, 4438–4449 (2016).
81. Moya-Cancino, J. G., Honkanen, A., van der Eerden, A. M. J., Oord, R., Monai, M., ten Have, I. C., Sahle, C. J., Meirer, F., Weckhuysen, B. M. & de Groot, F. M. F. In Situ X-ray Raman Scattering Spectroscopy of the Formation of Cobalt Carbides in a Co/TiO<sub>2</sub> Fischer-Tropsch Synthesis Catalyst. *ACS Catalysis* **11**, 809–819 (2021).
82. Zhong, L., Chen, D. & Zafeiratos, S. A mini review of in situ near-ambient pressure XPS studies on non-noble, late transition metal catalysts. *Catalysis Science and Technology* **9**, 3851–3867 (2019).
83. Fu, D., Schmidt, J. E., Ristanović, Z., Chowdhury, A. D., Meirer, F. & Weckhuysen, B. M. Highly Oriented Growth of Catalytically Active Zeolite ZSM-5 Films with a Broad Range of Si/Al Ratios. *Angewandte Chemie International Edition* **56**, 11217–11221 (2017).
84. Kwak, J. H., Hu, J., Lukaski, A., Kim, D. H., Szanyi, J. & Peden, C. H. F. Role of Pentacoordinated Al<sup>3+</sup> Ions in the High Temperature Phase Transformation of  $\gamma$ -Al<sub>2</sub>O<sub>3</sub>. *The Journal of Physical Chemistry C* **112**, 9486–9492 (2008).
85. Hagen, J. *Industrial Catalysis: A Practical Approach* **9783527684656**, (Wiley-VCH Verlag GmbH & Co. KGaA, Weinheim, 2015).
86. Chapman, J., Ismail, A. E. & Dinu, C. Z. Industrial Applications of Enzymes: Recent Advances, Techniques, and Outlooks. *Catalysts* 2018, Vol. 8, Page 238 **8**, 238 (2018).
87. Erisman, J. W., Sutton, M. A., Galloway, J., Klimont, Z. & Winiwarter, W. How a century of ammonia synthesis changed the world. *Nature Geoscience* **1**, 636–639 (2008).
88. Fischer, F. & Tropsch, H. The preparation of synthetic oil mixtures (synthol) from carbon monoxide and hydrogen. *Brennst.-Chem.* **4**, 276–285 (1923).
89. Fischer, F. & Tropsch, H. The synthesis of petroleum at atmospheric pressures from gasification products of coal. *Brennst.-Chem.* **7**, 97–104 (1926).
90. ten Have, I. C. & Weckhuysen, B. M. The active phase in cobalt-based Fischer-Tropsch synthesis. *Chem Catalysis* **1**, 339–363 (2021).
91. Tsakoumis, N. E., Rønning, M., Borg, Ø., Rytter, E. & Holmen, A. Deactivation of cobalt based Fischer-Tropsch catalysts: A review. *Catalysis Today* **154**, 162–182 (2010).

92. van de Loosdrecht, J., Botes, F. G., Ciobica, I. M., Ferreira, A., Gibson, P., Moodley, D. J., Saib, A. M., Visagie, J. L., Weststrate, C. J. & Niemantsverdriet, J. W. in *Comprehensive Inorganic Chemistry II: from elements to applications* **7**, 525-557 (Elsevier, Amsterdam, 2013).
93. Luk, H. T., Mondelli, C., Ferre, C., Stewart, J. A. & Pe, J. Status and prospects in higher alcohols synthesis from syngas. *Chemical Society Reviews* **46**, 1358-1426 (2016).
94. Fischer, F. & Tropsch, H. The preparation of synthetic oil mixtures (synthol) from carbon monoxide and hydrogen. *Brennst.-Chem.* **4**, 276-285 (1923).
95. Ye, R. P., Ding, J., Gong, W., Argyle, M. D., Zhong, Q., Wang, Y., Russell, C. K., Xu, Z., Russell, A. G., Li, Q., Fan, M. & Yao, Y. G. CO<sub>2</sub> hydrogenation to high-value products via heterogeneous catalysis. *Nature Communications* **10**, 5698 (2019).
96. Li, J., He, Y., Tan, L., Zhang, P., Peng, X., Oruganti, A., Yang, G., Abe, H., Wang, Y. & Tsubaki, N. Integrated tuneable synthesis of liquid fuels via Fischer-Tropsch technology. *Nature Catalysis* **1**, 787-793 (2018).
97. Li, W., Wang, H., Jiang, X., Zhu, J., Liu, Z., Guo, X. & Song, C. A short review of recent advances in CO<sub>2</sub> hydrogenation to hydrocarbons over heterogeneous catalysts. *RSC Advances* **8**, 7651-7669 (2018).
98. de Smit, E. & Weckhuysen, B. M. The renaissance of iron-based Fischer-Tropsch synthesis: On the multifaceted catalyst deactivation behaviour. *Chemical Society Reviews* **37**, 2758-2781 (2008).
99. Moodley, D. J., van de Loosdrecht, J., Saib, A. M., Overett, M. J., Datye, A. K. & Niemantsverdriet, J. W. Carbon deposition as a deactivation mechanism of cobalt-based Fischer-Tropsch synthesis catalysts under realistic conditions. *Applied Catalysis A: General* **354**, 102-110 (2009).
100. Cats, K. H. & Weckhuysen, B. M. Combined Operando X-ray Diffraction/Raman Spectroscopy of Catalytic Solids in the Laboratory: The Co/TiO<sub>2</sub> Fischer-Tropsch Synthesis Catalyst Showcase. *ChemCatChem* **8**, 1531-1542 (2016).
101. Loewert, M., Serrer, M. A., Carambia, T., Stehle, M., Zimina, A., Kalz, K. F., Lichtenberg, H., Saraçi, E., Pfeifer, P. & Grunwaldt, J. D. Bridging the gap between industry and synchrotron: An: Operando study at 30 bar over 300 h during Fischer-Tropsch synthesis. *Reaction Chemistry and Engineering* **5**, 1071-1082 (2020).
102. Böller, B., Durner, K. M. & Wintterlin, J. The active sites of a working Fischer-Tropsch catalyst revealed by operando scanning tunnelling microscopy. *Nature Catalysis* **2**, 1027-1034 (2019).
103. van Santen, R. A., Ciobîcă, I. M., van Steen, E. & Ghouri, M. M. Mechanistic Issues in Fischer-Tropsch Catalysis. *Advances in Catalysis* **54**, 127-187 (2011).
104. Zijlstra, B., Broos, R. J. P., Chen, W., Bezemer, G. L., Pilot, I. A. W. & Hensen, E. J. M. The Vital Role of Step-Edge Sites for Both CO Activation and Chain Growth on Cobalt Fischer-Tropsch Catalysts Revealed through First-Principles-Based Microkinetic Modeling Including Lateral Interactions. *ACS Catalysis* **10**, 9376-9400 (2020).
105. Weststrate, C. J., Sharma, D., Garcia Rodriguez, D., Gleeson, M. A., Fredriksson, H. O. A. & Niemantsverdriet, J. W. (Hans). Mechanistic insight into carbon-carbon bond formation on cobalt under simulated Fischer-Tropsch synthesis conditions. *Nature Communications* **11**, 750 (2020).
106. Inderwildi, O. R., Jenkins, S. J. & King, D. A. Fischer-Tropsch mechanism revisited: Alternative pathways for the production of higher hydrocarbons from synthesis gas. *Journal of Physical Chemistry C* **112**, 1305-1307 (2008).
107. Weststrate, C. J., Gericke, H. J., Verhoeven, M. W. G. M., Ciobîcă, I. M., Saib, A. M. & Niemantsverdriet, J. W. Ethanol decomposition on Co(0001): C-O bond scission on a close-packed cobalt surface. *Journal of Physical Chemistry Letters* **1**, 1767-1770 (2010).

108. Wolf, M., Fischer, N. & Claeys, M. Water-induced deactivation of cobalt-based Fischer-Tropsch catalysts. *Nature Catalysis* **3**, 962-965 (2020).
109. Melaet, G., Ralston, W. T., Li, C. S., Alayoglu, S., An, K., Musselwhite, N., Kalkan, B. & Somorjai, G. A. Evidence of highly active cobalt oxide catalyst for the Fischer-Tropsch synthesis and CO<sub>2</sub> hydrogenation. *Journal of the American Chemical Society* **136**, 2260-2263 (2014).
110. Paalanen, P. P., van Vreeswijk, S. H. & Weckhuysen, B. M. Combined in Situ X-ray Powder Diffractometry/Raman Spectroscopy of Iron Carbide and Carbon Species Evolution in Fe(-Na-S)/ $\alpha$ -Al<sub>2</sub>O<sub>3</sub> Catalysts during Fischer-Tropsch Synthesis. *ACS Catalysis* **10**, 9837-9855 (2020).
111. Paalanen, P. P., van Vreeswijk, S. H., Dugulan, A. I. & Weckhuysen, B. M. Identification of Iron Carbides in Fe(-Na-S)/ $\alpha$ -Al<sub>2</sub>O<sub>3</sub> Fischer-Tropsch Synthesis Catalysts with X-ray Powder Diffractometry and Mössbauer Absorption Spectroscopy. *ChemCatChem* **12**, 5121-5139 (2020).
112. Rahmati, M., Safdari, M. S., Fletcher, T. H., Argyle, M. D. & Bartholomew, C. H. Chemical and Thermal Sintering of Supported Metals with Emphasis on Cobalt Catalysts during Fischer-Tropsch Synthesis. *Chemical Reviews* **120**, 4455-4533 (2020).
113. Bartholomew, C. H. Mechanisms of catalyst deactivation. *Applied Catalysis A: General* **212**, 17-60 (2001).
114. van Deelen, T. W., Hernández Mejía, C. & de Jong, K. P. Control of metal-support interactions in heterogeneous catalysts to enhance activity and selectivity. *Nature Catalysis* **2**, 955-970 (2019).
115. Weststrate, C. J., Ciobîcă, I. M., Saib, A. M., Moodley, D. J. & Niemantsverdriet, J. W. Fundamental issues on practical Fischer-Tropsch catalysts: How surface science can help. *Catalysis Today* **228**, 106-112 (2014).
116. Wang, Z., Yan, Z., Liu, C. & Goodman, D. W. Surface Science Studies on Cobalt Fischer-Tropsch Catalysts. *ChemCatChem* **3**, 551-559 (2011).
117. Oosterbeek, H. Bridging the pressure and material gap in heterogeneous catalysis: cobalt Fischer-Tropsch catalysts from surface science to industrial application. *Physical Chemistry Chemical Physics* **9**, 3570-3576 (2007).
118. Weststrate, C. J., Kazalkaya, A. C., Rossen, E. T. R., Verhoeven, M. W. G. M., Ciobîcă, I. M., Saib, A. M. & Niemantsverdriet, J. W. Atomic and polymeric carbon on Co(0001): Surface reconstruction, graphene formation, and catalyst poisoning. *Journal of Physical Chemistry C* **116**, 11575-11583 (2012).
119. Bell, A. T., Bond, G. C., Thompson, D. T., Valden, M., Lai, X., Goodman, D. W., Blasko, T., Nieto, J. M. L., Chen, K., Bell, A. T., Iglesia, E., Koyama, T., Komaya, T., Gai, P. L., Weyland, M., Durscher, G., Browning, N. D., Pennycook, S. J., Besenbacher, F., Thune, P. C., Loss, J., Wenter, D., Leustra, P. J., Niemantsverdriet, J. W., Corker, J., Vidal, V., Theolier, A., Thivolle-Cazat, J., Basset, J.-M., Nozkaki, C., Lugmair, C. G., Bell, A. T., Tilley, T. D., Kolb, D., Jong, K. P. de & Geus, J. W. The impact of nanoscience on heterogeneous catalysis. *Science* **299**, 1688-1691 (2003).
120. Navarro, V., van Spronsen, M. A. & Frenken, J. W. M. In situ observation of self-assembled hydrocarbon Fischer-Tropsch products on a cobalt catalyst. *Nature Chemistry* **8**, 929-934 (2016).
121. Weststrate, C. J., van Helden, P. & Niemantsverdriet, J. W. Reflections on the Fischer-Tropsch synthesis: Mechanistic issues from a surface science perspective. *Catalysis Today* **275**, 100-110 (2016).
122. Price, S. W. T., Martin, D. J., Parsons, A. D., Sławiński, W. A., Vamvakeros, A., Keylock, S. J., Beale, A. M. & Mosselmans, J. F. W. Chemical imaging of Fischer-Tropsch catalysts under operating conditions. *Science Advances* **3**, e1602838 (2017).

123. Hoffman, A. S., Singh, J. A., Bent, S. F. & Bare, S. R. In situ observation of phase changes of a silica-supported cobalt catalyst for the Fischer-Tropsch process by the development of a synchrotron-compatible in situ/operando powder X-ray diffraction cell. *Journal of Synchrotron Radiation* **25**, 1673–1682 (2018).
124. Qi, Z., Chen, L., Zhang, S., Su, J. & Somorjai, G. A. A mini review of cobalt-based nanocatalyst in Fischer-Tropsch synthesis. *Applied Catalysis A: General* **602**, 117701 (2020).
125. Storch, H. H., Anderson, R. A. & Golumbic, N. *The Fischer-Tropsch and related syntheses: including a summary of theoretical and applied contact catalysis*. (John Wiley & Sons, New York, 1951).
126. Anderson, R. B. Catalysts for the Fischer-Tropsch synthesis. *Catalysis* **4**, 29–255 (1956).
127. Chen, W., Filot, I. A. W., Pestman, R. & Hensen, E. J. M. Mechanism of Cobalt-Catalyzed CO Hydrogenation: 2. Fischer-Tropsch Synthesis. *ACS Catalysis* **7**, 8061–8071 (2017).
128. Hindermann, J. P., Hutchings, G. J. & Kiennemann, A. Mechanistic aspects of the formation of hydrocarbons and alcohols from CO hydrogenation. *Catalysis Reviews—Science and Engineering* **35**, 1–127 (1993).
129. Chen, W., Pestman, R., Zijlstra, B., Filot, I. A. W. & Hensen, E. J. M. Mechanism of Cobalt-Catalyzed CO Hydrogenation: 1. Methanation. *ACS Catalysis* **7**, 8050–8060 (2017).
130. Lyu, S., Wang, L., Zhang, J., Liu, C., Sun, J., Peng, B., Wang, Y., Rappé, K. G., Zhang, Y., Li, J. & Nie, L. Role of Active Phase in Fischer-Tropsch Synthesis: Experimental Evidence of CO Activation over Single-Phase Cobalt Catalysts. *ACS Catalysis* **8**, 7787–7798 (2018).
131. Pestman, R., Chen, W. & Hensen, E. Insight into the Rate-Determining Step and Active Sites in the Fischer-Tropsch Reaction over Cobalt Catalysts. *ACS Catalysis* **9**, 4189–4195 (2019).
132. Filot, I. A. W., van Santen, R. A. & Hensen, E. J. M. The optimally performing Fischer-Tropsch catalyst. *Angewandte Chemie International Edition* **53**, 12746–12750 (2014).
133. Zijlstra, B., Broos, R. J. P., Chen, W., Oosterbeek, H., Filot, I. A. W. & Hensen, E. J. M. Coverage Effects in CO Dissociation on Metallic Cobalt Nanoparticles. *ACS Catalysis* **9**, 7365–7372 (2019).
134. Zijlstra, B., Broos, R. J. P., Chen, W., Filot, I. A. W. & Hensen, E. J. M. First-principles based microkinetic modeling of transient kinetics of CO hydrogenation on cobalt catalysts. *Catalysis Today* **342**, 131–141 (2020).
135. Lindsay, D. & Kerr, W. Cobalt close-up. *Nature Chemistry* **3**, 494 (2011).
136. Greenwood, N. N. & Earnshaw, A. in *Chemistry of the Elements*, 1113–1143 (Elsevier, Amsterdam, 2012).
137. Lu, X., Heal, K. R., Ingalls, A. E., Doxey, A. C. & Neufeld, J. D. Metagenomic and chemical characterization of soil cobalamin production. *ISME Journal* **14**, 53–66 (2020).
138. Li, C. S., Melaet, G., Ralston, W. T., An, K., Brooks, C., Ye, Y., Liu, Y. S., Zhu, J., Guo, J., Alayoglu, S. & Somorjai, G. A. High-performance hybrid oxide catalyst of manganese and cobalt for low-pressure methanol synthesis. *Nature Communications* **6**, 6538 (2015).
139. Lin, T., Gong, K., Wang, C., An, Y., Wang, X., Qi, X., Li, S., Lu, Y., Zhong, L. & Sun, Y. Fischer-Tropsch Synthesis to Olefins: Catalytic Performance and Structure Evolution of Co<sub>2</sub>C-Based Catalysts under a CO<sub>2</sub> Environment. *ACS Catalysis* **9**, 9554–9567 (2019).
140. Zhang, S., Liu, X., Shao, Z., Wang, H. & Sun, Y. Direct CO<sub>2</sub> hydrogenation to ethanol over supported Co<sub>2</sub>C catalysts: Studies on support effects and mechanism. *Journal of Catalysis* **382**, 86–96 (2020).
141. Zhang, Q., Deng, W. & Wang, Y. Recent advances in understanding the key catalyst factors for Fischer-Tropsch synthesis. *Journal of Energy Chemistry* **22**, 27–38 (2013).



142. Sabatier, P. & Senderens, J. B. Direct hydrogenation of oxides of carbon in presence of various finely divided metals. *CR Acad Sci* **134**, 689-691 (1902).
143. Fischer, F. & Tropsch, H. Verfahren zur Gewinnung mehrgliedriger Paraffinkohlenwasserstoffe aus Kohlenoxyden und Wasserstoff auf katalytischem Wege. Patent DE 484337. (1925).
144. Fischer, F. & Tropsch, H. Process for the Production of Paraffin-Hydrocarbons with More than One Carbon Atom. US Patent 1746464. (1930).
145. Craxford, S. R. & Rideal, E. K. The Mechanism of the Synthesis of Hydrocarbons from Water Gas. *Journal of the Chemical Society (Resumed)* **338**, 1604-1614 (1939).
146. Storch, H. H. Catalysis in Synthetic Liquid-Fuel Processes. *Industrial & Engineering Chemistry* **37**, 340-351 (1945).
147. Herington, E. F. G. & Woodward, L. A. Experiments on the Fischer-Tropsch synthesis of hydrocarbons from carbon monoxide and hydrogen. *Transactions of the Faraday Society* **35**, 958-966 (1939).
148. Hamai, S. Physico-Chemical Investigations on Catalytic Mechanism. II. Note on The Fischer-Tropsch Synthesis of Hydrocarbons with Special Reference to its Reaction Mechanism. *Bull Chem Soc Jpn* **16**, 213-228 (1941).
149. Hofer, L. J. E. & Peebles, W. C. X-Ray Diffraction Studies of the Action of Carbon Monoxide on Cobalt-Thoria-Kieselguhr Catalysts. *Journal of the American Chemical Society* **69**, 2497-2500 (1947).
150. Weller, S., Hofer, L. J. E., Anderson, R. B., Weller, S., Hofer, L. J. E. & Anderson, R. B. The Role of Bulk Cobalt Carbide in the Fischer-Tropsch Synthesis. *Journal of the American Chemical Society* **70**, 799-801 (1948).
151. Kummer, J. T., DeWitt, T. W. & Emmett, P. H. Some Mechanism Studies on the Fischer-Tropsch Synthesis Using C<sup>14</sup>. *Journal of the American Chemical Society* **70**, 3632-3643 (1948).
152. Mattox, W. J. US Patent 2,515,245. (1950).
153. Blyholder, G. & Emmett, P. H. Fischer-Tropsch synthesis mechanism studies. The addition of radioactive ketene to the synthesis gas. *Journal of Physical Chemistry* **63**, 962-965 (1959).
154. Biloen, P. & Sachtler, W. M. H. Mechanism of Hydrocarbon Synthesis over Fischer-Tropsch Catalysts. *Advances in Catalysis* **30**, 165-216 (1981).
155. Reuel, R. C. & Bartholomew, C. H. Effects of support and dispersion on the CO hydrogenation activity/selectivity properties of cobalt. *Journal of Catalysis* **85**, 78-88 (1984).
156. Reuel, R. C. & Bartholomew, C. H. The stoichiometries of H<sub>2</sub> and CO adsorptions on cobalt: Effects of support and preparation. *Journal of Catalysis* **85**, 63-77 (1984).
157. Bessell, S. Support effects in cobalt-based Fischer-Tropsch catalysis. *Applied Catalysis A, General* **96**, 253-268 (1993).
158. Kogelbauer, A., Weber, J. C. & Goodwin, J. G. The formation of cobalt silicates on Co/SiO<sub>2</sub> under hydrothermal conditions. *Catalysis Letters* **34**, 259-267 (1995).
159. van de Loosdrecht, J., van der Haar, M., van der Kraan, A. M., van Dillen, A. J. & Geus, J. W. Preparation and properties of supported cobalt catalysts for Fischer-Tropsch synthesis. *Applied Catalysis A: General* **150**, 365-376 (1997).
160. Ming, H. & Baker, B. G. Characterization of cobalt Fischer-Tropsch catalysts I. Unpromoted cobalt-silica gel catalysts. *Applied Catalysis A, General* **123**, 23-36 (1995).
161. Khodakov, A. Y., Lynch, J., Bazin, D., Rebours, B., Zanier, N., Moisson, B. & Chaumette, P. Reducibility of cobalt species in silica-supported Fischer-Tropsch catalysts. *Journal of Catalysis* **168**, 16-25 (1997).

162. Ernst, B., Libs, S., Chaumette, P. & Kiennemann, A. Preparation and characterization of Fischer-Tropsch active Co/SiO<sub>2</sub> catalysts. *Applied Catalysis A: General* **186**, 145-168 (1999).
163. Khodakov, A. Y. Fischer-Tropsch synthesis: Relations between structure of cobalt catalysts and their catalytic performance. *Catalysis Today* **144**, 251-257 (2009).
164. Saib, A. M., Claeys, M. & van Steen, E. Silica supported cobalt Fischer-Tropsch catalysts: Effect of pore diameter of support. *Catalysis Today* **71**, 395-402 (2002).
165. Khodakov, A. Y., Bechara, R. & Griboval-Constant, A. Fischer-Tropsch synthesis over silica supported cobalt catalysts: Mesoporous structure versus cobalt surface density. *Applied Catalysis A: General* **254**, 273-288 (2003).
166. Soled, S. L., Iglesia, E., Fiato, R. A., Baumgartner, J. E., Vroman, H. & Miseo, S. Control of metal dispersion and structure by changes in the solid-state chemistry of supported cobalt Fischer-Tropsch catalysts. *Topics in Catalysis* **26**, 101-109 (2003).
167. Enache, D. I., Roy-Auberger, M. & Revel, R. Differences in the characteristics and catalytic properties of cobalt-based Fischer-Tropsch catalysts supported on zirconia and alumina. *Applied Catalysis A: General* **268**, 51-60 (2004).
168. Morales, F., de Groot, F. M. F., Glatzel, P., Kleimenov, E., Bluhm, H., Hävecker, M., Knop-Gericke, A. & Weckhuysen, B. M. In Situ X-ray Absorption of Co/Mn/TiO<sub>2</sub> Catalysts for Fischer-Tropsch Synthesis. *The Journal of Physical Chemistry B* **108**, 16201-16207 (2004).
169. Morales Cano, F., Gijzeman, O. L. J., de Groot, F. M. F. & Weckhuysen, B. M. Manganese promotion in cobalt-based Fischer-Tropsch catalysis. *Studies in Surface Science and Catalysis* **147**, 271-276 (2004).
170. Morales, F., de Groot, F. M. F., Gijzeman, O. L. J., Mens, A., Stephan, O. & Weckhuysen, B. M. Mn promotion effects in Co/TiO<sub>2</sub> Fischer-Tropsch catalysts as investigated by XPS and STEM-EELS. *Journal of Catalysis* **230**, 301-308 (2005).
171. Morales, F., Grandjean, D., de Groot, F. M., Stephan, O. & Weckhuysen, B. M. Combined EXAFS and STEM-EELS study of the electronic state and location of Mn as promoter in Co-based Fischer-Tropsch catalysts. *Physical Chemistry Chemical Physics* **7**, 568-572 (2005).
172. Morales, F. & Weckhuysen, B. M. Promotion Effects in Co-based Fischer-Tropsch Catalysis. *Catalysis* **19**, 1-40 (2006).
173. Morales, F., Grandjean, D., Mens, A., de Groot, F. M. F. & Weckhuysen, B. M. X-ray absorption spectroscopy of Mn/Co/TiO<sub>2</sub> Fischer-Tropsch catalysts: Relationships between preparation method, molecular structure, and catalyst performance. *Journal of Physical Chemistry B* **110**, 8626-8639 (2006).
174. Morales, F., de Smit, E., de Groot, F. M. F., Visser, T. & Weckhuysen, B. M. Effects of manganese oxide promoter on the CO and H<sub>2</sub> adsorption properties of titania-supported cobalt Fischer-Tropsch catalysts. *Journal of Catalysis* **246**, 91-99 (2007).
175. Saib, A. M., Moodley, D. J., Ciobîc, I. M., Hauman, M. M., Sigwebela, B. H., Weststrate, C. J., Niemantsverdriet, J. W. & van de Loosdrecht, J. Fundamental understanding of deactivation and regeneration of cobalt Fischer-Tropsch synthesis catalysts. *Catalysis Today* **154**, 271-282 (2010).
176. van Hardeveld, R. & Hartog, F. The statistics of surface atoms and surface sites on metal crystals. *Surface Science* **15**, 189-230 (1969).
177. van Hardeveld, R. & van Montfoort, A. The influence of crystallite size on the adsorption of molecular nitrogen on nickel, palladium and platinum: An infrared and electron-microscopic study. *Surface Science* **4**, 396-430 (1966).
178. Xiang, Y. & Kruse, N. Tuning the catalytic CO hydrogenation to straight-and long-chain aldehydes/alcohols and olefins/paraffins. *Nature Communications* **7**, 13058 (2016).

179. Zhong, L., Yu, F., An, Y., Zhao, Y., Sun, Y., Li, Z., Lin, T., Lin, Y., Qi, X., Dai, Y., Gu, L., Hu, J., Jin, S., Shen, Q. & Wang, H. Cobalt carbide nanoprisms for direct production of lower olefins from syngas. *Nature* **538**, 84–87 (2016).
180. Yang, R., Xia, Z., Zhao, Z., Sun, F., Du, X., Yu, H., Gu, S., Zhong, L., Zhao, J., Ding, Y. & Jiang, Z. Characterization of CoMn catalyst by in situ X-ray absorption spectroscopy and wavelet analysis for Fischer-Tropsch to olefins reaction. *Journal of Energy Chemistry* **32**, 118–123 (2019).
181. Lebarbier, V. M., Mei, D., Kim, D. H., Andersen, A., Male, J. L., Holladay, J. E., Rousseau, R. & Wang, Y. Effects of  $\text{La}_2\text{O}_3$  on the mixed higher alcohols synthesis from syngas over Co catalysts: A combined theoretical and experimental study. *Journal of Physical Chemistry C* **115**, 17440–17451 (2011).
182. Pei, Y. P., Liu, J. X., Zhao, Y. H., Ding, Y. J., Liu, T., Dong, W. Da, Zhu, H. J., Su, H. Y., Yan, L., Li, J. L. & Li, W. X. High alcohols synthesis via Fischer-Tropsch reaction at cobalt metal/carbide interface. *ACS Catalysis* **5**, 3620–3624 (2015).
183. Gnanamani, M. K., Jacobs, G., Graham, U. M., Ribeiro, M. C., Noronha, F. B., Shafer, W. D. & Davis, B. H. Influence of carbide formation on oxygenates selectivity during Fischer-Tropsch synthesis over Ce-containing Co catalysts. *Catalysis Today* **261**, 40–47 (2016).
184. Chen, P. P., Liu, J. X. & Li, W. X. Carbon Monoxide Activation on Cobalt Carbide for Fischer-Tropsch Synthesis from First-Principles Theory. *ACS Catalysis* **9**, 8093–8103 (2019).
185. Zhao, Y. H., Su, H. Y., Sun, K., Liu, J. & Li, W. X. Structural and electronic properties of cobalt carbide  $\text{Co}_2\text{C}$  and its surface stability: Density functional theory study. *Surface Science* **606**, 598–604 (2012).
186. Claeys, M., Dry, M. E., van Steen, E., du Plessis, E., van Berge, P. J., Saib, A. M. & Moodley, D. J. In situ magnetometer study on the formation and stability of cobalt carbide in Fischer-Tropsch synthesis. *Journal of Catalysis* **318**, 193–202 (2014).
187. Khodakov, A. Y., Chu, W. & Fongarland, P. Advances in the development of novel cobalt Fischer-Tropsch catalysts for synthesis of long-chain hydrocarbons and clean fuels. *Chemical Reviews* **107**, 1692–1744 (2007).
188. He, Z. H., Jiang, C. S., Wang, K., Wang, Z. Y., Li, N., Wang, W. T. & Liu, Z. T. Photothermal  $\text{CO}_2$  hydrogenation to methanol over a  $\text{CoO/Co/TiO}_2$  catalyst in aqueous media under atmospheric pressure. *Catalysis Today* **356**, 579–588 (2020).
189. Wang, L., Wang, L., Liu, X., Wang, H., Zhang, W., Yang, Q., Ma, J., Dong, X., Yoo, S. J., Kim, J.-G., Meng, X. & Xiao, F. Selective hydrogenation of  $\text{CO}_2$  into ethanol over cobalt catalysts. *Angewandte Chemie International Edition* **130**, 6212–6216 (2018).
190. Chen, W., Kimpel, T. F., Song, Y., Chiang, F. K., Zijlstra, B., Pestman, R., Wang, P. & Hensen, E. J. M. Influence of Carbon Deposits on the Cobalt-Catalyzed Fischer-Tropsch Reaction: Evidence of a Two-Site Reaction Model. *ACS Catalysis* **8**, 1580–1590 (2018).
191. Ono, F. & Maeta, H. Determination of Lattice Parameters in Hcp Cobalt By Using X-Ray Bond's Method. *Le Journal de Physique Colloques* **49**, C8-63–C8-64 (1988).
192. van Helden, P., Ciobîcă, I. M. & Coetzer, R. L. J. The size-dependent site composition of FCC cobalt nanocrystals. *Catalysis Today* **261**, 48–59 (2016).
193. van Helden, P. & Ciobîcă, I. M. A DFT study of carbon in the subsurface layer of cobalt surfaces. *ChemPhysChem* **12**, 2925–2928 (2011).
194. Kitakami, O., Sato, H., Shimada, Y., Sato, F. & Tanaka, M. Size effect on the crystal phase of cobalt fine particles. *Physical Review B* **56**, 849–854 (1997).

195. Gnanamani, M. K., Jacobs, G., Keogh, R. A., Shafer, W. D., Sparks, D. E., Hopps, S. D., Thomas, G. A. & Davis, B. H. Fischer-Tropsch synthesis: Effect of pretreatment conditions of cobalt on activity and selectivity for hydrogenation of carbon dioxide. *Applied Catalysis A: General* **499**, 39–46 (2015).
196. Liu, J. X., Su, H. Y., Sun, D. P., Zhang, B. Y. & Li, W. X. Crystallographic dependence of CO activation on cobalt catalysts: HCP versus FCC. *Journal of the American Chemical Society* **135**, 16284–16287 (2013).
197. Bezemer, G. L., Bitter, J. H., Kuipers, H. P. C. E., Oosterbeek, H., Holeywijn, J. E., Xu, X., Kapteijn, F., van Dillen, A. J. & de Jong, K. P. Cobalt particle size effects in the Fischer-Tropsch reaction studied with carbon nanofiber supported catalysts. *Journal of American Chemical Society* **128**, 3956–3964 (2006).
198. Den Breejen, J. P., Radstake, P. B., Bezemer, G. L., Bitter, J. H., Froseth, V., Holmen, A. & de Jong, K. P. On the Origin of the Cobalt Particle Size Effects in Fischer-Tropsch Catalysis. *Journal of the American Chemical Society* **131**, 7197–7203 (2009).
199. Foppa, L., Copéret, C. & Comas-Vives, A. Increased Back-Bonding Explains Step-Edge Reactivity and Particle Size Effect for CO Activation on Ru Nanoparticles. *Journal of the American Chemical Society* **138**, 16655–16668 (2016).
200. Iglesia, E. Design, synthesis, and use of cobalt-based Fischer-Tropsch synthesis catalysts. *Applied Catalysis A: General* **161**, 59–78 (1997).
201. Bezemer, G. L., Bitter, J. H., Kuipers, H. P. C. E., Oosterbeek, H., Holeywijn, J. E., Xu, X., Kapteijn, F., van Dillen, A. J. & de Jong, K. P. Cobalt particle size effects in the Fischer-Tropsch reaction studied with carbon nanofiber supported catalysts. *Journal of the American Chemical Society* **128**, 3956–3964 (2006).
202. Fischer, N., van Steen, E. & Claeys, M. Preparation of supported nano-sized cobalt oxide and fcc cobalt crystallites. *Catalysis Today* **171**, 174–179 (2011).
203. Prieto, G., Martínez, A., Concepción, P. & Moreno-Tost, R. Cobalt particle size effects in Fischer-Tropsch synthesis: structural and in situ spectroscopic characterisation on reverse micelle-synthesised Co/ITQ-2 model catalysts. *Journal of Catalysis* **266**, 129–144 (2009).
204. Borg, Ø., Dietzel, P. D. C., Spjelkavik, A. I., Tveten, E. Z., Walmsley, J. C., Diplas, S., Eri, S., Holmen, A. & Rytter, E. Fischer-Tropsch synthesis: Cobalt particle size and support effects on intrinsic activity and product distribution. *Journal of Catalysis* **259**, 161–164 (2008).
205. Xiong, H., Motchelaho, M. A. M., Moyo, M., Jewell, L. L. & Coville, N. J. Correlating the preparation and performance of cobalt catalysts supported on carbon nanotubes and carbon spheres in the Fischer-Tropsch synthesis. *Journal of Catalysis* **278**, 26–40 (2011).
206. Gupta, S. & Carrizosa, S. B. Graphene-Inorganic Hybrids with Cobalt Oxide Polymorphs for Electrochemical Energy Systems and Electrocatalysis: Synthesis, Processing and Properties. *Journal of Electronic Materials* **44**, 4492–4509 (2015).
207. Cats, K. H., Gonzalez-Jimenez, I. D., Liu, Y., Nelson, J., van Campen, D., Meirer, F., van der Eerden, A. M. J., de Groot, F. M. F., Andrews, J. C. & Weckhuysen, B. M. X-ray nanoscopy of cobalt Fischer-Tropsch catalysts at work. *Chemical Communications* **49**, 4622–4624 (2013).
208. Tsakoumis, N. E., Walmsley, J. C., Rønning, M., van Beek, W., Rytter, E. & Holmen, A. Evaluation of Reoxidation Thresholds for  $\gamma$ -Al<sub>2</sub>O<sub>3</sub>-Supported Cobalt Catalysts under Fischer-Tropsch Synthesis Conditions. *Journal of the American Chemical Society* **139**, 3706–3715 (2017).

209. Senecal, P., Jacques, S. D. M., Di Michiel, M., Kimber, S. A. J., Vamvakeros, A., Odarchenko, Y., Lezcano-Gonzalez, I., Paterson, J., Ferguson, E. & Beale, A. M. Real-Time Scattering-Contrast Imaging of a Supported Cobalt-Based Catalyst Body during Activation and Fischer-Tropsch Synthesis Revealing Spatial Dependence of Particle Size and Phase on Catalytic Properties. *ACS Catalysis* **7**, 2284-2293 (2017).
210. Wolf, M., Mutuma, B. K., Coville, N. J., Fischer, N. & Claeys, M. Role of CO in the Water-Induced Formation of Cobalt Oxide in a High Conversion Fischer-Tropsch Environment. *ACS Catalysis* 3985-3989 (2018).
211. van Berge, P. J., van de Loosdrecht, J., Barradas, S. & van der Kraan, A. M. Oxidation of cobalt based Fischer-Tropsch catalysts as a deactivation mechanism. *Catalysis Today* **58**, 321-334 (2000).
212. Dubrovin, R. M., Siverin, N. V., Prosnikov, M. A., Chernyshev, V. A., Novikova, N. N., Christianen, P. C. M., Balboshov, A. M. & Pisarev, R. V. Lattice dynamics and spontaneous magnetodielectric effect in ilmenite  $\text{CoTiO}_3$ . *Journal of Alloys and Compounds* **858**, 0-2 (2021).
213. Moodley, D. J., Saib, A. M., van de Loosdrecht, J., Welker-Nieuwoudt, C. A., Sigwebela, B. H. & Niemantsverdriet, J. W. The impact of cobalt aluminate formation on the deactivation of cobalt-based Fischer-Tropsch synthesis catalysts. *Catalysis Today* **171**, 192-200 (2011).
214. Melaet, G., Lindeman, A. E. & Somorjai, G. A. Cobalt particle size effects in the Fischer-Tropsch synthesis and in the hydrogenation of  $\text{CO}_2$  studied with nanoparticle model catalysts on silica. *Topics in Catalysis* **57**, 500-507 (2014).
215. Nagakura, S. Study of metallic carbides by electron diffraction Part IV. Cobalt carbides. *Journal of the Physical Society of Japan* **16**, 1213-1219 (1961).
216. Shein, I. R., Medvedeva, N. I. & Ivanovskii, A. L. Electronic and structural properties of cementite-type  $\text{M}_3\text{X}$  ( $\text{M}=\text{Fe}, \text{Co}, \text{Ni}$ ;  $\text{X}=\text{C}$  or  $\text{B}$ ) by first principles calculations. *Physica B: Condensed Matter* **371**, 126-132 (2006).
217. Baker, R. T. K. In situ electron microscopy studies of catalyst particle behavior. *Catalysis Reviews—Science and Engineering* **19**, 161-209 (1979).
218. Niemantsverdriet, J. W. & van der Kraan, A. M. Time-dependent behavior of iron catalysts in Fischer-Tropsch synthesis. *Journal of Catalysis* **72**, 385-388 (1981).
219. Vannice, M. A. The catalytic synthesis of hydrocarbons from  $\text{H}_2/\text{CO}$  mixtures over the group VIII metals: I. The specific activities and product distributions of supported metals. *Journal of Catalysis* **37**, 449-461 (1975).
220. Wesner, D. A., Linden, G. & Bonzel, H. P. Alkali promotion on cobalt: Surface analysis of the effects of potassium on carbon monoxide adsorption and Fischer-Tropsch reaction. *Applied Surface Science* **26**, 335-356 (1986).
221. Li, Z., Zhong, L., Yu, F., An, Y., Dai, Y., Yang, Y., Lin, T., Li, S., Wang, H., Gao, P., Sun, Y. & He, M. Effects of Sodium on the Catalytic Performance of CoMn Catalysts for Fischer-Tropsch to Olefin Reactions. *ACS Catalysis* **7**, 3622-3631 (2017).
222. Zhao, Z., Lu, W., Yang, R., Zhu, H., Dong, W., Sun, F., Jiang, Z., Lyu, Y., Liu, T., Du, H. & Ding, Y. Insight into the Formation of  $\text{Co}@\text{Co}_2\text{C}$  Catalysts for Direct Synthesis of Higher Alcohols and Olefins from Syngas. *ACS Catalysis* **8**, 228-241 (2018).
223. Li, Z., Yu, D., Yang, L., Cen, J., Xiao, K., Yao, N. & Li, X. Formation Mechanism of the  $\text{Co}_2\text{C}$  Nanoprisms Studied with the CoCe System in the Fischer-Tropsch to Olefin Reaction. *ACS Catalysis* **11**, 2746-2753 (2021).
224. Singh, J. A., Hoffman, A. S., Schumann, J., Boubnov, A., Asundi, A. S., Nathan, S. S., Nørskov, J., Bare, S. R. & Bent, S. F. Role of  $\text{Co}_2\text{C}$  in ZnO-promoted Co catalysts for alcohol synthesis from syngas. *ChemCatChem* **11**, 1-11 (2018).

225. Zhao, Z., Lu, W., Yang, R., Zhu, H., Dong, W., Sun, F., Jiang, Z., Lyu, Y., Liu, T., Du, H. & Ding, Y. Insight into the Formation of Co@Co<sub>2</sub>C Catalysts for Direct Synthesis of Higher Alcohols and Olefins from Syngas. *ACS Catalysis* **8**, 228–241 (2018).
226. Zhao, Z., Lu, W., Zhu, H., Dong, W., Lyu, Y., Liu, T., Chen, X., Wang, Y. & Ding, Y. Tuning the Fischer-Tropsch reaction over Co<sub>x</sub>Mn<sub>y</sub>La/AC catalysts toward alcohols: Effects of La promotion. *Journal of Catalysis* **361**, 156–167 (2018).
227. Wang, X., Chen, W., Lin, T., Li, J., Yu, F., An, Y., Dai, Y., Wang, H., Zhong, L. & Sun, Y. Effect of the support on cobalt carbide catalysts for sustainable production of olefins from syngas. *Chinese Journal of Catalysis* **39**, 1869–1880 (2018).
228. Athariboroujeny, M., Raub, A., Iablokov, V., Chenakin, S., Kovarik, L. & Kruse, N. Competing Mechanisms in CO Hydrogenation over Co-MnO<sub>x</sub> Catalysts. *ACS Catalysis* **9**, 5603–5612 (2019).
229. An, Y., Zhao, Y., Yu, F., Lin, T., Lu, Y., Li, S., Li, Z., Dai, Y., Wang, X., Wang, H., Zhong, L. & Sun, Y. Morphology control of Co<sub>2</sub>C nanostructures via the reduction process for direct production of lower olefins from syngas. *Journal of Catalysis* **366**, 289–299 (2018).
230. Paterson, J., Peacock, M., Purves, R., Partington, R., Sullivan, K., Sunley, G. & Wilson, J. Manipulation of Fischer-Tropsch Synthesis for Production of Higher Alcohols Using Manganese Promoters. *ChemCatChem* **10**, 5154–5163 (2018).
231. Wang, Z., Kumar, N. & Spivey, J. J. Preparation and characterization of lanthanum-promoted cobalt-copper catalysts for the conversion of syngas to higher oxygenates: Formation of cobalt carbide. *Journal of Catalysis* **339**, 1–8 (2016).
232. Li, Z., Zhong, L., Yu, F., An, Y., Dai, Y., Yang, Y., Lin, T., Li, S., Wang, H., Gao, P., Sun, Y. & He, M. Effects of Sodium on the Catalytic Performance of CoMn Catalysts for Fischer-Tropsch to Olefin Reactions. *ACS Catalysis* **7**, 3622–3631 (2017).
233. Han, Y., Fang, C., Ji, X., Wei, J., Ge, Q. & Sun, J. Interfacing with Carbonaceous Potassium Promoters Boosts Catalytic CO<sub>2</sub> Hydrogenation of Iron. *ACS Catalysis* **10**, 12098–12108 (2020).
234. Huo, C.-F., Wu, B.-S., Gao, P., Yang, Y., Li, Y.-W. & Jiao, H. The Mechanism of Potassium Promoter: Enhancing the Stability of Active Surfaces. *Angewandte Chemie International Edition* **123**, 7541–7544 (2011).
235. Mohandas, J. C., Gnanamani, M. K., Jacobs, G., Ma, W., Ji, Y., Khalid, S. & Davis, B. H. Fischer-tropsch synthesis: Characterization and reaction testing of cobalt carbide. *ACS Catalysis* **1**, 1581–1588 (2011).
236. Dai, Y., Zhao, Y., Lin, T., Li, S., Yu, F., An, Y., Wang, X., Xiao, K., Sun, F., Jiang, Z., Lu, Y., Wang, H., Zhong, L. & Sun, Y. Particle Size Effects of Cobalt Carbide for Fischer-Tropsch to Olefins. *ACS Catalysis* **9**, 798–809 (2019).
237. Liu, B., Li, W., Xu, Y., Lin, Q., Jiang, F. & Liu, X. Insight into the Intrinsic Active Site for Selective Production of Light Olefins in Cobalt-Catalyzed Fischer-Tropsch Synthesis. *ACS Catalysis* **9**, 7073–7089 (2019).
238. Xiong, H., Jewell, L. L. & Coville, N. J. Shaped Carbons As Supports for the Catalytic Conversion of Syngas to Clean Fuels. *ACS Catalysis* **5**, 2640–2658 (2015).
239. Chen, W., Kimpel, T. F., Song, Y., Chiang, F. K., Zijlstra, B., Pestman, R., Wang, P. & Hensen, E. J. M. Influence of Carbon Deposits on the Cobalt-Catalyzed Fischer-Tropsch Reaction: Evidence of a Two-Site Reaction Model. *ACS Catalysis* **8**, 1580–1590 (2018).
240. Tauster, S. J., Fung, S. C. & Garten, R. L. Strong Metal-Support Interactions. Group 8 Noble Metals Supported on TiO<sub>2</sub>. *Journal of American Chemical Society* **100**, 170–175 (1978).
241. Tauster, S. J., Fung, S. C., Baker, R. T. & Horsley, J. A. Strong interactions in supported-metal catalysts. *Science* **211**, 1121–1125 (1981).

242. Tauster, S. J. Strong metal-support interactions. *Accounts of Chemical Research* **20**, 389-394 (1987).
243. Parastaev, A., Muravev, V., Huertas Osta, E., van Hoof, A. J. F., Kimpel, T. F., Kosinov, N. & Hensen, E. J. M. Boosting CO<sub>2</sub> hydrogenation via size-dependent metal-support interactions in cobalt/ceria-based catalysts. *Nature Catalysis* **3**, 526-533 (2020).
244. Kattel, S., Liu, P. & Chen, J. G. Tuning Selectivity of CO<sub>2</sub> Hydrogenation Reactions at the Metal/Oxide Interface. *Journal of the American Chemical Society* **139**, 9739-9754 (2017).
245. Hernández Mejía, C., van Deelen, T. W. & de Jong, K. P. Activity enhancement of cobalt catalysts by tuning metal-support interactions. *Nature Communications* **9**, 4459 (2018).
246. Fu, Q. & Wagner, T. Interaction of nanostructured metal overlayers with oxide surfaces. *Surface Science Reports* **62**, 431-498 (2007).
247. Prieto, G., de Mello, M. I. S., Concepción, P., Murciano, R., Pergher, S. B. C. & Martínez, A. Cobalt-catalyzed Fischer-Tropsch synthesis: Chemical nature of the oxide support as a performance descriptor. *ACS Catalysis* **5**, 3323-3335 (2015).
248. Boffa, A. B., Lin, C., Bell, A. T. & Somorjai, G. A. Lewis acidity as an explanation for oxide promotion of metals: implications of its importance and limits for catalytic reactions. *Catalysis Letters* **27**, 243-249 (1994).
249. Vannice, M. A. Hydrogenation of CO and carbonyl functional groups. *Catalysis Today* **12**, 255-267 (1992).
250. Maitlis, P. M. & Zanotti, V. The role of electrophilic species in the Fischer-Tropsch reaction. *Chemical Communications* **13**, 1619-1634 (2009).
251. Jiao, G., Ding, Y., Zhu, H., Li, X., Li, J., Lin, R., Dong, W., Gong, L., Pei, Y. & Lu, Y. Effect of La<sub>2</sub>O<sub>3</sub> doping on syntheses of C<sub>1</sub>-C<sub>18</sub> mixed linear  $\alpha$ -alcohols from syngas over the Co/AC catalysts. *Applied Catalysis A: General* **36**, 137-142 (2009).
252. Xie, J., Paalanen, P. P., van Deelen, T. W., Weckhuysen, B. M., Louwerse, M. J. & de Jong, K. P. Promoted cobalt metal catalysts suitable for the production of lower olefins from natural gas. *Nature Communications* **10**, 167 (2019).
253. Moya-Cancino, J. G., Honkanen, A. P., van der Eerden, A. M. J., Schaink, H., Folkertsma, L., Ghiasi, M., Longo, A., Meirer, F., de Groot, F. M. F., Huotari, S. & Weckhuysen, B. M. Elucidating the K-Edge X-Ray Absorption Near-Edge Structure of Cobalt Carbide. *ChemCatChem* **11**, 3042-3045 (2019).
254. Moya-Cancino, J. G., Honkanen, A. P., van der Eerden, A. M. J., Schaink, H., Folkertsma, L., Ghiasi, M., Longo, A., de Groot, F. M. F., Meirer, F., Huotari, S. & Weckhuysen, B. M. In-situ X-Ray Absorption Near Edge Structure Spectroscopy of a Solid Catalyst using a Laboratory-Based Set-up. *ChemCatChem* **11**, 1039-1044 (2019).
255. van Ravenhorst, I. K., Ho, A. S., Vogt, C., Boubnov, A., Patra, N., Oord, R., Akatay, C., Meirer, F., Bare, S. R. & Weckhuysen, B. M. On the Cobalt Carbide Formation in a Co/TiO<sub>2</sub> Fischer-Tropsch Synthesis Catalyst as Studied by High-Pressure, Long-Term Operando X-ray Absorption and Diffraction. *ACS Catalysis* **11**, 2956-2967 (2021).
256. Morales, F., de Groot, F. M. F., Glatzel, P., Kleimenov, E., Bluhm, H., Hävecker, M., Knop-Gericke, A. & Weckhuysen, B. M. In Situ X-ray Absorption of Co/Mn/TiO<sub>2</sub> Catalysts for Fischer-Tropsch Synthesis. *The Journal of Physical Chemistry B* **108**, 16201-16207 (2004).
257. Balachandran, U. & Eror, N. G. Raman spectra of titanium dioxide. *Journal of Solid State Chemistry* **42**, 276-282 (1982).
258. Cromer, D. T. & Herrington, K. The Structures of Anatase and Rutile. *Journal of the American Chemical Society* **77**, 4708-4709 (1955).

259. Adapted from: [http://henke.lbl.gov/optical\\_constants/atten2.html](http://henke.lbl.gov/optical_constants/atten2.html).
260. Andrews, J. C. & Weckhuysen, B. M. Hard X-ray spectroscopic nano-imaging of hierarchical functional materials at work. *ChemPhysChem* **14**, 3655–3666 (2013).
261. Meirer, F. & Weckhuysen, B. M. Spatial and temporal exploration of heterogeneous catalysts with synchrotron radiation. *Nature Reviews Materials* **3**, 324–340 (2018).
262. Xiong, L. Bin, Li, J. L., Yang, B. & Yu, Y.  $\text{Ti}^{3+}$  in the surface of titanium dioxide: Generation, properties and photocatalytic application. *Journal of Nanomaterials* **2012**, 831524 (2012).
263. Cats, K. H. & Weckhuysen, B. M. Combined Operando X-ray Diffraction/Raman Spectroscopy of Catalytic Solids in the Laboratory: The Co/TiO<sub>2</sub> Fischer-Tropsch Synthesis Catalyst Showcase. *ChemCatChem* **8**, 1531–1542 (2016).
264. van Schrojenstein Lantman, E. M., Deckert-Gaudig, T., Mank, A. J. G., Deckert, V. & Weckhuysen, B. M. Catalytic processes monitored at the nanoscale with tip-enhanced Raman spectroscopy. *Nature Nanotechnology* **7**, 583–586 (2012).
265. Fu, D., Park, K., Delen, G., Attila, Ö., Meirer, F., Nowak, D., Park, S., Schmidt, J. E. & Weckhuysen, B. M. Nanoscale infrared imaging of zeolites using photoinduced force microscopy. *Chemical Communications* **53**, 18–21 (2017).
266. Wu, C. Y., Wolf, W. J., Levartovsky, Y., Bechtel, H. A., Martin, M. C., Toste, F. D. & Gross, E. High-spatial-resolution mapping of catalytic reactions on single particles. *Nature* **541**, 511–515 (2017).
267. de Smit, E., Cinquini, F., Beale, A. M., Safonova, O. V., van Beek, W., Sautet, P. & Weckhuysen, B. M. Stability and reactivity of  $\epsilon$ -X- $\theta$  iron carbide catalyst phases in Fischer-Tropsch synthesis: Controlling  $\mu\text{c}$ . *Journal of the American Chemical Society* **132**, 14928–14941 (2010).
268. Last, G. V. & Schmick, M. T. A review of major non-power-related carbon dioxide stream compositions. *Environmental Earth Sciences* **74**, 1189–1198 (2015).
269. Tsakoumis, N. E., Dehghan, R., Johnsen, R. E., Voronov, A., van Beek, W., Walmsley, J. C., Borg, Ø., Rytter, E., Chen, D., Rønning, M. & Holmen, A. A combined in situ XAS-XRPD-Raman study of Fischer-Tropsch synthesis over a carbon supported Co catalyst. *Catalysis Today* **205**, 86–93 (2013).
270. van der Laan, G. P. & Beenackers, A. A. C. M. Kinetics and Selectivity of the Fischer-Tropsch Synthesis: A Literature Review. *Catalysis Reviews - Science and Engineering* **41**, 255–318 (1999).
271. Liu, Y., Wu, D., Yu, F., Yang, R., Zhang, H., Sun, F., Zhong, L. & Jiang, Z. In situ XAFS study on the formation process of cobalt carbide by Fischer-Tropsch reaction. *Physical Chemistry Chemical Physics* **21**, 10791–10797 (2019).





This Chapter is based on the following scientific articles:

ten Have, I. C., Hartman, T., van Bavel, A.P., Bezemer, G. L., Ferri, D., Geitner, R., Huang, T., Kupfer, S., Gräfe, S., Meirer, F., Weckhuysen, B. M. Through the Lens of *Operando* Spectroscopy: Mechanistic Insights in the Fischer-Tropsch Synthesis. *Submitted for publication*. (2022).

Werny, M. J., Zarupski, J., ten Have, I. C., Piovano, A., Hendriksen, C., Friederichs, N. H., Meirer, F., Groppo, E., Weckhuysen, B. M. (2021). Correlating the Morphological Evolution of Individual Catalyst Particles to the Kinetic Behavior of Metallocene-Based Ethylene Polymerization Catalysts. *JACS Au* 1, 1996-2008.

ten Have, I. C., Duijndam, A. J. A., Oord, R., van Berlo-van den Broek, H. J., Vollmer, I., Weckhuysen, B. M., Meirer, F. (2021). Photoinduced Force Microscopy as an Efficient Method Towards the Detection of Nanoplastics. *Chemistry-Methods* 1, 205-209.

Meirer, F., ten Have, I. C., Oord, R., Zettler, E. R., van Sebille, E., Amaral-Zettler, L. A., Weckhuysen, B. M. (2021). Nanoscale Infrared Spectroscopy Reveals Nanoplastics at 5000 m Depth in the South Atlantic Ocean, Research Square, preprint.

\* These authors contributed equally.

# **CHAPTER 2**

## **APPLICATIONS OF NANOSCALE SPECTROSCOPY: FROM MATERIALS SCIENCE TO ENVIRONMENTAL SCIENCE AND HETEROGENEOUS CATALYSIS**



**Abstract**

Spectroscopy with nanometer-scale spatial resolution is interesting for the catalysis community, as correlating spatially-resolved chemical information with the morphology of catalysts has been a topic of industrial and academic interest for many years. Photo-induced force microscopy (PiFM) is an emerging nanoscale chemical imaging technique that combines the spatial resolution of atomic force microscopy (AFM) with the chemical sensitivity of infrared (IR) spectroscopy. This technique first found applications in the polymer industry, as nanoscale domains of different compounds can easily be distinguished by their spectroscopic fingerprint. An obstacle that withholds this technique from expanding its applications to for example industrially relevant catalyst materials is the surface roughness of the materials under study. The scanning probe in the PiFM instrument requires a relatively flat ( $Z < 1\mu\text{m}$ ) surface, which most catalyst materials do not naturally have. Industrially relevant catalyst materials often consist of multiple components that interact with each other as well as with the reactants and reaction products. In this **Chapter**, we first introduce the PiFM method through several applications ranging from material science over environmental science to heterogeneous catalysis. The application of PiFM in the field of environmental science will be illustrated with the detection of nanoplastics in ocean water. Then, we discuss the barriers that have to be overcome to apply scanning probe microscopy (SPM) techniques, such as PiFM, under realistic catalytic conditions as well as the necessary parallel development of realistic model systems, which are enable to the SPM approach.

## 2.1 Introduction

Back in the 5<sup>th</sup> century B.C., ancient Greek scientists were already wondering whether matter was continuous or composed of small particles.<sup>1</sup> The latter are nowadays recognized by scientists as atoms. While curiosity about the composition of matter thus dates at least back to the ancient Greeks, the analytical tools to actually observe nanoscale structures were only invented in the 20<sup>th</sup> century. In 1981, the scanning tunneling microscope (STM) was invented<sup>2,3</sup> and the inventors, Gerd Binnig and Heinrich Rohrer, published images of individual Si atoms in 1983.<sup>4</sup> This microscope operates with a sharp metal tip attached to a cantilever that comes very close to the conductive surface of the sample. The electron wave functions of the atoms in the sample and the tip then overlap with each other. When a voltage is applied, the electrons can traverse, *i.e.*, tunnel, both ways through the vacuum gap between the sample and the tip. The intensity of the tunneling current describes the electronic density of states of the sample. When this current is set to a constant target value, a feedback loop system can adjust the tip-sample distance while the tip is scanning over the sample surface. For example, if the tunneling current exceeds the target value, the tip-sample distance is increased. This enables topography imaging with atomic resolution.<sup>4</sup>

The invention of the STM method received the Nobel Prize in Physics in 1986 and then led to the development of the atomic force microscope (AFM) and other scanning probe microscopy (SPM) techniques.<sup>5,6</sup> Contrary to the STM technique, the AFM method does not require a conducting surface. Instead, the sharp tip, coined a scanning probe, is attached to a cantilever, which bends as the tip contacts the surface. This degree to which the cantilever deflects, indicates the force of the tip-sample interaction. To protect the sample from damage by contact with the tip, the AFM can operate in non-contact mode. The scanning probe then vibrates in a sinusoidal way near its resonance frequency. This frequency is affected by either repulsive or attractive van der Waals tip-sample interactions as the tip moves closer to the sample surface. When the amplitude of the scanning probe's frequency is set to a constant target value, a feedback system adjusts the tip-sample distance based on the strength of the tip-sample interaction. Through scanning over the sample surface, topography images with atomic resolution can be obtained.<sup>5</sup>

AFM formed the foundation for spatially-resolved vibrational spectroscopy with nanometer-scale spatial resolution. Infrared (IR) spectroscopy, the most common vibrational spectroscopy technique, is normally restricted by the diffraction limit of IR light (~5-10  $\mu\text{m}$ ).<sup>7</sup> However, by combining the spatial resolution of the AFM method with the chemical sensitivity of IR spectroscopy (denoted in its combination as AFM-IR), the local chemical composition of the sample can be mapped with at least 50-200 nm spatial

resolution.<sup>7,8</sup> The working principle of AFM-IR is based on thermal expansion of the sample upon illumination with IR light. Another promising development involves the use of synchrotron-based IR radiation and its principle is based on scattering of IR light. The broad, bright, and spatially coherent IR light source of a particle accelerator led to synchrotron infrared nano-spectroscopy (SINS) with a spatial resolution of ~25 nm.<sup>9,10</sup> Another emerging nanoscale chemical imaging technique is photo-induced force microscopy (PiFM). Its working principle is based on measuring sample-tip dipole-dipole interactions upon irradiation with IR light and chemical mapping with 10-20 nm spatial resolution has been reported.<sup>11</sup>

This **Chapter** discusses nanoscale spectroscopy and how this methodology, which was first demonstrated in materials science research, can be used to answer open questions in the other fields, including those in environmental science and heterogeneous catalysis. In **Chapter 1**, we have already discussed various spectroscopy methods and how *operando* spectroscopy aims to study industrially relevant catalyst materials under realistic reaction conditions. In this **Chapter**, we will first introduce PiFM as a powerful new surface science tool and highlight some of its applications, including the detection of nano-sized plastic particles in environmental samples. Then, we will outline which barriers have to be overcome to make the combination of surface science and heterogeneous catalysis work properly. Consequently, we will discuss the development and characterization of realistic model catalysts that can be used in *operando* surface studies.

### 2.1.1 Nanoscale Vibrational Spectroscopy

In **Chapter 1**, we briefly highlighted that the widely used vibrational spectroscopy techniques infrared (IR) and Raman (micro)spectroscopy are promising analytical tools to study e.g. carbon-containing species on catalyst materials, like Co/TiO<sub>2</sub> Fischer-Tropsch Synthesis (FTS) catalysts. The spatial resolution of vibrational (micro)spectroscopy techniques is limited by the wavelength of the incoming light, which ranges from several hundreds of nanometers to several thousands of micrometers. The diffraction limitations of light can be overcome by combining vibrational spectroscopy with SPM techniques, such as AFM.<sup>9,11</sup> Examples of this include tip-enhanced Raman spectroscopy (TERS)<sup>12,13</sup> and PiFM.<sup>11,14</sup> In the following sections, we will mainly focus on the PiFM technique and we will outline how this analytical technique is applied in the fields of material science, environmental science, and finally in heterogeneous catalysis. The working principle of the PiFM method is slightly different from AFM-IR; PiFM relies on dipole-dipole interaction, whereas AFM-IR relies on thermal expansion. Consequently, a slightly better spatial resolution can be achieved with PiFM. Detailed explanations and review articles on the working principles of these methods can be found elsewhere.<sup>9,11,15,16</sup>

### 2.1.2 Use of Photo-induced Force Microscopy in the Field of Materials Science

To the best of our knowledge, the PiFM technique was for the first time successfully demonstrated on polymer films in 2016.<sup>11</sup> Even though PiFM is a relatively new technique and still under continuous development, PiFM devices have been commercially available for a couple of years now. PiFM first found its applications in the polymer industry, as nanoscale domains of different compounds could easily be distinguished by their spectroscopic fingerprint.<sup>11,15,17-19</sup> The detection principle of PiFM is, however, slightly different and more complex compared to conventional IR techniques, such as attenuated total reflectance - infrared (ATR-IR) spectroscopy. For comparison purposes, PiFM IR spectra were compared to ATR-IR spectra of PE, PS, and PET microplastic granulates (**Figure 2.1**). Although the IR peaks appeared at the same wavenumbers for both analytical techniques, the peak intensities were slightly different between the two methods due to the differences in detection method.

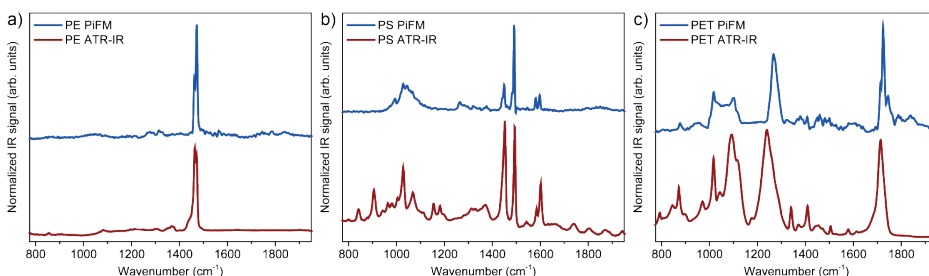


**Figure 2.1. Comparison of attenuated total reflection-infrared (ATR-IR) spectroscopy and photo-induced force microscopy (PiFM) for the studying polymers a) polyethylene (PE), b) polystyrene (PS), and c) polyethylene terephthalate (PET).** The differences in relative peak intensities from bands in the ATR-based and PiFM-based IR spectra clearly show how the detection method of the PiFM technique differs slightly from the more conventional IR spectroscopy techniques. For example, the PiFM method is very sensitive to dipoles and therefore detects certain vibrations much stronger than conventional IR spectroscopy.

### 2.1.3 Use of Photo-induced Force Microscopy in the Field of Environmental Science

Plastic products are essential in modern-day life and while they have supported economic growth in many countries, mismanaged plastic waste has become problematic.<sup>20</sup> Although plastic properties, such as being lightweight and shapeable, are beneficial, its durability makes it a main component of, amongst others, marine litter.<sup>21,22</sup> Of the 260-275 million tonnes of plastic waste produced annually,<sup>23</sup> 4.8-12.7 million tonnes have

entered the oceans in 2010.<sup>23</sup> Plastic waste fragments and degrades slowly, forming particles ranging from centimeters down to nanometers.<sup>24-26</sup> Recently, 11.6-21.1 million tonnes of microplastics were reported in the top 200 m of the Atlantic Ocean.<sup>27</sup>

Today it is recognized that most plastic in the ocean is neither visible nor floating on the surface<sup>28-30</sup> and the presence of nanoplastics<sup>31</sup> and its potential impact on the biosphere have been mentioned.<sup>24,32</sup> However, little is known about the origin, structure, and fate of nanoplastics in marine environments; even the definition 'nanoplastics' is still under debate defining it either as 1-1000<sup>33</sup> or 1-100 nm particles.<sup>34,35</sup> The reasons for this knowledge gap are the experimental challenge of sampling and the analytical challenge of detecting nanoplastics, as discussed in detail by recent reviews.<sup>31,34-37</sup>

Since PiFM had already been successfully demonstrated with 10-20 nm spatial resolution in the polymer industry,<sup>11</sup> one naturally starts wondering whether PiFM could also be used to detect nano-sized plastic particles that may be present in environmental samples. To answer this question, we set out to establish a suitable methodology to systematically analyze sub-100 nm polymer particles with photo-induced force microscopy (PiFM). We have recently studied commercially available nano-sized polystyrene (PS) spheres of varying sizes (20-400 nm) exposed to fresh and saline water. PS is widely used with an annual production of over 23 million tonnes worldwide.<sup>38</sup> When disposed in aquatic environments, it undergoes extremely slow depolymerization, leading to micro- and presumably also nanoplastics.<sup>39</sup> PS is denser (1.05 g cm<sup>-3</sup><sup>40</sup>) than fresh water and denser than seawater until a certain depth (of several 1000 m).<sup>41</sup> Therefore, it will sink to depths where it is unexposed to sunlight and remains there as a potential source of micro- and nanoplastics. We thus hypothesized that oxidative degradation and chain scission must be the predominate mechanisms for PS nanoplastics formation.<sup>40,42</sup> We showed with the PiFM technique that in saline aqueous environments, in the absence of light, oxidative degradation and chain scission are the main mechanisms to form and degrade PS micro- and nanoplastics (**Figure 2.2**).<sup>43</sup> The PS spheres maintained their original size (**Figure 2.2a**) and could easily be distinguished from NaCl crystals (**Figure 2.2c,e**) by recording IR maps at 1490 cm<sup>-1</sup>, corresponding to the PS aromatic ring stretch.<sup>43</sup> The PiFM point spectra of the PS particles (red, green, blue plots, **Figure 2.2b**) revealed that the chemical state of the PS surface had changed. Pristine PS is typically identified in IR spectra by its C-H<sub>2</sub> bending vibration at 1450 cm<sup>-1</sup> and aromatic ring stretch at 1490 cm<sup>-1</sup>.<sup>43</sup> The PiFM IR spectra in **Figure 2.2b** showed additional bands, which were indicative of degradation. The peak around ~1745 cm<sup>-1</sup> was attributed to C=O stretching,<sup>42</sup> indicating oxidative degradation. Additional peaks around ~1463 and ~1630 cm<sup>-1</sup>, attributed to C-H<sub>2</sub> bending and C=C stretching of an aliphatic group, respectively, indicated chain scission.<sup>40,42</sup> These chemical changes took place upon



exposure to saltwater, but not in fresh water. This suggests that (nano)plastics degrade in the marine environment, but not or to a lesser extent in e.g. rivers, an important microplastics pathway.<sup>43</sup>

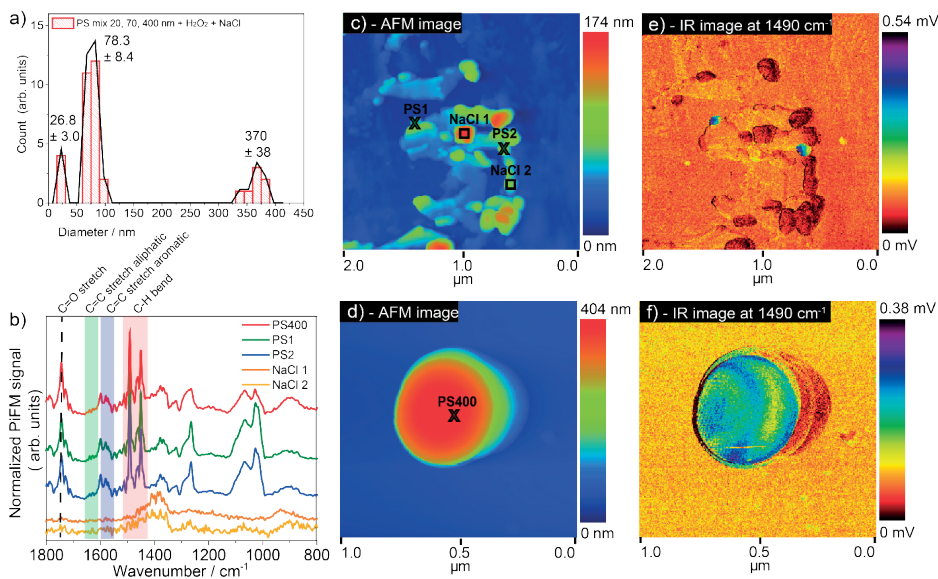


**Figure 2.2. Photo-induced force microscopy (PiFM) characterization of polystyrene (PS) nanospheres.** A PS nanosphere mixture (20, 70, 400 nm) was treated with  $\text{H}_2\text{O}_2$  to (partially) remove the protective sulfonate ligands and diluted in  $35 \text{ g L}^{-1}$  NaCl. **a)** Particle size distribution of the PS spheres. **b)** PiFM infrared (IR) spectra of PS spheres and NaCl crystals. **c, d)** Topographic images and **e, f)** IR maps recorded at  $1490 \text{ cm}^{-1}$  (C=C stretch indicative for PS). The positions of the point spectra are indicated in the topographic maps.

Then, we have utilized the established methodology to study nanoplastics from the South Atlantic Ocean gyre.<sup>44</sup> In the ocean, plastic pollution is generally evaluated based on floating macro- and microplastic surface concentrations.<sup>45</sup> However, plastics denser than seawater ( $\sim 1 \text{ g cm}^{-3}$ ) such as PET ( $1.38 \text{ g cm}^{-3}$ ) are thought to sink to the ocean depths.<sup>46-49</sup> Since the ocean water density gradually increases with depth, objects are expected to stay suspended at the depth where their density equals that of water. This fact, in combination with biofouling and remineralization,<sup>50</sup> is offered as a plausible explanation for particle concentration at the pycnocline,<sup>27,51</sup> where largest oceanic density gradients occur.<sup>50</sup> However, buoyancy or biofouling do not impact particles below a certain size, (e.g., nanometer-sized particles), but instead their movement follows a random walk.<sup>52</sup> This may lead to widespread transport of nanoplastics by ocean currents,<sup>53</sup> but experimental evidence for this hypothesis is lacking. With the PiFM method,

we have found PET-like nanoplastics at the bottom (i.e., 5179 m depth) of the South Atlantic Ocean, while conducting an exploratory cruise, organized by the Netherlands Organization for Research of the Sea (NIOZ), in which one of the researchers of the Inorganic Chemistry and Catalysis group, namely Dr. Ramon Oord, actively participated (Figure 2.3).<sup>44</sup>

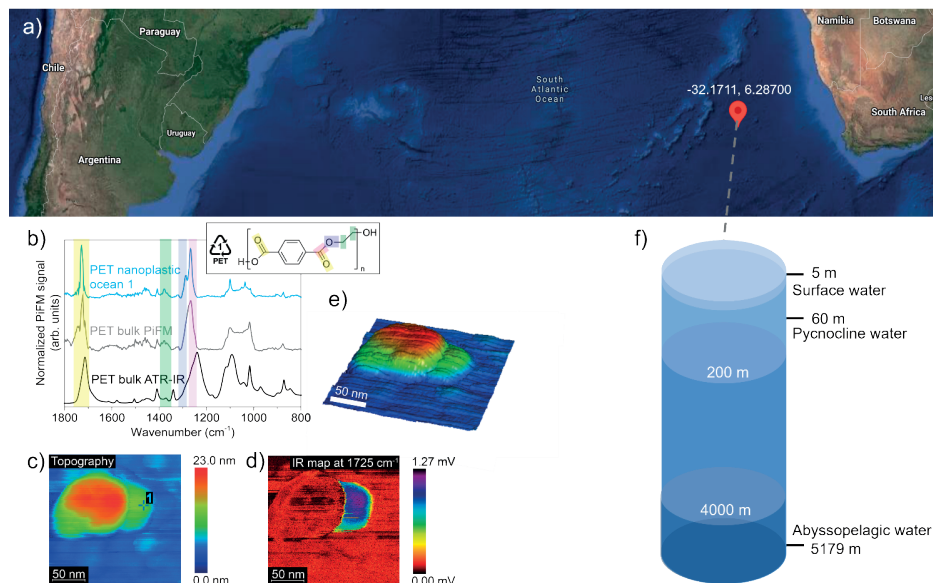


**Figure 2.3. Studying individual nanoplastics in the South Atlantic Ocean with the photo-induced force microscopy (PiFM) technique. a)** Sampling location in the South Atlantic Ocean close to the Cape Basin. **b)** Infrared (IR) spectra of a polyethylene terephthalate (PET) bulk reference, obtained with attenuated total reflectance - infrared (ATR-IR) spectroscopy and PiFM, and of a PET-like nanoplastic particle (1) found at 5179 m depth. **c)** Topography map of PET-like nanoplastic 1 and **d)** corresponding IR map recorded at the characteristic C=O stretching vibration of PET at  $1725\text{ cm}^{-1}$ . The location of the PiFM IR point spectrum from **b)** is indicated in the topography map by the label '1'. **e)** 3D topography map of the particles from **c)** indicating how the nanoplastic particle is half covered by another non-plastic particle. **f)** Depth profile of the sampling location.

### 2.1.4 Use of Photo-induced Force Microscopy in the Field of Heterogeneous Catalysis

In the field of heterogeneous catalysis, it has previously been demonstrated that PiFM can provide useful chemical insights on model catalysts, such as zeolite thin films<sup>14</sup> and metal-organic framework (MOF) thin films.<sup>54</sup> The nanoscale spectroscopy approach is highly interesting for the catalysis community, as correlating spatially-resolved chemical

information with the morphology of catalysts has been a topic of industrial and academic interest for many years. However, an obstacle that withholds this analytical technique from expanding its applications to industrially relevant catalyst materials is surface roughness. The scanning probe in the PiFM instrument requires a relatively flat ( $Z < 1 \mu\text{m}$ ) surface, which most industrially relevant catalyst materials do not naturally have.

We have recently demonstrated that horizontal dissection and flattening of the catalyst's surface with a focused ion beam (FIB) facilitates the application of the PiFM technique with sub-20 nm spatial resolution on the catalysts' inner surfaces,<sup>55</sup> which are normally too rough for tip-based techniques (Figure 2.4).

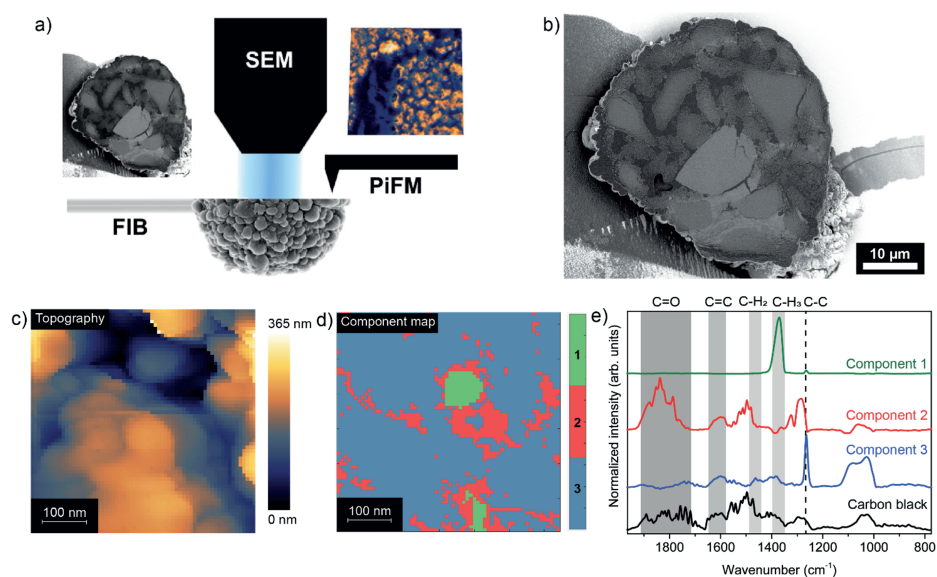


**Figure 2.4. Overview of photo-induced force microscopy (PiFM) approach on dissected ethylene polymerization and  $\text{CO}_2$  hydrogenation catalyst particles.** **a)** A focused ion beam (FIB) was used to dissect a catalyst particle. Scanning electron microscopy (SEM) and photo-induced force microscopy (PiFM) infrared (IR) images were recorded on the same location. **b)** SEM image of a  $\text{SiO}_2$ /methylaluminoxane(MAO)/Hf catalyst particle that was pre-polymerized in 1.6 bar ethylene for 30 min. The silica domains are light gray, while the polymer domains are dark gray. **c)** Topography map and **d)** corresponding spectral component map obtained with principal component analysis (PCA) and clustering on K-Co/ $\text{TiO}_2$  after  $\text{CO}_2$  hydrogenation ( $250^\circ\text{C}$ , 1 bar,  $\text{H}_2/\text{CO}_2=3$ , and 10 h time-on-stream (TOS)). **e)** PiFM infrared (IR) component spectra and PiFM IR spectrum of a carbon black reference material.

More specifically, an industrial-grade ethylene polymerization catalyst (**Figure 2.4a,b**) was investigated, as well as industrially relevant Co/TiO<sub>2</sub> catalysts used for CO<sub>2</sub> hydrogenation (**Figure 2.4c-e**; further discussion in **Chapter 5**). For the ethylene polymerization catalyst material, both layer-by-layer and sectioning were observed as fragmentation mechanisms (**Figure 2.4a,b**).<sup>55</sup> Insights were also obtained on the exposure of new active sites during the catalyst particle fragmentation process. For the Co/TiO<sub>2</sub> catalyst system, the influence of promoter element potassium (K) was investigated and different carbonaceous surface species were observed after CO<sub>2</sub> hydrogenation (**Figure 2.4c-e**). The species on both catalyst materials had similarities with the chemical structure of carbon black: a polyaromatic structure with various oxygen functionalities. Aliphatic, olefinic, and carbonyl groups were observed on unpromoted Co/TiO<sub>2</sub>. The K-promoted variant had domains that were very rich in conjugated carbonyl groups, as well as domains with methyl, aliphatic, and olefinic groups.

## 2.2 Surface Science and Operando Spectroscopy

Because of their working principles, many surface science techniques operate under ultra-high vacuum (UHV) conditions (i.e., 10<sup>-6</sup>-10<sup>-12</sup> bar).<sup>56-57,62</sup> However, during the past decade it has become increasingly apparent that both catalytic surfaces and reactants have completely different physical characteristics, such as surface stability, mobility of species, surface coverages, and surface energies under industrially relevant conditions compared to vacuum conditions.<sup>63-65</sup> For example, the impressive work on catalytic nitrogen splitting that Gerhard Ertl led to receive in 2007 the Nobel Prize in Chemistry was performed at 1·10<sup>-7</sup> - 1·10<sup>-9</sup> bar with single crystal iron facets.<sup>66</sup> However, the industrial Haber-Bosch process that it relates to, occurs above 150 bar and at 350-550°C on iron nanoparticles on a doped mesoporous iron-oxide support.<sup>67</sup> Hence, there is still both a materials and pressure gap between the model systems, researched by Ertl and the real-life catalysts employed in chemical industry. Recent theoretical data suggest that nearly all obtainable catalytic and surface parameters are orders of magnitude different under relevant process conditions than those obtained under vacuum conditions.<sup>68</sup> The two sections below will discuss two hurdles that have to be taken to make insights from surface science more applicable to industrial catalysis, namely the pressure gap and the material gap.

### 2.2.1 The Pressure Gap

Tip-based spectroscopy techniques, such as TERS and PIFM, can provide more detailed insights on the complex surface structure of catalyst materials with nanometer resolution.<sup>14,54,55</sup> For example, both layer-by-layer and sectioning were observed as

fragmentation mechanisms in olefin polymerization catalysts (**Figure 2.4**). The nanoscale domains of silica and polyethylene, indicating occurrence of the two fragmentation mechanisms, were easily distinguished with the PiFM technique. Applying surface-sensitive techniques in heterogeneous catalysis has been historically challenging, as they often require vacuum or low-pressure environments to function accordingly, which means that working in real *operando* mode is in principle impossible. This discrepancy is referred to as “pressure gap”.<sup>56,69,70</sup>

The surface science community has made significant efforts in terms of set-up and reactor design to bridge the pressure gap. For example, in 1992 a report was published on a multi-technique surface analysis chamber with high pressure capabilities (thereby creating the possibility to introduce several gas atmospheres).<sup>71,72</sup> In 1998, a research article was published on the size dependence of the CO oxidation reaction with gold clusters on titania thin films using the X-ray photoelectron spectroscopy (XPS) and STM capabilities of the multi-technique set-up,<sup>71</sup> as reported in 1992.<sup>71,72</sup> More recent approaches to study model surfaces at conditions relevant to industrial applications are, for example, high pressure (up to 6 bar) STM studies of model hydrodesulfurization catalysts.<sup>73,74</sup> The same group is now working on integrating the STM and AFM techniques in one reactor in a single microscope, applicable at high pressures up to 20 bar.<sup>75</sup> Furthermore, nanoscale IR spectroscopy measurements, using a combination of AFM and IR spectroscopy, have been performed in gaseous environments with spatial resolutions down to 25 nm.<sup>10</sup> These developments clearly demonstrate the important steps, which have been made in the past decades to adapt the SPM methodology to harvest more relevant information on increasingly complex heterogeneous catalyst materials.

### 2.2.2 The Material Gap

Within the field of surface science, a relatively flat and well-defined model catalyst, such as a single crystal surface, is often desired, as tip-based microscopy techniques, like AFM and STM, and its related spectroscopy variants, such as PiFM and TERS, cannot operate well on rough surfaces as maximum height differences should typically be below  $\sim 1 \mu\text{m}$ . Heterogeneous catalysts are generally complex multi-component materials with intrinsically rough surfaces (*i.e.*, more than  $1 \mu\text{m}$  maximum height differences). Besides, in terms of chemical composition they are typically more complex compared to single crystal surfaces. They consist of metal nanoparticles, a 3-dimensional support material to stabilize the nanoparticles, and often one or multiple promoter elements. The single crystal materials used to model industrial catalysis thus inherently lack the structural and compositional complexity required to unravel many of the factors, which are important to catalytic performance.<sup>56</sup> These factors include but are not limited to

nanoparticle size effects, metal-support interactions, and (electronic) promoter effects. The discrepancy between model-based catalysts and industrially relevant catalysts is referred to as "material gap".<sup>56,69,70,76,77</sup> However, it is important to stress here that both approaches and hence materials have their own merit in increasing our knowledge on the processes taking place in heterogeneous catalysts. A schematic overview of the currently existing material gap is depicted in **Figure 2.5**.

Endeavors to bridge this material gap have been made from multiple research angles. For example, nanofabrication techniques have been used to produce thin film oxides.<sup>77</sup> Such materials may be able to represent support oxides used in heterogeneous catalysis and would be flat enough for analysis with surface-sensitive, tip-based characterization methods, such as PiFM and TERS.

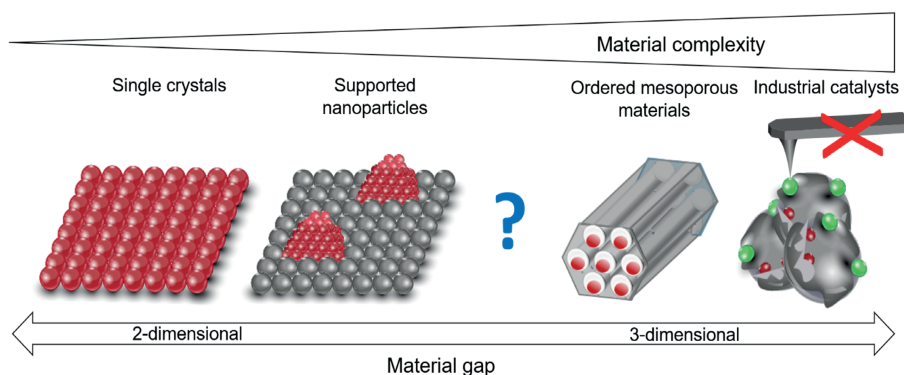


**Figure 2.5.** Schematic overview of the material gap in surface science. More realistic model catalysts are clearly needed, but often are not suitable to be researched by very spatially and sensitive analytical methods.

### 2.3 Development and Characterization of Model Catalysts

Model systems are used in scientific research to understand phenomena that occur in more complex, real systems. For example, in pharmacology model organisms, such as bacteria or mice, are used to provide insights into the effects of medication on humans. In heterogeneous catalysis research, 3-dimensional ordered mesoporous materials (**Figure 2.5**) have been used as model systems for industrial catalyst supports. This section describes how ordered mesoporous thin films were a source of inspiration for the development of micro-islands. Micro-islands can function as realistic model catalyst supports during surface science studies, as explored in this PhD Thesis. The materials are flat enough to be characterized with surface-sensitive techniques, such as PiFM, but realistic enough to represent heterogeneous catalysts.

### 2.3.1 Ordered Mesoporous Materials

The two most well-known ordered mesoporous materials, Mobil Crystalline Materials (MCM)-41 and Santa Barbara Amorphous (SBA)-15, were developed in 1992<sup>78</sup> and 1986,<sup>79</sup> respectively. The researchers who invented them, intended to use the silica materials as molecular sieves. Currently, such materials find applications in drug delivery,<sup>80</sup> energy and gas storage,<sup>81</sup> water and gas filtration,<sup>82</sup> imaging, and catalysis.<sup>83</sup> The sol-gel synthesis method to create ordered mesoporous particles has also been demonstrated with a multitude of other compounds, such as titania and alumina. The texture of such high surface area materials has been efficient in terms of controlling the metal nanoparticle size in heterogeneous catalysis research.<sup>83-85</sup> However, surface science characterization tools often utilize a scanning probe, which requires a relatively flat surface, preferably with maximum height differences below 1  $\mu\text{m}$ , to function properly. Even though 3-dimensional ordered mesoporous materials are generally interesting for heterogeneous catalysis research purposes, surface science requires materials with a more 2-dimensional character.

### 2.3.2 Thin films

Thin films of various (metal) oxides are used in surface science research to represent the support material of industrial catalysts.<sup>86</sup> Metal nanoparticles are deposited on the non-porous (metal) oxide films to mimic a real catalyst. Although such model systems are already a step up from simple single crystal surfaces, industrially relevant catalysts are structured differently. They normally consist of metal nanoparticles dispersed in a high surface area support. Apart from increasing the surface area, the support material may also play a role in inhibiting metal nanoparticle growth.

Titania thin films have numerous applications such as energy conversion, membranes, optical applications, controlled delivery, and (photo)catalysis. Mesoporous titania thin films are of interest for all of these applications because of their high surface area. Such films could be prepared by deposition and sintering of titania nanoparticles, which leads to irregular porosity.<sup>87</sup> However, for many applications, including heterogeneous catalysis research, ordered mesopores could be beneficial, for example to control the metal nanoparticle size and/or to ensure a uniform metal nanoparticle size distribution. Nanoparticle growth may occur during catalysis and could lead to a decrease in the observed catalytic activity during an experiment. Therefore, controlling the metal nanoparticle size is often desired in fundamental catalysis research to rule out nanoparticle growth as a contributing factor to the observed effects. Besides, for the cobalt-based FTS reaction, the optimum cobalt nanoparticle size is established at 6-8 nm.<sup>88,89</sup> Nanoparticles below or above that size have different catalytic properties, such

as a higher undesired methane selectivity (<6 nm) or a lower catalytic activity (>8 nm). Hence, to draw meaningful fundamental conclusions, having a uniform metal nanoparticle size distribution is desirable. Sol-gel methods to synthesize ordered mesoporous titania thin films in various structural configurations have been developed in the materials science field in the early 2000s.<sup>87,90</sup> For various analytical techniques, such as scanning transmission X-ray microscopy (STXM) and tip-based vibrational spectroscopy, namely TERS, an empty space or background in the vicinity of the catalytic site(s) of interest is desired for facile data analysis. A background is typically subtracted from the spectral region of interest (*i.e.*, the catalyst (particle)) to ensure that the signal obtained is from the catalyst only and not (partially) from *e.g.*, a sample carrier. This sparked the idea to develop micro-islands from the thin film material. References<sup>90</sup> and<sup>87</sup> in particular formed an inspiration for the development of ordered mesoporous titania micro-islands, which will be described in the next section.

### 2.3.3 Micro-islands

Ordered mesoporous titania micro-islands were synthesized tweaking a sol-gel recipe<sup>87,90</sup> and micro-patterning approach<sup>91,92</sup> from the open literature. The micro-islands displayed in **Figure 2.6** were about 20  $\mu\text{m}$  in diameter and 300 nm in height. Cu transmission electron microscopy (TEM) grids with a 600-mesh hexagonal structure were used during the synthesis as photomasks. The diameter of the micro-islands and the spacing between them could be altered by using a different photomask. The thickness could be adapted *via* spin coating conditions, such as rotational speed. The  $\sim 5$  nm mesopores in the micro-island were hexagonally arranged with a repeating structure distance of  $\sim 15$  nm.

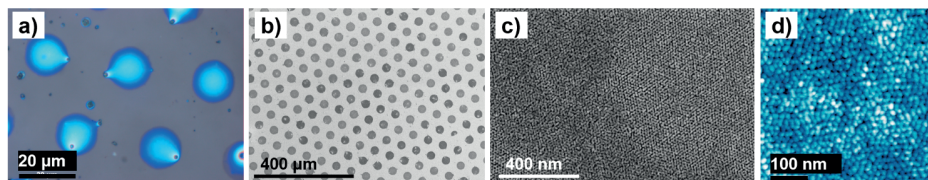


**Figure 2.6. Microscopy overview of  $\text{TiO}_2$  micro-islands  $\text{SiO}_2/\text{Si}(100)$  wafer.** **a)** Optical microscopy image of as-synthesized  $\text{TiO}_2$  micro-islands. **b,c)** Scanning electron microscopy (SEM) images displaying  $\text{TiO}_2$  micro-islands and their mesoporous structure. **d)** Atomic force microscopy (AFM) image showing the mesoporous structure of the  $\text{TiO}_2$  micro-islands.

The titania islands were impregnated with an aqueous cobalt nitrate solution and calcined at 250°C to form cobalt oxide nanoparticles. The resulting Co/ $\text{TiO}_2$  micro-island catalyst was analyzed with a combination of scanning electron microscopy (SEM), trans-



mission electron microscopy (TEM) and X-ray diffraction (XRD) to observe the porous structure from the inside of the island and to determine the average cobalt nanoparticle size (**Figure 2.7**). The titania micro-islands were synthesized on a non-transparent  $\text{SiO}_2/\text{Si}(100)$  wafer carrier. Hence, a slice of the island was cut out with a focused ion beam (FIB) (**Figure 2.7a**) to enable the transmission of electrons and high-resolution element mapping via transmission electron microscopy – energy dispersive X-ray (TEM-EDX) spectroscopy (**Figure 2.7b-f**). The average cobalt nanoparticle size determined with TEM was  $4.5 \pm 2.2$  nm, while grazing incidence X-ray diffraction (GI-XRD) yielded 6.0 nm.

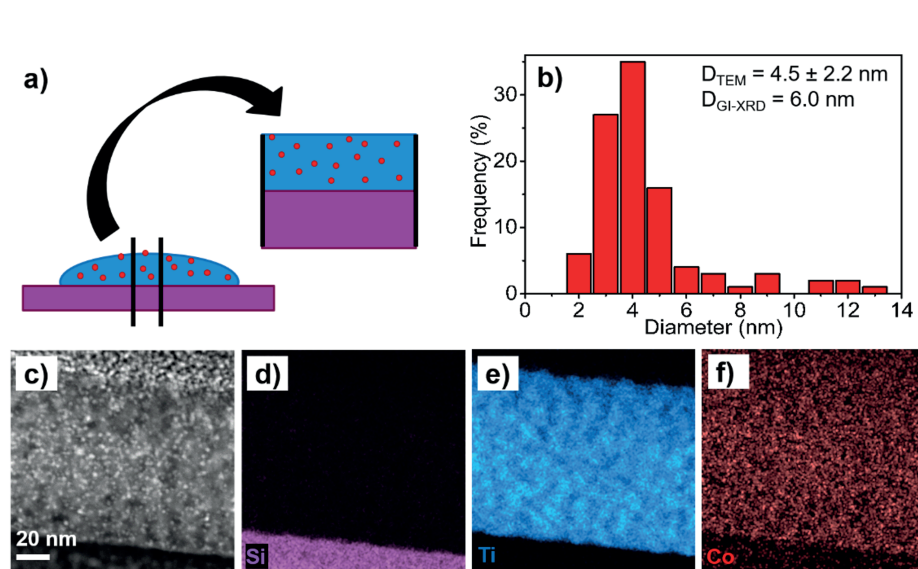


**Figure 2.7. Overview of Co/TiO<sub>2</sub> micro-islands.** **a)** Cutting a slice out of the micro-island with a focused ion beam (FIB) to prepare for scanning transmission electron microscopy (STEM). **b)** Cobalt nanoparticle size analysis with STEM-energy dispersive X-ray (EDX) spectroscopy. **c-f)** High-angle annular dark field (HAADF) STEM image (**c**) and EDX elemental maps of Si, Ti, and Co (**d-f**).

In addition to the ordered mesoporous titania micro-islands, ordered mesoporous alumina and silica micro-islands were successfully synthesized during the course of this PhD Thesis work. Both systems were impregnated and calcined to yield cobalt-based micro-island catalyst materials (**Figure 2.8**) as described above. Although the successful syntheses of  $\text{Co}/\text{Al}_2\text{O}_3$  and  $\text{Co}/\text{SiO}_2$  micro-island model catalysts are promising for employing surface science tools in heterogeneous catalysis research, the remaining section will be focused on  $\text{Co}/\text{TiO}_2$ .

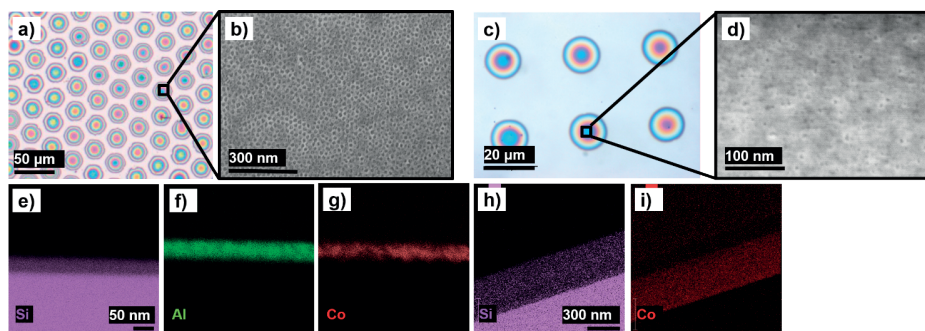


**Figure 2.8. Overview of  $\text{Co}/\text{Al}_2\text{O}_3$  and  $\text{Co}/\text{SiO}_2$  micro-islands.** a-d) Optical microscopy and scanning electron microscopy (SEM) images of  $\text{Al}_2\text{O}_3$  (a, b) and  $\text{SiO}_2$  (c, d). e-i) X-ray elemental maps of slices from the  $\text{Al}_2\text{O}_3$  and  $\text{SiO}_2$  micro-islands, after performing a focused ion beam (FIB) milling procedure on the samples.

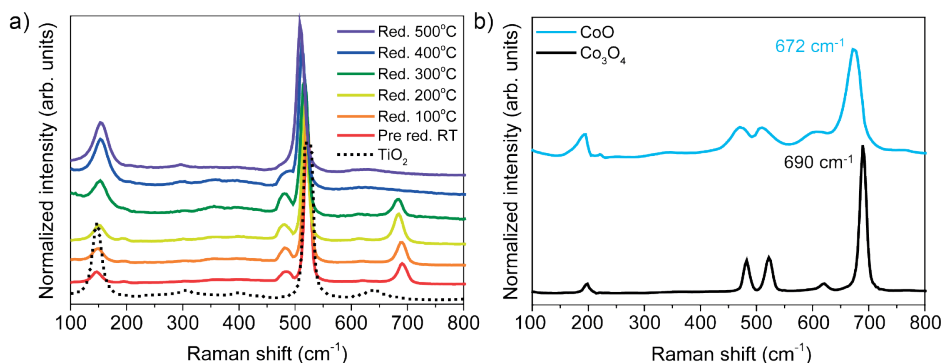


**Figure 2.9. Assessing the reduction profile of the  $\text{Co}/\text{TiO}_2$  micro-island model catalyst.** a) Raman spectra of the fresh sample and at increasing temperatures in  $\text{Ar}/\text{H}_2=4$ . b) Raman spectra of reference compounds  $\text{Co}_3\text{O}_4$  and  $\text{CoO}$ .

For 3-dimensional catalyst materials, the next steps in terms of analysis would be to apply a multitude of standard characterization techniques. For example,  $\text{H}_2$ -temperature programmed reduction (TPR) to assess the reduction profile of the cobalt (oxide) nanoparticles. For the micro-island model systems, many standard characterization techniques cannot be employed due to the detection limits of these methods.  $\text{H}_2$ -TPR typically requires 50 mg of catalyst material, while the micro-island model systems are in the range of micrograms. However, the unique built-up of the micro-islands allows other precise methods, such as *in situ* Raman micro-spectroscopy, to be employed for following the reduction of cobalt oxide nanoparticles to metallic cobalt (Figure 2.9). The  $\text{Co}_3\text{O}_4$  nanoparticles gradually transition to a pure  $\text{CoO}$  phase at 300°C.  $\text{CoO}$  transitions to metallic  $\text{Co}$ , which is Raman inactive and does not display any peaks, between 300 and 400°C.

Then, PiFM<sup>11</sup> was used to assess whether or not the micro-island model catalyst materials were suitable for SPM analysis. As mentioned above, PiFM is a combination of AFM and infrared IR spectroscopy. By combining these two techniques, the diffraction limit of IR light is overcome and IR spectra can be recorded with nanoscale spatial resolution and monolayer sensitivity.<sup>11</sup> Co/TiO<sub>2</sub> micro-islands were assessed with the PiFM technique as-synthesized and after 70 min FTS reaction. **Figure 2.10a,b** display the AFM image and corresponding IR map at 1060 cm<sup>-1</sup>, the Si-O stretching vibration of the wafer background and/or the Ti-O stretching vibration of the micro-island,<sup>93</sup> for the as-synthesized Co/TiO<sub>2</sub> micro-island. **Figure 2.10c,d** display the AFM image and corresponding IR map at 1260 cm<sup>-1</sup>, the C-C stretching vibration<sup>94</sup> of carbon deposition that occurred during the FTS reaction on the Co/TiO<sub>2</sub> island. PiFM IR point spectra are displayed in **Figure 2.10e** and a 3-dimensional AFM map of the Co/TiO<sub>2</sub> micro-island after 70 min of FTS reaction in **Figure 2.10f**. The micro-islands appear to be suitable model catalysts for surface-sensitive characterization techniques that require a scanning probe. In **Chapter 3**, we will employ the Co/TiO<sub>2</sub> micro-islands for a thorough mechanistic study on carbon deposition during the FTS reaction.

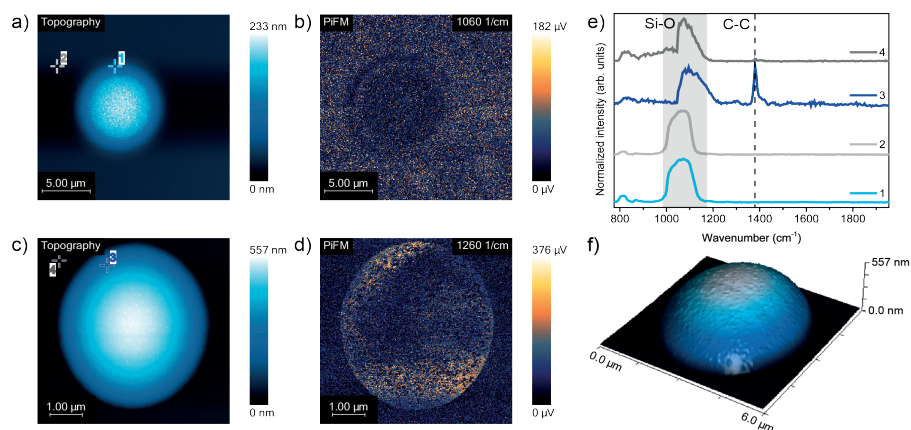


**Figure 2.10. Photo-induced force microscopy (PiFM) on Co/TiO<sub>2</sub> micro-islands.** Atomic force microscopy (AFM) images and infrared (IR) maps of **a,c** Co/TiO<sub>2</sub> as-synthesized and **b,d** after 70 min of Fischer-Tropsch Synthesis (FTS) reaction at 220°C, 1 bar, and H<sub>2</sub>/CO=2. **e**) PiFM IR point spectra recorded at the locations indicated in the AFM images. **f**) 3-dimensional AFM image of the Co/TiO<sub>2</sub> micro-island in **c**.

## 2.4 Conclusions

While curiosity about the composition of matter dates at least back to the ancient Greeks, the tools to actually observe nanoscale structures were only invented in the 20<sup>th</sup> century. These so-called nanoscale chemical imaging tools include scanning probe microscopy (SPM) methods, which overcome the diffraction limitations of light by operating with a very sharp tip, which scans over the sample under investigation. This **Chapter** introduced photo-induced force microscopy, a powerful tip-based spectroscopy method that combines infrared (IR) spectroscopy with atomic force microscopy (AFM) to record IR spectra with 10-20 nm spatial resolution. This analytical tool first found applications in the polymer science field and could later also be employed for e.g., nanoplastic detection in environmental samples and for catalysis research, but certainly has the potential to be applied in a wide variety of applications in the broad field of materials, life and environmental sciences.

Although significant breakthroughs were made over the past 20 years, *operando* spectroscopy and tip-based nanoscale characterization techniques, based on SPM and AFM methods, remain an interesting, but very challenging combination. To make this combination ultimately work and applied on a variety of catalyst systems, both the so-called pressure and material gaps should be bridged. In an attempt to bridge the material gap, in this **Chapter** ordered mesoporous titania micro-islands were synthesized to function as realistic model support material in heterogeneous catalysis research. A Co/TiO<sub>2</sub> micro-island model catalyst was successfully created and analyzed with the PiFM technique. In **Chapter 3**, this Co/TiO<sub>2</sub> micro-island model catalyst will be utilized to analyze carbon deposition in the Fischer-Tropsch Synthesis (FTS) reaction in more detail, thereby illustrating that it is feasible to investigate industrially relevant catalyst materials with the PiFM method.

## 2.5 Materials and Methods

### 2.5.1. Materials, Chemicals, and Synthesis

Mesoporous thin films and micro-islands were synthesized on 7x7 mm<sup>2</sup> SiO<sub>2</sub>/Si(100) wafers (Siegert Wafer) from a sol gel. The silica sol-gel contained tetraethyl orthosilicate (TEOS) (Sigma-Aldrich, ≥99.0%), the alumina sol-gel contained aluminum isopropoxide (AIP) (Sigma-Aldrich, ≥99.0%), and the titania sol-gel contained titanium isopropoxide (TIP) (Acros Organics, ≥98%) as precursor. The precursor was added to 4.0 mL of a 1.25 g L<sup>-1</sup> solution of poly(ethylene glycol)-*block*-poly(propylene glycol)-*block*-poly(ethylene glycol) (P123) (Sigma-Aldrich) in dry ethanol, containing 0.20-0.40 mL hydrochloric acid (HCl, 37 vol%, Sigma-Aldrich) to increase the acidity. The exact amounts used for the

different sol-gels can be found in **Table 2.1**. The reaction proceeded under magnetic stirring (600 rpm) for 10-60 min. For thin films, 10  $\mu\text{L}$  of sol gel solution was spin coated directly onto the wafers at 3000 rpm for 30 s. For micro-islands, the wafer surfaces were first made hydrophobic by emerging them in octadecyltrichlorosilane (ODTS) (Sigma-Aldrich,  $\geq 90\%$ ) in dry toluene (99.8%, water  $< 0.0002\%$ , Sigma-Aldrich) for 10 min. After washing with toluene, drying with pressurized argon, and baking at  $120^\circ\text{C}$  for 5 min, the wafers were covered with Cu photomasks (400-600 mesh) and UV/ozone ( $\text{O}_3$ ) cleaned (Ossila) for 5 min to partially remove ODTS from the surface. Typically, 10  $\mu\text{L}$  sol gel was spin coated on the wafers at 3000 rpm for 30 s. The coated wafers were aged in air at room temperature for 24 h, dried at  $80^\circ\text{C}$  for 3 h, and calcined at  $500^\circ\text{C}$  for 4 h with  $5^\circ\text{C min}^{-1}$ .

**Table 2.1.** Overview of sol gel compositions for mesoporous thin films and micro-islands synthesis.

Material	Precursor	Amount precursor	Ethanol (mL)	Water (mL)	HCl (37%) (mL)	P123 (mg)	Gel time (min)
$\text{SiO}_2$	TEOS	0.20 mL	4.0	1.5-2.0	0.20	50	15-60
$\text{Al}_2\text{O}_3$	AIP	0.20 g	4.0	0.0	0.40	50	15-60
$\text{TiO}_2$	TIP	0.25 mL	2.0	0.0	0.40	50	10-20

In a typical procedure, 10  $\mu\text{L}$  of an aqueous cobalt nitrate hexahydrate (Sigma-Aldrich, 99.999% trace metals basis) solution was spin coated on a wafer with micro-islands at 3000 rpm for 30 s. The wafers were dried at  $60^\circ\text{C}$  for 2 h and then calcined at  $250^\circ\text{C}$  for 2 h with  $5^\circ\text{C min}^{-1}$ . The cobalt loading was typically 20-30 wt.% with respect to the thin films or micro-islands support material based on energy dispersive X-ray (EDX) spectroscopy.

### 2.5.2. Methods

Optical microscopy images were recorded with an optical light microscope (50x objective). Focused ion beam - scanning electron microscopy (FIB-SEM) and the EDX chemical mapping analyses were performed using a FEI Helios NanoLab G3 UC SEM instrument equipped with a XMax<sup>N</sup> Silicon Drift Detector for EDX elemental mapping. High-angle annular dark-field (HAADF) - scanning transmission electron microscopy (STEM) and the corresponding EDX mapping analyses were performed on a FEI Talos F200X.

Grazing incidence X-ray diffraction (GI-XRD) and grazing incidence small angle X-ray scattering (GI-SAXS) were performed with a D8 ADVANCE at Bruker AXS advanced X-ray solutions (Karlsruhe, Germany). For the GI-XRD measurements, the XRD patterns were recorded under an incident angle  $\omega = 0.5^\circ$  and  $2\theta$  ranging from  $10^\circ$  to  $70^\circ$  with an increment of  $0.060^\circ$  and 7 s per step. The data were analyzed and average cobalt particle diameters were obtained with the TOPAS5 software. For the GI-SAXS measurements, scans were recorded under an incident angle  $\omega = 0.3^\circ$ . The data were analyzed and the repeating structure distance was calculated with the DIFFRAC.EVA software.

Raman spectra were recorded with an XploRA Plus Micro-Raman from Horiba Scientific. The spectra were recorded using a 50x or 100x (*ex situ*) objective, a 532 nm laser (either  $3.64 \cdot 10^5$  W/cm<sup>2</sup> or  $4.28 \cdot 10^5$  W/cm<sup>2</sup>, corresponding to setting of 1% or 10% maximum laser power respectively), and a 1200 mm<sup>-1</sup> grating. For *operando* experiments a Linkam THMS600 cell was used. The composition of the gas phase was monitored (0-60 amu) with online mass spectrometry (MS) using an OmniStar Thermostar GSD320 Gas Analysis System (Pfeiffer Vacuum). The catalyst was reduced *in situ* in a dilute H<sub>2</sub> flow (25 vol% H<sub>2</sub> in Ar, 40 mL min<sup>-1</sup> in total) at 450°C for 1 h (5°C min<sup>-1</sup> ramp). Then, the gas flow was switched to Ar and the cell was cooled to 220°C. The flow was then switched to a 5 mL min<sup>-1</sup> H<sub>2</sub> and 2.5 mL min<sup>-1</sup> CO flow (H<sub>2</sub>/CO = 2) for 1-24 h.

Nanoscale infrared spectroscopy (nano IR) was performed using a VistaScope photo-induced force microscope (PiFM) from Molecular Vista (San Jose, CA, USA). This instrument is equipped with a quantum cascade laser (QCL) unit, as well as an optical parametric oscillator (OPO) laser. IR spectra were recorded in the 775-1950 cm<sup>-1</sup> range with the QCL and in the 2250-4400 cm<sup>-1</sup> range with the OPO laser. Prior to hyperspectral analysis, AFM topography images were recorded in non-contact mode together with IR maps and IR point spectra (60 accumulations of 500 ms; 1 cm<sup>-1</sup> spectral resolution). Typical image sizes were 2-30  $\mu\text{m}^2$ . The data were analyzed using the VistaScan 1.7, SurfaceWorks 2.4 software, MATLAB, and Origin 9.

## 2.6 Author Contributions and Acknowledgements

This **Chapter** is based on the manuscript “ten Have, I. C., Hartman, T., van Bavel, A.P., Bezemer, G. L., Ferri, D., Geitner, R., Huang, T., Kupfer, S., Gräfe, S., Meirer, F., Weckhuysen, B. M. Through the Lens of *Operando* Spectroscopy: Mechanistic Insights in the Fischer-Tropsch Synthesis. *submitted for publication*. (2022).”. Bert Weckhuysen and Iris ten Have conceived the main research ideas in this **Chapter**, including its general outline. The **Chapter** was further constructed by Iris ten Have under the supervision of Florian Meirer and Bert Weckhuysen.

## 2.7 References

1. Bayda, S., Adeel, M., Tuccinardi, T., Cordani, M. & Rizzolio, F. The history of nanoscience and nanotechnology: From chemical-physical applications to nanomedicine. *Molecules* **25**, 1–15 (2020).
2. Binnig, G., Rohrer, H., Gerber, C. & Weibel, E. Tunneling through a controllable vacuum gap. *Applied Physics Letters* **40**, 178–180 (1982).
3. Binnig, G., Rohrer, H., Gerber, Ch. & Weibel, E. Surface Studies by Scanning Tunneling Microscopy. *Physical Review Letters* **49**, 57 (1982).
4. Binnig, G., Rohrer, H., Gerber, Ch. & Weibel, E. 7 x 7 Reconstruction on Si(111) Resolved in Real Space. *Physical Review Letters* **50**, 120 (1983).
5. Binnig, G., Quate, C. F. & Gerber, C. Atomic Force Microscope. *Physical Review Letters* **56**, 930–934 (1986).
6. Binnig, G. Atomic Force Microscope and Method for Imaging Surfaces with Atomic Resolution. U.S. Patent 4724318A. (1990).
7. Prater, C., Kjoller, K. & Shetty, R. Nanoscale infrared spectroscopy. *Materials Today* **13**, 56–60 (2010).
8. Dazzi, A. & Prater, C. B. AFM-IR: Technology and applications in nanoscale infrared spectroscopy and chemical imaging. *Chemical Reviews* **117**, 5146–5173 (2017).
9. Bechtel, H. A., Johnson, S. C., Khatib, O., Muller, E. A. & Raschke, M. B. Synchrotron infrared nano-spectroscopy and -imaging. *Surface Science Reports* **75**, 100493 (2020).
10. Wu, C. Y., Wolf, W. J., Levartovsky, Y., Bechtel, H. A., Martin, M. C., Toste, F. D. & Gross, E. High-spatial-resolution mapping of catalytic reactions on single particles. *Nature* **541**, 511–515 (2017).
11. Nowak, D., Morrison, W., Wickramasinghe, H. K., Jahng, J., Potma, E., Wan, L., Ruiz, R., Albrecht, T. R., Schmidt, K., Frommer, J., Sanders, D. P. & Park, S. Nanoscale chemical imaging by photoinduced force microscopy. *Science Advances* **2**, e1501571 (2016).
12. Hartman, T., Wondergem, C. S., Kumar, N., van den Berg, A. & Weckhuysen, B. M. Surface- and Tip-Enhanced Raman Spectroscopy in Catalysis. *Journal of Physical Chemistry Letters* **7**, 1570–1584 (2016).
13. van Schrojenstein Lantman, E. M., Deckert-Gaudig, T., Mank, A. J. G., Deckert, V. & Weckhuysen, B. M. Catalytic processes monitored at the nanoscale with tip-enhanced Raman spectroscopy. *Nature Nanotechnology* **7**, 583–586 (2012).
14. Fu, D., Park, K., Delen, G., Attila, Ö., Meirer, F., Nowak, D., Park, S., Schmidt, J. E. & Weckhuysen, B. M. Nanoscale infrared imaging of zeolites using photoinduced force microscopy. *Chemical Communications*. **53**, 18–21 (2017).
15. Jahng, J., Potma, E. O. & Lee, E. S. Nanoscale spectroscopic origins of photoinduced tip-sample force in the midinfrared. *Proceedings of the National Academy of Sciences of the United States of America* **116**, 26359–26366 (2019).
16. Jarzembski, A., Shaskey, C. & Park, K. Review: Tip-based vibrational spectroscopy for nanoscale analysis of emerging energy materials. *Frontiers in Energy* **12**, 43–71 (2018).
17. Almajhadi, M. A., Uddin, S. M. A. & Wickramasinghe, H. K. Observation of nanoscale opto-mechanical molecular damping as the origin of spectroscopic contrast in photo induced force microscopy. *Nature Communications* **11**, 5691 (2020).
18. Ramer, G., Aksyuk, V. A. & Centrone, A. Quantitative Chemical Analysis at the Nanoscale Using the Photothermal Induced Resonance Technique. *Analytical Chemistry* **89**, 13524–13531 (2017).

19. Murdick, R. A., Morrison, W., Nowak, D., Albrecht, T. R., Jahng, J. & Park, S. Photoinduced force microscopy: A technique for hyperspectral nanochemical mapping. *Japanese Journal of Applied Physics* **56**, (2017).
20. Vollmer, I., Jenks, M. J. F., Roelands, M. C. P., White, R. J., van Harmelen, T., de Wild, P., van der Laan, G. P., Meirer, F., Keurentjes, J. T. F. & Weckhuysen, B. M. Beyond Mechanical Recycling: Giving New Life to Plastic Waste. *Angewandte Chemie International Edition* **59**, 15402-15423 (2020).
21. UNEP 2009. *Marine Litter: A Global Challenge*. (2009).
22. Bergmann, M., Gutow, L. & Klages, M. *Marine anthropogenic litter*. *Marine Anthropogenic Litter* **9783319165103**, (Springer, Cham, 2015).
23. Jambeck, J. R., Gayer, R., Wilcox, C., Siegler, R. T., Perryman, M., Andrady, A., Narayan, R. & Law, L. K. Plastic waste inputs from land into the ocean. *Science* **347**, 768-771 (2015).
24. Cole, M., Lindeque, P., Halsband, C. & Galloway, T. S. Microplastics as contaminants in the marine environment: A review. *Marine Pollution Bulletin* **62**, 2588-2597 (2011).
25. Cózar, A., Echevarría, F., González-Gordillo, J. I., Irigoien, X., Úbeda, B., Hernández-León, S., Palma, Á. T., Navarro, S., García-de-Lomas, J., Ruiz, A., Fernández-de-Puelles, M. L. & Duarte, C. M. Plastic debris in the open ocean. *Proceedings of the National Academy of Sciences of the United States of America* **111**, 10239-10244 (2014).
26. Eriksen, M., Lebreton, L. C. M., Carson, H. S., Thiel, M., Moore, C. J., Borerro, J. C., Galgani, F., Ryan, P. G. & Reisser, J. Plastic Pollution in the World's Oceans: More than 5 Trillion Plastic Pieces Weighing over 250,000 Tons Afloat at Sea. *PLoS ONE* **9**, 1-15 (2014).
27. Pabortsava, K. & Lampitt, R. S. High concentrations of plastic hidden beneath the surface of the Atlantic Ocean. *Nature Communications* **11**, 4073 (2020).
28. van Sebille, E., Wilcox, C., Lebreton, L., Maximenko, N., Hardesty, B. D., van Franeker, J. A., Eriksen, M., Siegel, D., Galgani, F. & Law, K. L. A global inventory of small floating plastic debris. *Environmental Research Letters* **10**, 124006 (2015).
29. Hardesty, B. D., Harari, J., Isobe, A., Lebreton, L., Maximenko, N., Potemra, J., van Sebille, E., Dick Vethaak, A. & Wilcox, C. Using numerical model simulations to improve the understanding of micro-plastic distribution and pathways in the marine environment. *Frontiers in marine science* **4**, 30 (2017).
30. ter Halle, A., Ladirat, L., Gendre, X., Goudouneche, D., Pusineri, C., Routaboul, C., Tenailleau, C., Duployer, B. & Perez, E. Understanding the Fragmentation Pattern of Marine Plastic Debris. *Environmental Science and Technology* **50**, 5668-5675 (2016).
31. Gigault, J., Pedrono, B., Maxit, B. & ter Halle, A. Marine plastic litter: The unanalyzed nano-fraction. *Environmental Science: Nano* **3**, 346-350 (2016).
32. Andrady, A. L. Microplastics in the marine environment. *Marine Pollution Bulletin* **62**, 1596-1605 (2011).
33. Gigault, J., Halle, A. ter, Baudrimont, M., Pascal, P. Y., Gauffre, F., Phi, T. L., El Hadri, H., Grassl, B. & Reynaud, S. Current opinion: What is a nanoplastic? *Environmental Pollution* **235**, 1030-1034 (2018).
34. Ferreira, I., Venâncio, C., Lopes, I. & Oliveira, M. Nanoplastics and marine organisms: What has been studied? *Environmental Toxicology and Pharmacology* **67**, 1-7 (2019).
35. Schwaferts, C., Niessner, R., Elsner, M. & Ivleva, N. P. Methods for the analysis of submicrometer- and nanoplastic particles in the environment. *Trends in Analytical Chemistry* **112**, 52-65 (2019).



36. Koelmans, A. A., Besseling, E., Foekema, E., Kooi, M., Mintenig, S., C. Ossendorp, B., E. Redondo-Hasselerharm, P., Verschoor, A., P. van Wezel, A. & Scheffer, M. Risks of Plastic Debris: Unravelling Fact, Opinion, Perception, and Belief. *Environmental Science & Technology* **51**, 11513-11519 (2017).
37. Shen, M., Zhang, Y., Zhu, Y., Song, B., Zeng, G., Hu, D., Wen, X. & Ren, X. Recent advances in toxicological research of nanoplastics in the environment: A review. *Environmental Pollution* **252**, 511-521 (2019).
38. Lithner, D., Larsson, A. & Dave, G. Environmental and health hazard ranking and assessment of plastic polymers based on chemical composition. *Science of the Total Environment* **409**, 3309-3324 (2011).
39. Bergami, E., Bocci, E., Vannuccini, M. L., Monopoli, M., Salvati, A., Dawson, K. A. & Corsi, I. Nano-sized polystyrene affects feeding, behavior and physiology of brine shrimp *Artemia franciscana* larvae. *Ecotoxicology and Environmental Safety* **123**, 18-25 (2016).
40. Chen, K. & Vyazovkin, S. Mechanistic differences in degradation of polystyrene and polystyrene-clay nanocomposite: Thermal and thermo-oxidative degradation. *Macromolecular Chemistry and Physics* **207**, 587-595 (2006).
41. Safarov, J., Berndt, S., Millero, F., Feistel, R., Heintz, A. & Hassel, E. (p,p,T) properties of seawater Extensions to high salinities. *Deep-Sea Research Part I* **65**, 146-156 (2012).
42. Vilaplana, F., Ribes-Greus, A. & Karlsson, S. Degradation of recycled high-impact polystyrene. Simulation by reprocessing and thermo-oxidation. *Polymer Degradation and Stability* **91**, 2163-2170 (2006).
43. ten Have, I. C., Duijndam, A. J. A., Oord, R., Berlo-van den Broek, H. J. M., Vollmer, I., Weckhuysen, B. M. & Meirer, F. Photoinduced Force Microscopy as an Efficient Method Towards the Detection of Nanoplastics. *Chemistry-Methods* **1**, 205-209 (2021).
44. Meirer, F., ten Have, I. C., Oord, R., Zettler, E. R., van Sebille, E. & Amaral-Zettler, L.A. Weckhuysen, B. M. Nanoscale Infrared Spectroscopy Reveals Nanoplastics at 5000 m Depth in the South Atlantic Ocean. *Research Square preprint*, 1-14 (2021).
45. ter Halle, A., Jeanneau, L., Martignac, M., Jardé, E., Pedrono, B., Brach, L. & Gigault, J. Nanoplastic in the North Atlantic Subtropical Gyre. *Environmental Science & Technology* **51**, 13689-13697 (2017).
46. Gerritse, J., Leslie, H. A., de Tender, C. A., Devriese, L. I. & Vethaak, A. D. Fragmentation of plastic objects in a laboratory seawater microcosm. *Scientific Reports* **10**, 10945(2020).
47. Zhang, C., Zhou, H., Cui, Y., Wang, C., Li, Y. & Zhang, D. Microplastics in offshore sediment in the Yellow Sea and East China Sea, China. *Environmental Pollution* **244**, 827-833 (2019).
48. Zhang, F., Yao, C., Xu, J., Zhu, L., Peng, G. & Li, D. Composition, spatial distribution and sources of plastic litter on the East China Sea floor. *Science of the Total Environment* **742**, 140525 (2020).
49. Kanhai, L. D. K., Gårdfeldt, K., Lyashevskaya, O., Hassellöv, M., Thompson, R. C. & O'Connor, I. Microplastics in sub-surface waters of the Arctic Central Basin. *Marine Pollution Bulletin* **130**, 8-18 (2018).
50. Kooi, M., van Nes, E. H., Scheffer, M. & Koelmans, A. A. Ups and Downs in the Ocean: Effects of Biofouling on Vertical Transport of Microplastics. *Environmental Science and Technology* **51**, 7963-7971 (2017).

51. Choy, C. A., Robison, B. H., Gagne, T. O., Erwin, B., Firl, E., Halden, R. U., Hamilton, J. A., Katija, K., Lisin, S. E., Rolsky, C. & S. van Houtan, K. The vertical distribution and biological transport of marine microplastics across the epipelagic and mesopelagic water column. *Scientific Reports* **9**, 7843 (2019).
52. de la Fuente, R., Drótos, G., Hernández-García, E., López, C. & van Sebille, E. Sinking microplastics in the water column: Simulations in the Mediterranean Sea. *Ocean Science* **17**, 431–453 (2021).
53. Wichmann, D., Delandmeter, P. & van Sebille, E. Influence of Near-Surface Currents on the Global Dispersal of Marine Microplastic. *Journal of Geophysical Research: Oceans* **124**, 6086–6096 (2019).
54. Delen, G., Monai, M., Meirer, F. & Weckhuysen, B. M. In situ Nanoscale Infrared Spectroscopy of Water Adsorption on Nanoislands of Surface-Anchored Metal–Organic Frameworks. *Angewandte Chemie International Edition* **60**, 1620–1624 (2020).
55. Werny, M. J., Zarupski, J., ten Have, I. C., Piovano, A., Hendriksen, C., Friederichs, N. H., Meirer, F., Groppo, E. & Weckhuysen, B. M. Correlating the Morphological Evolution of Individual Catalyst Particles to the Kinetic Behavior of Metallocene-Based Ethylene Polymerization Catalysts. *JACS Au* **1**, 1996–2008 (2021).
56. Park, J. Y. *Current trends of surface science and catalysis. Current Trends of Surface Science and Catalysis* **9781461487**, (Springer, New York, 2014).
57. Wolff, J., Papathanasiou, A. G., Kevrekidis, I. G., Rotermund, H. H. & Ertl, G. Spatiotemporal addressing of surface activity. *Science* **294**, 134–137 (2001).
58. Ertl, G. Reactions at Surfaces: From Atoms to Complexity (Nobel Lecture). *Angewandte Chemie International Edition* **47**, 3524–3535 (2008).
59. Kleinle, G., Penka, V., Behm, R. J., Ertl, G. & Moritz, W. Structure determination of an adsorbate-induced multilayer reconstruction: (1x2)-H/Ni(110). *Physical Review Letters* **58**, 148–151 (1987).
60. Somorjai, G. A. & McCrea, K. Roadmap for catalysis science in the 21st century: A personal view of building the future on past and present accomplishments. *Applied Catalysis A: General* **222**, 3–18 (2001).
61. Somorjai, G. A. The experimental evidence of the role of surface restructuring during catalytic reactions. *Catalysis Letters* **12**, 17–34 (1992).
62. Somorjai, G. A., Contreras, A. M., Montano, M. & Rioux, R. M. Clusters, surfaces, and catalysis. *Proceedings of the National Academy of Sciences of the United States of America* **103**, 10577–10583 (2006).
63. Qian, J., An, Q., Fortunelli, A., Nielsen, R. J. & Goddard, W. A. Reaction Mechanism and Kinetics for Ammonia Synthesis on the Fe(111) Surface. *Journal of the American Chemical Society* **140**, 6288–6297 (2018).
64. Eren, B., Zherebetsky, D., Patera, L. L., Wu, C. H., Bluhm, H., Africh, C., Wang, L.-W., Somorjai, G. A. & Salmeron, M. Activation of Cu(111) surface by decomposition into nanoclusters driven by CO adsorption. *Science* **351**, 475–478 (2016).
65. Somorjai, G. A. & McCrea, K. Roadmap for catalysis science in the 21st century: A personal view of building the future on past and present accomplishments. *Applied Catalysis A: General* **222**, 3–18 (2001).
66. Ertl, G. Reactions at Surfaces: From Atoms to Complexity (Nobel Lecture). *Angewandte Chemie International Edition* **47**, 3524–3535 (2008).
67. Rase, H. F. *Handbook of Commercial Catalysts - Heterogeneous Catalysts*. (CRC Press, Boca Raton, 2000).

68. Qian, J., An, Q., Fortunelli, A., Nielsen, R. J. & Goddard, W. A. Reaction Mechanism and Kinetics for Ammonia Synthesis on the Fe(111) Surface. *Journal of the American Chemical Society* **140**, 6288–6297 (2018).
69. Oosterbeek, H. Bridging the pressure and material gap in heterogeneous catalysis: cobalt Fischer-Tropsch catalysts from surface science to industrial application. *Physical Chemistry Chemical Physics* **9**, 3570–3576 (2007).
70. Somorjai, G. A., York, R. L., Butcher, D. & Park, J. Y. The evolution of model catalytic systems; studies of structure, bonding and dynamics from single crystal metal surfaces to nanoparticles, and from low pressure ( $<10^{-3}$  Torr) to high pressure ( $>10^{-3}$  Torr) to liquid interfaces. *Physical Chemistry Chemical Physics* **9**, 3500–3513 (2007).
71. Valden, M., Lai, X. & Goodman, D. W. Onset of catalytic activity of gold clusters on titania with the appearance of nonmetallic properties. *Science* **281**, 1647–1650 (1998).
72. Campbell, R. A. & Goodman, D. W. A new design for a multitechnique ultrahigh vacuum surface analysis chamber with high pressure capabilities. *Review of Scientific Instruments* **63**, 172–174 (1992).
73. Mom, R. V., Louwen, J. N., Frenken, J. W. M. & Groot, I. M. N. In situ observations of an active MoS<sub>2</sub> model hydrodesulfurization catalyst. *Nature Communications* **10**, 2546 (2019).
74. Frenken, J. W. M. & Groot, I. M. N. Seeing dynamic phenomena with live scanning tunneling microscopy. *MRS Bulletin* **42**, 834–841 (2017).
75. Frenken, J. W. M. & Groot, I. M. N. Seeing dynamic phenomena with live scanning tunneling microscopy. *MRS Bulletin* **42**, 834–841 (2017).
76. Rupprechter, G. A surface science approach to ambient pressure catalytic reactions. *Catalysis Today* **126**, 3–17 (2007).
77. Centi, G., Passalacqua, R., Perathoner, S., Su, D. S., Weinberg, G. & Schlo, R. Oxide thin films based on ordered arrays of 1D nanostructure. A possible approach toward bridging material gap in catalysis. *Physical Chemistry Chemical Physics* **9**, 4930–4938 (2007).
78. Beck, J. S., Vartuli, J. C., Roth, W. J., Leonowicz, M. E., Kresge, C. T., Schmitt, K. D., Chu, C. T. W., Olson, D. H., Sheppard, E. W., McCullen, S. B., Higgins, J. B. & Schlenker, J. L. A New Family of Mesoporous Molecular Sieves Prepared with Liquid Crystal Templates. *Journal of the American Chemical Society* **114**, 10834–10843 (1992).
79. Zhao, D., Feng, J., Huo, Q., Melosh, N., Fredrickson, G. H., Chmelka, B. F. & Stucky, G. D. Triblock copolymer syntheses of mesoporous silica with periodic 50 to 300 angstrom pores. *Science* **279**, 548–552 (1998).
80. Katiyar, A., Yadav, S., Smirniotis, P. G. & Pinto, N. G. Synthesis of ordered large pore SBA-15 spherical particles for adsorption of biomolecules. *Journal of Chromatography A* **1122**, 13–20 (2006).
81. Danon, A., Stair, P. C. & Weitz, E. FTIR study of CO<sub>2</sub> adsorption on amine-grafted SBA-15: Elucidation of adsorbed species. *Journal of Physical Chemistry C* **115**, 11540–11549 (2011).
82. Pham, A. L. T., Sedlak, D. L. & Doyle, F. M. Dissolution of mesoporous silica supports in aqueous solutions: Implications for mesoporous silica-based water treatment processes. *Applied Catalysis B: Environmental* **126**, 258–264 (2012).
83. Khodakov, A. Y., Chu, W. & Fongarland, P. Advances in the development of novel cobalt Fischer-Tropsch catalysts for synthesis of long-chain hydrocarbons and clean fuels. *Chemical Reviews* **107**, 1692–1744 (2007).
84. Xiong, H., Zhang, Y., Liew, K. & Li, J. Fischer-Tropsch synthesis: The role of pore size for Co/SBA-15 catalysts. *Journal of Molecular Catalysis A: Chemical* **295**, 68–76 (2008).

85. Martínez, A., López, C., Márquez, F. & Díaz, I. Fischer-Tropsch synthesis of hydrocarbons over mesoporous Co/SBA-15 catalysts: The influence of metal loading, cobalt precursor, and promoters. *Journal of Catalysis* **220**, 486–499 (2003).
86. Gunter, P. L. J., Niemantsverdriet, J. W. (Hans), Riberio, F. H. & Somoraji, G. A. Surface Science Approach to Modeling Supported Catalysts. *Catalysis Reviews - Science and Engineering* **39**, 77–168 (1997).
87. Crepaldi, E. L., Soler-Illia, G. J. de A. A., Grosso, D., Cagnol, F., Ribot, F. & Sanchez, C. Controlled formation of highly organized mesoporous titania thin films: From mesostructured hybrids to mesoporous nanoanatase TiO<sub>2</sub>. *Journal of the American Chemical Society* **125**, 9770–9786 (2003).
88. Bezemer, G. L., Bitter, J. H., Kuipers, H. P. C. E., Oosterbeek, H., Holewijn, J. E., Xu, X., Kapteijn, F., van Dillen, A. J. & de Jong, K. P. Cobalt particle size effects in the Fischer-Tropsch reaction studied with carbon nanofiber supported catalysts. *Journal of American Chemical Society* **128**, 3956–3964 (2006).
89. den Breejen, J. P., Radstake, P. B., Bezemer, G. L., Bitter, J. H., Froseth, V., Holmen, A. & de Jong, K. P. On the Origin of the Cobalt Particle Size Effects in Fischer-Tropsch Catalysis. *Journal of the American Chemical Society* **131**, 7197–7203 (2009).
90. Alberius, P. C. A., Frindell, K. L., Hayward, R. C., Kramer, E. J., Stucky, G. D. & Chmelka, B. F. General predictive syntheses of cubic, hexagonal, and lamellar silica and titania mesostructured thin films. *Chemistry of Materials* **14**, 3284–3294 (2002).
91. Masuda, Y., Sugiyama, T., Lin, H., Seo, W. S. & Koumoto, K. Selective deposition and micro-patterning of titanium dioxide thin film on self-assembled monolayers. *Thin Solid Films* **382**, 153–157 (2001).
92. Masuda, Y., Jinbo, Y., Yonezawa, T. & Koumoto, K. Templated site-selective deposition of titanium dioxide on self-assembled monolayers. *Chemistry of Materials* **14**, 1236–1241 (2002).
93. Coates, J. in *Encyclopedia of analytical chemistry: applications, theory and instrumentation* (ed. Meyers, R. A.) 10815–10837 (John Wiley & Sons, New York, 2006).
94. Lazar, G., Zellama, K., Vascan, I., Stamate, M., Lazar, I. & Rusu, I. Infrared absorption properties of amorphous carbon films. *Journal of Optoelectronics and Advanced Materials* **7**, 647–652 (2005).



This Chapter is based on the following scientific article:

ten Have, I. C., Hartman, T., van Bavel, A.P., Bezemer, G. L., Ferri, D., Geitner, R., Huang, T., Kupfer, S., Gräfe, S., Meirer, F., Weckhuysen, B. M. (2022). Through the Lens of *Operando* Spectroscopy: Mechanistic Insights in the Fischer-Tropsch Synthesis. *Submitted for publication*.

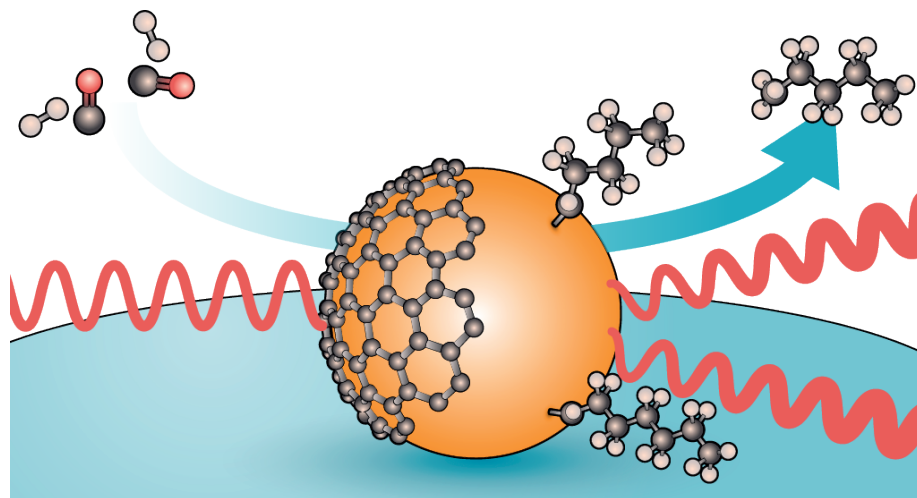
# **CHAPTER 3**

## **THROUGH THE LENS OF OPERANDO SPECTROSCOPY: MECHANISTIC INSIGHTS IN THE FISCHER-TROPSCH SYNTHESIS**



### Abstract

Fischer-Tropsch Synthesis (FTS) is one of the most resilient industrial scale catalytic reactions leading to a wide variety of clean fuels and chemicals produced from syngas, a mixture of carbon monoxide (CO) and hydrogen ( $H_2$ ). Although this process has been invented more than a century ago, settling the mechanistic debate around the formation of long-chain hydrocarbons from syngas remains very challenging. While most scientists advocate the direct dissociation of CO, followed by hydrogenation of surface carbon and the subsequent polymerization of the surface  $CH_x$  fragments, we show herein that multiple reaction mechanisms occur simultaneously on an industrially relevant cobalt-titania FTS catalyst. By employing various advanced vibrational spectroscopy techniques under industrially relevant reaction conditions, we were able to identify surface  $CH_x$  moieties as well as oxygen-containing surface intermediates. While supported cobalt nanoparticles are responsible for CO dissociation and subsequent hydrogenation of the surface carbon species, the titania support participates in the functioning of the catalyst by supplying surface oxygenate species. Besides the formation of linear reaction products, unsaturated hydrocarbon deposits appear to grow as well on the catalyst surface. While 99% of the products are linear hydrocarbons, oxygenated products constitute a minority fraction of 1%. Carbon deposits remain adsorbed on the catalyst surface, therefore suggesting that they may be involved in catalyst deactivation phenomena.





### 3.1 Introduction

Nowadays, there is an increasing interest in chemical production technologies that offer an alternative to our fossil-based manufacturing processes. The production of synthetic fuels from syngas (CO/H<sub>2</sub> mixtures), also known as Fischer-Tropsch Synthesis (FTS)<sup>1</sup>, serves as an example as it may offer a route to convert small molecules, like CO and the related greenhouse gas molecule CO<sub>2</sub>, obtained from e.g., municipal and agricultural waste, such as plastic, or lignin into transportation fuels and chemicals<sup>2</sup>. As thoroughly discussed in **Chapter 1**, the FTS process is commercially conducted with cobalt- and iron-based solid catalysts and the technology dates back to the 1920s<sup>3,4</sup>. However, due to the complexity of the overall chemical conversion process, the plausible catalytically active phases and the reaction mechanisms are still highly debated.

Supported cobalt nanoparticles are one of the main ingredients of a typical commercial FTS catalyst. These nanoparticles are attached to a porous support material to avoid undesired metal sintering, which would lead to a decrease in catalytic activity. The support material is typically a solid with a high surface area, such as titania, silica, or alumina<sup>5</sup>. Linear paraffins and olefins are the targeted FTS output and high selectivity towards these products is thus an important requirement<sup>1</sup>. In specific instances, where supported cobalt nanoparticles were combined with an oxidic component, such as MnO, and an alkali metal, such as K or Na, high selectivity towards oxygenates has been reported as well<sup>6,7</sup>. An undesired yet inevitable side product of the FTS reaction is CH<sub>4</sub>. While the step-edge sites of supported cobalt nanoparticles are held responsible for high C-C coupling activity<sup>8,9</sup>, the flat terrace sites may be responsible for CH<sub>4</sub> formation. CH<sub>x</sub> intermediates namely bind less firmly on cobalt terrace sites than on cobalt stepped surfaces. As a result, one expects more facile CH<sub>x</sub> hydrogenation and thus CH<sub>4</sub> formation on terraces<sup>10-12</sup>. Besides, hydrocarbon and carbonaceous species will be formed during the FTS process on cobalt-based catalysts in different forms and are considered to be one of the causes of catalyst deactivation when they are irreversibly adsorbed on the catalyst surface<sup>2,13,14</sup>. However, detecting such carbon species is challenging due to insufficient detection limits of most bulk spectroscopic techniques and the strong absorption of visible light by the very dark colored catalyst materials used in FTS, which makes optical spectroscopy using visible light rather difficult if not simply impossible.

For the formation of conventional FTS products, various mechanistic options have been proposed<sup>2,10</sup>. The direct dissociation of CO followed by hydrogenation of C atoms and polymerization of CH<sub>x</sub> (**Figure 3.1a**) is advocated by most researchers<sup>2,10,15-17</sup>, but certainly not unchallenged. In the most widely accepted alternative, adsorbed CO is first hydrogenated to a formyl/aldehyde intermediate and then dissociated<sup>10,15,18,19</sup> (**Figure 3.1a**). Chain growth consequently occurs *via* insertion of CO moieties<sup>20-22</sup>. For cobalt terrace

sites, it has previously been established that H-assisted C-O scission has a lower energy barrier than the direct dissociation of CO<sup>10,23,24</sup>. It could thus be speculated that graphitic carbon deposits, which prefer a flat cobalt surface<sup>11,15,25-28</sup>, are formed via the H-assisted mechanism and grow via CO insertion. Nevertheless, this has not yet been substantiated by experimental evidence, nor has the chemical structure of the carbon deposits been clarified in detail. In general, the reaction mechanisms that take place during the FTS reaction and which particular pathways lead to which particular products is still highly debated<sup>29</sup>. Due to the wide variety of products that an FTS catalyst can form, it is likely that multiple reaction mechanisms occur, perhaps even simultaneously, during the FTS<sup>2</sup>.

From an analytical viewpoint, the so-called pressure and material gaps, as discussed in **Chapter 2**, should be bridged to study solid catalysts at the best possible resolution and under realistic reaction conditions. The pressure gap describes the difference between industrially relevant reaction conditions, *i.e.*, elevated temperatures and pressures, and ultra-high vacuum (UHV) environments often used in academic research<sup>30,31</sup>. We aim to address the pressure gap by employing shell-isolated nanoparticle-enhanced Raman spectroscopy (SHINERS)<sup>29</sup> during the FTS reaction with Co/TiO<sub>2</sub> as catalyst (**Figure 3.1c**). This technique has previously been used by our group to successfully study reaction pathways and intermediates on Rh-based catalysts during the FTS reaction up to 350°C<sup>29</sup>. However, in this **Chapter** we will push the boundaries of the technique by operating at temperatures up to 450°C and pressures up to 20 bar. The material gap describes the discrepancy between industrial catalysts and simple planar model systems, like single crystals, often used in academic research. In this **Chapter**, we also attempt to bridge the material gap by employing the Co/TiO<sub>2</sub> micro-island model catalysts, as introduced in **Chapter 2**. These are realistic enough to represent realistic as possible Co-based FTS catalysts, but still flat enough to use surface-sensitive techniques on ( $Z < 1 \mu\text{m}$ ), such as atomic force microscopy (AFM).

In an attempt to answer the open mechanistic questions related to the FTS reaction, we deploy in this **Chapter** a multi-technique analytical approach. To observe active species and intermediates, *operando* modulation excitation diffuse-reflectance infrared Fourier-transform spectroscopy (ME DRIFTS) was used as transient analytical method. With this methodology, the concentration of reactant CO was periodically varied to provoke a transient response, which allows for the spectral detection of active species and intermediates (**Figure 3.1b**). Carboxylate intermediates were observed on Co/TiO<sub>2</sub> and the role of the performance-enhancing TiO<sub>2</sub> support appeared related to supplying essential building blocks during the FTS reaction. To observe surface species during the FTS reaction at elevated pressure, we have used *operando* SHINERS.

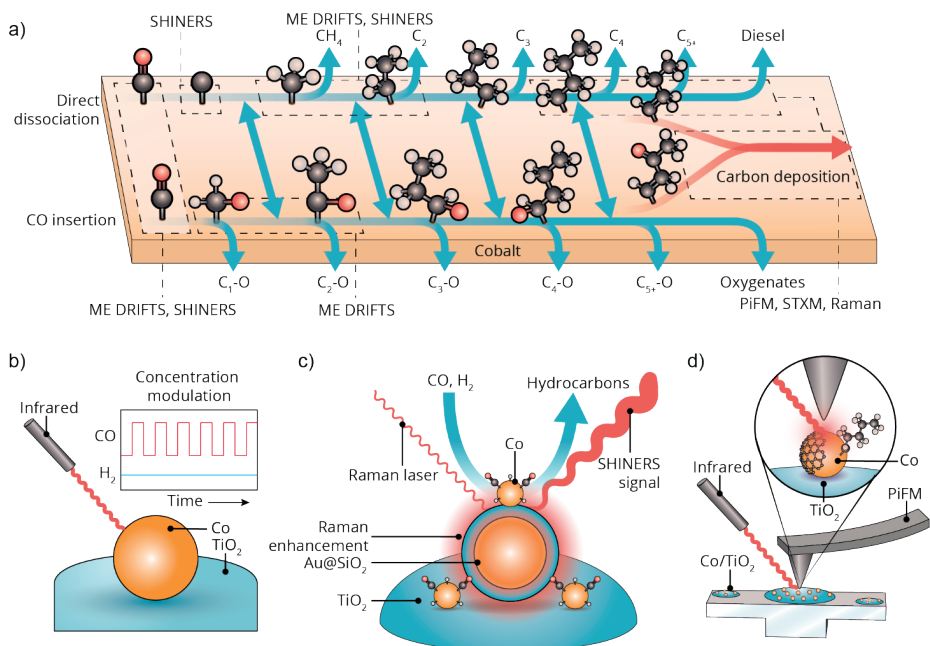


**Figure 3.1. Schematic illustration of the two main reaction pathways in Fischer-Tropsch Synthesis (FTS) and the analytical strategies used in this Chapter to elucidate the occurrence of these reaction pathways.** **a)** Schematic illustration of the most widely accepted reaction pathways in FTS over cobalt, including the surface species observed in this Chapter.  $C_n$  denotes the main product output of the FTS reaction: linear hydrocarbons.  $C_n-O$  indicates the oxygenated minority products: alcohols, aldehydes, and acids. **b)** Schematic illustration of *operando* modulation excitation diffuse reflectance Fourier-transform infrared spectroscopy (ME DRIFTS) during FTS over a Co/TiO<sub>2</sub> catalyst. **c)** Schematic illustration of *operando* shell-isolated nanoparticle-enhanced Raman spectroscopy (SHINERS) methodology to study surface species during FTS over a Co/TiO<sub>2</sub> catalyst at elevated temperatures (up to 450°C) and pressures (up to 20 bar). **d)** photo-induced force microscopy (PiFM) methodology to study carbon deposition on Co/TiO<sub>2</sub> after the FTS reaction.

The signal enhancing shell-isolated nanoparticles (SHINs) were able to withstand temperatures up to 450°C and pressures up to 20 bar. The catalytic performance improved with increasing pressure, which coincided with the appearance of Ti-OH surface groups. Besides, evidence was observed for the occurrence of the direct dissociation mechanism (Figure 3.1a), as Co-C vibrations were identified in the SHINER spectra. To study carbon deposition, we have used photo-induced force microscopy (PiFM) (Figure 3.1d), Raman micro-spectroscopy (micro-Raman), and scanning transmission X-ray microscopy (STXM) with the Co/TiO<sub>2</sub> micro-island model catalysts. Unsaturated hydrocarbon deposits were detected with the three different analytical techniques during and after the FTS reaction. Through isotope labelling experiments, conjugated carbonyl function-

alities were identified as precursors for irreversibly adsorbed carbon deposits. Finally, to underline the mechanistic versatility of FTS catalysts, formaldehyde was fed and co-fed to Co/TiO<sub>2</sub> during the FTS reaction. This carbonyl functionality formed both carbon deposition and (oxygenated) hydrocarbon products, thereby suggesting that this molecule could be actively involved in the gradual formation of carbon deposits, covering the active sites, and hence, decreasing the overall performance of the catalyst.

## 3.2 Materials and Methods

### 3.2.1. Materials Synthesis

A Co/TiO<sub>2</sub> powder catalyst with a loading of ~10 wt.% was prepared via incipient wetness impregnation (IWI) using P25 TiO<sub>2</sub> and an aqueous solution of Co(NO<sub>3</sub>)<sub>2</sub>·6H<sub>2</sub>O (Sigma-Aldrich, 99.999% trace metals basis). The sample was dried overnight in static air at 60°C and then calcined at 250°C in flowing N<sub>2</sub> for 4 h.

3.8 g P25 TiO<sub>2</sub> (CRI catalyst company) was put in a Caleva Mixer Torque Rheometer with 0.2 g methylcellulose and water. The obtained paste was transferred to a single mini-screw extruder (Caleva) and extruded into 2-mm diameter cylindrical extrudates. The obtained catalyst extrudates were dried overnight at room temperature and afterwards calcined at 600°C. The extrudates were put in a Co(NO<sub>3</sub>)<sub>2</sub>·6H<sub>2</sub>O solution overnight to obtain 0.2 wt.% loading. The samples were calcined at 250°C for 1 h in static air.

TiO<sub>2</sub> micro-islands were synthesized on 7x7 mm<sup>2</sup> SiO<sub>2</sub>/Si(100) wafers (Siegert Wafer) from a titanium isopropoxide (TIP) (Acros Organics, 98+%) sol gel, as described in **Chapter 2**. Hexagonally ordered mesopores were obtained by using triblock copolymer Pluronic123 as structure-directing agent. The calcined TiO<sub>2</sub> micro-islands were impregnated with an aqueous solution of Co(NO<sub>3</sub>)<sub>2</sub>·6H<sub>2</sub>O and calcined, as described in **Chapter 2**.

### 3.2.2. Materials Characterization

*Operando* modulation excitation diffuse reflectance infrared Fourier transform spectroscopy (ME DRIFTS) experiments using the powder catalyst materials were carried out with a Bruker Vertex70V Fourier Transform (FT)-IR spectrometer equipped with a liquid nitrogen cooled Mercury Cadmium Telluride (MCT) detector and a Harrick Praying Mantis unit. The samples were sieved to a grain size of 150-425 μm and were firmly fixed in a 2 mm thick stainless-steel block which acts as a sample holder using two quartz wool plugs<sup>32</sup>. The sample holder was closed using a CaF<sub>2</sub> window, to allow the

reflection of IR radiation, and a graphite window. The inlet of the cell was connected to two solenoid valves (Series 9, Parker), allowing fast switching needed for the modulation experiments. The outlet of the cell was connected to an on-line mass spectrometer (MS; Pfeiffer Vacuum Omnistar). The 10 wt.% Co/TiO<sub>2</sub> catalyst and TiO<sub>2</sub> powder (P25) were pre-treated in H<sub>2</sub> for 1 h at 450°C. During modulation of CO gas, the H<sub>2</sub>/CO ratio was 2, while  $T=220^{\circ}\text{C}$  and  $P=1$  bar. In total, at least 10 modulation periods were performed by alternating flows of CO and H<sub>2</sub> at a ratio of 1:2 (60 s) versus H<sub>2</sub> (60 s). During each period of 120 s, 120 spectra were recorded at 80 kHz scanner velocity and 4 cm<sup>-1</sup> resolution. The 10 modulation periods of 120 s each resulted in a 20 min experiment. After spectral acquisition, the sets of time-resolved data were treated by phase-sensitive detection (PSD)<sup>33</sup> to obtain phase-resolved data. Phase-resolved amplitude spectra were obtained by taking the absolute maxima at every single wavenumber using a MATLAB script.

Shell-isolated nanoparticles (SHINs) were synthesized as reported elsewhere<sup>29</sup>. 30 μL SHINs solution was mixed with 20 μL of the Co(NO<sub>3</sub>)<sub>2</sub>·6H<sub>2</sub>O solution and deposited with a Finn pipette on the exterior surface of the Co/TiO<sub>2</sub> extrudate. The samples were then calcined at 250°C for 1 h in static air prior to Raman spectroscopy experiments. Raman spectra of the extrudate catalyst materials were recorded with an XploRA Plus Micro-Raman instrument from Horiba Scientific. The spectra were recorded using a 50x objective, a 638 nm laser (either 3.64·10<sup>5</sup> W/cm<sup>2</sup> corresponding 1% maximum laser), and a 1200 mm<sup>-1</sup> grating. The composition of the gas phase was monitored (0-50 amu) with online mass spectrometry (MS) using an OmniStar thermostat GSD320 Gas Analysis System (Pfeiffer Vacuum). For the high-pressure (1-20 bar) experiments a Raman High Temperature Reaction Chamber from Harrick Scientific was used. The chamber was connected to an in-house built high-pressure system controlling the pressure with a back pressure regulator and the gas flow with mass flow controllers. Raman spectra were recorded using the LabSpec 6 software from Horiba Scientific and analyzed using Fityk and Origin 9.

Optical microscopy images of the model catalysts were recorded with an optical light microscope (50x objective). Focused ion beam - scanning electron microscopy (FIB-SEM) and the energy dispersive X-ray (EDX) mapping analyses were performed using a FEI Helios NanoLab G3 UC scanning electron microscope equipped with a Xmax<sup>N</sup> Silicon Drift Detector for EDX elemental mapping. High-angle annular dark-field (HAADF) - scanning transmission electron microscopy (STEM) and the corresponding EDX mapping analyses were performed on a FEI Talos F200X.

Nanoscale infrared spectroscopy (nano IR) of the model catalysts was performed using a VistaScope photo-induced force microscope (PiFM) from Molecular Vista (San Jose, CA, USA). This instrument is equipped with a quantum cascade laser (QCL) unit, as well as an optical parametric oscillator (OPO) laser. IR spectra were recorded in the 775-1950  $\text{cm}^{-1}$  range with the QCL and in the 2250-4400  $\text{cm}^{-1}$  range with the OPO laser. Prior to hyperspectral analysis, AFM topography images were recorded in non-contact mode together with IR maps and IR point spectra (60 accumulations of 500 ms; 1  $\text{cm}^{-1}$  spectral resolution). Typical image sizes were 2-30  $\mu\text{m}^2$ . The data were analyzed using the VistaScan 1.7, SurfaceWorks 2.4 software, MATLAB, Fityk, and Origin 9.

For the model catalysts, Raman spectra were recorded with the same microscope as mentioned above using a 50x or 100x (*ex situ*) objective, a 532 nm laser (either  $3.64 \cdot 10^5$   $\text{W cm}^{-2}$  or  $4.28 \cdot 10^5$   $\text{W cm}^{-2}$ , corresponding to setting of 1% or 10% maximum laser power respectively), and a 1200  $\text{mm}^{-1}$  grating. For *operando* Raman spectroscopy experiments a Linkam THMS600 cell was used. The model catalyst materials were reduced *in situ* in a dilute  $\text{H}_2$  flow (25%  $\text{H}_2$  in Ar, 40  $\text{mL min}^{-1}$  in total) at 450°C for 1 h (5°C  $\text{min}^{-1}$  ramp). Then, the gas flow was switched to Ar and the cell was cooled to 220°C. The flow was then switched to a 5  $\text{mL min}^{-1}$   $\text{H}_2$  and 2.5  $\text{mL min}^{-1}$  CO flow ( $\text{H}_2/\text{CO}=2$ ) for 1-24 h.

Scanning transmission X-ray microscopy (STXM) of the model catalysts was performed at the Advanced Light Source (ALS) 11.0.2 beamline of the Lawrence Berkeley National Laboratory (LBNL, Berkeley, CA, USA). The monochromatic X-ray beam was focused onto the sample by a 45 nm/120  $\mu\text{m}$  zone plate and a 90  $\mu\text{m}$  Order Sorting Aperture (OSA). X-ray absorption spectra were recorded at the carbon K-edge, Co  $\text{L}_{2,3}$ -edges, and Ti  $\text{L}_{2,3}$ -edges.

All quantum chemical simulations of the molecules to determine their vibrational spectra were performed using the Gaussian16 software<sup>34</sup>. The ground state equilibrium structures and electronic properties were obtained at the density functional (DFT) level of theory utilizing the B3LYP<sup>35,36</sup> XC functional in the gas phase; *i.e.* of benzaldehyde (BA), 1-naphthaldehyde (1-NA), formaldehyde (FA), and acetic aldehyde (AA). The def2-SVP basis set<sup>37,38</sup> was applied for all atoms. A subsequent vibrational analysis was carried out for each optimized ground state structure, with respect to different isotopes of oxygen atom, *i.e.*  $^{16}\text{O}$  vs.  $^{18}\text{O}$ , to verify that a minimum on the potential energy (hyper)surface (PES) was obtained. All calculations were performed including D3 dispersion correction with Becke-Johnson damping<sup>39</sup>. The simulated IR-spectra were obtained from the corresponding vibrational analyses by applying a Voigt profile with a Full Width at Half Maximum (FWHM) of 18  $\text{cm}^{-1}$  to each vibration.

### 3.2.3. Catalyst Testing

Catalyst performance testing at 20 bar for 10-100 h was carried using in-house built high-pressure set-up. A steel reactor was filled with 200 mg of catalyst sample sieved to a grain size of 150-450  $\mu\text{m}$ . The sample was plugged between two quartz wool plugs. The reactor was placed in an oven and connected to the gas inlet and outlet. A back-pressure controller (BPC) was incorporated in the gas line connected to the outlet to maintain a defined pressure. An on-line gas Thermo Fischer Trace 1300 gas chromatograph (GC) was used for product analysis. The GC was injected with 1  $\mu\text{L}$  of the reactor outlet stream every 23 min. The sample was heated to 450°C with a 10°C  $\text{min}^{-1}$  ramp in a 10:20  $\text{mL min}^{-1}$   $\text{H}_2/\text{N}_2$  flow and held at that temperature for 1 h to reduce the catalyst prior to the FTS reaction. After the reduction step, the sample was cooled to 180-220°C with a 10°C  $\text{min}^{-1}$  ramp. At this temperature, the gas flow was switched to  $\text{Ar}/\text{H}_2/\text{CO}$  ( $\text{H}_2/\text{CO}=2$ ) and once the gasses were flowing, pressure was built up to 20 bar with a 1 bar  $\text{min}^{-1}$  ramp. The CO conversion and product selectivities were calculated from the following relationships:

$$X_{\text{CO}} (\%) = \left(1 - \frac{A_{\text{CO}}/A_{\text{Ar}}}{A_{\text{CO}}^0/A_{\text{Ar}}^0}\right) * 100\% \quad (\text{Equation 3.1})$$

$A_{\text{CO}}$  and  $A_{\text{Ar}}$  represent the thermal conductivity detector (TCD) peak area of CO and Ar during the reaction.  $A_{\text{CO}}^0$  and  $A_{\text{Ar}}^0$  are the TCD peak areas of CO and Ar recorded during a blank measurement. The selectivity was calculated using **Equation 3.2**.

$$S_i(\%) = \left(\frac{A_i * F_i}{\sum_{n=1}^{\infty} A_n * F_n}\right) * 100\% \quad (\text{Equation 3.2})$$

In this equation,  $A_i$  corresponds to the peak area of product  $i$  and  $F_i$  represents the response factor of the analyte. To describe the catalytic activity, cobalt-time-yield (CTY) was used. This parameter reports the amount of CO converted in mol per gram of cobalt per second. The parameter yield was used to describe the amounts of specific products obtained. This was reported either in mol of product per gram of cobalt per second or in (m)mol per hour per gram of catalyst.

The kinetic parameters reaction order ( $n$ ,  $m$ ) and apparent activation energy ( $E_a$ ) were determined by varying the reactant ( $\text{CO}$ ,  $\text{H}_2$ ) concentration and the temperature, respectively. At  $T=220^\circ\text{C}$  and  $P=20$  bar, the  $\text{H}_2/\text{CO}$  ratio was varied while the  $\text{H}_2$  concentration was kept constant and the  $\text{H}_2/\text{CO}$  ratio was varied while the CO concentration was

kept constant. This was repeated three times in order to obtain standard deviations. The measured intrinsic reaction rates were used to calculate the reaction order ( $n$ ) in CO and ( $m$ ) in H<sub>2</sub> according to the rate law (Equation 3.3), where  $k$  is the rate constant,  $n$  the reaction order in CO, and  $m$  the reaction order in H<sub>2</sub>. Besides, the temperature was varied between 180 and 220°C at  $P=20$  bar and the measured intrinsic rates were used to calculate the apparent activation energy ( $E_a$ ) according to the Arrhenius equation (Equation 3.4), where  $k$  is the rate constant,  $A$  is the pre-exponential factor,  $R$  the universal gas constant, and  $T$  the absolute temperature in Kelvin.

$$\text{rate} = k[\text{CO}_2]^n[\text{H}_2]^m \quad (\text{Equation 3.3})$$

$$k = Ae^{-E_a/RT} \quad (\text{Equation 3.4})$$

### 3.3 Results and Discussion

#### 3.3.1 Long-Term Catalyst Stability and Related Kinetics

For the 10 wt.% Co/TiO<sub>2</sub> powder catalyst material under study, the activity, selectivity and stability were assessed during Fischer-Tropsch Synthesis (FTS) at 220°C, 20 bar, and H<sub>2</sub>/CO=2 for 100 h time-on-stream (TOS). It was found that the CO conversion decreased from ~8.3% till ~7.7% over 100 h. The methane selectivity increased slightly from ~20% from till ~25%, while the C<sub>5+</sub> selectivity decreased from ~55% till ~50% (Figure 3.2 and Table 3.1). The paraffin/olefin ratio in the hydrocarbon reaction products decreased over time, indicating that the olefin production increased with increasing reaction time. As oxygenated products, particularly alcohols and aldehydes, have been reported previously in the cobalt-catalyzed FTS reaction,<sup>6</sup> an extensive analysis of oxygenated products was performed. To make this possible, the reaction products were captured by bubbling the outlet gas stream of the reactor system through deionized water. The aqueous solution was then subsequently analyzed and it was found that the total product output contained 1.05% alcohols, 0.03% acids, and 0.01% aldehydes by weight. From the oxygenated fraction, 53% was methanol and 20% ethanol, but alcohols up to C<sub>10</sub> were detected. For the organic acids, up to C<sub>4</sub> was detected and for the aldehydes only formaldehyde and acetaldehyde were found in the reactor outlet (Tables 3.2-3.4). Additional post-mortem X-ray diffraction (XRD) and Raman spectroscopy characterization of the Co/TiO<sub>2</sub> catalyst after 100 h of FTS can be found in Figures 3.3-3.4. It appeared that the Co/TiO<sub>2</sub> catalyst remained in metallic Co state during the FTS reaction. Even after exposure to ambient air, only metallic Co was detected with XRD and Raman



spectroscopy. XRD additionally indicated the face-centered cubic (FCC) metallic Co phase (Figure 3.3), while Raman spectroscopy showed hydrocarbon waxes on the Co/TiO<sub>2</sub> surface post FTS reaction (Figure 3.4).

Moreover, the reaction orders in both CO and H<sub>2</sub> were determined during FTS at 220°C and 20 bar by varying the partial pressures of the reactants. The total reaction order in CO was  $-0.32 \pm 0.12$ , while the total reaction order in H<sub>2</sub> was  $0.73 \pm 0.14$  (Table 3.5). These values match well with earlier in-depth kinetic studies on Co/TiO<sub>2</sub>, where a value of -0.24 was found for CO and 0.74 for H<sub>2</sub>.<sup>40</sup> The apparent activation energy, calculated between 180 and 220°C at 20 bar (Figure 3.5), was  $83.3 \pm 1.1$  kJ/mol, also matching well with earlier reports<sup>40</sup>. We have additionally determined the reaction orders in CO and H<sub>2</sub> for specific products. For paraffins, the reaction order in CO was always negative, while the reaction order in H<sub>2</sub> was positive. The opposite was observed for olefins (Table 3.5). It has been shown previously that the FTS reaction rate over cobalt is determined by the availability of hydrogen atoms on the catalyst surface<sup>41,42</sup>. A positive reaction order in H<sub>2</sub>, signifying that the reaction rate increases with the H<sub>2</sub> partial pressure, supports this finding (Table 3.5). On the other hand, a higher CO partial pressure resulted in competitive adsorption, decreased the amount of hydrogen atoms on the cobalt surface, and led to a lower reaction rate<sup>42</sup>. This is reflected by the negative reaction order in CO (Table 3.5). The positive reaction order in H<sub>2</sub> for methane and C<sub>2+</sub> paraffins also indicates that the rate-determining step involves the hydrogenation step. The formation of C<sub>2+</sub> olefins, however, requires less hydrogen atoms and its rate-determining step did not necessarily seem to involve hydrogenation, as reflected by the negative H<sub>2</sub> reaction orders and positive CO reaction orders (Table 3.5). These results are in accordance with previous work, where the same trend was observed<sup>42</sup>.

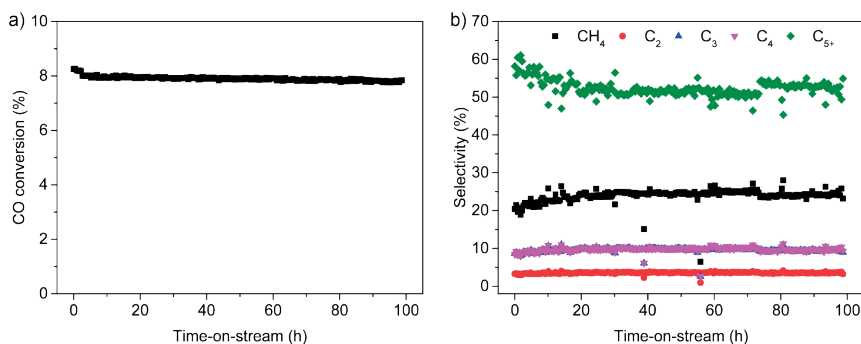


**Figure 3.2** Long-term stability testing for the 10 wt.% Co/TiO<sub>2</sub> powder catalyst material under study. **a)** CO conversion and **b)** product selectivity over the course of 100 h time-on-stream (TOS) during the Fischer-Tropsch Synthesis (FTS) reaction at 220°C, 20 bar, and H<sub>2</sub>/CO=2.

**Table 3.1. Average hydrocarbon distribution over 100 h catalytic testing during the Fischer-Tropsch Synthesis (FTS) with the 10 wt.% Co/TiO<sub>2</sub> powder catalyst material.** The reaction conditions were 220°C, 20 bar, H<sub>2</sub>/CO=2 and Gas Hourly Space Velocity (GHSV) = 3200 h<sup>-1</sup>.

	CO conversion	CH <sub>4</sub>	C <sub>2</sub>	C <sub>3</sub>	C <sub>4</sub>	C <sub>5+</sub>
mol%	7.90	22.7	3.36	9.08	9.28	55.6
P/O <sup>a</sup> total	n.a.	n.a.	1.17	1.39	1.77	2.45 <sup>b</sup>
P/O <sup>a</sup> 0-20 h	n.a.	n.a.	1.30	1.51	1.91	2.47 <sup>b</sup>
P/O <sup>a</sup> 80-100 h	n.a.	n.a.	1.09	1.25	1.46	2.66 <sup>b</sup>

<sup>a</sup> P/O: n-paraffin/1-olefin

<sup>b</sup> C<sub>5</sub> n-paraffin/1-olefin

**Table 3.2. Average aldehyde distribution over 100 h catalytic testing during the Fischer-Tropsch Synthesis (FTS) with the 10 wt.% Co/TiO<sub>2</sub> powder catalyst material under study.** The reaction conditions were 220°C, 20 bar, H<sub>2</sub>/CO=2 and Gas Hourly Space Velocity (GHSV) = 3200 h<sup>-1</sup>.

Compound	Amount (mg)	Relative wt.% in total products	Relative wt.% in oxygenate fraction
Glycolaldehyde	0	0	0
Formaldehyde	0.08	0	0.15
Acetaldehyde	0.11	0	0.20
Propionaldehyde	0	0	0
Butyraldehyde	0	0	0
Valeraldehyde	0	0	0
Hexaldehyde	0	0	0
Total	0.19	0.01	0.35

**Table 3.3. Average alcohol distribution over 100 h catalytic testing during the Fischer-Tropsch Synthesis (FTS) with the 10 wt.% Co/TiO<sub>2</sub> powder catalyst material under study.** The reaction conditions were 220°C, 20 bar, H<sub>2</sub>/CO=2 and Gas Hourly Space Velocity (GHSV) = 3200 h<sup>-1</sup>.

Compound	Amount (mg)	Relative wt.% in total products	Relative wt.% in oxygenate fraction
Methanol	14.5	0.57	26.7
Ethanol	5.46	0.22	10.1
Propanol	1.41	0.06	2.59
Butanol	1.02	0.04	1.88
Pentanol	0.71	0.03	1.31
Hexanol	0.44	0.02	0.81
Heptanol	0.28	0.01	0.52
Octanol	0.20	0.01	0.37
Nonanol	0	0	0
Decanol	0.06	0	0.12
Undecanol	0	0	0
Isopropanol	2.29	0.09	4.22
2-Methyl-1-propanol	0	0	0
2-Methyl-1-butanol	0.14	0.01	0.26
2,2-Dimethylpropanol	0	0	0
2-Methyl-2-butanol	0	0	0
3-Methyl-2-butanol	0.14	0.01	0.25
3-Methyl-1-butanol	0	0	0
Total	26.6	1.05	49.1

**Table 3.4. Average carboxylic acid distribution over 100 h catalytic testing during the Fischer-Tropsch Synthesis (FTS) with the 10 wt.% Co/TiO<sub>2</sub> powder catalyst material under study.** The reaction conditions were 220°C, 20 bar, H<sub>2</sub>/CO=2 and Gas Hourly Space Velocity (GHSV) = 3200 h<sup>-1</sup>.

Compound	Amount (mg)	Relative wt.% in total products	Relative wt.% in oxygenate fraction
Formic acid	0.11	0	0.20
Acetic acid	0.44	0.02	0.81
Propionic acid	0.07	0	0.12
Butyric acid	0.03	0	0.06
Pentanoic acid	0	0	0
Hexanoic acid	0	0	0
Total	0.65	0.03	1.19

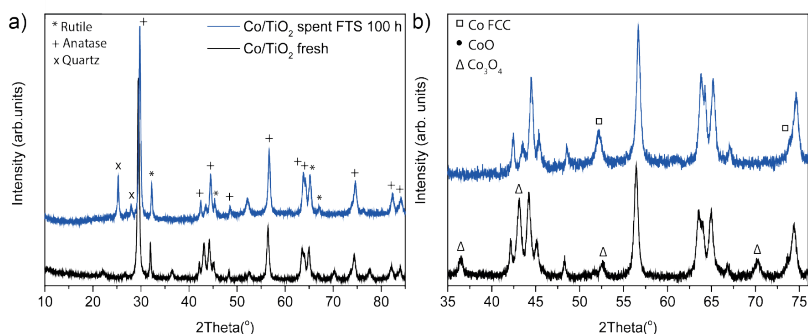


**Figure 3.3. X-ray diffraction (XRD) of the Co/TiO<sub>2</sub> powder catalyst after calcination and after 100 h of Fischer-Tropsch Synthesis (FTS).** a) Full range XRD pattern and b) zoom-in of the region relevant for the cobalt phase is provided on the right.

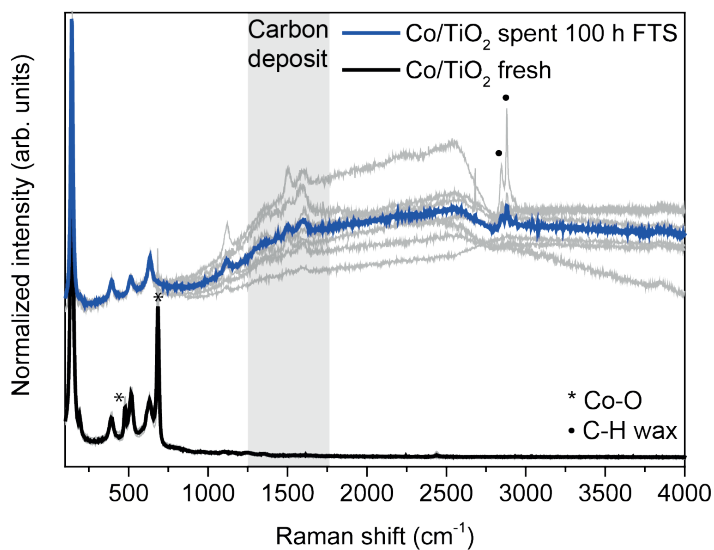


**Figure 3.4. Raman micro-spectroscopy on the 10 wt.% Co/TiO<sub>2</sub> powder catalyst materials after calcination and after 100 h of Fischer-Tropsch Synthesis (FTS).** The black (fresh sample) and blue (spent sample) Raman spectra are averages of 7 spectra. All spectra are displayed in light gray. The Co-O stretching vibrations are indicated with an asterisk, C-H stretching vibrations of FTS waxes with a dot and the carbon deposition region is shaded in light gray.

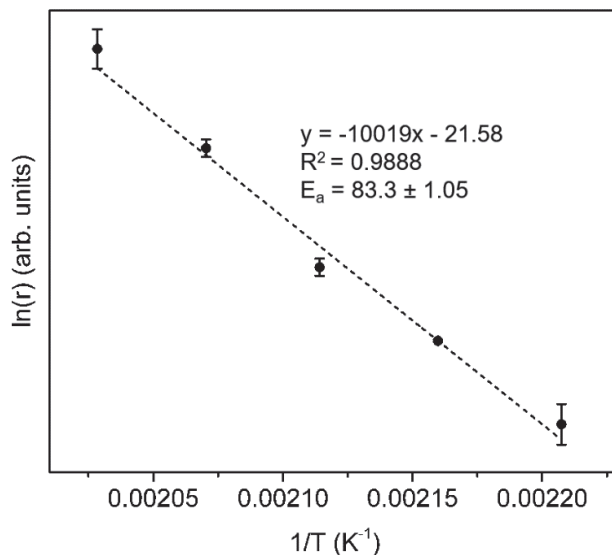


**Figure 3.5. Arrhenius plot to determine the activation energy ( $E_a$ ) for the 10 wt.% Co/TiO<sub>2</sub> powder catalyst material.** The activity was measured in steady-state at temperatures between 180 and 220°C at 20 bar and H<sub>2</sub>/CO=2. Each point consists of the average of 6 gas chromatography (GC) injections.

**Table 3.5.** Reaction orders for the 10 wt.% Co/TiO<sub>2</sub> powder catalyst material during the Fischer-Tropsch Synthesis (FTS) reaction at 220°C and 20 bar.

Reaction order	CO	H <sub>2</sub>
Total	-0.32 ± 0.12	0.73 ± 0.14
CH <sub>4</sub>	-0.72 ± 0.25	1.06 ± 0.01
Ethane	-0.85 ± 0.19	1.31 ± 0.36
Ethene	1.29 ± 0.68	-0.73 ± 0.39
Propane	-0.68 ± 0.35	0.84 ± 0.05
1-propene	0.70 ± 0.10	-0.28 ± 0.16
n-butane	-0.85 ± 0.29	1.00 ± 0.37
1-butene	0.28 ± 0.05	-0.64 ± 0.18
C <sub>5+</sub>	-0.25 ± 0.11	0.76 ± 0.35

### 3.3.2 Oxygen-containing Intermediates and the Role of the TiO<sub>2</sub> Support

The same 10 wt.% Co/TiO<sub>2</sub> powder catalyst material was used to investigate active species and surface reaction intermediates during the cobalt-based FTS reaction and to decipher the role of the TiO<sub>2</sub> support material. The thorough reaction product analysis (Tables 3.1-3.4) showed 98.9% hydrocarbons, of which 55.6% were C<sub>5+</sub>, and 1.1% oxygenates, mainly consisting of alcohols (97.0%); although organic acids and aldehydes were detected as well. This indicated that the CO insertion route, which could either be a growth or a termination step, as depicted in Figure 3.1a, inevitably took place on Co/TiO<sub>2</sub>, as the formation of oxygenated products requires either CO or HCO insertion<sup>43</sup>. However, mechanistic conclusions could not yet be drawn for the formation of hydrocarbon products on the Co/TiO<sub>2</sub> catalyst under study. To gain more mechanistic insights, *operando* modulation excitation diffuse reflectance Fourier-transform infrared spectroscopy (ME DRIFTS) was carried out with the Co/TiO<sub>2</sub> catalyst as well as with the bare TiO<sub>2</sub> support. The concept of modulation excitation spectroscopy (MES) is to apply an external stimulus to a system (Figure 3.1b), while spectra are continuously recorded to monitor the transient response of the system<sup>44,45</sup>. When the obtained spectroscopic data are converted from the time domain to the phase domain, also known as demodulation, the noise and other (static) signals, *i.e.*, signals that do not respond to the modulation signal, such as the signal of permanently adsorbed surface species, are filtered out. The resulting phase-resolved amplitude spectra, which show the absolute maximum of the signal at every single wavenumber, therefore only contain dynamic species that respond to the applied stimulus. In this case, the CO concentration was varied and used as a periodic external stimulus, while keeping the H<sub>2</sub> concentration constant during FTS at 220°C, 1 bar, and H<sub>2</sub>/CO=2.

In the time-resolved DRIFTS spectra (Figure 3.6a,b and Table 3.6), a multitude of surface species was already visible. For the Co/TiO<sub>2</sub> material, CO species adsorbed on cobalt was indicated by the asymmetric IR peak at ~2038 cm<sup>-1</sup><sup>46-49</sup>, while surface formate species were indicated by the IR peaks at 1364, 1565, and 1578 cm<sup>-1</sup><sup>50,51</sup>. Besides, the bending vibrations of methyl (CH<sub>3</sub>) and methylene (CH<sub>2</sub>) groups were observed at 1380 and 1461 cm<sup>-1</sup>, respectively<sup>50-52</sup>, while the C-H stretching vibrations appeared only very weakly between 2850 and 2970 cm<sup>-1</sup><sup>52</sup>. To separate the dynamic species from the static ones, the IR data were transformed from the time domain (Figure 3.6a,b) to the phase domain (Figure 3.6c-f). In the phase-resolved amplitude spectrum (Figure 3.6f) the surface species responding to the CO stimulus became clearly visible and peaks overlapped less compared to the signal in the time domain (where peaks corresponding to static species are still present). For Co/TiO<sub>2</sub> (Figure 3.6d,f), both linear (2047 cm<sup>-1</sup>) and bridged (1989 cm<sup>-1</sup>) carbonyls of adsorbed CO on metallic cobalt were observed<sup>46-49</sup>. Besides, surface carboxylates (characterized by a peak at 1522 cm<sup>-1</sup>), which were not

visible in the time-resolved IR spectrum, and surface formates (characterized by peaks at 1357 and 1606  $\text{cm}^{-1}$ ) were observed in the phase-resolved amplitude IR spectrum (**Figure 3.6f** and **Table 3.7**). This indicated that these oxygenated species were active species (*i.e.*, actively responding to the stimulus) during the FTS reaction<sup>47-50</sup> and thus suggested the occurrence of the CO and/or HCO insertion mechanism<sup>49</sup>. It has been reported previously that surface carboxylates can form on a Co/TiO<sub>2</sub> catalyst when an acid intermediate reacts with a titanol group on the catalyst surface according to:  $\text{RCOOH} + \text{TiOH} \rightarrow \text{RCOO}^- + \text{Ti}^+ + \text{H}_2\text{O}$ <sup>50</sup>. The methyl and methylene bending peaks only appeared as weak shoulders at 1389 and 1456  $\text{cm}^{-1}$ , respectively. In the C-H stretching region, very weak IR peaks appeared at 2873, 2889, and 2912  $\text{cm}^{-1}$ , indicating methylene and methylidyne (C-H) species<sup>52</sup>. The emergence of the dynamic surface species in the phase-resolved amplitude spectrum coincided with an increase in the amount of hydrocarbon fragments in the mass spectrometer (MS) (**Figure 3.7**). However, to draw conclusions on the occurrence of the direct CO dissociation mechanism, complementary Raman spectroscopy measurements are needed and will be carried out in the next subsection, as with Raman spectroscopy Co-C vibrations should be observable between 400 and 600  $\text{cm}^{-1}$  <sup>29,53,54</sup>.

The desorption and reaction of the different surface species in the time domain after turning the CO gas flow off was used as a measure for their relative hydrogenation kinetics and binding energy<sup>45</sup>. Adsorbed CO displayed the steepest desorption slope and was thus the fastest disappearing or reacting surface species. Interestingly, the peak of linearly adsorbed CO disappeared faster than bridged CO (**Figure 3.8** and **3.9**) after turning the CO gas off, suggesting that the linear sites are more reactive for CO hydrogenation compared to the bridged sites. The observed difference in kinetics between linear and bridged sites was further supported by the phase-resolved spectra in **Figure 3.6d**. Linearly adsorbed CO (2047  $\text{cm}^{-1}$ ) appeared completely out of phase with bridged CO (1989  $\text{cm}^{-1}$ ); the former displaying a peak maximum at phase angle 160°, while the latter displayed a maximum at phase angle 340°. After adsorbed CO, adsorbed CH<sub>3</sub> disappeared, followed by adsorbed CH<sub>2</sub>, indicating that these species were hydrogenated consequently. The surface formate and carbonate species were in the same kinetic regime and the last ones to disappear and hence the most stable at an active catalyst surface (**Figures 3.8-3.9**).

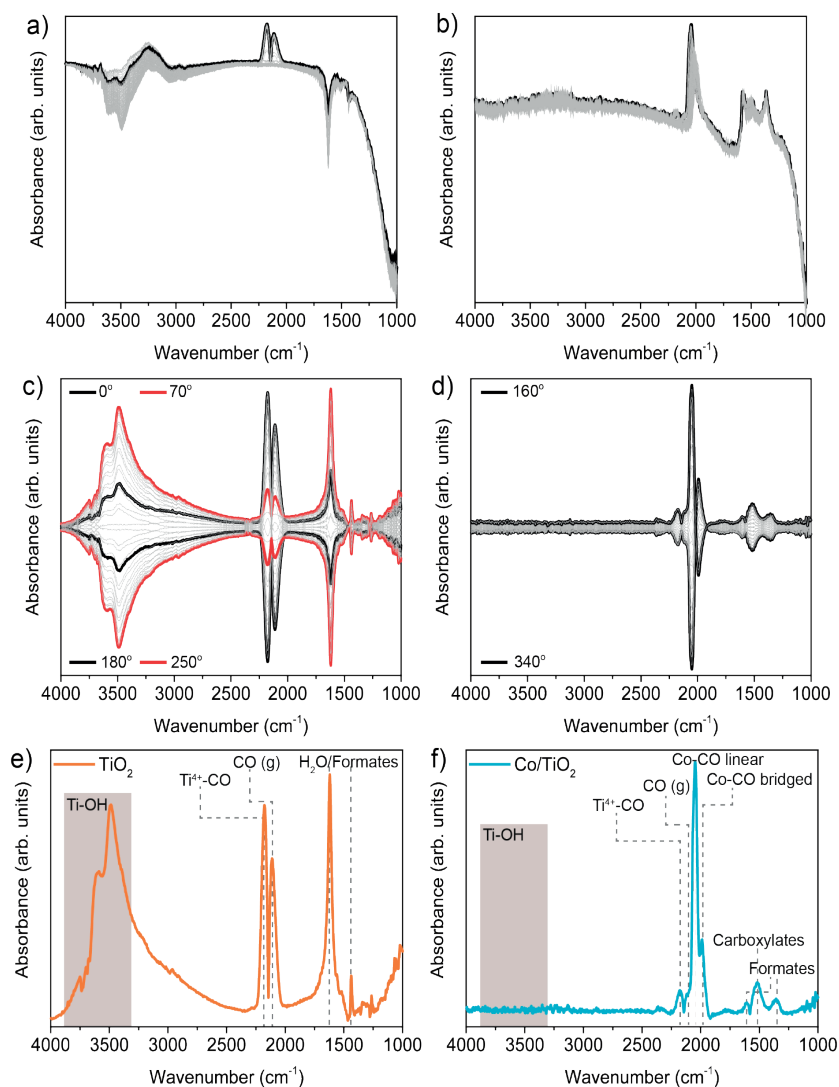


**Figure 3.6. Operando modulation excitation diffuse reflectance Fourier transform infrared spectroscopy (ME DRIFTS).** **a, b)** Time-resolved infrared spectra for **a)**  $\text{TiO}_2$  and **b)**  $\text{Co/TiO}_2$  during modulation of  $\text{H}_2/\text{CO}(=2)$  versus  $\text{H}_2$  at  $220^\circ\text{C}$  and 1 bar. The spectrum where the  $\text{C}=\text{O}$  vibration has a maximum is highlighted in black. **c, d)** Corresponding phase-resolved spectra for **c)**  $\text{TiO}_2$  and **d)**  $\text{Co/TiO}_2$ . The maxima and minima are highlighted in black or red. **e, f)** Phase-resolved amplitude spectra for **e)**  $\text{TiO}_2$  and **f)**  $\text{Co/TiO}_2$  during the Fischer-Tropsch Synthesis (FTS) at  $220^\circ\text{C}$ , 1 bar, and  $\text{H}_2/\text{CO}=2$ . Both of the samples were pre-treated at  $450^\circ\text{C}$  in  $\text{N}_2/\text{H}_2=2$  for 1 h.



TiO<sub>2</sub> has been reported as a performance-enhancing support in many other studies within and beyond the field of heterogeneous catalysis<sup>2</sup>. To understand the role of TiO<sub>2</sub>, the same type of ME DRIFTS experiments as described above was carried out with bare TiO<sub>2</sub> support. The phase-resolved amplitude spectrum of TiO<sub>2</sub> (**Figure 3.6e**) displayed a large and broad band corresponding to Ti-OH groups on both anatase and rutile phases at 3605 and 3485, respectively<sup>55,56</sup>. The  $\nu(\text{C}=\text{O})$  vibration of adsorbed CO was observed at 2178 cm<sup>-1</sup>, indicating the presence of Ti<sup>4+</sup>-CO, *i.e.*, CO adsorbed on a titanium in the vicinity of an oxygen vacancy<sup>57</sup>. Besides, CO(g), adsorbed water, and surface formate species were observed. Adsorbed CO also displayed the steepest desorption slope on bare TiO<sub>2</sub> support (**Figures 3.8-3.9**) and was thus the fastest disappearing surface species. Interestingly, TiO<sub>2</sub> appeared to form CO<sub>2</sub> and methanol as products rather than hydrocarbons (**Figure 3.7** (MS)). While TiO<sub>2</sub> was thus perfectly capable of cleaving H-H bonds, the C=O bond remained intact. Hydrogen bond cleavage is expected to occur on coordinatively unsaturated and thus basic O<sup>2-</sup> sites, providing the H atoms required for hydroxyl groups and surface formate<sup>49</sup>. The formation of methanol from surface formate species on oxidic phases has been reported previously<sup>47</sup>. Besides providing titanol surface groups, the performance-enhancing role of the TiO<sub>2</sub> support appears related to supplying essential building blocks to the cobalt surface, where C=O cleavage and C-C coupling can occur.

**Table 3.6.** Peaks observed in the averaged time-resolved spectra using modulation excitation (ME) diffuse reflectance infrared Fourier transform spectroscopy (DRIFTS) during the Fischer-Tropsch synthesis (FTS) reaction at 220°C, 1 bar, an H<sub>2</sub>/CO=2.

Co/TiO <sub>2</sub>		TiO <sub>2</sub>	
Peak (cm <sup>-1</sup> )	Assignment	Peak (cm <sup>-1</sup> )	Assignment
2176	$\nu(\text{C}=\text{O})$ Ti <sup>4+</sup> -CO <sup>57</sup> or CO (g)	3493	$\nu(\text{O}-\text{H})$ Ti-OH (rutile) <sup>55,56</sup>
2038	$\nu(\text{C}=\text{O})$ Co-CO (linear) <sup>46-49</sup>	3614	$\nu(\text{O}-\text{H})$ Ti-OH (anatase) <sup>55,56</sup>
2003	$\nu(\text{C}=\text{O})$ Co-CO (bridged) <sup>46</sup>	2178	$\nu(\text{C}=\text{O})$ Ti <sup>4+</sup> -CO <sup>57</sup> or CO (g)
1578	$\nu_{\text{as}}(\text{COO}^-)$ m-formate <sup>51</sup> or C=C <sup>45</sup>	2111	CO (g)
1565	$\nu_{\text{as}}(\text{COO}^-)$ b-formate <sup>51</sup> or C=C <sup>45</sup>	1620	H <sub>2</sub> O <sup>58</sup> or $\nu_{\text{as}}(\text{COO}^-)$ formate <sup>59</sup>
1461	$\delta(\text{C}-\text{H})$ methylene (CH <sub>2</sub> ) <sup>50</sup>	1437	$\nu_{\text{s}}(\text{COO}^-)$ formate <sup>50</sup>
1380	$\delta(\text{C}-\text{H})$ methyl (CH <sub>3</sub> ) <sup>51,52</sup>	1050	$\nu(\text{C}-\text{O})$ methoxy CH <sub>3</sub> O <sup>59</sup>
1364	$\nu_{\text{s}}(\text{COO}^-)$ formate <sup>50,51</sup> or $\omega(\text{CH}_2)$ <sup>49</sup>	1008	MeOH (g) <sup>59</sup>

m-formate: monodentate formate, b-formate: bidentate formate,  $\nu_{\text{s}}$ : symmetric stretching,  $\nu_{\text{as}}$ : asymmetric stretching,  $\delta$ : bending,  $\omega$ : wagging.

**Table 3.7.** Peaks observed in the phase-resolved amplitude spectra using modulation excitation (ME) diffuse reflectance infrared Fourier transform spectroscopy (DRIFTS) during the Fischer-Tropsch synthesis (FTS) at 220°C, 1 bar, an  $H_2/CO=2$ .

Co/TiO <sub>2</sub>		TiO <sub>2</sub>	
Peak (cm <sup>-1</sup> )	Assignment	Peak (cm <sup>-1</sup> )	Assignment
2178	$\nu(C=O)$ Ti <sup>4+</sup> -CO <sup>57</sup> or CO (g)	3485	$\nu(O-H)$ Ti-OH (rutile) <sup>55,56</sup>
2047	$\nu(C=O)$ Co-CO (linear) <sup>46-49</sup>	3605	$\nu(O-H)$ Ti-OH (anatase) <sup>55,56</sup>
1989	$\nu(C=O)$ Co-CO (bridged) <sup>46</sup>	2178	$\nu(C=O)$ Ti <sup>4+</sup> -CO <sup>57</sup> or CO (g)
1775	$\nu(C=O)$ carboxylic acid/aldehyde <sup>60</sup> or tilted CO <sup>29,49</sup>	2111	CO (g)
1606	$\nu_{as}(COO^-)$ formate <sup>45,50</sup>	1620	H <sub>2</sub> O <sup>58</sup> or $\nu_{as}(COO^-)$ formate <sup>59</sup>
1522	Carboxylates <sup>50</sup>	1438	COO <sup>-</sup> (formate) <sup>50</sup>
1456	$\delta(C-H)$ methylene (CH <sub>2</sub> ) <sup>50</sup>		
1389	$\delta(C-H)$ methyl (CH <sub>3</sub> ) <sup>49,51,52</sup>	1057	$\nu(C-O)$ methoxy CH <sub>3</sub> O <sup>59</sup>
1357	$\nu_s(COO^-)$ formate <sup>50,51</sup>	1022	MeOH (g) <sup>59</sup>

$\nu_s$ : symmetric stretching,  $\nu_{as}$ : asymmetric stretching,  $\delta$ : bending,  $\omega$ : wagging.

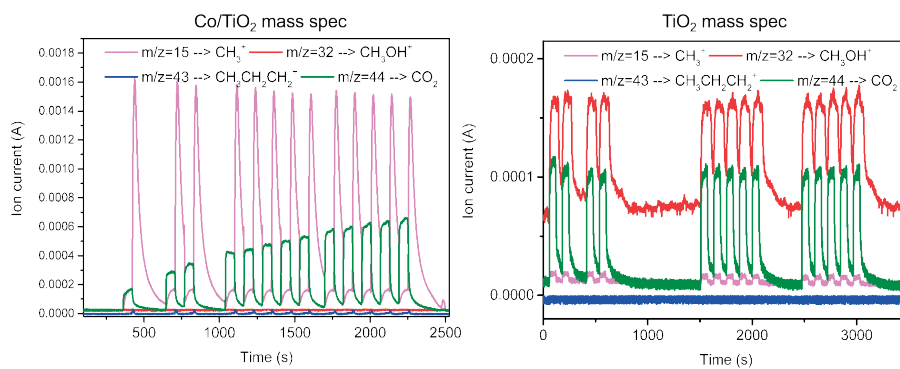


**Figure 3.7. Mass spectrometry (MS) during the *operando* modulation excitation diffuse reflectance Fourier transform infrared spectroscopy (ME DRIFTS) experiments with 10wt.% Co/TiO<sub>2</sub> and bare TiO<sub>2</sub> support powder materials.** The Fischer-Tropsch Synthesis (FTS) reaction conditions were 220°C, 1 bar, and  $H_2/CO=2$  in all cases. The Co/TiO<sub>2</sub> MS results are displayed on the left and TiO<sub>2</sub> MS results on the right.

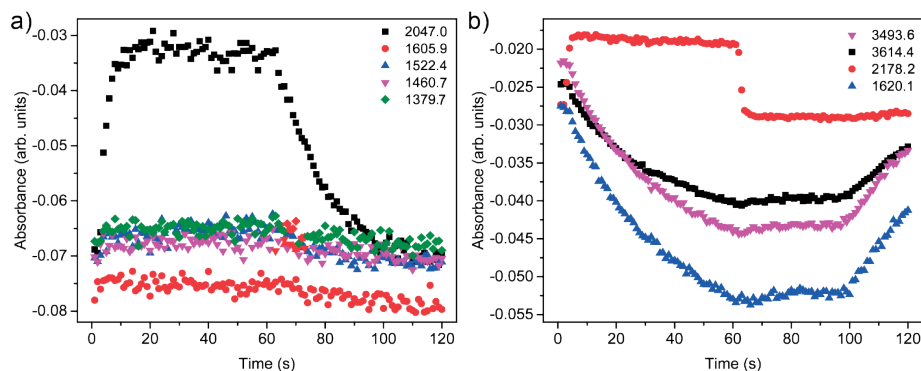


**Figure 3.8. Absorbance of selected species during *operando* modulation excitation diffuse reflectance Fourier transform infrared spectroscopy (ME DRIFTS) experiments with 10 wt.% Co/TiO<sub>2</sub> and bare TiO<sub>2</sub> support powder materials.** The IR signal intensities of selected species for a) Co/TiO<sub>2</sub> (\*CH<sub>3</sub>: 1380, \*CH<sub>2</sub>: 1461, \*RCOO: 1522, \*CHOO: 1606, \*CO: 2047 cm<sup>-1</sup>) and b) bare TiO<sub>2</sub> support (\*H<sub>2</sub>O: 1620, \*CO: 2178, \*OH: 3614, \*OH: 3693 cm<sup>-1</sup>) were followed during the modulation of CO gas (CO+H<sub>2</sub> vs. H<sub>2</sub>). The signals were averaged over 10 modulation periods.

3

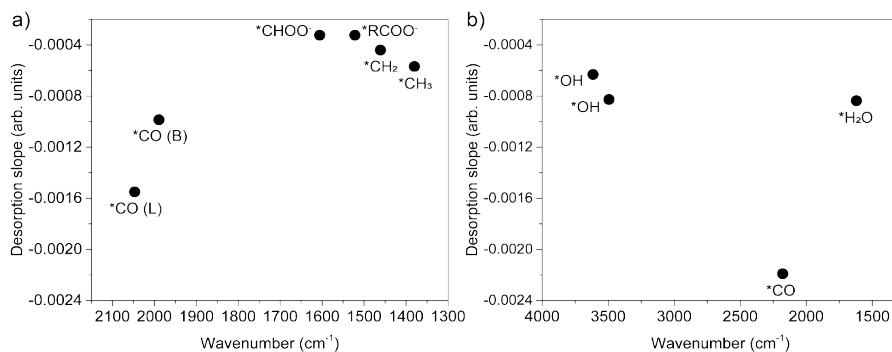


**Figure 3.9. Desorption slope analysis during *operando* modulation excitation diffuse reflectance Fourier transform infrared spectroscopy (ME DRIFTS) with 10 wt.% Co/TiO<sub>2</sub> and bare TiO<sub>2</sub> support powder materials of selected surface species.** The IR signal intensities of selected species for a) Co/TiO<sub>2</sub> (\*CH<sub>3</sub>: 1380, \*CH<sub>2</sub>: 1461, \*RCOO: 1522, \*CHOO: 1606, \*CO bridged (B): 1989, \*CO linear (L): 2047 cm<sup>-1</sup>) and b) bare TiO<sub>2</sub> support (\*H<sub>2</sub>O: 1620, \*CO: 2178, \*OH: 3614, \*OH: 3693 cm<sup>-1</sup>) were followed in the time domain during 10 seconds (second 60-69) after the CO gas was turned off. For bare TiO<sub>2</sub> support, seconds 3-12 were used for \*H<sub>2</sub>O and \*OH, as the intensity of these species decreased when the CO gas was turned on. The desorption slopes were calculated using the 10 spectra during the first 10 seconds of desorption.

### 3.3.3 Surface Species and Catalyst Performance Vary with Reaction Pressure

To investigate the influence of reaction pressure on surface species and catalytic performance the *operando* shell-isolated nanoparticle enhanced Raman spectroscopy (SHINERS) method was used<sup>29</sup>. Benefits of *operando* Raman spectroscopy include complementary information to *operando* IR spectroscopy, the reduced contribution of water to the spectra due to the low Raman scattering cross-section of H<sub>2</sub>O, and the possibility to detect Co-C vibrations, typically observed between 400 and 600 cm<sup>-1</sup><sup>29,53,54</sup>. The Co-C vibration could provide evidence for the occurrence of the direct dissociation mechanism, which has been postulated for the Fischer-Tropsch process over supported cobalt nanoparticles. To induce spectral signal enhancement, the shell-isolated nanoparticles (SHINs) must be in close proximity of each other<sup>29</sup>. The SHINs proximity was hampered by the 10 wt.% cobalt loading and hence we had to use 2 wt.% Co/TiO<sub>2</sub> catalyst extrudates instead (**Figures 3.10-3.12**) to overcome this practical problem. Scanning electron microscopy (SEM) images with X-ray elemental mapping of the 2 wt.% Co/TiO<sub>2</sub> sample with SHINs can be found in **Figures 3.10-3.11**, while X-ray diffraction (XRD) patterns of the 2 wt.% Co/TiO<sub>2</sub> catalyst material are shown in **Figure 3.12**. The catalytic performance of this catalyst (after pre-treatment in N<sub>2</sub>/H<sub>2</sub>=2 at 450°C for 1 h) was assessed at pressures between 1 and 20 bar during FTS at 220°C and H<sub>2</sub>/CO=2. The activity was found to increase upon increasing the pressure from 1 to 20 bar, while the methane selectivity decreased and the C<sub>5+</sub> selectivity increased (**Figure 3.13a,b**).

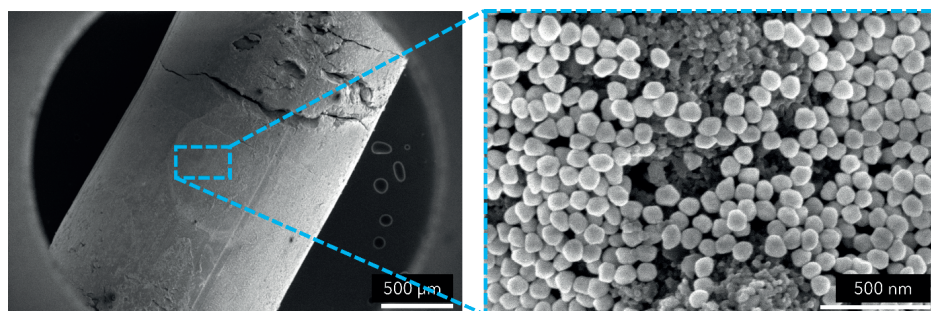


**Figure 3.10.** Scanning electron microscopy (SEM) images of a 2 wt.% Co/TiO<sub>2</sub> catalyst extrudate, mixed with shell-isolated nanoparticles (SHINs) to allow *operando* shell-isolated nanoparticle enhanced Raman spectroscopy (SHINERS) experiments. Image of Co/TiO<sub>2</sub> extrudate (left) and zoom-in of the SHINs on the surface (right).

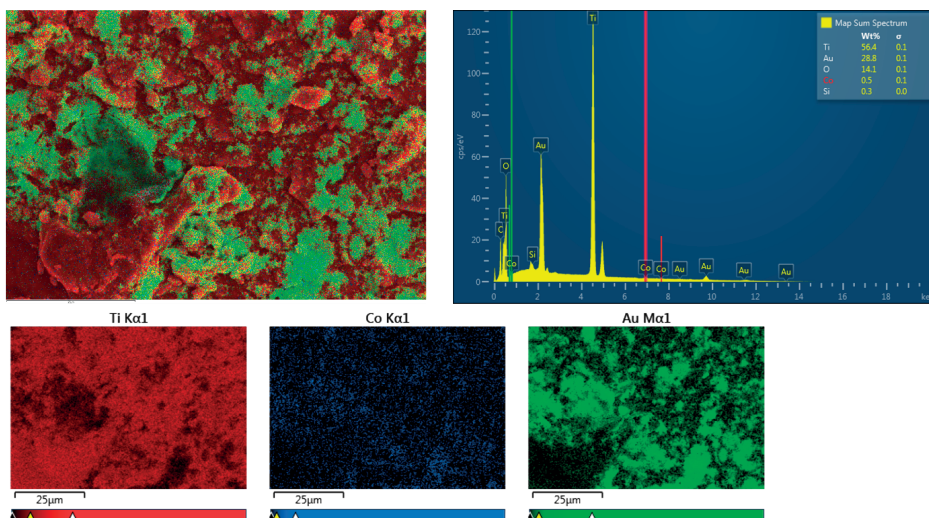


**Figure 3.11.** Energy dispersive X-ray (EDX) elemental analysis of the 2 wt.% Co/TiO<sub>2</sub> catalyst extrudate, mixed with shell-isolated nanoparticles (SHINs). Ti is displayed in red, Co in blue, and Au in green. The top right panel displays a sum spectrum with estimated weight percentages of the elements Ti, Au, O, Co, and Si.

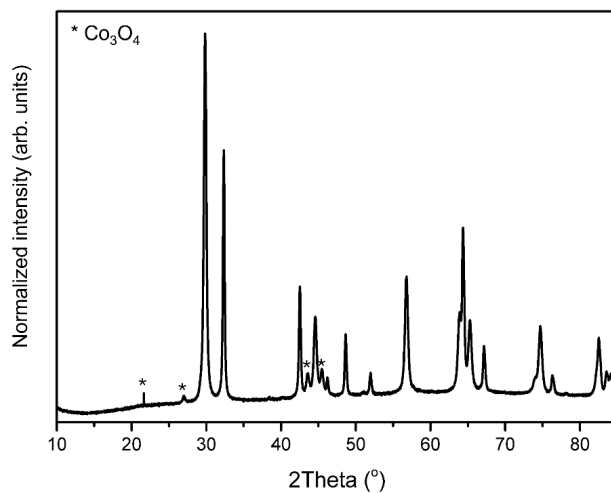


**Figure 3.12.** X-ray diffraction (XRD) pattern of the 2 wt.% Co/TiO<sub>2</sub> catalyst extrudate. Diffraction peaks corresponding to Co<sub>3</sub>O<sub>4</sub> are indicated with an asterisk. The average Co<sub>3</sub>O<sub>4</sub> crystallite size was 14.1 nm.

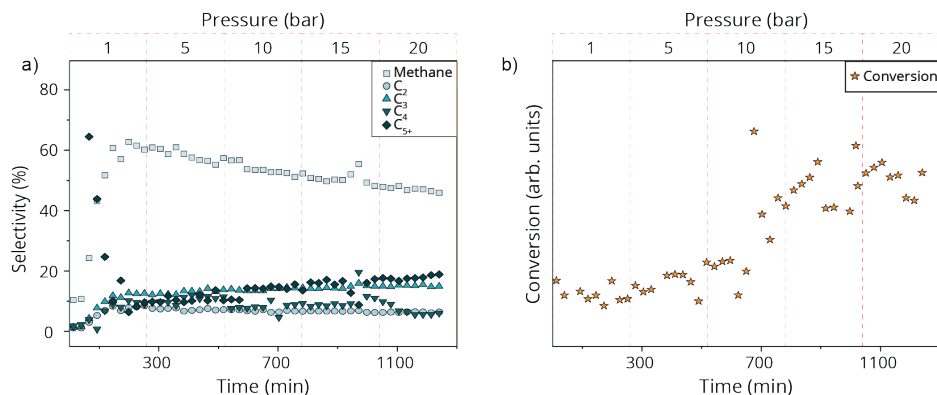


**Figure 3.13. Catalytic performance of the 2 wt.% Co/TiO<sub>2</sub> catalyst extrudates, mixed with shell-isoalted nanoparticles (SHINs), with increasing reaction pressure. a)** Product selectivity and **b)** CO conversion by Co/TiO<sub>2</sub> during Fischer-Tropsch Synthesis (FTS) at 220°C and H<sub>2</sub>/CO=2 with increasing pressure from 1 to 20 bar measured with gas chromatography (GC).

To investigate and understand the reaction pressure-dependent catalytic performance, *operando* SHINERS experiments were performed during the FTS reaction with the 2 wt.% Co/TiO<sub>2</sub> catalyst extrudate (Figure 3.14a,b). The pressure was varied between 1 and 20 bar during FTS at 220°C and H<sub>2</sub>/CO=2. On-line mass spectrometry (MS) results can be found in Figure 3.15. Due to the signal enhancement facilitated by SHINs, a multitude of surface species became visible in the Raman spectra during the FTS experiments (Figure 3.14a,b). At 1 bar pressure, the C=O stretching vibration of linearly adsorbed CO on metallic cobalt<sup>61</sup> was observed at ~2012 cm<sup>-1</sup> and the Co-C stretching vibration at ~451 cm<sup>-1</sup>. The C=O peak was shaped asymmetrically, suggesting the additional presence of adsorbed CO in a bridged conformation<sup>61</sup> or linearly adsorbed CO in a slightly different linear configuration. Besides, a weak, multicomponent band just below 3000 cm<sup>-1</sup> indicated the presence of saturated aliphatic C-H stretching vibrations<sup>52</sup>. Upon increasing the reaction pressure, the linearly adsorbed C=O band shifted to higher frequencies, reaching 2028 cm<sup>-1</sup> at P=20 bar. The shift in band position to higher energies can be ascribed to the increasing dipole-dipole interactions of adsorbed CO due to the higher coverage as a result of the increasing pressure<sup>62</sup>. This Raman peak displayed a small shoulder centered at ~1980 cm<sup>-1</sup>, suggesting the presence of bridged CO species<sup>61</sup>. At P=20 bar, we additionally observed the Co-C stretching vibration at ~460 cm<sup>-1</sup>, the disordered (D) and graphitic (G) bands of carbonaceous species between 1300 and 1600 cm<sup>-1</sup> indicating carbon deposition<sup>63</sup>, as well as C-H stretching vibrations at 2800-3000 cm<sup>-1</sup><sup>52</sup> and the Ti-OH vibration at ~3650 cm<sup>-1</sup><sup>55,56</sup>.

The appearance of Ti-OH surface groups at elevated pressures implied that they potentially play a role in the enhanced catalytic performance of Co/TiO<sub>2</sub> at P=20 bar. It has

been reported previously that Ti-OH groups can react with surface acid intermediates to form surface carboxylates and water and that this reaction pathway is not related to catalyst deactivation<sup>50</sup>. Carboxylate surface species would display vibrations between 1300 and 1600  $\text{cm}^{-1}$ <sup>148</sup>, which are challenging to detect with Raman spectroscopy, as they overlap with the D and G bands of carbon deposits. Interestingly, formyl (CHO) or other linear aldehyde functionalities, which would give rise to a C=O stretching peak at  $\sim 1690\text{-}1725\text{ cm}^{-1}$ <sup>64,65</sup>, were not observed in the SHINERS spectra. The absence of such species at elevated pressure could indicate that the C=O bond is cleaved directly rather than reacting through the assistance of hydrogen. Nevertheless, we have to keep in mind that formyl and formaldehyde ( $\text{CH}_2\text{O}$ ) surface species are short-lived and could be missed as the SHINERS spectra were recorded under steady-state conditions<sup>23,66</sup>.

In a second set of the *operando* SHINERS experiments, the  $\text{H}_2/\text{CO}$  ratio was varied between 1 and 3 at  $T=220^\circ\text{C}$ , first at  $P=1$  bar and then at  $P=20$  bar (**Figure 3.14c**). The asymmetrically shaped adsorbed CO peak was again observed and shifted to a higher frequency upon decreasing the  $\text{H}_2/\text{CO}$  ratio from 3, to 2, to 1 at  $P=1$  bar. At  $P=20$  bar, the same trend, ascribed to the CO surface coverage effect<sup>62</sup>, was observed. Besides, carbon deposition and C-H groups were visible. Interestingly, the Ti-OH band at  $\sim 3650\text{ cm}^{-1}$  only became apparent again at  $P=20$  bar. We additionally investigated the role of temperature on the C=O vibration by feeding CO/Ar to the Co/TiO<sub>2</sub> catalyst without H<sub>2</sub>. At 1 bar pressure, the vibrational frequency decreased from 2052  $\text{cm}^{-1}$  at  $T=20^\circ\text{C}$  to 2036  $\text{cm}^{-1}$  when  $T=220^\circ\text{C}$  was reached. The pressure was then increased to 20 bar. When that pressure was reached, the sample was cooled down from  $220^\circ\text{C}$  to  $20^\circ\text{C}$ . At 20 bar pressure, the vibrational frequency increased from 2041  $\text{cm}^{-1}$  at  $T=220^\circ\text{C}$  to 2056  $\text{cm}^{-1}$  at  $T=20^\circ\text{C}$  (**Figure 3.16**). The effect of reaction temperature appeared reversible and can be ascribed either to C=O bond weakening at elevated temperatures and/or to the CO coverage effect<sup>62</sup>.

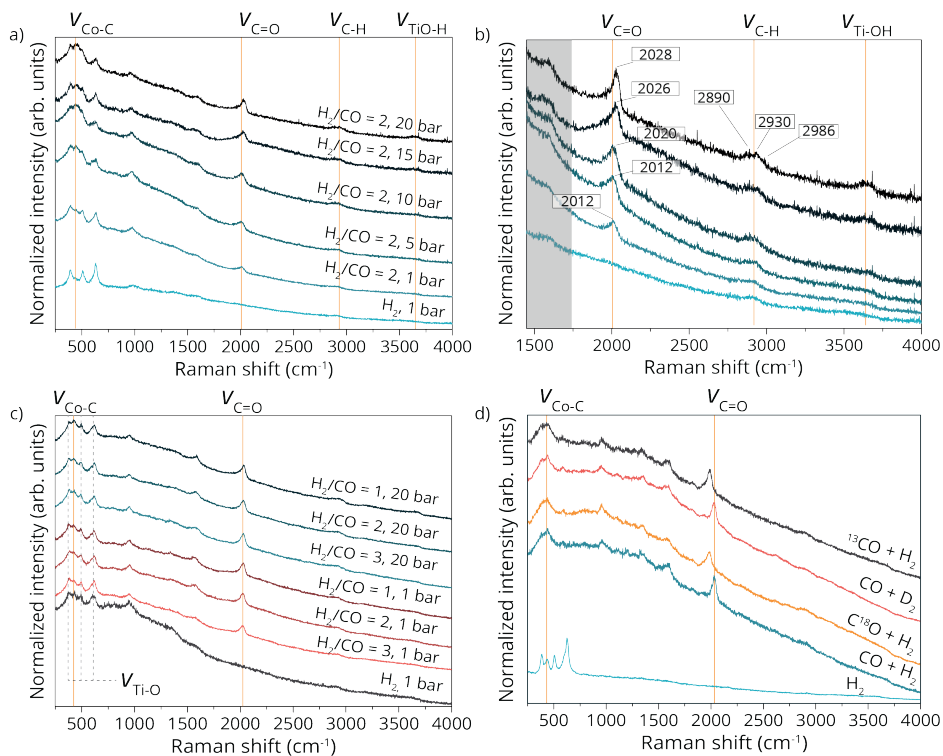


**Figure 3.14. High-pressure operando shell-isolated nanoparticle-enhanced Raman spectroscopy (SHINERS) with the 2 wt.% Co/TiO<sub>2</sub> catalyst extrudate, mixed with shell-isolated nanoparticles (SHINs) for different reaction pressures and gas compositions. a)** Operando SHINERS with Co/TiO<sub>2</sub> during Fischer-Tropsch Synthesis (FTS) at 220°C,  $H_2/CO=2$ , and increasing pressure from 1 to 20 bar. **b)** Zoom-in on the C=O, C-H, and Ti-OH region. **(c)** Operando SHINERS with Co/TiO<sub>2</sub> during FTS at 220°C, 1 and 20 bar pressure, and varying the  $H_2/CO$  ratio between 1 and 3. **(d)** Operando SHINERS isotope-labelling experiments using <sup>13</sup>CO, C<sub>18</sub>O and D<sub>2</sub> during FTS at 220°C, 1 bar, and  $H_2/CO=2$ .



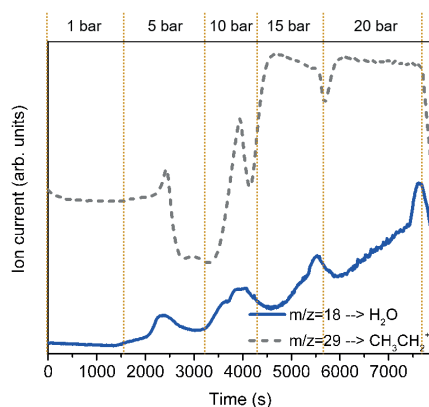


**Figure 3.15.** On-line mass spectrometry (MS) during the *operando* shell-isolated nanoparticle-enhanced Raman spectroscopy (SHINERS) experiments of the 2 wt.% Co/TiO<sub>2</sub> catalyst material, mixed with shell-isolated nanoparticles (SHINs) with increasing reaction pressure. The Fischer-Tropsch Synthesis (FTS) reaction was carried out with the Co/TiO<sub>2</sub> extrudate + shell-isolated nanoparticles (SHINs) catalyst at 220°C and H<sub>2</sub>/CO=2. Water is represented by m/z=18 (blue line) and ethane by m/z=29 (gray dashed line).

3

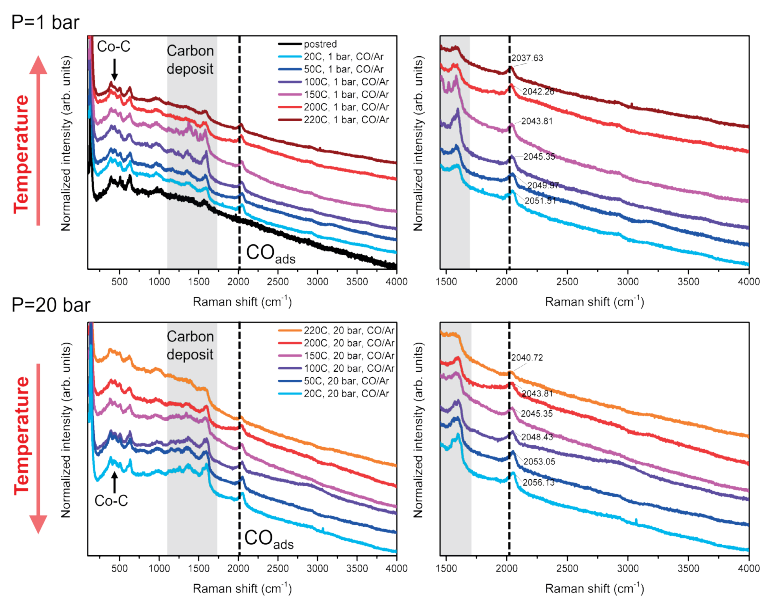


**Figure 3.16.** Shell-isolated nanoparticle-enhanced Raman spectroscopy (SHINERS) during CO adsorption on the 2 wt.% Co/TiO<sub>2</sub> catalyst extrudate material mixed with shell-isolated nanoparticles (SHINs) and measured at 1 and 20 bar and varying reaction temperatures. The top row shows SHINERS spectra during CO adsorption at 1 bar and increasing temperatures between 20 and 220°C. The bottom row shows SHINERS spectra during CO adsorption at 20 bar and decreasing temperatures between 220 and 20°C. The left side displays the full spectra, while the right side displays zoom-ins. CO:Ar=2:5 mL min<sup>-1</sup> in all cases.

To further investigate the nature of the observed surface species, we have performed additional *operando* SHINERS experiments where regular CO was replaced with  $^{13}\text{CO}$  and  $\text{C}^{18}\text{O}$  and  $\text{H}_2$  was replaced with  $\text{D}_2$ . When the atoms are replaced with an isotope of a larger mass, the reduced mass increases, resulting in a shift of the involved vibrational frequencies of C-O and/or C-H bonds to lower wavenumbers. And indeed, during the FTS at  $T=220^\circ\text{C}$ ,  $P=1$  bar, and  $\text{H}_2/\text{CO}=2$  the vibrational frequency of C=O shifted down from  $2036\text{ cm}^{-1}$  to  $1996\text{ cm}^{-1}$  with  $^{13}\text{CO}$  and to  $1990\text{ cm}^{-1}$  with  $\text{C}^{18}\text{O}$  (**Figure 3.14d**). Because these experiments were carried out at 1 bar pressure, signals for C-H and Ti-OH were not clearly observed. Co-CO, Co- $\text{CH}_3$ , Co- $\text{CH}_2$ , and Co- $\text{CH}_2\text{CH}_3$  vibrations typically appear between  $400$  and  $600\text{ cm}^{-1}$  <sup>29,53,54</sup>. In this **Chapter**, a broad Raman band was observed at  $\sim 450\text{ cm}^{-1}$  that moved to  $\sim 440\text{ cm}^{-1}$  upon replacing CO with  $^{13}\text{CO}$  but did not move upon replacing CO with  $\text{C}^{18}\text{O}$  nor upon replacing  $\text{H}_2$  with  $\text{D}_2$ . These *operando* SHINERS results suggested that the  $450\text{ cm}^{-1}$  band belonged to the Co-C stretching vibration, indicative that the direct dissociation mechanism, as depicted in **Figure 3.1a**, is also taking place during FTS. In other work, surface Co- $\text{CH}_3$  species have been reported between  $505$  and  $560\text{ cm}^{-1}$  <sup>53,54</sup>, while surface Co- $\text{CH}_2\text{CH}_3$  species have been reported at  $\sim 470\text{ cm}^{-1}$  <sup>54</sup>, and surface Co- $\text{CH}_2$  species have been observed at  $\sim 580\text{ cm}^{-1}$  <sup>53</sup>. However, in our work these Raman bands were not clearly observed and potentially even obscured by the vibrations arising from the  $\text{TiO}_2$  support at  $\sim 395$ ,  $\sim 508$ , and  $\sim 632\text{ cm}^{-1}$  <sup>67</sup>.

### 3.3.4 Carbon Deposition Occurs via Unsaturated bonds

Carbon deposition was observed on the Co/ $\text{TiO}_2$  catalyst material under study during the high-pressure *operando* SHINERS experiments. Irreversible deposition of hydrocarbons and carbonaceous species has been postulated before as potential deactivation mechanism in the FTS reaction<sup>68,69</sup>. The formation of unsaturated (hydro)carbon species on the catalyst surface is considered an irreversible process<sup>69</sup> and could thus block certain (active) sites<sup>2</sup>. Although, oxygenated aromatic species have been previously observed on the Co/ $\text{TiO}_2$  catalyst material with scanning transmission X-ray microscopy (STXM)<sup>70</sup>, vibrational spectroscopy could potentially yield a more complete picture and clarify the structure of (deactivating) carbon deposits. However, detecting carbon deposits with vibrational spectroscopy on an FTS catalyst is very challenging. The very dark colored catalyst materials typically absorb most of the visible light and thereby obstruct the spectral signal output. In this **Chapter**, we have used photo-induced force microscopy (PiFM), which combines IR spectroscopy with AFM and thereby overcomes the diffraction limit of IR light, so that spectra can be recorded with nanoscale spatial resolution and monolayer sensitivity<sup>71</sup> (**Figure 3.1d**). PiFM requires relatively flat surfaces for optimal performance and therefore the Co/ $\text{TiO}_2$  micro-island model system,

as introduced in **Chapter 2**, was employed to study the formation of carbonaceous deposits during the FTS process.

Using a model catalyst of Co/TiO<sub>2</sub> micro-island on a SiO<sub>2</sub>/Si(100) wafer (**Chapter 2**), the formation and nature of hydrocarbons and carbon-containing deposits were evaluated after 0, 1, 2, 6, and 24 h FTS reaction (220°C, 1 bar, H<sub>2</sub>/CO=2). After the reaction, the samples were cooled down to room temperature in Ar gas and subsequently a passivation step was done in 2 vol.% O<sub>2</sub>/Ar. For the carbonaceous region 1100-1700 cm<sup>-1</sup> ( $\nu$ (C=C),  $\nu$ (C-C),  $\delta$ (C-H)), the micro-islands were analyzed with ~30 nm spatial resolution in hyperspectral imaging mode using a QCL laser. The average spectrum over each micro-island was obtained by spectrally segmenting the hyperspectral data into background and micro-island. To obtain information about the relevant peak positions, the resulting data were fitted and the fitted PiFM IR spectra on the micro-islands are displayed in **Figure 3.17a**. The higher wavenumber region (2800-3300 cm<sup>-1</sup> ( $\nu$ (C-H))) was recorded using an OPO laser and **Figure 3.17a** displays PiFM IR point spectra that were smoothed using the Loess function with 30 points in Origin 9. After 1 h FTS, the IR bands at 1260 cm<sup>-1</sup> and 1380 cm<sup>-1</sup> were the most prominent spectroscopic features. These IR bands indicate C-C stretching vibrations and C-H bending vibrations from methyl groups, respectively<sup>72-75</sup>. Additionally, some weaker vibrational bands in the 1450-1900 cm<sup>-1</sup> region, indicating the presence of alkanes, poly-ethenes, aromatics, and oxygenates<sup>73</sup>, were observed. The most prominent band in this area was the one at 1610 cm<sup>-1</sup>, caused by C=C stretching vibrations in hydrogen-deficient carbonaceous species<sup>73,74</sup>. Symmetric C=C vibrations are normally considered IR inactive, but become IR active when the symmetry is broken<sup>76-78</sup>. This points towards the presence of structural irregularities in the carbon deposits on the catalyst surface. After 2 h FTS, the bands at ~1260, 1380, and 1610 cm<sup>-1</sup> became more prominent. Especially the intensity of the  $\nu$ (C=C) at ~1610 cm<sup>-1</sup> increased, implying that the carbon deposits became more unsaturated/graphitic. This trend progressed till 6 h and 24 h FTS, indicating an increasing degree of graphitization over time. When looking at the C-H stretching region (2800-3300 cm<sup>-1</sup>) of the PiFM IR spectra, the same trend was observed: The IR bands above 3000 cm<sup>-1</sup>, indicating the presence of unsaturated C-H species<sup>52</sup>, increased in intensity with increasing FTS reaction time relative to the IR bands between 2800 and 3000 cm<sup>-1</sup>, representative for the presence of aliphatic C-H species<sup>73,74</sup>. The intensity ratios between 1380 cm<sup>-1</sup> ( $\delta$ (C-H) vibrations (*sp*<sup>3</sup> C)) and 1610 cm<sup>-1</sup> ( $\nu$ (C=C) vibrations from (*sp*<sup>2</sup> C)) were used as a measure for the degree of graphitization in the carbon deposits. Both the intensity ratios at  $I_{1610}/I_{1380}$  and  $I_{3150}/I_{2925}$  increased with increasing reaction time (**Figure 3.17b**), proving that the carbon deposits become more graphitic and less methylated with increasing time-on-stream.

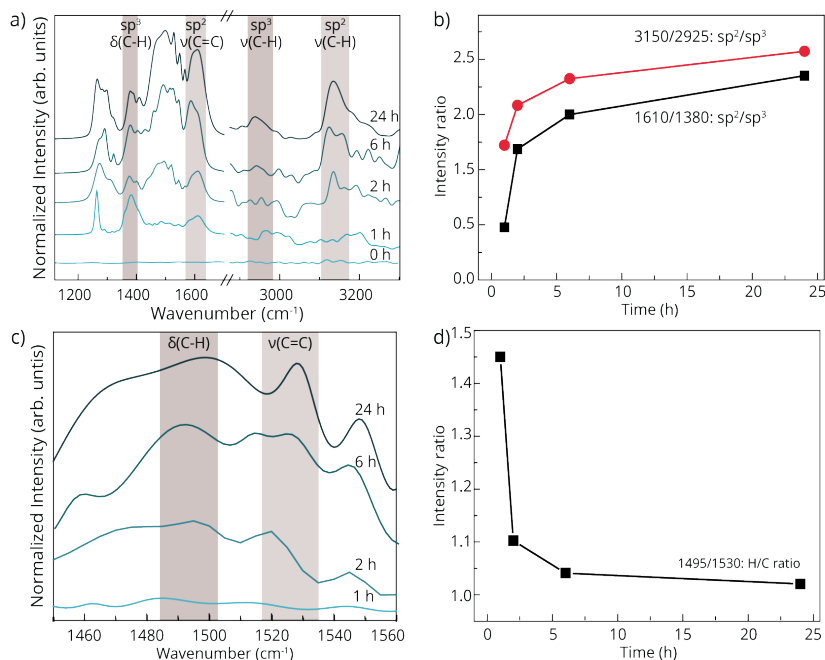


**Figure 3.17. Detecting unsaturated (hydro)carbon deposits on the Co/TiO<sub>2</sub> model catalyst system after Fischer-Tropsch Synthesis (FTS) with photo-induced force microscopy (PiFM).** **a)** PiFM (IR) spectra recorded on the Co/TiO<sub>2</sub> micro-island catalysts after 0, 1, 2, 6, and 24 h of FTS reaction. **b)** Intensity ratios of 1610/1380 and 3150/2925 IR bands, indicating sp<sup>2</sup>/sp<sup>3</sup> bonds versus FTS reaction time. **c)** Zoom in of the 1450-1560 cm<sup>-1</sup> region. **d)** Calculated relative H/C ratio of the carbon deposits (1495 cm<sup>-1</sup>/1530 cm<sup>-1</sup> bands) versus FTS reaction time.

Photo-induced force microscopy (PiFM), used in this Chapter to record the nanoscale IR spectra, is a relatively new analytical technique. Its principle, as also outlined in **Chapter 2**, is based on dipole-dipole interaction between sample and tip, when illuminated with coherent monochromatic light<sup>71,79</sup>. PiFM thus has a slightly different and more complex detection mechanism compared to more conventional IR techniques, such as attenuated total reflection (ATR) IR spectroscopy. In **Figure 3.18** we have compared the ATR-IR method with PiFM IR method and the related spectra for both polyethylene (PE) and a FTS wax with 41C average chain length are shown. For both samples, PiFM appears more sensitive to the detection of the 1473 cm<sup>-1</sup> vibration, commonly assigned to  $\delta_{\text{asym}}\text{CH}_3$ <sup>52,80-82</sup>. However, in the field of olefin polymerization, 1463 and 1473 cm<sup>-1</sup> are often both assigned to -CH<sub>2</sub>- vibrations and used to determine the PE crystallinity<sup>83</sup>. Besides, the peak at 1473 cm<sup>-1</sup> has also been ascribed to a combination band of -CH<sub>2</sub>- and -CH<sub>3</sub> groups by some studies<sup>81</sup>. Although the different assignments are interesting,

we have therefore not used these bands for any additional chain length correlations in our work. Further analysis and related interpretation of the data are needed to confirm the provided assignments and discussions.

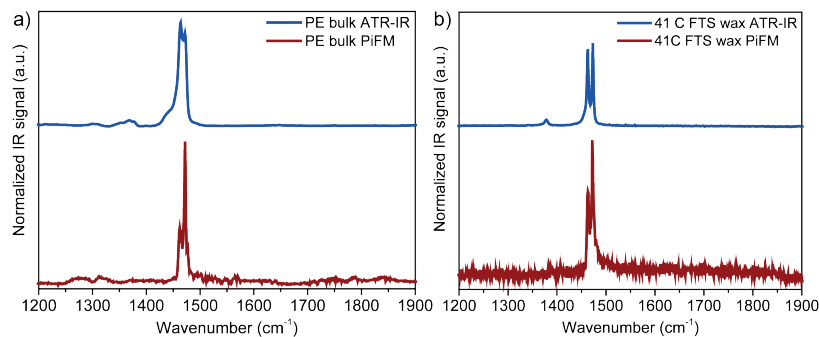


**Figure 3.18. Comparison of attenuated total reflection (ATR) and photo-induced force microscopy (PiFM) infrared (IR) spectra.** **a**, polyethylene (PE) and **b**, 41C Fischer-Tropsch Synthesis (FTS) wax. The difference in intensity ratio between the 1463 and 1473  $\text{cm}^{-1}$  peaks from ATR-IR versus PiFM clearly shows how the detection method of PiFM differs slightly from conventional IR techniques. PiFM is very sensitive to dipoles and therefore detects certain vibrations much stronger than conventional IR.

The PiFM IR data contained more information than just the degree of graphitization. The  $\delta(\text{C-H})$  at 1495  $\text{cm}^{-1}$  and  $\nu(\text{C=C})$  at 1530  $\text{cm}^{-1}$  were used as fingerprint bands for coke species, *i.e.*, irreversibly adsorbed carbon deposits<sup>73,74</sup>. The intensity ratio ( $I_{1495}/I_{1530}$ ) was used as a qualitative proxy for the relative H/C ratio of the coke species, helping to identify which organic structures were formed on the catalyst surface (**Figure 3.17d**). For example, benzene, a monoaromatic, has H/C=1, whereas naphthalene, a diaromatic, has H/C=0.8. For polyaromatic species, the H/C ratio is generally between 0.35 and 0.70<sup>84</sup>. Although quantitative determination of the H/C ratio is not feasible with IR spectroscopy alone due to the different IR activities of the  $\delta(\text{C-H})$  and  $\nu(\text{C=C})$  bands, the intensity ratio was used as a relative measure in our work. The relative H/C proxy decreased with FTS reaction time (**Figure 3.17d**), indicating the formation and growth of unsaturated structures on the catalyst surface.

The IR bands at 1700-1900  $\text{cm}^{-1}$  (**Figure 3.19**) pointed towards the presence of conjugated C=O functionalities. The PiFM IR spectra of bare  $\text{TiO}_2$  micro-islands after FTS did not show carbonaceous species (**Figure 3.20**), supporting the earlier observation made with *operando* ME DRIFTS that  $\text{TiO}_2$  by itself is unable to cleave the C-O bonds. Consequently, carbon deposition does not occur on  $\text{TiO}_2$  only during the FTS reaction. Theoretical vibrational spectra, obtained by density functional theory (DFT) calcula-

tions, for conjugated as well as linear aldehydes, carboxylic acids, and ketones provide a range of structural possibilities and can be found in **Figures 3.21-3.24**. Aldehydes (**Figure 2.21**), carboxylic acids (**Figure 2.22** and **3.23**), and ketones (**Figure 3.24**) were selected, as these could be relevant to carbon deposits on the Co/TiO<sub>2</sub> catalyst surface. Benzoquinone-type species have, for example, been reported in earlier work by our group on a Co/TiO<sub>2</sub> FTS catalyst using operando X-ray microscopy<sup>70</sup>. Comparing the theoretical vibrational spectra with the PiFM IR data led, however, to the conclusion that the PiFM IR data are too convoluted to pinpoint only one species. The carbon deposits on Co/TiO<sub>2</sub> may thus contain multiple different (oxygenated) hydrocarbon species.

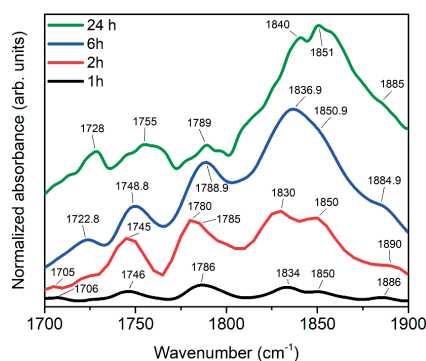


**Figure 3.19. Photo-induced force microscopy (PiFM) infrared (IR) data of the Co/TiO<sub>2</sub> model catalyst material** after Fischer-Tropsch Synthesis (FTS) (220°C, 1 bar, H<sub>2</sub>/CO=2) in the region 1700-1900 cm<sup>-1</sup>, showing C=O stretching bands of (conjugated) oxygenates.

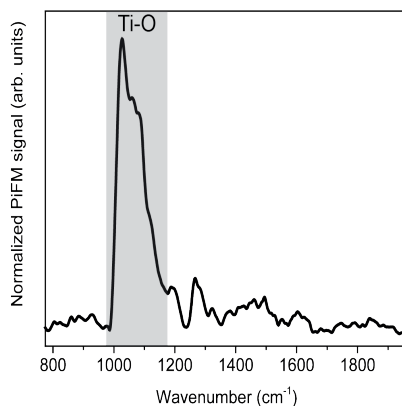


**Figure 3.20. Average photo-induced force microscopy (PiFM) infrared (IR) spectrum of bare TiO<sub>2</sub> micro-islands after 2 h of Fischer-Tropsch Synthesis (FTS) at 220°C, 1 bar, and H<sub>2</sub>/CO=2.** The gray shaded area indicates the Ti-O stretching vibration. The low intensity signals observed between 1250 and 1700 cm<sup>-1</sup> originate from water vapor<sup>86</sup>, omnipresent in the PiFM enclosure box.

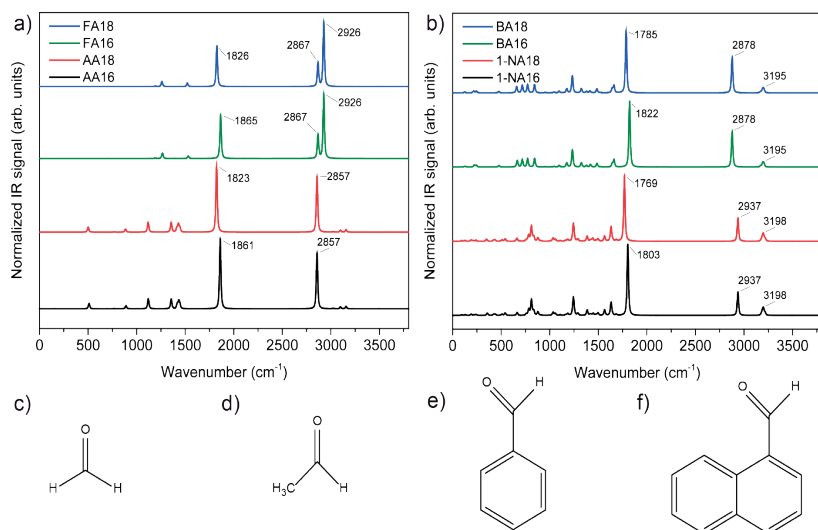


**Figure 3.21. Theoretical infrared (IR) spectra for aldehydes, as calculated with density functional theory (DFT) for linear (a) and conjugated (b) aldehydes both with  $^{16}\text{O}$  and  $^{18}\text{O}$  a, formaldehyde (FA) and acetic aldehyde (AA) and b, benzaldehyde (BA) and 1-naphthaldehyde (1-NA). c-f, Structural formulas for c, formaldehyde (FA), d, acetic aldehyde (AA), e, benzaldehyde (BA), f, 1-naphthaldehyde (1-NA).**

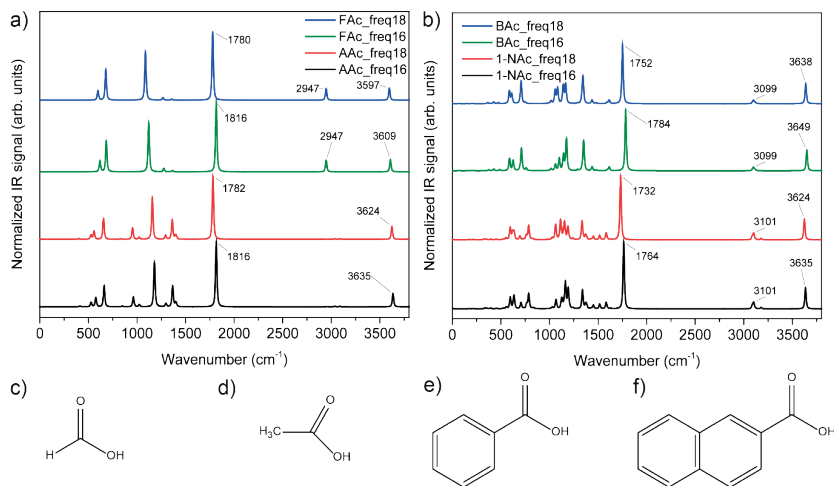


**Figure 3.22. Theoretical infrared (IR) spectra for carboxylic acids, as calculated with density functional theory (DFT) for linear (a) and conjugated (b) carboxylic acids both with  $^{16}\text{O}$  and  $^{18}\text{O}$  a, formic acid (FAc) and acetic acid (AAc) and b, benzoic acid (BAc) and 1-naphthoic acid (1-NAc). c-f, Structural formulas for c, formic acid (FAc), d, acetic acid (AAc), e, benzoic acid (BAc), f, 1-naphthoic acid (1-NAc).**

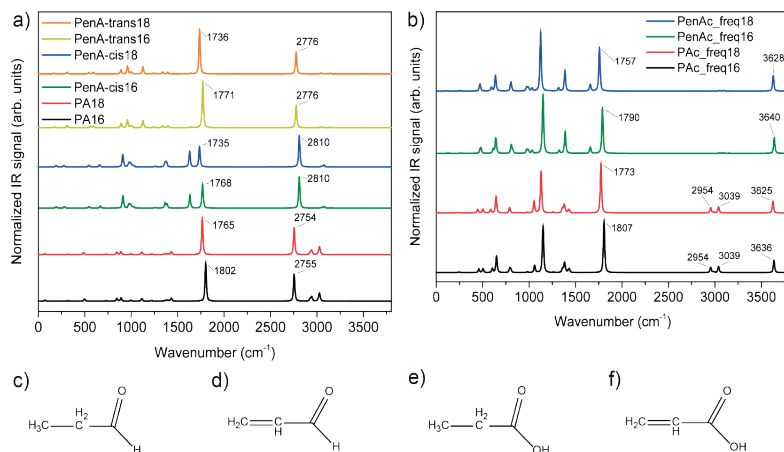


**Figure 3.23. Theoretical infrared (IR) spectra for linear saturated and unsaturated C<sub>3</sub> aldehydes and carboxylic acids, as calculated with density functional theory (DFT) for aldehydes (a) and carboxylic acids (b) both with <sup>16</sup>O and <sup>18</sup>O a, propionaldehyde (PA) and unsaturated propionaldehyde (PenA) cis and trans and b, propionic acid (PAC) and unsaturated propionic acid (PenAc) c-f, Structural formulas for c, propionaldehyde (PA), d, unsaturated propionaldehyde (PenA) cis and trans, e, propionic acid (PAC), f, unsaturated propionic acid (PenAc).**

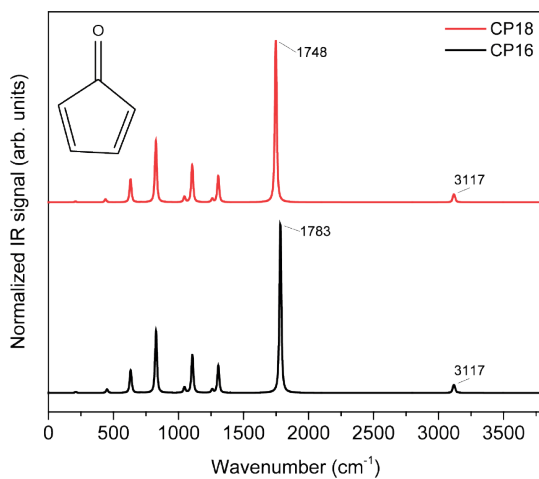


**Figure 3.24. Theoretical infrared (IR) spectra for cyclopentanone (CP), as calculated with density functional theory (DFT) both with <sup>16</sup>O and <sup>18</sup>O.**



To verify the experimental observations made with PiFM, we have additionally performed *operando* Raman micro-spectroscopy and STXM (Figures 3.25-3.26). With *operando* Raman micro-spectroscopy, we have observed that the amount of unsaturated species increased with increasing reaction time, which coincided with a decrease in methane selectivity (Figure 3.26).

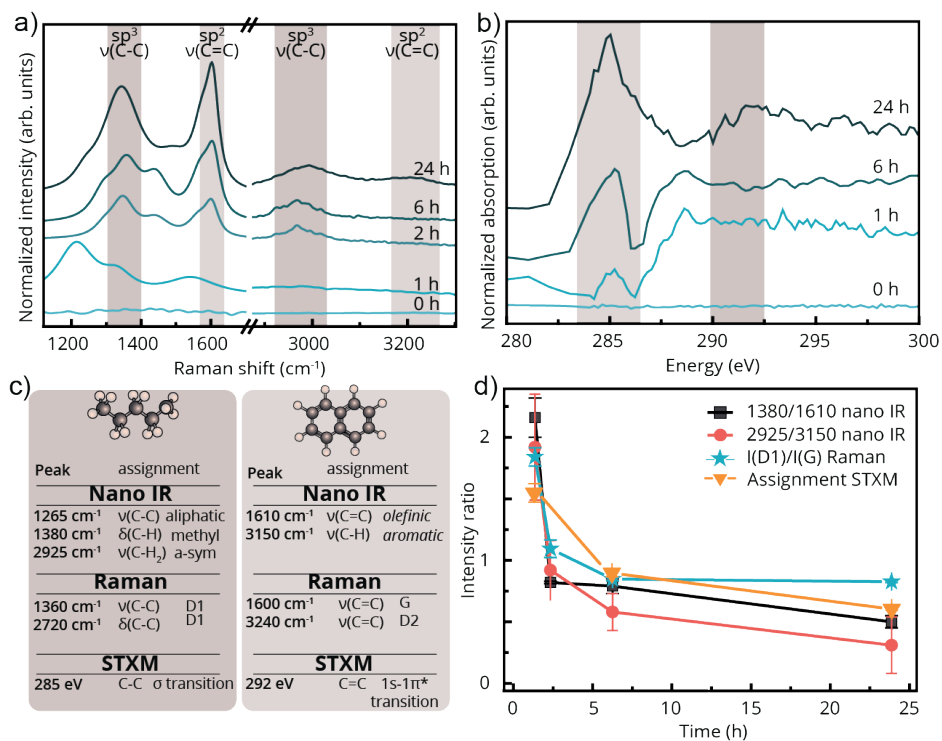


**Figure 3.25. Overview of the Raman micro-spectroscopy and scanning transmission X-ray microscopy (STXM) on the Co/TiO<sub>2</sub> micro-islands fresh as well as after Fischer-Tropsch Synthesis (FTS).** **a**, Raman micro-spectroscopy and **b**, STXM of the fresh and spent Co/TiO<sub>2</sub> micro-islands after FTS (220°C, 1 bar, H<sub>2</sub>/CO=2). **c**, Table with relevant peaks for linear and unsaturated (hydro)carbons from photo-induced force microscopy (PiFM), Raman, and STXM. **d**, Intensity ratios of peaks indicating aliphatic/unsaturated bonds versus FTS reaction time.

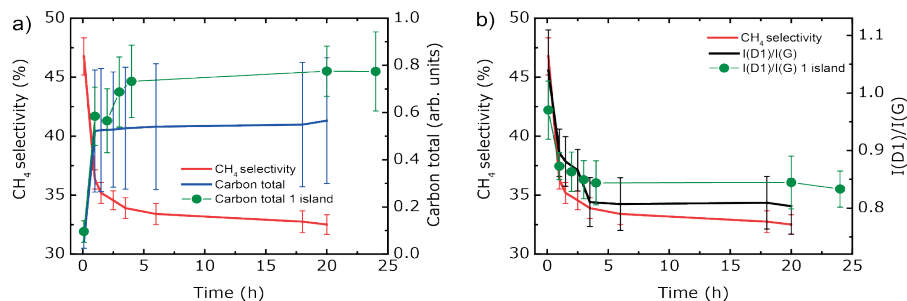


**Figure 3.26. Operando Raman micro-spectroscopy with Co/TiO<sub>2</sub> micro-islands during the Fischer-Tropsch Synthesis (FTS).** Statistics of mapped island amongst the other 20 islands. **a**, Total carbon formation and CH<sub>4</sub> selectivity plotted over time. **b**, I(D1)/I(G) and CH<sub>4</sub> selectivity plotted over time.

On the other hand, *operando* STXM results confirmed these findings and are in accordance with earlier X-ray microscopy work from our group on a Co/TiO<sub>2</sub> FTS catalyst, reporting a build-up and consequently consumption of oxygenated carbon species with increasing time-on-stream<sup>70</sup>. Another research group has also previously found conjugated aldehydes and branched carboxylic acids, which can form *via* dehydrocyclization or hydroformylation of  $\alpha$ -olefins, in the wax-extracted carbon species from a spent Co/Al<sub>2</sub>O<sub>3</sub> catalyst using gas chromatography (GC)-MS<sup>87</sup>. Besides, it has been proposed that aromatic carbon structure formation is an irreversible process on cobalt catalysts and occurs *via* cyclopolymerization of C<sub>2</sub>H<sub>x</sub> species<sup>88,89</sup>. To test whether aldehyde (C=O) functionalities would also be able to transform into hydrocarbon products over a Co/TiO<sub>2</sub> catalyst, a co-feeding experiment was conducted during the FTS reaction (220°C, 1 bar, H<sub>2</sub>/CO=2) with <sup>13</sup>C formaldehyde and an experiment with only <sup>12</sup>C formaldehyde and H<sub>2</sub> (220°C, 1 bar, H<sub>2</sub>/CH<sub>2</sub>O=2). Both experiments indicated carbon deposition and the conversion of formaldehyde into a variety of (oxygenated) hydrocarbons (**Figure 3.27**). Conversion of oxygenates and H<sub>2</sub> into hydrocarbon products by cobalt-based FTS catalysts has been documented before<sup>7,22</sup>. Such findings underline the dynamicity of FTS catalyst materials in general as they seem to adapt to the gas feed that is supplied. Certain reaction pathways may become more favorable and thus selectively turned on depending on the gas feed composition.

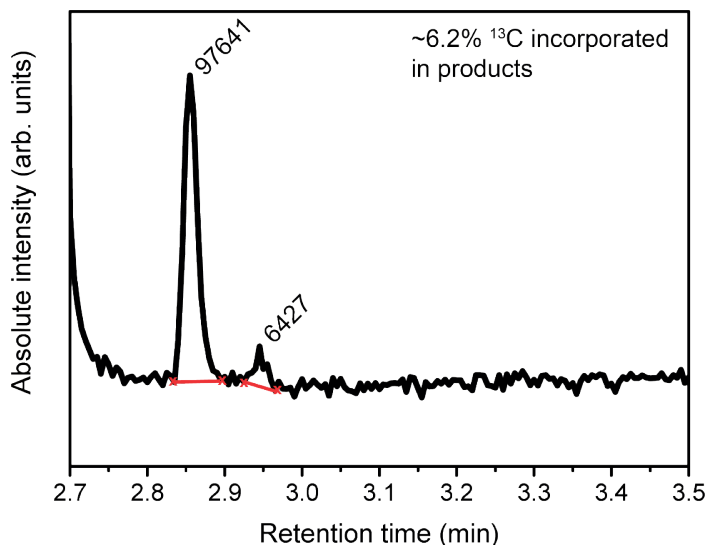


**Figure 3.27. Gas chromatography (GC) pattern of the gas outlet stream of  $^{13}\text{C}$  formaldehyde co-feeding during Fischer-Tropsch Synthesis (FTS) with  $\text{Co}/\text{TiO}_2$ .** Integration of the first ( $^{12}\text{C}$ ) and second ( $^{13}\text{C}$ ) hydrocarbon peaks indicates that roughly 6.2% of the hydrocarbon products has  $^{13}\text{C}$  incorporated. The FTS reaction conditions were  $220^\circ\text{C}$ , 1 bar,  $\text{H}_2/\text{CO}=2$ . During co-feeding  $\text{H}_2:\text{CO}:\text{formaldehyde}=5:2:1$ .

### 3.4 Conclusions

ME DRIFTS, SHINERS, and PiFM were used to study the mechanistic pathways that are treaded during the cobalt-based FTS reaction. The *operando* ME DRIFTS technique revealed amongst others the presence of carboxylates as active species on  $\text{Co}/\text{TiO}_2$ , suggesting the occurrence of the CO or HCO insertion mechanism during the FTS process. The performance-enhancing role of the  $\text{TiO}_2$  support appeared related to supplying essential building blocks to the cobalt catalyst during the reaction. Complementary *operando* SHINERS measurements at pressures up to 20 bar indicated the presence of Co-C and thus the occurrence of the direct CO dissociation mechanism. The catalytic activity and selectivity towards the desired  $\text{C}_{5+}$  products increased with increasing pressure. Various surface species were observed during the FTS reaction with  $\text{Co}/\text{TiO}_2$  at  $220^\circ\text{C}$  and pressures between 1 and 20 bar. We found that the formation of Ti-OH surface groups only emerged at elevated pressure, suggesting that Ti-OH groups play a role in enhancing the catalytic performance at higher pressures as well. With PiFM, we have observed that unsaturated hydrocarbon deposits emerge and grow with increasing reaction time. Employing a variety of analytical methods allowed us to see the long-standing mechanistic problem in FTS catalysis from multiple different angles. Proof was observed for the parallel occurrence of the most widely accepted reaction

mechanisms, direct dissociation of CO and CO insertion. It is important to realize that confusion about reaction mechanisms in the academic world may arise from the multitude of (home-made) catalysts, reaction conditions, and equipment used in different characterization studies. This work shows that these intrinsic differences in materials and analytical methods can be bridged by presenting a comprehensive study on Co/TiO<sub>2</sub> FTS materials. Particularly vital in terms of future perspectives and sustainable development is that the results obtained in academic research can directly be translated to industrially relevant catalysis. Collaborations between academia and industry, as well as conducting *operando* experiments under industrially relevant conditions, *i.e.*, elevated temperature and pressures, are therefore essential and will improve the relevance of the physicochemical insights obtained from such detailed investigations.

### 3.5 Author Contributions and Acknowledgements

This Chapter is based on the manuscript "ten Have, I. C., Hartman, T., van Bavel, A.P., Bezemer, G. L., Ferri, D., Geitner, R., Huang, T., Kupfer, S., Gräfe, S., Meirer, F., Weckhuysen, B. M. (2022). Through the Lens of *Operando* Spectroscopy: Mechanistic Insights in the Fischer-Tropsch Synthesis. *Submitted for publication*."

The research was conceptualized by Bert Weckhuysen and Iris ten Have. Iris ten Have performed catalyst syntheses, catalytic testing, kinetic measurements, SHINERS, PiFM, and STXM and subsequently analyzed the results. Thomas Hartman synthesized the SHINs and provided strategy, planning, and discussions regarding the SHINERS experiments. Thomas Hartman formatted all figures for the main text and made the table of contents figure. Sander van Bavel (Shell Global Solutions International B.V.) provided the Fischer-Tropsch wax references, as well as discussions, further inspiration for experiments, and ideas for the manuscript. Leendert Bezemer (Shell Global Solutions International B.V.) arranged the analysis of oxygenate products, participated in the scientific discussions, and provided further insights for the manuscript. Davide Ferri (Paul Scherrer Institute) conducted ME DRIFTS experiments and helped with the interpretation of the results. Florian Meirer wrote the codes for the PiFM and STXM data analysis and helped with interpretation of the results. Robert Geitner, Tianbai Huang, Stephan Kupfer, and Stefanie Gräfe (University of Jena) performed the DFT calculations. The work was written by Iris ten Have under the supervision of Florian Meirer and Bert Weckhuysen and with input from all co-authors.

### 3.6 References

1. van de Loosdrecht, J., Botes, F. G., Ciobica, I. M., Ferreira, A., Gibson, P., Moodley, D. J., Saib, A. M., Visagie, J. L., Weststrate, C. J. & Niemantsverdriet, J. W. in *Comprehensive Inorganic Chemistry II: from elements to applications* **7**, 525-557 (Elsevier, Amsterdam, 2013).
2. ten Have, I. C. & Weckhuysen, B. M. The active phase in cobalt-based Fischer-Tropsch synthesis. *Chem Catalysis* **1**, 339-363 (2021).
3. Fischer, F. & Tropsch, H. The preparation of synthetic oil mixtures (synthol) from carbon monoxide and hydrogen. *Brennst.-Chem.* **4**, 276-285 (1923).
4. Fischer, F. & Tropsch, H. The synthesis of petroleum at atmospheric pressures from gasification products of coal. *Brennst.-Chem.* **7**, 97-104 (1926).
5. Bell, A. T., Bond, G. C., Thompson, D. T., Valden, M., Lai, X., Goodman, D. W., Blasko, T., Nieto, J. M. L., Chen, K., Bell, A. T., Iglesia, E., Koyama, T., Komaya, T., Gai, P. L., Weyland, M., Durscher, G., Browning, N. D., Pennycook, S. J., Besenbacher, F., Thune, P. C., Loss, J., Wenter, D., Leustra, P. J., Niemantsverdriet, J. W., Corker, J., Vidal, V., Theolier, A., Thivolle-Cazat, J., Basset, J.-M., Nozkaki, C., Lugmair, C. G., Bell, A. T., Tilley, T. D., Kolb, D., Jong, K. P. de & Geus, J. W. The impact of nanoscience on heterogeneous catalysis. *Science* **299**, 1688-1691 (2003).
6. Xiang, Y. & Kruse, N. Tuning the catalytic CO hydrogenation to straight-and long-chain aldehydes/alcohols and olefins/paraffins. *Nature Communications* **7**, 13058 (2016).
7. Hutchings, G. J., Riet, M. van der & Hunter, R. CO Hydrogenation using Cobalt/Manganese Oxide Catalysts. *Journal of the Chemical Society, Faraday Transactions 1 Physical Chemistry in Condensed Phases* **85**, 2875-2890 (1989).
8. Saib, A. M., Moodley, D. J., Ciobîc, I. M., Hauman, M. M., Sigwebela, B. H., Weststrate, C. J., Niemantsverdriet, J. W. & van de Loosdrecht, J. Fundamental understanding of deactivation and regeneration of cobalt Fischer-Tropsch synthesis catalysts. *Catalysis Today* **154**, 271-282 (2010).
9. van Helden, P., Ciobîc, I. M. & Coetzer, R. L. J. The size-dependent site composition of FCC cobalt nanocrystals. *Catalysis Today* **261**, 48-59 (2016).
10. van Santen, R. A., Ciobîc, I. M., van Steen, E. & Ghouri, M. M. Mechanistic Issues in Fischer-Tropsch Catalysis. *Advances in Catalysis* **54**, 127-187 (2011).
11. Weststrate, C. J., Kazalkaya, A. C., Rossen, E. T. R., Verhoeven, M. W. G. M., Ciobîc, I. M., Saib, A. M. & Niemantsverdriet, J. W. Atomic and polymeric carbon on Co(0001): Surface reconstruction, graphene formation, and catalyst poisoning. *Journal of Physical Chemistry C* **116**, 11575-11583 (2012).
12. Zijlstra, B., Broos, R. J. P., Chen, W., Oosterbeek, H., Filot, I. A. W. & Hensen, E. J. M. Coverage Effects in CO Dissociation on Metallic Cobalt Nanoparticles. *ACS Catalysis* **9**, 7365-7372 (2019).
13. Moodley, D. J., van de Loosdrecht, J., Saib, A. M., Overett, M. J., Datye, A. K. & Niemantsverdriet, J. W. Carbon deposition as a deactivation mechanism of cobalt-based Fischer-Tropsch synthesis catalysts under realistic conditions. *Applied Catalysis A: General* **354**, 102-110 (2009).
14. Batista, M. S., Santos, R. K. S., Assaf, E. M., Assaf, J. M. & Ticianelli, E. A. Characterization of the activity and stability of supported cobalt catalysts for the steam reforming of ethanol. *Journal of Power Sources* **124**, 99-103 (2003).
15. Böller, B., Durner, K. M. & Wintterlin, J. The active sites of a working Fischer-Tropsch catalyst revealed by operando scanning tunnelling microscopy. *Nature Catalysis* **2**, 1027-1034 (2019).

16. Zijlstra, B., Broos, R. J. P., Chen, W., Bezemer, G. L., Pilot, I. A. W. & Hensen, E. J. M. The Vital Role of Step-Edge Sites for Both CO Activation and Chain Growth on Cobalt Fischer-Tropsch Catalysts Revealed through First-Principles-Based Microkinetic Modeling Including Lateral Interactions. *ACS Catalysis* **10**, 9376–9400 (2020).
17. Weststrate, C. J., Sharma, D., Garcia Rodriguez, D., Gleeson, M. A., Fredriksson, H. O. A. & Niemantsverdriet, J. W. (Hans). Mechanistic insight into carbon-carbon bond formation on cobalt under simulated Fischer-Tropsch synthesis conditions. *Nature Communications* **11**, 750 (2020).
18. Ojeda, M., Nabar, R., Nilekar, A. U., Ishikawa, A., Mavrikakis, M. & Iglesia, E. CO activation pathways and the mechanism of Fischer-Tropsch synthesis. *Journal of Catalysis* **272**, 287–297 (2010).
19. Hibbitts, D., Dybeck, E., Lawlor, T., Neurock, M. & Iglesia, E. Preferential activation of CO near hydrocarbon chains during Fischer-Tropsch synthesis on Ru. *Journal of Catalysis* **337**, 91–101 (2016).
20. Zhuo, M., Borgna, A. & Saeys, M. Effect of the CO coverage on the Fischer-Tropsch synthesis mechanism on cobalt catalysts. *Journal of Catalysis* **297**, 217–226 (2013).
21. Todic, B., Ma, W., Jacobs, G., Davis, B. H. & Bukur, D. B. CO-insertion mechanism based kinetic model of the Fischer-Tropsch synthesis reaction over Re-promoted Co catalyst. *Catalysis Today* **228**, 32–39 (2014).
22. Raub, A., Karroum, H., Athariboroujny, M. & Kruse, N. Chemical Transient Kinetics in Studies of the Fischer-Tropsch Reaction and Beyond. *Catalysis Letters* **151**, 613–626 (2021).
23. Inderwildi, O. R., Jenkins, S. J. & King, D. A. Fischer-Tropsch mechanism revisited: Alternative pathways for the production of higher hydrocarbons from synthesis gas. *Journal of Physical Chemistry C* **112**, 1305–1307 (2008).
24. Weststrate, C. J., Gericke, H. J., Verhoeven, M. W. G. M., Ciobîcă, I. M., Saib, A. M. & Niemantsverdriet, J. W. Ethanol decomposition on Co(0001): C-O bond scission on a close-packed cobalt surface. *Journal of Physical Chemistry Letters* **1**, 1767–1770 (2010).
25. Navarro, V., van Spronsen, M. A. & Frenken, J. W. M. In situ observation of self-assembled hydrocarbon Fischer-Tropsch products on a cobalt catalyst. *Nature Chemistry* **8**, 929–934 (2016).
26. Cheng, J., Gong, X. Q., Hu, P., Lok, C. M., Ellis, P. & French, S. A quantitative determination of reaction mechanisms from density functional theory calculations: Fischer-Tropsch synthesis on flat and stepped cobalt surfaces. *Journal of Catalysis* **254**, 285–295 (2008).
27. Chen, W., Pilot, I. A. W., Pestman, R. & Hensen, E. J. M. Mechanism of Cobalt-Catalyzed CO Hydrogenation: 2. Fischer-Tropsch Synthesis. *ACS Catalysis* **7**, 8061–8071 (2017).
28. Chen, W., Kimpel, T. F., Song, Y., Chiang, F. K., Zijlstra, B., Pestman, R., Wang, P. & Hensen, E. J. M. Influence of Carbon Deposits on the Cobalt-Catalyzed Fischer-Tropsch Reaction: Evidence of a Two-Site Reaction Model. *ACS Catalysis* **8**, 1580–1590 (2018).
29. Hartman, T., Geitenbeek, R. G., Whiting, G. T. & Weckhuysen, B. M. Operando monitoring of temperature and active species at the single catalyst particle level. *Nature Catalysis* **2**, 986–996 (2019).
30. Park, J. Y. *Current trends of surface science and catalysis. Current Trends of Surface Science and Catalysis* **9781461487**, (Springer, Berlin, 2014).
31. Frenken, J. & Groot, I. *Operando Research in Heterogeneous Catalysis* **9789038608969**, (Springer, Berlin, 2017).

32. Chiarello, G. L., Nachtegaal, M., Marchionni, V., Quaroni, L. & Ferri, D. Adding diffuse reflectance infrared Fourier transform spectroscopy capability to extended x-ray-absorption fine structure in a new cell to study solid catalysts in combination with a modulation approach. *Review of Scientific Instruments* **85**, 074102 (2014).
33. Baurecht, D. & Fringeli, U. P. Quantitative modulated excitation Fourier transform infrared spectroscopy. *Review of Scientific Instruments* **72**, 3782–3792 (2001).
34. Frisch, M. J. et al. Gaussian 16 (Revision B.01). *Gaussian, Inc, Wallingford, CT, USA* (2016).
35. Becke, A. D. Density-functional exchange-energy approximation with correct asymptotic behavior. *Physical Review A* **38**, 3098–3100 (1988).
36. Becke, A. D. Density-functional thermochemistry. III. The role of exact exchange. *The Journal of Chemical Physics* **98**, 5648–5652 (1993).
37. Weigend, F. & Ahlrichs, R. Balanced basis sets of split valence, triple zeta valence and quadruple zeta valence quality for H to Rn: Design and assessment of accuracy. *Physical Chemistry Chemical Physics* **7**, 3297–3305 (2005).
38. Weigend, F. Accurate Coulomb-fitting basis sets for H to Rn. *Physical Chemistry Chemical Physics* **8**, 1057–1065 (2006).
39. Allouche, A. Software News and Updates Gabedit – A Graphical User Interface for Computational Chemistry Softwares. *Journal of Computational Chemistry* **32**, 174–182 (2012).
40. Zennaro, R., Tagliabue, M. & Bartholomew, C. H. Kinetics of Fischer – Tropsch synthesis on titania-supported cobalt. *Catalysis Today* **58**, 309–319 (2000).
41. Banerjee, A., van Bavel, A. P., Kuipers, H. P. C. E. & Saeys, M. CO Activation on Realistic Cobalt Surfaces: Kinetic Role of Hydrogen. *ACS Catalysis* **7**, 5289–5293 (2017).
42. Yang, J., Qi, Y., Zhu, J., Zhu, Y. A., Chen, D. & Holmen, A. Reaction mechanism of CO activation and methane formation on Co Fischer-Tropsch catalyst: A combined DFT, transient, and steady-state kinetic modeling. *Journal of Catalysis* **308**, 37–49 (2013).
43. Zhao, Y. H., Sun, K., Ma, X., Liu, J., Sun, D., Su, H. Y. & Li, W. X. Carbon chain growth by formyl insertion on rhodium and cobalt catalysts in syngas conversion. *Angewandte Chemie International Edition* **50**, 5335–5338 (2011).
44. Müller, P. & Hermans, I. Applications of Modulation Excitation Spectroscopy in Heterogeneous Catalysis. *Industrial & Engineering Chemistry Research* **56**, 1123–1136 (2017).
45. ten Have, I. C., Kromwijk, J. J. G., Monai, M., Meirer, F., Weckhuysen, B. M. & Sterk, E. B. Uncovering the reaction mechanism behind CoO as active phase for CO<sub>2</sub> hydrogenation. *Nature Communications* **13**, 324 (2022).
46. Yang, N. & Bent, S. F. Investigation of inherent differences between oxide supports in heterogeneous catalysis in the absence of structural variations. *Journal of Catalysis* **351**, 49–58 (2017).
47. Lorito, D., Paredes-Nunez, A., Mirodatos, C., Schuurman, Y. & Meunier, F. C. Determination of formate decomposition rates and relation to product formation during CO hydrogenation over supported cobalt. *Catalysis Today* **259**, 192–196 (2016).
48. Paredes-Nunez, A., Lorito, D., Guilhaume, N., Mirodatos, C., Schuurman, Y. & Meunier, F. C. Nature and reactivity of the surface species observed over a supported cobalt catalyst under CO/H<sub>2</sub> mixtures. *Catalysis Today* **242**, 178–183 (2015).
49. Schweicher, J., Bundhoo, A., Frennet, A., Kruse, N., Daly, H. & Meunier, F. C. DRIFTS/MS studies during chemical transients and SSITKA of the CO/H<sub>2</sub> reaction over Co-MgO catalysts. *Journal of Physical Chemistry C* **114**, 2248–2255 (2010).

50. Gonugunta, P., Dugulan, A. I., Bezemer, G. L. & Brück, E. Role of surface carboxylate deposition on the deactivation of cobalt on titania Fischer-Tropsch catalysts. *Catalysis Today* **369**, 144–149 (2020).
51. Chen, T., Feng, Z., Wu, G., Shi, J., Ma, G., Ying, P. & Li, C. Mechanistic studies of photocatalytic reaction of methanol for hydrogen production on Pt/TiO<sub>2</sub> by in situ fourier transform IR and time-resolved IR spectroscopy. *Journal of Physical Chemistry C* **111**, 8005–8014 (2007).
52. Coates, J. in *Encyclopedia of analytical chemistry: applications, theory and instrumentation* (ed. Meyers, R. A.) 10815–10837 (John Wiley & Sons, New York, 2006).
53. Burghgraef, H., Jansen, A. P. J. & van Santen, R. A. Methane activation and dehydrogenation on nickel and cobalt: a computational study. *Surface Science* **324**, 345–356 (1995).
54. Dong, S., Padmakumar, R., Banerjee, R. & Spiro, T. G. Co-C force constants from resonance Raman spectra of alkylcobalamins: Insensitivity to dimethylbenzylimidazole coordination. *Inorganica Chimica Acta* **270**, 392–398 (1998).
55. Crocker, M., Herold, R. H. M., Wilson, A. E., Mackay, M., Emeis, C. A. & Hoogendoorn, A. M. <sup>1</sup>H NMR spectroscopy of titania: Chemical shift assignments for hydroxy groups in crystalline and amorphous forms of TiO<sub>2</sub>. *Journal of the Chemical Society Faraday Transactions* **92**, 2791–2798 (1996).
56. Lin, W. & Frei, H. Photochemical and FT-IR probing of the active site of hydrogen peroxide in Ti silicalite sieve. *Journal of the American Chemical Society* **124**, 9292–9298 (2002).
57. Yang, C. & Wöll, C. IR spectroscopy applied to metal oxide surfaces: adsorbate vibrations and beyond. *Advances in Physics: X* **2**, 373–408 (2017).
58. Powell, C. D., Daigh, A. W., Pollock, M. N., Chandler, B. D. & Pursell, C. J. Co adsorption on Au/TiO<sub>2</sub> Catalysts: Observations, quantification, and explanation of a broad-band infrared signal. *Journal of Physical Chemistry C* **121**, 24541–24547 (2017).
59. Martin, O., Mondelli, C., Cervellino, A., Ferri, D., Curulla-ferrø, D. & Pørez-ramírez, J. Heterogeneous Catalysis Operando Synchrotron X-ray Powder Diffraction and Modulated-Excitation Infrared Spectroscopy Elucidate the CO<sub>2</sub> Promotion on a Commercial Methanol Synthesis Catalyst. *Angewandte Chemie International Edition* **55**, 11031–11036 (2016).
60. Hasan, M. A., Zaki, M. I. & Pasupulety, L. Oxide-catalyzed conversion of acetic acid into acetone: An FTIR spectroscopic investigation. *Applied Catalysis A: General* **243**, 81–92 (2003).
61. Xiong, H., Zhang, Y., Liew, K. & Li, J. Fischer-Tropsch synthesis: The role of pore size for Co/SBA-15 catalysts. *Journal of Molecular Catalysis A: Chemical* **295**, 68–76 (2008).
62. Chen, W., Zijlstra, B., Pilot, I. A. W., Pestman, R. & Hensen, E. J. M. Mechanism of Carbon Monoxide Dissociation on a Cobalt Fischer-Tropsch Catalyst. *ChemCatChem* **10**, 136–140 (2018).
63. Cats, K. H. & Weckhuysen, B. M. Combined Operando X-ray Diffraction/Raman Spectroscopy of Catalytic Solids in the Laboratory: The Co/TiO<sub>2</sub> Fischer-Tropsch Synthesis Catalyst Showcase. *ChemCatChem* **8**, 1531–1542 (2016).
64. Chuang, S. S. C., Stevens, R. W. & Khatri, R. Mechanism of C<sub>2+</sub> oxygenate synthesis on Rh catalysts. *Topics in Catalysis* **32**, 225–232 (2005).
65. Visconti, C. G., Lietti, L., Tronconi, E., Forzatti, P., Zennaro, R. & Finocchio, E. Fischer-Tropsch synthesis on a Co/Al<sub>2</sub>O<sub>3</sub> catalyst with CO<sub>2</sub> containing syngas. *Applied Catalysis A: General* **355**, 61–68 (2009).
66. Maitlis, P. M. & Zanotti, V. The role of electrophilic species in the Fischer-Tropsch reaction. *Chemical Communications* **13**, 1619–1634 (2009).



67. Martínez Tejada, L. M., Muñoz, A., Centeno, M. A. & Odriozola, J. A. In-situ Raman spectroscopy study of Ru/TiO<sub>2</sub> catalyst in the selective methanation of CO. *Journal of Raman Spectroscopy* **47**, 189-197 (2016).
68. Tsakoumis, N. E., Rønning, M., Borg, Ø., Rytter, E. & Holmen, A. Deactivation of cobalt based Fischer-Tropsch catalysts: A review. *Catalysis Today* **154**, 162-182 (2010).
69. Keyvanloo, K., Fisher, M. J., Hecker, W. C., Lancee, R. J., Jacobs, G. & Bartholomew, C. H. Kinetics of deactivation by carbon of a cobalt Fischer-Tropsch catalyst: Effects of CO and H<sub>2</sub> partial pressures. *Journal of Catalysis* **327**, 33-47 (2015).
70. van Ravenhorst, I. K., Vogt, C., Oosterbeek, H., Bossers, K. W., Moya-Cancino, J. G., van Bavel, A. P., van der Eerden, A. M. J., Vine, D., de Groot, F. M. F., Meirer, F. & Weckhuysen, B. M. Capturing the Genesis of an Active Fischer-Tropsch Synthesis Catalyst with Operando X-ray Nanospectroscopy. *Angewandte Chemie International Edition* **57**, 11957-11962 (2018).
71. Nowak, D., Morrison, W., Wickramasinghe, H. K., Jahng, J., Potma, E., Wan, L., Ruiz, R., Albrecht, T. R., Schmidt, K., Frommer, J., Sanders, D. P. & Park, S. Nanoscale chemical imaging by photoinduced force microscopy. *Science Advances* **2**, e1501571 (2016).
72. Jackson, D., Thomson, S. J. & Webb, G. Carbonaceous deposition associated with the catalytic steam-reforming of hydrocarbons over nickel alumina catalysts. *Journal of Catalysis* **70**, 249-263 (1981).
73. Palumbo, L., Bonino, F., Beato, P., Bjørgen, M., Zecchina, A. & Bordiga, S. Conversion of methanol to hydrocarbons: Spectroscopic characterization of carbonaceous species formed over H-ZSM-5. *Journal of Physical Chemistry C* **112**, 9710-9716 (2008).
74. Bleken, F. L., Barbera, K., Bonino, F., Olsbye, U., Lillerud, K. P., Bordiga, S., Beato, P., Janssens, T. V. W. & Svelle, S. Catalyst deactivation by coke formation in microporous and desilicated zeolite H-ZSM-5 during the conversion of methanol to hydrocarbons. *Journal of Catalysis* **307**, 62-73 (2013).
75. Park, J. W. & Seo, G. IR study on methanol-to-olefin reaction over zeolites with different pore structures and acidities. *Applied Catalysis A: General* **356**, 180-188 (2009).
76. Lazar, G., Zellama, K., Vascan, I., Stamate, M., Lazar, I. & Rusu, I. Infrared absorption properties of amorphous carbon films. *Journal of Optoelectronics and Advanced Materials* **7**, 647-652 (2005).
77. Kaufman, J. H., Metin, S. & Saperstein, D. D. Symmetry breaking in nitrogen-doped amorphous carbon: Infrared observation of the Raman-active G and D bands. *Physical Review B* **39**, 13053-13060 (1989).
78. Sánchez-López, J. C., Donnet, C., Lefèbvre, F., Fernández-Ramos, C. & Fernández, A. Bonding structure in amorphous carbon nitride: A spectroscopic and nuclear magnetic resonance study. *Journal of Applied Physics* **90**, 675-681 (2001).
79. Jahng, J., Potma, E. O. & Lee, E. S. Nanoscale spectroscopic origins of photoinduced tip-sample force in the midinfrared. *Proceedings of the National Academy of Sciences of the United States of America* **116**, 26359-26366 (2019).
80. Hernandez, E. D., Jentoft, F. C., Hernandez, E. D. & Jentoft, F. C. Spectroscopic Signatures Reveal Cyclopentenyl Cation Contributions in Methanol-to-Olefins Catalysis. *ACS Catalysis* **10**, 5764-5782 (2020).
81. Gómez Bernal, H., Cedeño Caero, L., Finocchio, E. & Busca, G. An FT-IR study of the adsorption and reactivity of tert-butyl hydroperoxide over oxide catalysts. *Applied Catalysis A: General* **369**, 27-35 (2009).

82. Busca, G., Ramis, G., Lorenzelli, V., Janin, A. & Lavalley, J. C. FT-i.r. study of molecular interactions of olefins with oxide surfaces. *Spectrochimica Acta Part A: Molecular Spectroscopy* **43**, 489–496 (1987).
83. Han, W. Supported Homogeneous Catalysts on Flat Model Surfaces for Ethylene Polymerization **9789038608969**, (Technical University of Eindhoven, Eindhoven, 2007).
84. Guisnet, M. & Magnoux, P. Organic chemistry of coke formation. *Applied Catalysis A: General* **212**, 83–96 (2001).
85. Byrn, M. & Calvin, M. Oxygen-18 Exchange Reactions of Aldehydes and Ketones. *Journal of the American Chemical Society* **88**, 1916–1922 (1966).
86. NIST. Water - the NIST Webbook. <https://webbook.nist.gov/cgi/inchi?ID=C7732185&Type=IR-SPEC&Index=0> (2022).
87. Peña, D., Griboval-Constant, A., Lancelot, C., Quijada, M., Visez, N., Stéphan, O., Lecocq, V., Diehl, F. & Khodakov, A. Y. Molecular structure and localization of carbon species in alumina supported cobalt Fischer-Tropsch catalysts in a slurry reactor. *Catalysis Today* **228**, 65–76 (2014).
88. Weststrate, C. J., Ciobîcă, I. M., Saib, A. M., Moodley, D. J. & Niemantsverdriet, J. W. Fundamental issues on practical Fischer-Tropsch catalysts: How surface science can help. *Catalysis Today* **228**, 106–112 (2014).
89. Weststrate, C. J., Kazalkaya, A. C., Rossen, E. T. R., Verhoeven, M. W. G. M., Ciobîcă, I. M., Saib, A. M. & Niemantsverdriet, J. W. Atomic and polymeric carbon on Co(0001): Surface reconstruction, graphene formation, and catalyst poisoning. *Journal of Physical Chemistry C* **116**, 11575–11583 (2012).



This Chapter is based on the following scientific article:

ten Have, I. C., Kromwijk, J. J.G., Monai, M., Ferri, D., Sterk, E. B., Meirer, F., Weckhuysen B. M. (2022). Uncovering the Reaction Mechanism behind CoO as Active Phase in CO<sub>2</sub> Hydrogenation, *Nature Communications* 13, 324.

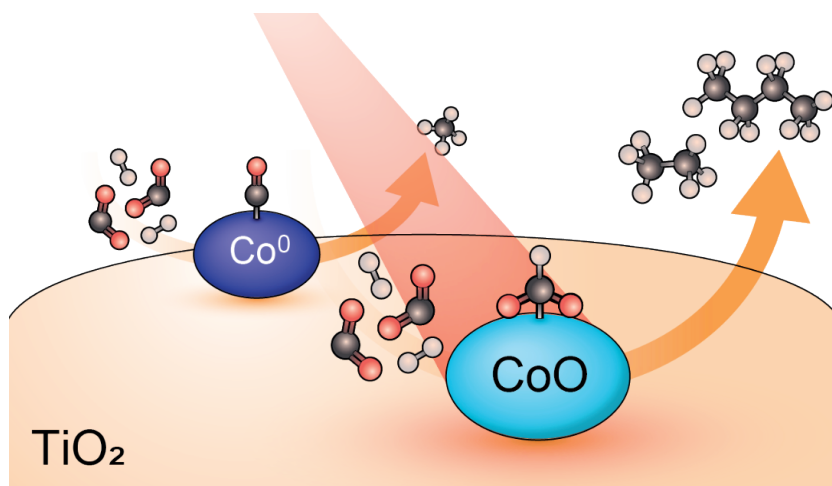
# **CHAPTER 4**

**THE REACTION MECHANISM BEHIND  
COBALT OXIDE AS ACTIVE PHASE FOR  
THE CATALYTIC HYDROGENATION OF CO<sub>2</sub>**



## Abstract

Transforming carbon dioxide into valuable chemicals and fuels is a promising tool for environmental and industrial purposes. In this **Chapter**, we present solid catalysts comprising of cobalt (oxide) nanoparticles stabilized on various support oxides for hydrocarbon production from carbon dioxide and hydrogen. When heated in hydrogen, the support oxides displayed an increasing reducibility in the order of  $\text{SiO}_2 < \text{Al}_2\text{O}_3 < \text{TiO}_2 < \text{CeO}_2$ . We demonstrate that the activity and selectivity during the catalytic hydrogenation of  $\text{CO}_2$  over supported cobalt (oxide) catalysts can be tuned by selection of the support oxide as well as by fine-tuning the cobalt oxidation state. Modulation excitation-diffuse reflectance infrared Fourier transform spectroscopy (ME DRIFTS) revealed that cobalt oxide-based catalyst materials followed the hydrogen-assisted pathway, whereas metallic cobalt-based catalyst materials mainly followed the direct dissociation pathway.  $\text{TiO}_2$  support appeared optimal in terms of reducibility, as  $\text{Co}/\text{TiO}_2$  system was the most active catalyst in both cobalt oxide and metallic cobalt state. Most catalyst materials displayed a high selectivity towards methane (84-97%), apart from  $\text{Co}/\text{Al}_2\text{O}_3$  in metallic state, which produced 61% CO. In terms of selectivity towards  $\text{C}_{2+}$  hydrocarbons, the cobalt oxide variant of  $\text{Co}/\text{Al}_2\text{O}_3$  and  $\text{Co}/\text{TiO}_2$  performed best with 10 and 11%, respectively. Contrary to the commonly considered metallic active phase of cobalt-based catalysts, cobalt oxide on titania support was the most active catalyst and produced 11%  $\text{C}_{2+}$  hydrocarbons. The  $\text{C}_{2+}$  selectivity increased to 39% (yielding  $104 \text{ mmol} \cdot \text{h}^{-1} \cdot \text{g}_{\text{cat}}^{-1}$   $\text{C}_{2+}$  hydrocarbons) upon co-feeding CO and  $\text{CO}_2$  at a ratio of 1:2 at  $250^\circ\text{C}$  and 20 bar, thus outperforming the majority of typical cobalt-based catalysts.



## 4.1 Introduction

With rising CO<sub>2</sub> levels in the atmosphere leading to climate change, it is of high interest to investigate methods to reduce the amount of anthropogenically emitted CO<sub>2</sub>. A transition towards a greener energy mix and to more sustainable processes for chemical production is on the way, but it will require years or perhaps even decades and huge investments to permeate the market. Moreover, some sectors intrinsically emit CO<sub>2</sub> (e.g., cement industry). Carbon capture and storage (CCS) and carbon capture and utilization (CCU) can be used to help curb persisting CO<sub>2</sub> emissions<sup>1-3</sup>. CCS is an efficient strategy to cut CO<sub>2</sub> emissions and store carbon in geological formations, but this technology is energy intensive and expensive<sup>4</sup>. Therefore, CCU is a more attractive and promising option<sup>1</sup>. Captured CO<sub>2</sub> can be used as a renewable resource to produce e.g., long-chain hydrocarbons, which can be used as transportation fuels. However, due to the thermodynamic stability of CO<sub>2</sub> the use of this greenhouse gas as a chemical feedstock is currently limited to a small number of industrial processes. For instance, the synthesis of urea and its derivatives, salicylic acid and carbonates<sup>5</sup>, as well as more recently to the synthesis of methane in Power-to-Methane (PtM) plants<sup>6</sup>. Another example is the methanol synthesis process, in which CO/CO<sub>2</sub>/H<sub>2</sub> mixtures are converted to methanol with a Cu/ZnO/Al<sub>2</sub>O<sub>3</sub> catalyst<sup>7,8</sup>. Several approaches, like the photochemical<sup>9</sup>, electrochemical<sup>10-12</sup>, and thermochemical<sup>13-17</sup> conversion of CO<sub>2</sub> into more valuable long-chain hydrocarbons, have been investigated. However, up to now only thermochemical CO<sub>2</sub> conversion has been proven to produce hydrocarbons longer than methane at high conversion yields<sup>14,15</sup>, although Cu is known to electrochemically produce ethanol and ethylene<sup>10,18,19</sup>. Several catalyst materials, mainly based on Ni, Fe, Ru, Rh, Pt, and Pd, have been investigated, but most of them produce mainly methane, as is the case for Ni<sup>20-23</sup>. Creating reaction products with longer hydrocarbon chains than methane is beneficial because they store more energy<sup>24</sup> and are easier to transport off-grid compared to gaseous methane. Creating long-chain hydrocarbons from CO<sub>2</sub> is thus a promising pathway towards a circular economy and will be useful in the next decade to produce, for example, fuels for aviation and for diesel engines.

As discussed in detail in **Chapter 1**, cobalt is an interesting candidate to investigate, since it has high C-C coupling activity in the similar CO hydrogenation reaction. This industrial process, better known as the Fischer-Tropsch Synthesis (FTS), converts CO and H<sub>2</sub> into e.g., fuels and chemicals with iron- or cobalt-based heterogeneous catalysts<sup>25</sup>. Iron generally produces lower olefins and oxygenates, whereas cobalt produces mainly long-chain paraffins. There are several parameters that influence the performance of FTS catalyst materials. For the cobalt-based FTS, the optimum cobalt nanoparticle size has been reported to be between 6-10 nm<sup>26-28</sup>. For nanoparticles smaller than 6 nm, the activity is generally lower and the selectivity towards CH<sub>4</sub>, an unwanted product in

the FTS, is higher. For catalyst materials with cobalt nanoparticles larger than 10 nm, the turnover frequencies (TOFs) were comparable to catalyst materials with 6-10 nm particles. For catalytic CO<sub>2</sub> hydrogenation, it has been reported that 10 nm cobalt particles display higher TOFs compared to 3 and 7 nm particles<sup>29</sup>. Besides nanoparticle size, the cobalt oxidation state, the cobalt phase, and the support oxide used to stabilize the metal nanoparticles greatly influence the activity and selectivity of the resulting catalyst<sup>30,31</sup>. CoO/TiO<sub>2</sub> has for example been reported to be more active in CO and CO<sub>2</sub> hydrogenation compared to its metallic equivalent<sup>32-34</sup>. However, Co/SiO<sub>2</sub> was found to be more active with metallic cobalt<sup>32</sup>. In another study, it was found that Co/Al<sub>2</sub>O<sub>3</sub> converted CO<sub>2</sub> into ethanol with high selectivity due to co-existing Co and CoO phases<sup>35</sup>. Moreover, a well-balanced coexistence of Co and CoO on SiO<sub>2</sub> support, with cobalt phyllosilicate structure, has also been reported to exhibit high methanol selectivity in the CO<sub>2</sub> hydrogenation reaction<sup>36</sup>. Recently, Parastaev *et al.* were able to improve the CO<sub>2</sub> methanation activity of Co/CeO<sub>2</sub> by tuning the calcination temperature to create optimal metal-support interactions<sup>37</sup>.

Elucidating the reaction mechanisms for hydrocarbon production from CO<sub>2</sub> remains elusive due to the complexity of the process and the large number of species involved.<sup>2,38,39</sup> For FTS catalysts, such as Co, a two-step process has been proposed: CO<sub>2</sub> is first converted to CO *via* the reverse water-gas-shift (RWGS) and then transformed into hydrocarbons through FTS.<sup>39</sup> Several mechanisms have been suggested for the RWGS and FTS individually, but most likely it is the nature of the catalyst that determines which of the pathways is dominant. For the RWGS, the direct dissociation pathway (also known as the redox or carbide mechanism) and the hydrogen(H)-assisted pathway (also known as the associative or formate mechanism) have been proposed.<sup>2,38</sup> The direct dissociation is facilitated by adsorbed CO as intermediate, whereas the H-assisted pathway is enabled by carbonate, formate, and formyl intermediates.<sup>2,38</sup> These intermediates can either be fully hydrogenated to form methane or they can undergo chain propagation *via* the FTS to form long-chain hydrocarbons, like paraffins and olefins. To investigate this, infrared (IR) spectroscopy is a promising tool for mechanistic studies,<sup>2,40</sup> as it can probe the molecular vibrations of surface intermediates and active species. Nevertheless, mechanistic investigations remain challenging owing to sensitivity limitations of analytical tools, especially under relevant reaction conditions.

In this **Chapter**, the influence of both reducible (*i.e.*, TiO<sub>2</sub> and CeO<sub>2</sub>) and non-reducible (*i.e.*, SiO<sub>2</sub> and Al<sub>2</sub>O<sub>3</sub>) metal oxide supports and the effect of the cobalt oxidation state (CoO *versus* metallic Co) were investigated. Catalytic tests showed that metallic Co was typically more active than CoO, except for Co/TiO<sub>2</sub>. Besides, CoO possessed less hydrogenation ability than metallic Co, resulting in the formation of C<sub>2+</sub> olefins rather



than C<sub>2+</sub> paraffins. Using *operando* modulation excitation-diffuse reflectance infrared Fourier transform spectroscopy (ME DRIFTS) with phase-sensitive detection (PSD) we observed that CoO catalysts followed the H-assisted pathway, whereas metallic Co catalyst materials followed the direct dissociation pathway. Co/TiO<sub>2</sub> was the most active catalyst in both oxidized and reduced state. For reduced Co/TiO<sub>2</sub>, this was explained based on the red shift of the CO<sub>ads</sub> peak by 14 cm<sup>-1</sup>, indicating a weaker C-O bond when changing from Co/SiO<sub>2</sub> to Co/TiO<sub>2</sub>. In the case of the most active catalyst, CoO/TiO<sub>2</sub>, the C<sub>2+</sub> selectivity could be improved from 11% to 39% upon co-feeding CO:CO<sub>2</sub> at a ratio of 1:2 - this led to a high overall C<sub>2+</sub> yield of 104 mmol h<sup>-1</sup> g<sub>cat</sub><sup>-1</sup> at 17.5% carbon conversion, T=250°C, P=20 bar, and a gas hourly space velocity (GHSV) of 3000 h<sup>-1</sup>.

## 4.2 Materials and Methods

# 4

### 4.2.1. Catalyst Synthesis

Cobalt-based catalyst materials with a loading of ~10 wt.% were prepared *via* incipient wetness impregnation (IWI) using SiO<sub>2</sub>, TiO<sub>2</sub>, Al<sub>2</sub>O<sub>3</sub>, and CeO<sub>2</sub> as support oxide materials. All support oxides were purchased from companies (Table 4.1), apart from CeO<sub>2</sub>, which was synthesized in-house by homogeneous deposition precipitation (HDP) using urea as a precipitation agent. In 1.7 L of deionized water, 50 g cerium (III) nitrate hexahydrate (99.99% trace metals basis, Sigma-Aldrich) and 27 g of urea were dissolved. The mixture was added to a double-walled glass vessel and heated to 90°C for ~20 h while stirring at 600 rpm. The sample was washed three times with 500 mL deionized water, dried at 60°C, and then at 120°C. Calcination was performed at 500°C for 2 h (5°C min<sup>-1</sup> ramp). The aqueous metal precursor solution (Co(NO<sub>3</sub>)<sub>2</sub>·6H<sub>2</sub>O; Sigma-Aldrich, 99.999% trace metal basis), with a volume equal to the pore volume of the support, was added to the support material under vacuum and continuous stirring. The CeO<sub>2</sub> sample was prepared in two steps, as the solubility of Co(NO<sub>3</sub>)<sub>2</sub>·6H<sub>2</sub>O was not sufficient to dissolve in a volume of water equal to the pore volume of the CeO<sub>2</sub> support. The resulting powder was dried in an oven at 60°C overnight. Subsequently, the samples were calcined at 250°C for 2 h (heating ramp of 5°C min<sup>-1</sup>) in a tube furnace in a N<sub>2</sub> flow of 100 mL min<sup>-1</sup>.

### 4.2.2. Catalyst Characterization

The Brunauer-Emmett-Teller (BET) surface areas and pore volumes of the support materials under study were determined from N<sub>2</sub> adsorption-desorption isotherms measured at -196°C using a Micromeritics TriStar II PLUS instrument. Prior to the physisorption measurements, the samples were dried at 300°C overnight in N<sub>2</sub> flow.

Transmission electron microscopy (TEM) was performed with a FEI Talos F200X instrument. The TEM samples were prepared suspending the catalyst materials in absolute ethanol using sonication. Consequently, the suspension was drop-casted on a carbon/formvar-coated Cu grid (200 mesh). The microscope was operated at 200 kV and equipped with a high-brightness field emission gun (X-FEG) and a Super-X G2 energy dispersive X-ray (EDX) detector. The samples were analyzed with scanning (S) TEM combined with high-angle annular dark-field (HAADF-STEM). To determine the average cobalt particle size, the STEM images were analyzed using the ImageJ software.

X-ray diffraction (XRD) was performed using a Bruker D2 phaser instrument equipped with a Co radiation source ( $\lambda = 1.789 \text{ \AA}$ ). The XRD patterns of calcined and spent catalysts were recorded between  $5$  and  $85^\circ 2\theta$  with an increment of  $0.05^\circ$  and  $1 \text{ s/step}$ . The average cobalt crystallite size was calculated from the peak at  $43^\circ$  using the Bruker EVA software.

$\text{H}_2$ -temperature programmed reduction (TPR) measurements were performed using a Micromeritics AutoChem II 2920. Samples were placed on quartz wool into a U-tube quartz reactor. The gas mixture consisted of  $5\% \text{ H}_2$  in Ar with a total gas flow of  $40 \text{ ml min}^{-1}$ .  $\text{H}_2$ -TPR was carried out by heating with  $5^\circ\text{C min}^{-1}$  up to  $1000^\circ\text{C}$  for all cobalt-based catalysts and held for  $30 \text{ min}$  at this temperature. A constant initial sample weight of  $0.05 \text{ g}$  was used and  $\text{H}_2$  consumption was continuously monitored by a thermal conductivity detector. To assess reducibility, a centroid was calculated for each data set. This was done by calculating the integral (MATLAB) of the  $\text{H}_2$ -TPR data for each sample and then taking  $\frac{1}{2}$  of that.

$\text{CO}_2$  temperature programmed desorption (TPD) measurements were carried out on a Micromeritics ASAP2920 instrument equipped with a thermal conductivity detector (TCD). In a typical experiment,  $100 \text{ mg}$  of sample ( $\text{SiO}_2$ ,  $\text{Al}_2\text{O}_3$ ,  $\text{TiO}_2$ , or  $\text{CeO}_2$ ; see **Table 4.1** for details) was loaded in a quartz tube and dried *in situ* by ramping with  $5^\circ\text{C min}^{-1}$  to  $300^\circ\text{C}$  in a He flow and remained at that temperature for  $60 \text{ min}$ . Subsequently, the sample was cooled down to  $60^\circ\text{C}$ ; at this temperature pulses of  $10\% \text{ CO}_2$  in He of  $25 \text{ cm}^3 \text{ min}^{-1}$  were applied. After saturation with  $\text{CO}_2$ , the sample was outgassed for  $30 \text{ min}$  at  $60^\circ\text{C}$  to ensure removal of physisorbed  $\text{CO}_2$ . Finally, the sample was heated to  $700^\circ\text{C}$  with a ramp of  $5^\circ\text{C min}^{-1}$  to measure  $\text{CO}_2$  desorption. To assess support basicity, the integral of the  $\text{CO}_2$ -TPD data was calculated for each data set and divided by the BET surface area of the respective sample.

### 4.2.3. Density Functional Theory Calculations

Quantum-chemical calculations were performed using a planewave density function theory (DFT) approach with the projector-augmented wave (PAW) method<sup>41,42</sup> in conjunction with a Perdew-Becke-Ernzerhof (PBE) exchange-correlation functional<sup>43</sup> as implemented in Vienna Ab-initio Simulation Package (VASP)<sup>44,45</sup>. The kinetic energy cutoff for the plane wave basis set was 400 eV. For all calculations spin polarization was considered explicitly. A conventional fcc-Co and fcc-CoO unit cell was used to build the surface terminations. Herein, the bulk lattice constant of Co and CoO in their face-centered cubic crystal (fcc) structure was optimized yielding a theoretical optimum of 3.34 Å and 4.265 Å respectively. These values correspond well to the documented bulk lattice constant of 3.42 Å for Co and 4.260 Å for CoO<sup>46,47</sup>.

The Co(111), Co(110) and CoO(100) surfaces were modeled using a (3x3) surface, with 6, 4 and 6 metal layers, respectively. A Monkhorst-Pack mesh of k-points of (5x5x1) for Co(110) and (3x3x1) for Co(111) and CoO(100) were used<sup>48</sup>. A vacuum layer of 15 Å perpendicular to the surface was employed to avoid the spurious interaction of neighboring supercells. To avoid the build-up of a large dipole moment between neighboring supercells, the adsorbates were placed on both sides of the surface slabs retaining a point of inversion. All atoms were allowed to relax. Partial occupancies were determined using a first-order Methfessel-Paxton scheme with a smearing width of 0.2 eV and 0.03 eV for the Co and CoO slabs, respectively<sup>49</sup>. Electronic convergence was set to 10<sup>-5</sup> eV, and geometries were converged to 10<sup>-4</sup> eV using a conjugant gradient algorithm for the Co systems and a quasi-Newton algorithm for CoO system. For the gas-phase calculation of CO<sub>2</sub>, the molecule was placed in a 10x10x10 Å unit cell. Gaussian smearing with a width of 2x10<sup>-5</sup> eV was used for electron smearing and only the gamma-point was used to sample the Brillouin zone.

The adsorption energy,  $E_{\text{ads}}$ , is defined as follows:

$$E_{\text{ads}} = E_{\text{slab+adsorbate}} - E_{\text{slab}} - E_{\text{adsor}} \quad (\text{Equation 4.1})$$

where  $E_{\text{slab+adsorbate}}$  represents the total energy of the optimized adsorbate on the surface,  $E_{\text{slab}}$  is the energy of the nickel slab and  $E_{\text{adsorbate}}$  is the energy of the adsorbate in the gas phase. The total density of states was calculated in the energy range of -30 eV to 15 eV over 4500 grid points. Then, the partial charge density corresponding to the energy interval of each molecular orbital was calculated. The contour plots of the electron density from these intervals were plotted on a cutting plane running parallel through CO<sub>2</sub> adsorbed on the top of the slab.

#### 4.2.4. Catalyst Testing

Catalyst performance testing at 20 bar for 10 h was carried using in-house built high-pressure set-up. A steel reactor was filled with 200 mg of catalyst sample sieved to a grain size of 150-450  $\mu\text{m}$ . The sample was plugged between two quartz wool plugs. The reactor was placed in an oven and connected to the gas inlet and outlet. A back-pressure controller (BPC) was incorporated in the gas line connected to the outlet to maintain a defined pressure. An on-line gas Thermo Fischer Trace 1300 gas chromatograph (GC) was used for product analysis. The GC was injected with 1  $\mu\text{L}$  of the reactor outlet stream every 23 min. The sample was heated to either 250°C for CoO catalysts or 450°C for metallic Co catalysts with a 10°C  $\text{min}^{-1}$  ramp in a 10:20  $\text{mL min}^{-1}$   $\text{H}_2/\text{N}_2$  flow and held at that temperature for 1 h. After the reduction step, the sample was cooled to 250°C with a 10°C  $\text{min}^{-1}$  ramp. At this temperature, the gas flow was switched to 2:36:12  $\text{mL min}^{-1}$   $\text{Ar}/\text{H}_2/\text{CO}_2$  (GHSV=3000  $\text{h}^{-1}$ ) and once the gasses were flowing, pressure was built up to 20 bar with a 1 bar  $\text{min}^{-1}$  ramp. The  $\text{CO}_2$  conversion and product selectivities were calculated from the following relationships:

$$X_{\text{CO}_2} (\%) = \left(1 - \frac{A_{\text{CO}_2}/A_{\text{Ar}}}{A_{\text{CO}_2}^0/A_{\text{Ar}}^0}\right) * 100\% \quad (\text{Equation 4.2})$$

$A_{\text{CO}_2}$  and  $A_{\text{Ar}}$  represent the thermal conductivity detector (TCD) peak area of  $\text{CO}_2$  and Ar during the reaction.  $A_{\text{CO}_2}^0$  and  $A_{\text{Ar}}^0$  are the TCD peak areas of  $\text{CO}_2$  and Ar recorded during a blank measurement. The selectivity was calculated using **Equation 4.3**.

$$S_i (\%) = \left(\frac{A_i * F_i}{\sum_{n=1}^{\infty} A_n * F_n}\right) * 100\% \quad (\text{Equation 4.3})$$

In this equation,  $A_i$  corresponds to the peak area of product  $i$  and  $F_i$  represents the response factor of the analyte<sup>50</sup>. To describe the catalytic activity, cobalt-time-yield (CTY) was used. This parameter reports the amount of  $\text{CO}_2$  converted in mol per gram of cobalt per second. The parameter yield was used to describe the amounts of specific products obtained. This was reported either in mol of product per gram of cobalt per second or in (m)mol per hour per gram of catalyst.

The kinetic parameters reaction order ( $n$ ,  $m$ ) and apparent activation energy ( $E_a$ ) were determined by varying the reactant ( $\text{CO}_2$ ,  $\text{H}_2$ ) concentration and the temperature, respectively. The catalyst was either pre-treated at 250°C in  $\text{H}_2$  for 1 h to obtain the CoO

phase (Co/TiO<sub>2</sub>-ox) or at 450°C in H<sub>2</sub> for 1 h to obtain the metallic Co phase (Co/TiO<sub>2</sub>-red). Then, at  $T=250^{\circ}\text{C}$  and  $P=20$  bar, the H<sub>2</sub>/CO<sub>2</sub> ratio was varied at 2, 3, and 4 while the H<sub>2</sub> concentration was kept constant and the H<sub>2</sub>/CO<sub>2</sub> ratio was varied at 2 and 3 while the CO<sub>2</sub> concentration was kept constant. This was repeated three times in order to obtain standard deviations. The measured intrinsic reaction rates were used to calculate the reaction order ( $n$ ) in CO<sub>2</sub> and ( $m$ ) in H<sub>2</sub> according to the rate law (Equation 4.4)<sup>53</sup>, where  $k$  is the rate constant,  $n$  the reaction order in CO<sub>2</sub>, and  $m$  the reaction order in H<sub>2</sub>. Besides, the temperature was varied between 200 and 280°C at  $P=20$  bar and the measured intrinsic rates were used to calculate the apparent activation energy ( $E_a$ ) according to the Arrhenius equation (Equation 4.5)<sup>53</sup>, where  $k$  is the rate constant,  $A$  is the pre-exponential factor,  $R$  the universal gas constant, and  $T$  the absolute temperature in Kelvin.

$$\text{rate} = k[\text{CO}_2]^n[\text{H}_2]^m \quad (\text{Equation 4.4})$$

$$k = Ae^{-E_a/RT} \quad (\text{Equation 4.5})$$

Finally, thermodynamic calculations were performed using the software HSC 9.6.1, in the Gem equilibrium composition module, based on Gibbs free energy minimization<sup>54</sup>.

#### 4.2.5. Operando Modulation Excitation Infrared Spectroscopy

*Operando* modulation excitation diffuse reflectance infrared Fourier transform spectroscopy (ME DRIFTS) experiments were conducted on the set of cobalt-based catalyst materials. The samples were first sieved to a grain size of 63-250 μm and were firmly fixed in a 2 mm thick stainless-steel block, which acts as a sample holder using two quartz wool plugs<sup>51</sup>. The sample holder was closed using a CaF<sub>2</sub> window, to allow the reflection of IR radiation, and a graphite window. The inlet of the cell was connected to two solenoid valves (Series 9, Parker), allowing fast switching needed for the modulation excitation experiments. The outlet of the cell was connected to an on-line mass spectrometer (MS; Pfeiffer Vacuum Omnistar). The experiments were carried out with a Bruker Vertex70V Fourier Transform (FT)-IR spectrometer equipped with a liquid nitrogen cooled Mercury Cadmium Telluride (MCT) detector and a Harrick Praying Mantis unit. The samples were heated to 250°C at 10°C min<sup>-1</sup> in H<sub>2</sub>/N<sub>2</sub>=1. At this temperature 10 modulation periods were performed by alternating flows of CO<sub>2</sub>:H<sub>2</sub> at a ratio of 1:3 (60 s) and H<sub>2</sub> (60 s). During each period of 120 s, 120 spectra were recorded at 80 kHz scanner velocity and 4 cm<sup>-1</sup> resolution. The 10 modulation periods of 120s each resulted in a 20 min experi-

ment. After the modulation experiment, the sample was heated to 450°C at 10°C min<sup>-1</sup> in H<sub>2</sub>/N<sub>2</sub>=1 and was held for 1 h to reduce the metal oxide nanoparticles. Then, the sample was cooled to 250°C at 10°C min<sup>-1</sup> and the modulation experiment described above was repeated. After spectral acquisition, the sets of time-resolved data were treated by phase-sensitive detection (PSD)<sup>52</sup> to obtain phase-resolved data. Phase-resolved amplitude spectra were obtained by taking the absolute maxima at every single wavenumber.

## 4.3 Results and Discussion

### 4.3.1 Catalyst Characterization and Catalytic Performance

To investigate the dependence of activity and selectivity on the type of support oxide in the cobalt-based CO<sub>2</sub> hydrogenation reaction, we have compared cobalt nanoparticles supported on SiO<sub>2</sub>, Al<sub>2</sub>O<sub>3</sub>, TiO<sub>2</sub>, and CeO<sub>2</sub>. The physicochemical properties of the support materials, such as surface area and pore size, can be found in **Table 4.1**. To avoid interfering particle size effects on the activity, we have ensured that the average cobalt particle size was above 10 nm in all catalysts. The SiO<sub>2</sub>, Al<sub>2</sub>O<sub>3</sub>, and TiO<sub>2</sub>-supported catalyst materials contained cobalt particles of similar sizes (*i.e.*, 14–17 nm), whereas the CeO<sub>2</sub>-supported cobalt particles were larger (*i.e.*, 37 nm) (**Figure 4.1a–h**).

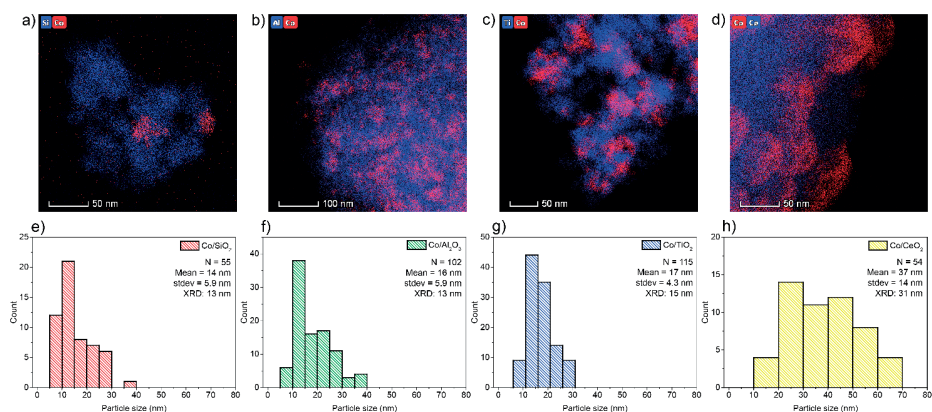


**Figure 4.1. Cobalt particle size analysis of the cobalt-based catalyst materials under study. a–d)** Energy dispersive X-ray (EDX) spectroscopy mapping of the calcined catalyst materials (250°C in N<sub>2</sub>) **a)** Co/SiO<sub>2</sub>, **b)** Co/Al<sub>2</sub>O<sub>3</sub>, **c)** Co/TiO<sub>2</sub>, and **d)** Co/CeO<sub>2</sub>. **e–h)** Cobalt oxide particle size distributions determined with transmission electron microscopy (TEM) and average crystallite sizes calculated based on X-ray diffraction (XRD) results for **e)** Co/SiO<sub>2</sub>, **f)** Co/Al<sub>2</sub>O<sub>3</sub>, **g)** Co/TiO<sub>2</sub>, and **h)** Co/CeO<sub>2</sub>.

**Table 4.1.** Support properties and amounts of precursor, support, and water used for incipient wetness impregnation catalyst synthesis.

Support material	Supplier	Purity	BET surface area (m <sup>2</sup> g <sup>-1</sup> )	Pore volume (cm <sup>3</sup> g <sup>-1</sup> )	Co(NO <sub>3</sub> ) <sub>2</sub> ·6H <sub>2</sub> O (g)	Support (g)	Water (mL)
SiO <sub>2</sub> (Davasil grade 643)	Sigma-Aldrich	≥99%	300	1.15	0.981	1.812	2.0
γ-Al <sub>2</sub> O <sub>3</sub>	CRI Catalyst Company	≥99%	262	1.03	0.949	1.818	2.0
TiO <sub>2</sub> (P25)	CRI Catalyst Company	≥99%	52.7	0.31	0.991	1.815	0.6
CeO <sub>2</sub>	n.a.	n.a.	88.5	0.06	0.949	1.792	0.3

It was found that all catalyst materials contained  $\text{Co}_3\text{O}_4$  after calcination, as determined with X-ray diffraction (XRD) (**Figure 4.2** and **Table 4.2**). Catalytic testing in a fixed bed reactor at  $T=250^\circ\text{C}$  and  $P=20$  bar was conducted using CoO (suffix: -ox) and metallic Co (suffix: -red) catalysts. Prior to testing, the indicated cobalt oxidation states were obtained by heating in 33 vol%  $\text{H}_2/\text{N}_2$  at  $250^\circ\text{C}$  for the CoO and  $450^\circ\text{C}$  for the metallic Co catalysts.  $\text{H}_2$ -temperature programmed reduction (TPR) was performed to assess the reducibility of all catalysts (**Figure 4.3a**) and  $\text{CO}_2$ -temperature programmed desorption (TPD) was used to determine the basicity of the support materials (**Figure 4.3b** and **Table 4.3**). In the  $\text{H}_2$ -TPR profiles (**Figure 4.3a**) the first peak is typically assigned to the reduction of  $\text{Co}_3\text{O}_4$  to CoO (@ $250\text{--}290^\circ\text{C}$ ), while the second peak is ascribed to the reduction of CoO to metallic Co (@ $300\text{--}420^\circ\text{C}$ )<sup>55</sup>. For  $\text{Co}/\text{Al}_2\text{O}_3$ , two other peaks were clearly visible at  $673$  and  $958^\circ\text{C}$ , which have been ascribed to cobalt aluminates species. Similarly, for  $\text{Co}/\text{SiO}_2$ , an additional peak was observed around at  $635^\circ\text{C}$ , which could indicate the reduction of cobalt silicates<sup>55,56</sup>. In the  $\text{CO}_2$ -TPD profiles (**Figure 4.3b**), different types of basic sites were identified: weak ( $<150^\circ\text{C}$ ), medium ( $150\text{--}350^\circ\text{C}$ ), and strong ( $>350^\circ\text{C}$ )<sup>57</sup>. The TPD peaks generally shift to higher temperature and increase in intensity when the basic sites become stronger and increase in quantity<sup>58</sup>. Both the non-reducible supports  $\text{SiO}_2$  and  $\text{Al}_2\text{O}_3$  were dominated by strong basic sites<sup>59</sup>, with their main desorption peaks at  $430^\circ\text{C}$  and  $393^\circ\text{C}$ , respectively. The reducible supports displayed different basic sites. For  $\text{TiO}_2$ , two peaks were observed: one at  $199^\circ\text{C}$ , which was assigned to bidentate carbonate decomposition from medium strength basic sites, and a smaller peak at  $390^\circ\text{C}$ , which was attributed to monodentate carbonate decomposition from strong basic sites. For  $\text{CeO}_2$ , we observed a peak at  $135^\circ\text{C}$ , ascribed to bidentate carbonate decomposition from weak-medium strength basic sites, and another peak at  $397^\circ\text{C}$ , interpreted as monodentate carbonate decomposition from strong basic sites<sup>57</sup>. The total amount of desorbed  $\text{CO}_2$  was estimated from the integral of the  $\text{CO}_2$ -TPD peak area. The  $\text{CO}_2$  surface density quantification was used as a measure for the basicity and increases from  $\text{SiO}_2 < \text{Al}_2\text{O}_3 < \text{CeO}_2 < \text{TiO}_2$  (**Table 4.3**), which is conform with earlier reports in the literature<sup>60,61</sup>. Though, some studies report that  $\text{CeO}_2$  was more basic compared to  $\text{TiO}_2$ <sup>62,63</sup>, it has also been reported that the basicity decreased with increasing calcination temperature of the metal oxide<sup>64</sup> and is consequently a more complex cohesion than just the chemical element.



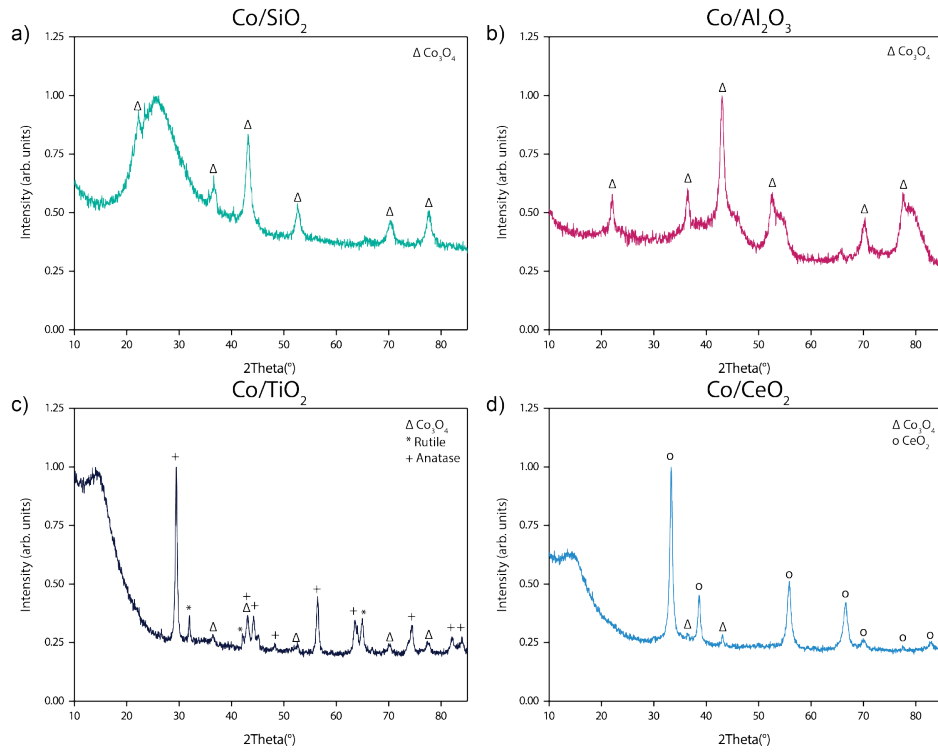


**Figure 4.2.** X-ray diffractograms (XRD) of the cobalt-based catalyst materials after calcination at 250°C in N<sub>2</sub> (a) Co/SiO<sub>2</sub>, (b) Co/Al<sub>2</sub>O<sub>3</sub>, (c) Co/TiO<sub>2</sub>, and (d) Co/CeO<sub>2</sub>.

**Table 4.2.** Average crystallite size of cobalt particles on various supported cobalt-based catalyst materials. The diffraction peak at 43° was used to determine the crystallite size using the Scherrer equation in the Bruker EVA software.

Catalyst	Cobalt phase	Average crystallite size (nm)
Co/SiO <sub>2</sub>	Co <sub>3</sub> O <sub>4</sub>	12.5
Co/Al <sub>2</sub> O <sub>3</sub>	Co <sub>3</sub> O <sub>4</sub>	13.2
Co/TiO <sub>2</sub>	Co <sub>3</sub> O <sub>4</sub>	14.6
Co/CeO <sub>2</sub>	Co <sub>3</sub> O <sub>4</sub>	30.7

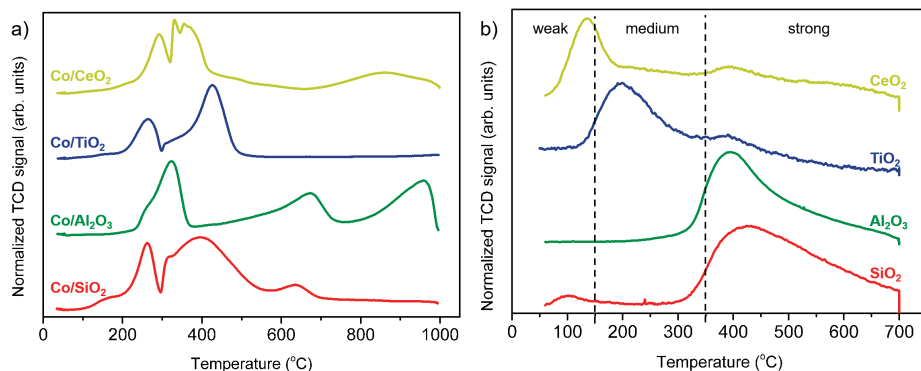


**Figure 4.3.** **a)** H<sub>2</sub>-temperature programmed reduction (TPR) profiles of the cobalt-based catalyst materials and **b)** CO<sub>2</sub>-temperature programmed desorption (TPD) profiles of the support materials used recorded with a thermal conductivity detector (TCD).

**Table 4.3.** Basicity of the support oxide materials, used in this Chapter as estimated from CO<sub>2</sub>-temperature programmed desorption (TPD) data.

Sample	CO <sub>2</sub> -TPD integral (arb. units)	Sample mass (g)	BET surface area (m <sup>2</sup> g <sup>-1</sup> )	Basicity (μmol CO <sub>2</sub> m <sup>-2</sup> )
SiO <sub>2</sub>	43.3	0.0980	300	9.1
Al <sub>2</sub> O <sub>3</sub>	107	0.1090	262	15
TiO <sub>2</sub>	85.7	0.0990	52.7	68
CeO <sub>2</sub>	71.4	0.1004	88.5	33

All catalyst materials under study displayed higher cobalt-time-yield (CTY) in their metallic state, except for Co/TiO<sub>2</sub>, which was more active in its CoO state (**Figure 4.4**). The CeO<sub>2</sub>-supported catalysts displayed a high selectivity towards methane (95-97%) in both metallic Co and CoO state. The SiO<sub>2</sub>-supported catalyst had slightly lower methane selectivities of 92 and 86% in metallic Co and CoO state, respectively. The other products were CO, as well as C<sub>2</sub> and C<sub>3</sub> hydrocarbons. Co/Al<sub>2</sub>O<sub>3</sub> mainly produced CO (61%) in metallic state and 10% C<sub>2+</sub> hydrocarbons in CoO state. Co/TiO<sub>2</sub> displayed the highest CTY in both metallic Co and CoO state. The Co/TiO<sub>2</sub>-ox catalyst was the most active catalyst in this Chapter with 11% selectivity to C<sub>2+</sub> hydrocarbons. The active phase in the cobalt-based FTS has been debated for almost a century. Classically, metallic cobalt is believed to be the active phase in the FTS process<sup>25</sup>. However, our results showed that CoO on the reducible TiO<sub>2</sub> support is more active than metallic Co. This is in accordance with a study by Melaet *et al.*<sup>32</sup>, where CoO/TiO<sub>2</sub> was more active than metallic Co for both CO and CO<sub>2</sub> hydrogenation. They have attributed the phenomena to an interface formed between CoO and TiO<sub>2</sub> and they mentioned that strong

metal-support interactions (SMSI), where TiO<sub>x</sub> species encapsulate some of the active sites, could have decreased the activity of the metallic Co/TiO<sub>2</sub> catalyst. The reaction mechanisms at play, and especially whether or not these are different for CoO and metallic Co, are yet to be elucidated. In the section below, we will uncover active species and reaction mechanisms for the set of cobalt-based catalyst materials under study by means of *operando* modulation excitation diffuse reflectance infrared Fourier transform spectroscopy (ME DRIFTS) with phase-sensitive detection (PSD).

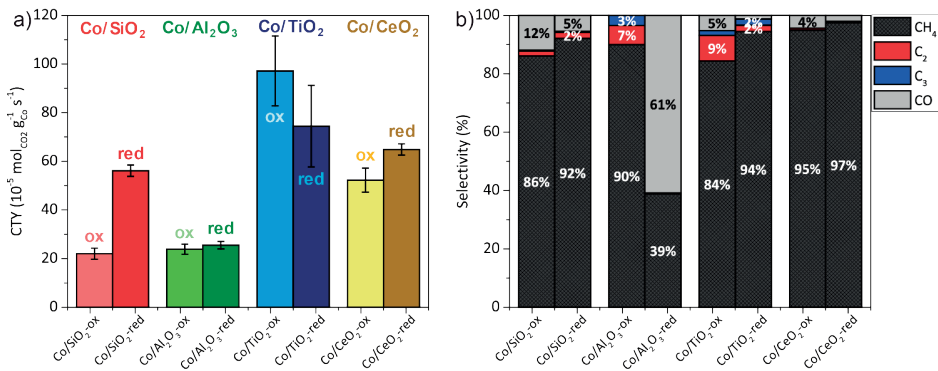


**Figure 4.4. Effect of support and oxidation state on the catalytic activity of the cobalt-based catalyst materials.** a) b) Catalytic activity and selectivity of cobalt-based catalysts as measured with gas chromatography (GC) over 10 h time-on-stream in CoO (suffix: -ox) and metallic Co (suffix: -red) state at  $T=250^{\circ}\text{C}$ ,  $P=20$  bar,  $\text{H}_2/\text{CO}_2=3$ . The automated GC injections were performed every 23 min and the whiskers indicate the standard deviation in the 26 data points per sample.

### 4.3.2 Reaction Mechanism Elucidation from Modulation Excitation Infrared Spectroscopy

Detecting active species with infrared (IR) spectroscopy is often limited by the sensitivity of the characterization technique under reaction conditions and is generally challenging. Relevant signals could for example overlap strongly with irrelevant background signals, complicating the interpretation. To overcome the sensitivity problem, we have used in this Chapter *operando* ME DRIFTS with PSD. This method is based on the periodic variation of an external stimulus, in our case CO<sub>2</sub> gas, while IR spectroscopic data are recorded. The obtained spectra contain mixed signals of the active species, spectator species, deactivating species, and noise. The time-resolved IR data can be converted from the time domain to the phase domain by applying a set of mathematical transformations based on Fourier series, also known as PSD (Figure 4.5)<sup>65,66</sup>. By demodulating the periodically varying IR signals, the dynamic signals can then be separated from the static ones<sup>67,68</sup>. The spectator species and the noise are canceled out in the

phase domain, as they do not exhibit a periodic response to the external stimulus. The resulting high-quality phase-resolved IR data only contain the periodically responding species and provide direct insights into the CO<sub>2</sub> hydrogenation mechanism, the nature of the active site(s), and kinetics.

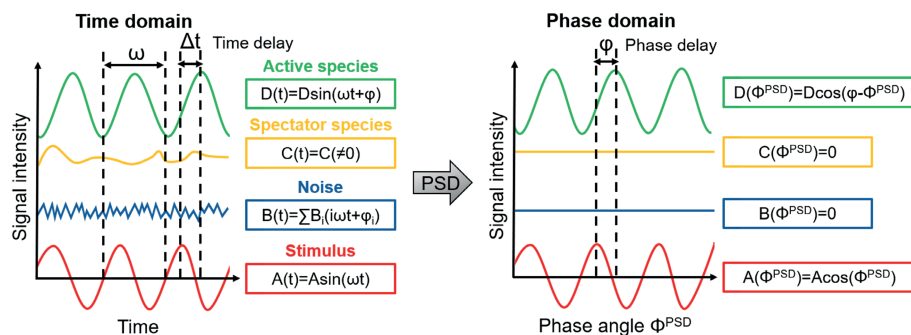


**Figure 4.5. Schematic overview of the principle of phase-sensitive detection (PSD).**  $A(t)$  is the external stimulus,  $B(t)$  is noise,  $C(t)$  is the response of a spectator species, and  $D(t)$  is the response of an active species. The external stimulus is a sinusoidal or square-wave function with frequency  $\omega$ . Once the full set of time-resolved data (time domain) is measured along a given number of modulation periods, each spectrum is averaged along the modulation periods to obtain a set of average time-resolved spectra (spectrum  $i$  is the average of spectrum  $i$  from each modulation period)<sup>69</sup>. Demodulation by PSD transforms the set of averaged time-resolved data into a set of phase-resolved data (phase domain). In this set of data, the active species appear with a phase delay  $\Phi$  instead of appearing with a time delay  $\Delta t$ . The phase delay contains additional kinetic information about the system that is often hidden in the kinetic information delivered by the time-resolved data (for example because of strong band overlap).

In the averaged time-resolved IR spectra (**Figure 4.6a**), surface (bi)carbonates, formates, and CO (**Figure 4.6c-g**) could already be observed on the cobalt-based FTS catalysts, but the corresponding IR peaks were broad and convoluted. In general, the averaged time-resolved IR spectra of the catalyst materials with Co(O) supported on reducible supports displayed evident and broad signals of surface (bi)carbonates and formates, whereas the spectra of catalyst materials with Co(O) on non-reducible supports did not. This can be explained by the basicity of the support oxides, which we defined as the amount of CO<sub>2</sub> adsorbed per surface area unit measured with CO<sub>2</sub>-TPD (**Fig 4.3b** and **Table 4.3**).

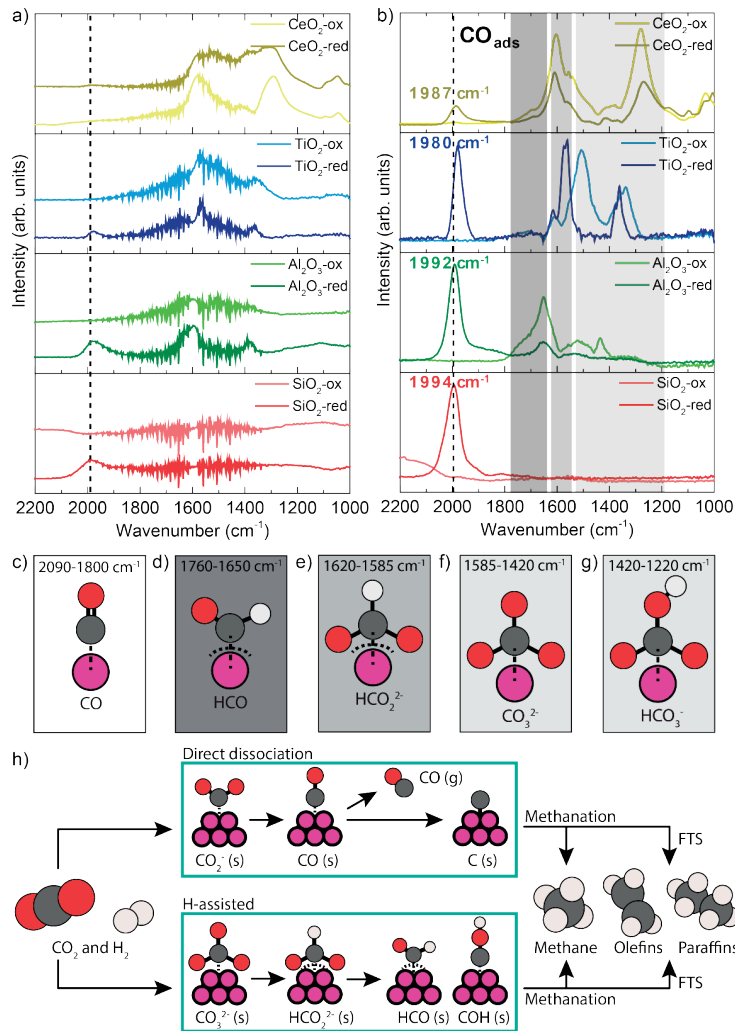


**Figure 4.6. Operando Modulation excitation diffuse reflectance infrared Fourier transform spectroscopy (ME DRIFTS) during CO<sub>2</sub> hydrogenation with the cobalt-based catalyst materials.**

**a)** Averaged time-resolved DRIFT spectra and **b)** phase-resolved amplitude spectra of CoO (suffix: -ox) and metallic Co (suffix: -red) supported catalysts (T=250°C, P=1 bar, H<sub>2</sub>/CO<sub>2</sub>=3). **c-g)** Adsorbed surface species with characteristic vibrational energies: **c)** CO, **d)** formyl, **e)** formate, **f)** carbonate, and **g)** bicarbonate. **h)** Simplified reaction pathways for cobalt-catalyzed CO<sub>2</sub> hydrogenation to hydrocarbons. In the direct dissociation mechanism CO<sub>ads</sub> is an intermediate, which either desorbs or forms C<sub>ads</sub>, and then hydrocarbon products. The H-assisted mechanism involves surface carbonates, formates, and formyl as intermediates. The reaction intermediates can either be fully hydrogenated to methane or converted into olefins or paraffins via carbon-carbon coupling (FTS).

The basicity of the supports used increases in the order  $\text{SiO}_2 < \text{Al}_2\text{O}_3 < \text{CeO}_2 < \text{TiO}_2$ . Interactions between basic  $\text{O}^{2-}$  surface ions and  $\text{CO}_2$  facilitate the formation of carbonates, whereas  $-\text{OH}$  surface groups enable the formation of bicarbonates from  $\text{CO}_2$ <sup>70</sup>. Surface vacancies, as present in large numbers on reducible supports like  $\text{TiO}_2$  and  $\text{CeO}_2$ , aid the generation of formate species<sup>63</sup>. Besides, hydrogen spillover, replenishing e.g.  $-\text{OH}$  surface groups, is significant onto reducible supports, such as titania and ceria<sup>71</sup>. Additionally, weaker signals of adsorbed CO appeared around  $2000\text{ cm}^{-1}$ <sup>72</sup> in the averaged time-resolved IR spectra (**Figure 4.6a**).

PSD revealed species on the cobalt-based catalyst materials that would otherwise not have been visible so clearly. This can be seen by comparing the averaged time-resolved IR spectra (**Figure 4.6a**) and the phase-resolved amplitude spectra (**Figure 4.6b**), that are composed of the absolute maxima (in the phase domain) at every single wavenumber<sup>73</sup>. The surface (bi)carbonates observed on  $\text{Co}/\text{TiO}_2$  and  $\text{Co}/\text{CeO}_2$  and to some extent on  $\text{Co}/\text{Al}_2\text{O}_3$  were dynamic surface species that varied with the external stimulus and thus became visible in the phase-resolved amplitude spectra (**Figure 4.6b**). However, we cannot unambiguously conclude that they actively take part in the conversion of  $\text{CO}_2$  to hydrocarbons, as the adsorption and desorption of these species could as well lead to the appearance of dynamic signals. Peak splitting was observed for the surface carbonates on  $\text{Co}/\text{TiO}_2$ . For  $\text{Co}/\text{TiO}_2$ -red  $\nu_{\text{asym}}(\text{CO}_3^{2-})$  split into  $1362$  and  $1378\text{ cm}^{-1}$  and  $\nu_{\text{sym}}(\text{CO}_3^{2-})$  split into  $1562$  and  $1574\text{ cm}^{-1}$ . Such splits have been observed in earlier studies<sup>74-76</sup> and ascribed to different types of coordination and/or different adsorption centers<sup>74</sup>, suggesting the formation of an interfacial area between Co and  $\text{TiO}_2$  with different adsorption properties.

The most evident difference between the CoO (suffix: -ox) and metallic Co (suffix: -red) catalyst materials was the presence of adsorbed CO around  $2000\text{ cm}^{-1}$  (**Figure 4.6c**) only on all the metallic Co catalyst materials. In the averaged time-resolved IR spectra, adsorbed CO was visible as a broad band on the metallic Co catalysts (**Figure 4.6a**). Though, for  $\text{Co}/\text{CeO}_2$ -red this band could barely be observed, possibly due to the intense contributions of (bi)carbonates and/or formates. In the phase-resolved amplitude spectra (**Figure 4.6b**), on the other hand, the adsorbed CO signals became clear and sharp signals with peak maxima that varied per support material. Hence, irrespective of the support material, the metallic Co catalysts mainly followed the direct dissociation mechanism (**Figure 4.6h**), as indicated by the presence of adsorbed CO as an intermediate. The energy of the peak of linearly adsorbed CO ( $\nu(\text{CO})$ ) is a measure of the C=O bond strength. When CO is coordinated to a metal atom, the metal d-orbitals donate electrons to the  $n^*$  orbital of CO (**Fig 4.7a**), formally decreasing the bond order and weakening the C=O bond. Thus, the vibrational frequency of adsorbed CO decreases

and the resulting wavenumber in the IR spectrum shifts down. In the series of the metallic cobalt catalysts, Co/TiO<sub>2</sub> exhibited the lowest wavenumber for  $\nu(\text{CO})$  (Figure 4.7b), indicating that the C=O bond was the weakest and providing a plausible explanation for the highest activity of Co/TiO<sub>2</sub>. Besides, based on the position of the C=O stretching vibration from the phase-resolved amplitude spectra, there was an apparent optimum for the support reducibility, as determined from H<sub>2</sub>-TPR data (Figure 4.3a), around Co/TiO<sub>2</sub>. This is depicted in Figure 4.7b.

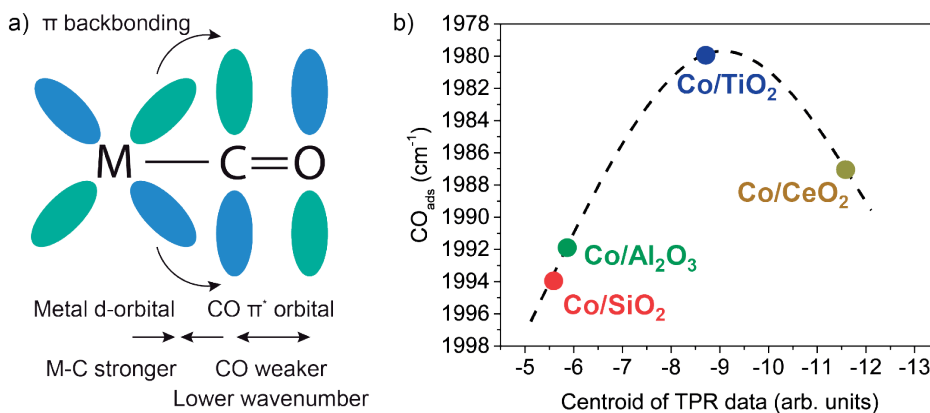


**Figure 4.7. Support-dependent CO adsorption strengths for the metallic cobalt-based catalyst materials.** a) schematic drawing of  $\pi$  backbonding when C=O coordinates to a metal center. b) Position of linearly adsorbed CO from the phase-resolved amplitude spectra versus the support reducibility, which was determined from H<sub>2</sub>-temperature programmed reduction (TPR) data.

On the other hand, the CoO-containing catalyst materials did not show any adsorbed CO species. Instead, different types of formyl, formate, and carbonate species (Figure 4.6d-g) were observed on their surfaces in the phase-resolved amplitude spectra (Figure 4.6b). The CoO catalysts thus followed a different mechanism than the metallic Co counterparts, namely the H-assisted mechanism (Figure 4.6h). This observation is in accordance with theoretical work, where they found that CO<sub>ads</sub> adsorption is strong on metallic Co (-1.99 eV = -192 kJ/mol) and weak on CoO (-0.33 eV = -32 kJ/mol)<sup>77</sup>. Consequently, the CO<sub>ads</sub> vibration is observed on metallic Co, but not on CoO. Besides, the CoO catalysts produced more olefinic C<sub>2</sub> and C<sub>3</sub> products, while metallic Co primarily produced paraffins (Table 4.4).

**Table 4.4.** Catalytic performance of the cobalt-based catalyst materials under study.  $T=250^{\circ}\text{C}$ ,  $P=20$  bar,  $\text{H}_2/\text{CO}_2=3$  GHSV=3000  $\text{h}^{-1}$ , 10 h time-on-stream.

Catalyst	$\text{CO}_2$ conversion (%)	CO selectivity (%)	$\text{CH}_4$ selectivity (%)	$\text{C}_2$ selectivity (%)	$\text{C}_2 \text{O/P}^a$	$\text{C}_3$ selectivity (%)	$\text{C}_3 \text{O/P}^a$	$\text{C}_4$ selectivity (%)
Co/SiO <sub>2</sub> -ox	1.13 ± 0.12	11.9 ± 3.7	86.1 ± 3.6	1.69 ± 0.11	0.003	0.34 ± 0.03	0.01	n.a.
Co/SiO <sub>2</sub> -red	3.02 ± 0.12	5.38 ± 0.25	92.1 ± 0.2	2.03 ± 0.07	0.002	0.48 ± 0.02	0.01	n.a.
Co/Al <sub>2</sub> O <sub>3</sub> -ox	1.21 ± 0.11	0.00 ± 0.00	89.9 ± 19.6	6.60 ± 16.2	0.90	3.44 ± 10.4	1.54	n.a.
Co-Al <sub>2</sub> O <sub>3</sub> -red	1.35 ± 0.33	60.8 ± 0.8	38.8 ± 0.8	0.35 ± 1.54	0.66	0.05 ± 0.00	1.15	n.a.
Co/TiO <sub>2</sub> -ox	5.46 ± 0.81	5.26 ± 4.12	85.6 ± 13.6	8.87 ± 8.90	0.40	1.72 ± 2.18	1.68	0.18 ± 0.87



For example, Co/TiO<sub>2</sub>-ox, exhibited olefin/paraffin ratios for C<sub>2</sub> and C<sub>3</sub> of 0.4 and 1.7, respectively. Co/TiO<sub>2</sub>-red, on the other hand, almost exclusively produced paraffins. These results suggest that the hydrogenation steps are less favorable and/or that the hydrogen availability is lower on CoO compared to a metallic Co surface, which may positively affect C-C coupling. To underline that CoO and metallic Co are simply different surfaces when it comes to CO<sub>2</sub> adsorption, *i.e.*, altering the CO<sub>2</sub> hybridization, we have performed density functional theory (DFT) calculations on the face-centered cubic (FCC) CoO and metallic Co surface facets. Geometry optimizations were performed using Co(110), Co(111), and CoO(100), the most active facets, both with and without adsorbed CO<sub>2</sub>. The obtained structures are visualized in **Figure 4.8**. The geometry optimization of CO<sub>2</sub> on the Co(111) surface resulted in a stable structure with a positive adsorption energy of 35.4 kJ/mol, indicating an endothermic process and it is likely that CO<sub>2</sub> activation does not take place on this facet<sup>78</sup>. The stable structure on the Co(110) surface led to a negative adsorption energy of -63.2 kJ/mol and -34.1 kJ/mol was obtained on CoO(100) (**Table 4.5**). These results indicate that both Co(110) and CoO(100) can activate CO<sub>2</sub> molecules upon adsorption. Besides, C-O bond elongation and the angle of the O-C-O bond after adsorption were evaluated to qualitatively assess to what extent CO<sub>2</sub> is activated upon adsorption on the three surfaces. The sp hybridized free CO<sub>2</sub> molecule possesses a O-C-O bond angle of 180°. To activate a CO<sub>2</sub> molecule on a catalytic surface, the angle of O-C-O has to change. From the results in **Table 4.5**, we can learn for example that CO<sub>2</sub> is least deformed, to 145.4°, on CoO(100) after adsorption, as the O-C-O bond angle changes the least. The highest deformation of 120.6° was observed on Co(110). Besides, C-O bond elongation and thus potentially dissociation is most severe on Co(110). These theoretical results indicate that metallic cobalt activates CO<sub>2</sub> molecules more compared to CoO, which is in line with our experimental observations, where we observe CO<sub>ads</sub> only on metallic cobalt. Please note that we have adopted a simplified approach herein, reporting the optimized geometry. There are other possibilities in which CO<sub>2</sub> can bind to each of the chosen surfaces, depending on the orientation of the CO<sub>2</sub> adsorbate with respect to the surface as well as the chosen adsorption site of the surface. This generally results in varying possibilities for the adsorption energy<sup>78</sup>. For example, oxygen vacancies on the cobalt oxide surface could be good docking sites for CO<sub>2</sub>, which would facilitate the adsorption<sup>79</sup>. Moreover, the support material, which we excluded from our calculations, plays a significant role in the resulting adsorption energy<sup>80</sup>.

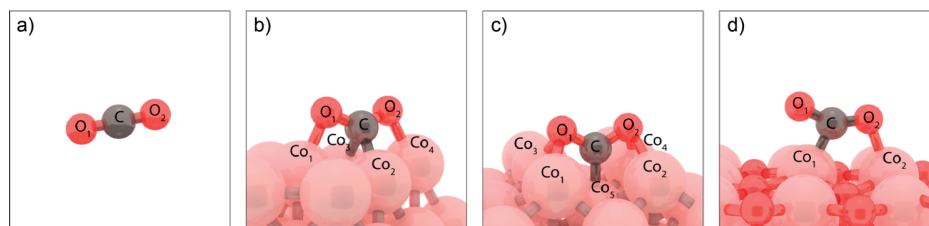


**Figure 4.8.** Visualizations of geometry optimization using density functional theory (DFT). **a)** A free CO<sub>2</sub> molecule. CO<sub>2</sub> adsorbed on **b)** Co(111) **c)** Co(110) and **d)** CoO(100).

**Table 4.5.** Adsorption energies and structural parameters of CO<sub>2</sub> adsorbed on Co(110), Co(111), and CoO(100).

	CO <sub>2</sub> (g)	*CO <sub>2</sub> on Co(110)	*CO <sub>2</sub> on Co(111)	*CO <sub>2</sub> on CoO(100)
$E_{\text{ads}}$ (kJ/mol)		-63.2	35.4	-34.1
O–C–O (°)	180	120.6	129.5	145.4
C–O <sub>1</sub> (Å)	1.18	1.32	1.28	1.23
C–O <sub>2</sub> (Å)	1.18	1.31	1.28	1.24
O <sub>1</sub> –Co <sub>1</sub> (Å)		2.08	2.08	
O <sub>2</sub> –Co <sub>4</sub> (Å)		2.08	2.08	
O <sub>1</sub> –Co <sub>3</sub> (Å)		2.08		
O <sub>2</sub> –Co <sub>2</sub> (Å)		2.09		1.12
C–Co <sub>1</sub> (Å)				1.93
C–Co <sub>2</sub> (Å)			1.93	
C–Co <sub>3</sub> (Å)			2.21	
C–Co <sub>5</sub> (Å)		1.90		

### 4.3.3 Reaction Kinetics Elucidation

#### 4.3.3.1 Kinetic Insights from Phase-sensitive Detection Analysis

From the phase shift  $\varphi$  we can derive kinetic information about the cobalt-based catalyst materials<sup>66,81</sup>. The phase shift describes the difference between the external stimulus and the maximum intensity of a responding active species. We have used  $\varphi$  as a diagnostic tool to identify the responding signals and to distinguish between different (overlapping) contributions within one signal. For the identified signals, we looked at the intensity in the time domain. More specifically, we followed the intensity decrease of the signals in the first 10 s after the CO<sub>2</sub> was turned off during the modulation experiment. The steepness of the slope of desorption was then used as a measure for relative

kinetics; the steeper the slope, the faster the species. By comparing the responses of all the active species identified with PSD, we obtained relative kinetics of the species participating in the different CO<sub>2</sub> hydrogenation reaction mechanisms. We will explain the concept by focusing on Co/TiO<sub>2</sub>, the most active catalyst in this **Chapter**. We have learned from the phase-resolved amplitude spectra that Co/TiO<sub>2</sub>-ox mainly followed the H-assisted pathway, while Co/TiO<sub>2</sub>-red mainly followed the direct dissociation pathway (**Figure 4.9a,b**).

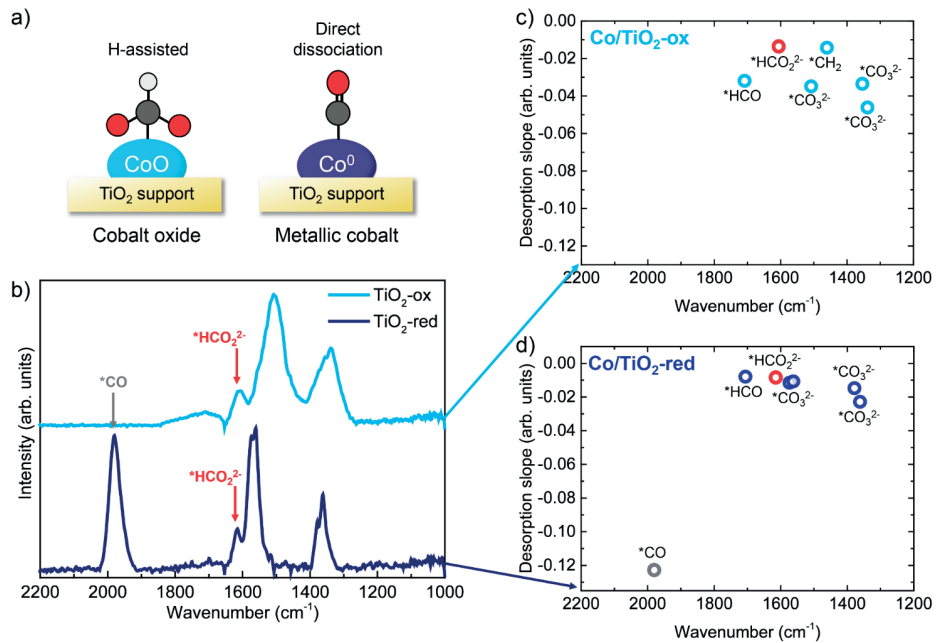


**Figure 4.9. Kinetic information derived from phase-sensitive detection (PSD) analysis for the Co/TiO<sub>2</sub> catalyst materials, either in its oxidic or reduced form. a)** Schematic representation of the H-assisted mechanism, dominant for CoO catalysts, and the direct dissociation mechanism, dominant for metallic Co catalysts. **b)** Phase-resolved amplitude spectra for Co/TiO<sub>2</sub>-ox and Co/TiO<sub>2</sub>-red. Desorption slopes (first 10s after turning the CO<sub>2</sub> gas off) of selected species for **c)** Co/TiO<sub>2</sub>-ox and **d)** Co/TiO<sub>2</sub>-red. Both samples showed carbonate, formate (\*HCO<sub>2</sub><sup>-</sup> indicated in red; 1609-1615 cm<sup>-1</sup>), and formyl species. Co/TiO<sub>2</sub>-ox additionally showed \*CH<sub>2</sub> species. For Co/TiO<sub>2</sub>-red, \*CO (gray; 1980 cm<sup>-1</sup>) displayed faster kinetics (steeper slope) than the carbonate, formate, and formyl species. The direct dissociation mechanism was thus faster than the H-assisted mechanism.

To visualize the relative kinetics of the different species, we plotted the desorption slopes of the respective signal intensity decrease during the first 10s after turning the CO<sub>2</sub> gas off for carbonate, formate, formyl, and adsorbed CO in **Figure 4.9c,d**. Co/TiO<sub>2</sub>-ox, as well as the other CoO-containing catalysts (**Figure 4.10**) displayed carbonate,

formate (indicated in red in **Figure 4.9c,d**), and formyl species in a similar kinetic regime. However, for Co/TiO<sub>2</sub>-red, as well as for the other metallic Co catalysts, adsorbed CO (indicated in gray in **Figure 4.9d**) displayed a steeper desorption slope, suggesting that CO responded faster than the carbonate, formate, and formyl species. This tells us that the direct dissociation pathway, of which adsorbed CO is a key intermediate, occurred at a higher rate than the H-assisted pathway. However, the product distributions (**Figure 4.4b**) indicated that the H-assisted pathway was more beneficial for the production of C<sub>2+</sub> hydrocarbons. For example, Co/Al<sub>2</sub>O<sub>3</sub>-ox and Co/TiO<sub>2</sub>-ox produced more C<sub>2+</sub> hydrocarbons compared to the metallic counterparts. **Figure 4.11** depicts a schematic overview of elementary reaction steps in the CO<sub>2</sub> hydrogenation to methane and C<sub>2+</sub> hydrocarbons based on the intermediates detected on the Co/TiO<sub>2</sub> catalysts using ME DRIFTS.

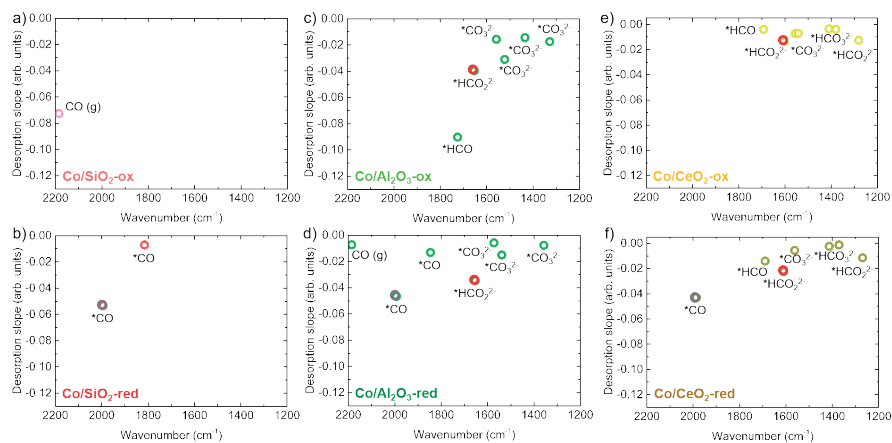


**Figure 4.10. Slopes of the desorption branches** of the time-resolved DRIFT spectra after turning off the CO<sub>2</sub> gas for **a, b**) Co/SiO<sub>2</sub>, **c, d**) Co/Al<sub>2</sub>O<sub>3</sub>, and **e, f**) Co/CeO<sub>2</sub>. The top panels display the CoO-containing (suffix: -ox) catalysts and the bottom panels the metallic Co (suffix: -red) catalysts. Co/SiO<sub>2</sub>-ox only showed gaseous CO, while Co/SiO<sub>2</sub>-red only displayed \*CO. Co/Al<sub>2</sub>O<sub>3</sub>-ox and Co/CeO<sub>2</sub>-ox showed carbonate, formate (\*HCO<sub>2</sub><sup>2-</sup> indicated in red; 1609-1615 cm<sup>-1</sup>), and formyl species. The metallic Co catalysts (bottom) displayed \*CO (gray; 1980-1994 cm<sup>-1</sup>), which had faster kinetics (steeper slopes) compared to the carbonate, formate, and formyl species.

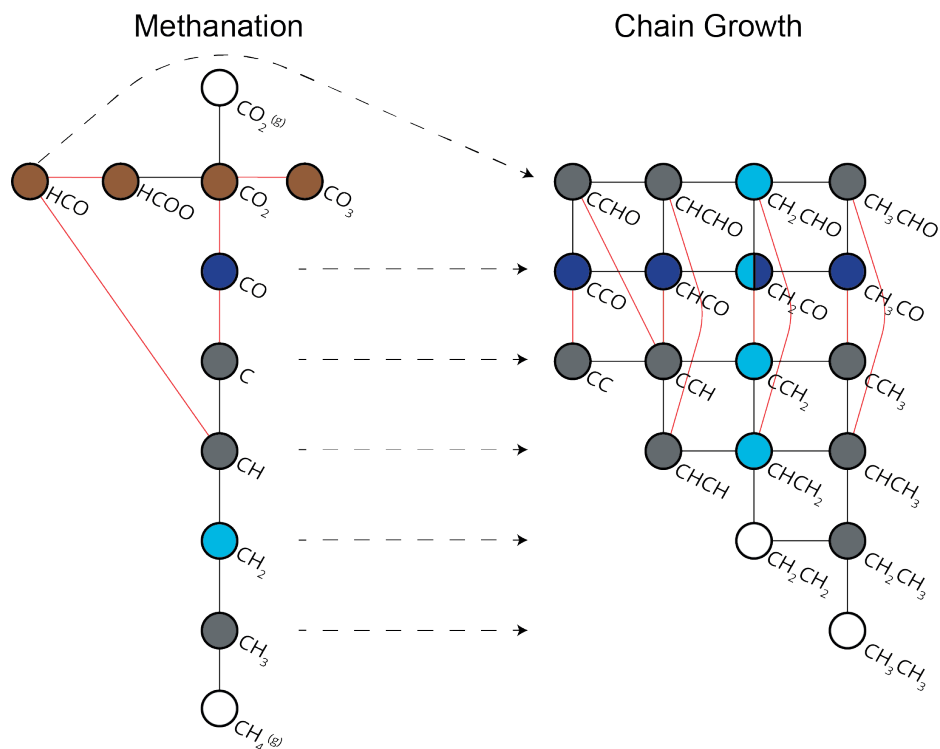


**Figure 4.11. Schematic overview of elementary reaction steps in CO<sub>2</sub> hydrogenation on Co/TiO<sub>2</sub>.**

The white nodes indicate reactant and product molecules, the brown nodes correspond to reaction intermediates that were detected via ME DRIFTS on both CoO and metallic Co. The light blue node for CH<sub>2</sub> on the left side was detected only on CoO and the dark blue node for CO only on metallic Co. On the right side the C-C coupled species with either CH<sub>2</sub> or CO are colored light blue or dark blue respectively. Black lines connecting the nodes represent (de)hydrogenation steps and the red lines indicate (de)coupling of an oxygen atom. The arrows with a dotted line represent C-C coupling events.

#### 4.3.3.2 Determination of Reaction Orders and Activation Energies

For the best performing catalyst in our study, namely Co/TiO<sub>2</sub>, we have additionally determined a set of kinetic parameters at P=20 bar in both the CoO and metallic Co state. The overall apparent activation energy (E<sub>a</sub>) for CO<sub>2</sub> hydrogenation was slightly lower for Co/TiO<sub>2</sub>-ox, 113 ± 3, compared to Co/TiO<sub>2</sub>-red, 122 ± 5 (Table 4.6). This is in line with the better performance of Co/TiO<sub>2</sub>-ox compared to Co/TiO<sub>2</sub>-red. Moreover, all the apparent activation energies for CH<sub>4</sub>, C<sub>2+</sub>, and CO were considerably lower for Co/TiO<sub>2</sub>-ox than for Co/TiO<sub>2</sub>-red (Table 4.6). C<sub>2+</sub> products, for example, displayed an apparent activation energy of 98 ± 3 kJ/mol with the Co/TiO<sub>2</sub>-ox catalyst, whereas Co/TiO<sub>2</sub>-red resulted in a value of 115 ± 5 kJ/mol. All Arrhenius plots used for calculating the apparent activation energies are displayed in Figure 4.12-4.13. When compar-

ing the activation energies obtained for CO<sub>2</sub> hydrogenation with Co/TiO<sub>2</sub>-red to the values obtained for FTS with Co/TiO<sub>2</sub>-red (**Chapter 3**), it stood out that the  $E_a$  values for methane were remarkably similar for the two different reactions, namely 121 and 117 kJ mol<sup>-1</sup>. For C<sub>2+</sub> products, on the other hand, the values were far apart: 115 kJ mol<sup>-1</sup> for CO<sub>2</sub> hydrogenation and 57.5 kJ mol<sup>-1</sup> for FTS. This implies that methane formation from CO and CO<sub>2</sub> hydrogenation costs a similar amount of energy, while C-C coupling costs about twice as much effort from CO<sub>2</sub> than from the more reactive CO molecule on the exact same catalytic surface. To gain more insights, the reaction orders in CO<sub>2</sub> and in H<sub>2</sub> were determined for both samples. The higher reaction order in CO<sub>2</sub> of Co/TiO<sub>2</sub>-ox (0.38 ± 0.09) compared to Co/TiO<sub>2</sub>-red (0.15 ± 0.04) indicated that a strongly adsorbed intermediate derived from CO<sub>2</sub> on the Co/TiO<sub>2</sub>-red surface, most likely adsorbed CO, hinders the reaction<sup>82</sup>. For metallic Co, a reaction order of 0.14 in CO<sub>2</sub> has been reported previously for the CO<sub>2</sub> hydrogenation reaction<sup>83</sup>. Besides, the reaction orders in H<sub>2</sub> were almost completely opposite for the 2 samples: a positive order of 1.24 ± 0.40 for Co/TiO<sub>2</sub>-ox versus a negative order of -1.15 ± 0.07 for Co/TiO<sub>2</sub>-red. This particularly substantiates the hypothesis that the Co/TiO<sub>2</sub>-ox catalyst, following the H-assisted mechanism, benefits from a higher partial pressure in H<sub>2</sub>. On the other hand, the Co/TiO<sub>2</sub>-red catalyst, following mainly the direct dissociation mechanism, benefits from a lower partial pressure in H<sub>2</sub>, as H<sub>2</sub> may be competing with adsorbed CO, the most important intermediate in the direct dissociation mechanism. The negative H<sub>2</sub> reaction orders and positive CO<sub>2</sub> reaction orders obtained for Co/TiO<sub>2</sub>-red indicated involvement of C-O bond breaking and/or C-C coupling, rather than hydrogenation, in the rate-determining step. This is reminiscent of C<sub>2+</sub> olefin formation in the FTS with Co/TiO<sub>2</sub>-red (**Chapter 3**), which required less H atoms and its rate-determining step did not necessarily seem to involve hydrogenation, also reflected by the negative H<sub>2</sub> reaction orders and positive CO reaction orders.

**Table 4.6.** Kinetic parameters for the two sets of Co/TiO<sub>2</sub> catalyst materials used for CO<sub>2</sub> hydrogenation.

Catalyst		$E_a$ (kJ/mol) <sup>a</sup>	R <sup>2</sup>	CO <sub>2</sub> reaction order <sup>b</sup>	H <sub>2</sub> reaction order
Co/TiO <sub>2</sub> -ox	Total	113 ± 3	0.98	0.38 ± 0.09	1.24 ± 0.40
	CH <sub>4</sub>	113 ± 2	0.98	0.22 ± 0.11	1.36 ± 0.35
	C <sub>2+</sub>	98 ± 3	0.98	0.64 ± 0.07	-0.13 ± 0.07
	CO	146 ± 7	1.00	0.49 ± 0.20	0.92 ± 0.13
Co/TiO <sub>2</sub> -red	Total	122 ± 5	0.99	0.15 ± 0.04	-1.15 ± 0.07
	CH <sub>4</sub>	121 ± 4	0.99	0.19 ± 0.05	-1.21 ± 0.06
	C <sub>2+</sub>	115 ± 5	1.00	0.28 ± 0.16	-1.13 ± 0.16
	CO	156 ± 8	0.99	1.04 ± 0.18	-1.35 ± 0.20

<sup>a</sup>  $E_a$  was calculated with 6 data points at T=200-280°C and P=20 bar. The R<sup>2</sup> values of the trendlines are reported in the 3<sup>rd</sup> column.

<sup>b</sup> CO<sub>2</sub> and H<sub>2</sub> reaction orders were determined at T=250°C and P=20 bar.

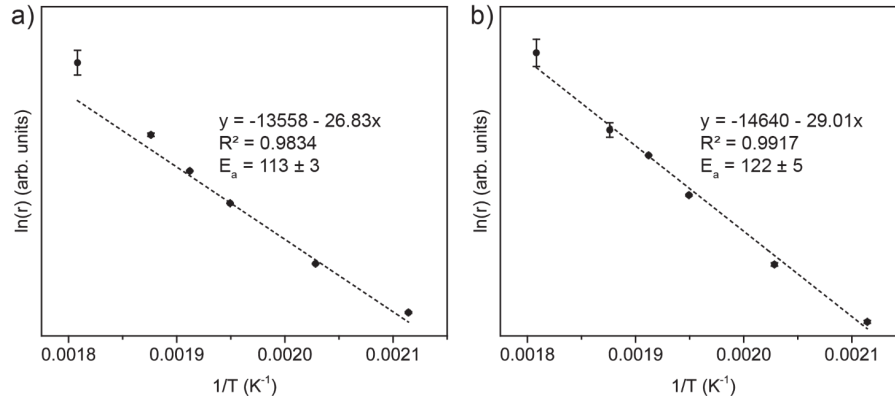


**Figure 4.12. Arrhenius plots for the two sets of Co/TiO<sub>2</sub> materials during CO<sub>2</sub> hydrogenation.** Arrhenius plots for **a)** Co/TiO<sub>2</sub>-ox (pre-treated for 1 h at 250°C in N<sub>2</sub>/H<sub>2</sub>=2) and **b)** Co/TiO<sub>2</sub>-red (pre-treated for 1 h at 450°C in N<sub>2</sub>/H<sub>2</sub>=2) during CO<sub>2</sub> hydrogenation at 20 bar and H<sub>2</sub>/CO<sub>2</sub>=3 at temperatures between 220 and 280°C. Every point is an average of 4-6 on-line gas chromatography (GC) injections and the whiskers indicate the standard deviation.

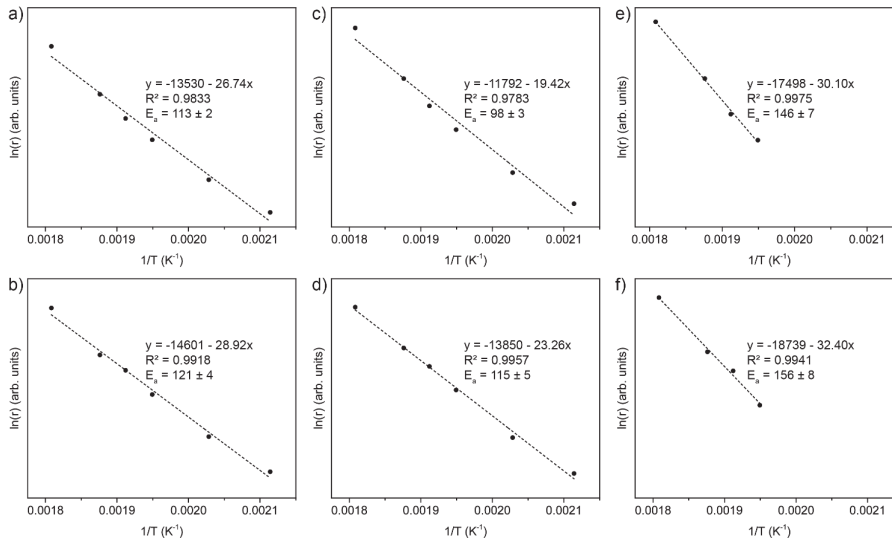


**Figure 4.13. Arrhenius plots for the two sets of Co/TiO<sub>2</sub> catalyst materials during CO<sub>2</sub> hydrogenation.** Arrhenius plots for the reaction products **a, b)** methane, **c, d)** C<sub>2+</sub> hydrocarbons, and **e, f)** CO during CO<sub>2</sub> hydrogenation at 20 bar and H<sub>2</sub>/CO<sub>2</sub>=3 at temperatures between 220 and 280°C. The top row displays the plots for Co/TiO<sub>2</sub>-ox (pre-treated for 1 h at 250°C in N<sub>2</sub>/H<sub>2</sub>=2) and the bottom row displays the plots for Co/TiO<sub>2</sub>-red (pre-treated for 1 h at 450°C in N<sub>2</sub>/H<sub>2</sub>=2). Every point is an average of 4-6 on-line gas chromatography (GC) injections and the whiskers indicate the standard deviation.

### 4.3.4 Shifting the Selectivity towards the Formation of Long-chain Hydrocarbons

With all these fundamental insights in hand, we are still left with the question how to directly obtain more long-chain hydrocarbon products from  $\text{CO}_2$ . In an attempt to answer this question, we took the best performing catalyst material in this **Chapter**, namely the  $\text{Co}/\text{TiO}_2$  system, and conducted experiments in which  $\text{CO}$  gas was co-fed at a  $\text{CO}_2$  to  $\text{CO}$  ratio of 2. This approach was inspired by the industrial methanol synthesis process, where optimum performance of  $\text{Cu}/\text{ZnO}/\text{Al}_2\text{O}_3$  catalysts is generally obtained by the synergistic effects of  $\text{CO}$  and  $\text{CO}_2$  gas combined<sup>7,8</sup>. We found that upon co-feeding  $\text{CO}$ , the  $\text{CO}_2$  conversion of  $\text{Co}/\text{TiO}_2\text{-ox}$  doubled and the  $\text{C}_{2+}$  selectivity increased from 11 to 39%, leading to an overall  $\text{C}_{2+}$  yield of  $104 \text{ mmol h}^{-1} \text{ g}_{\text{cat}}^{-1}$  (**Figure 4.14a**).

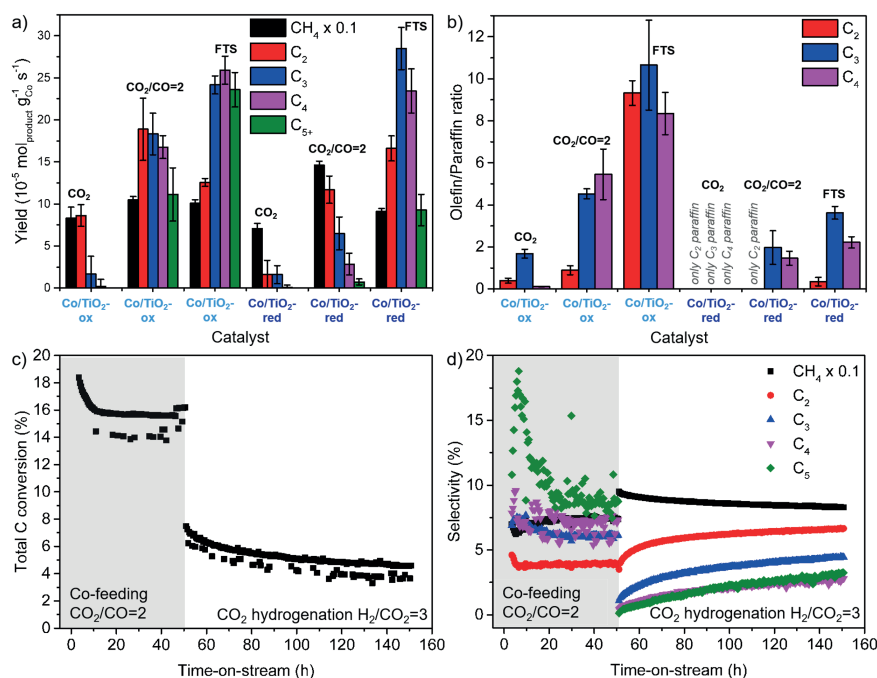


**Figure 4.14. Co-feeding  $\text{CO}/\text{CO}_2$  to the  $\text{Co}/\text{TiO}_2$  catalyst material to shift the selectivity towards long-chain hydrocarbons and long-term stability** **a)** catalytic testing results ( $T=250^\circ\text{C}$ ,  $P=20$  bar,  $\text{GHSV}=3000 \text{ h}^{-1}$ , 10 h time-on-stream) comparing the product yields of  $\text{CO}_2$  hydrogenation ( $\text{H}_2/\text{CO}_2=3$ ) to  $\text{CO}/\text{CO}_2$  ( $\text{H}_2/\text{CO}_2/\text{CO}=9/2/1$ ) hydrogenation and Fischer-Tropsch synthesis (FTS;  $\text{H}_2/\text{CO}=2$ ) for  $\text{Co}/\text{TiO}_2$  containing  $\text{CoO}$  (-ox) or metallic  $\text{Co}$  (-red). **b)** Olefin/Paraffin ratios for  $\text{C}_2$ ,  $\text{C}_3$ , and  $\text{C}_4$  products during  $\text{CO}_2$  hydrogenation,  $\text{CO}/\text{CO}_2$  ( $\text{H}_2/\text{CO}_2/\text{CO}=9/2/1$ ) hydrogenation, and FTS ( $\text{H}_2/\text{CO}=2$ ). The whiskers in **a** and **b** indicate the standard deviation. **c, d)** Stability test ( $T=250^\circ\text{C}$ ,  $P=20$  bar,  $\text{GHSV}=3000 \text{ h}^{-1}$ ) of  $\text{Co}/\text{TiO}_2\text{-ox}$  operated for 150 h displaying conversion (**c**) and selectivity (**d**) first while co-feeding  $\text{CO}/\text{CO}_2$  ( $\text{H}_2/\text{CO}_2/\text{CO}=9/2/1$ ) for 50 h and then during  $\text{CO}_2$  hydrogenation only ( $\text{H}_2/\text{CO}_2=3$ ) for 100 h.



**Table 4.7.** Comparison of various cobalt-containing catalyst materials for CO/CO<sub>2</sub> conversion to C<sub>2+</sub> hydrocarbons.

Catalyst	Reactant	H <sub>2</sub> /C ratio	Temperature (°C)	Pressure (bar)	Conversion (%)	C <sub>2+</sub> selectivity (%)	C <sub>2+</sub> yield (%)	C <sub>2+</sub> yield (mL h <sup>-1</sup> g <sub>cat</sub> <sup>-1</sup> )	Space time yield (L h <sup>-1</sup> g <sub>cat</sub> <sup>-1</sup> ) <sup>b</sup>	Ref.
CoO/TiO <sub>2</sub>	CO <sub>2</sub>	3	250	20	5.46	10.7	0.58	19.3	0.18 <sup>e</sup>	This work
Co/TiO <sub>2</sub>	CO <sub>2</sub>	3	250	20	4.12	4.44	0.18	6.22	0.14 <sup>e</sup>	This work
CoO/TiO <sub>2</sub>	CO/CO <sub>2</sub>	3	250	20	17.5 <sup>a</sup>	39.0	6.83	222	0.57 <sup>e</sup>	This work
Co/TiO <sub>2</sub>	CO/CO <sub>2</sub>	3	250	20	18.8 <sup>a</sup>	13.0	2.43	79.3	0.61 <sup>e</sup>	This work
Co-Pt-K/SiO <sub>2</sub>	CO <sub>2</sub>	3	370	1	36.5	47.3	17.3	N.A. <sup>f</sup>	N.A. <sup>f</sup>	84
Co-Na-Mo/TiO <sub>2</sub>	CO <sub>2</sub>	3	200	1	13.5	7.69	1.04	1.54	0.02 <sup>e</sup>	85
Co <sub>2</sub> /MnO <sub>x</sub>	CO <sub>2</sub>	1	200	80	15.1	53.2	8.03	5.32	0.01 <sup>e</sup>	86
Co-Pt/Al <sub>2</sub> O <sub>3</sub>	CO <sub>2</sub>	1	220	19	6.8	6.9	0.47	18.8	0.27 <sup>e</sup>	87
CuFe <sub>2</sub> O <sub>4</sub>	CO <sub>2</sub>	3	300	10	13.3	50.3 <sup>c</sup>	6.69	35.2	0.07 <sup>c</sup>	88
K-Co/SiO <sub>2</sub>	CO <sub>2</sub>	3	270	1	16.0	38.3	6.13	56.4	0.15 <sup>e</sup>	89
2.5K-CoCu/TiO <sub>2</sub>	CO <sub>2</sub>	3	250	50	13.0	66.4	8.63	62.2	0.10 <sup>e</sup>	90
Co/TiO <sub>2</sub>	CO/CO <sub>2</sub>	3	200	20	75.3	60.0	45.2	118	0.27 <sup>e</sup>	91
Fe-Co/Al <sub>2</sub> O <sub>3</sub>	CO <sub>2</sub>	3	320	20	49.0	36.9	18.1	118	0.32 <sup>e</sup>	92
FeCo/NC-600	CO <sub>2</sub>	3	320	20	37.0	54.4	20.1	288	0.53 <sup>e</sup>	93
K-Fe-Co/Al <sub>2</sub> O <sub>3</sub>	CO <sub>2</sub>	3	300	11	30.2	57.8	17.5	376	0.65 <sup>e</sup>	94
Co/CNF	CO/CO <sub>2</sub>	0.7	250	20	76.4 <sup>a</sup>	45.9	35.1	434	1.24 <sup>e</sup>	95
CoO/TiO <sub>2</sub>	CO	3	250	20	13.8	46.2	6.38	208	0.45 <sup>e</sup>	This work

Table 4.7 (Continued)

Catalyst	Reactant	H <sub>2</sub> /C ratio	Temperature (°C)	Pressure (bar)	Conversion (%)	C <sub>2+</sub> selectivity (%)	C <sub>2+</sub> yield (mL h <sup>-1</sup> g <sub>cat</sub> <sup>-1</sup> )	C <sub>2+</sub> yield (L h <sup>-1</sup> g <sub>cat</sub> <sup>-1</sup> ) <sup>b</sup>	Space time yield	Ref.
Co/TiO <sub>2</sub>	CO	3	250	20	12.6	45.9	188	0.41 <sup>e</sup>	0.41 <sup>e</sup>	This work
K-Fe/N-CNT	CO	1	300	1	16.5	54.6 <sup>d</sup>	158	0.29 <sup>d</sup>	0.29 <sup>d</sup>	<sup>96</sup>
Co-Mn	CO	1	250	1	15.5	53.7 <sup>d</sup>	354	0.66 <sup>d</sup>	0.66 <sup>d</sup>	<sup>97</sup>

<sup>a</sup> Total C (CO and CO<sub>2</sub>) conversion

<sup>b</sup> Calculation based on reported conversion, selectivity (all products), catalyst weight, and GHSV.

<sup>c</sup> Molar percentage excluding CO selectivity

<sup>d</sup> Molar percentage excluding CO<sub>2</sub> selectivity.

<sup>e</sup> Molar percentage based on all products.

<sup>f</sup> GHSV not indicated in this study

This catalyst even outperformed the majority of other cobalt-based catalyst materials that have been used for CO/CO<sub>2</sub> hydrogenation to C<sub>2+</sub> products (**Table 4.7**). The main fraction of the long-chain hydrocarbons was C<sub>2</sub> and C<sub>3</sub> (59%). However, C<sub>4</sub> (27%) and even C<sub>5+</sub> (14%) products were observed as well (**Figure 4.14a**). For Co/TiO<sub>2</sub>-red, the CO<sub>2</sub> conversion increased slightly more than for Co/TiO<sub>2</sub>-ox upon co-feeding CO/CO<sub>2</sub>, but the C<sub>2+</sub> selectivity only increased from 5 to 13%, leading to an overall C<sub>2+</sub> yield of 37.3 mmol h<sup>-1</sup> g<sub>cat</sub><sup>-1</sup>. This suggests that the H-assisted mechanism is a more favorable pathway to produce long-chain hydrocarbons than the direct dissociation mechanism. This hypothesis was substantiated by comparing the olefin/paraffin ratios (**Figure 4.14b**).

During CO<sub>2</sub> hydrogenation the Co/TiO<sub>2</sub>-ox catalyst had a 0.4 and 1.7 olefin/paraffin ratio for C<sub>2</sub> and C<sub>3</sub> hydrocarbons, respectively. The Co/TiO<sub>2</sub>-red catalyst, on the other hand, almost exclusively produced paraffins. This confirmed that CoO had a lower hydrogenation activity than metallic Co, explaining the higher selectivity to C<sub>2+</sub> products. This is in accordance with earlier observations that CoO possesses a lower hydrogenation activity compared to metallic Co and thus produced more olefins<sup>32</sup>. The concept is reminiscent of oxidic promoters, such as MnO, used in the FTS process to steer the selectivity from paraffins towards olefins<sup>98-101</sup>. Here, MnO decreases the cobalt reducibility, resulting in a more oxidic composition of the cobalt surface.<sup>100,101</sup> Such a surface favors β-hydrogen abstraction to produce olefins over α-hydrogen addition to produce paraffins<sup>99,101,102</sup>. And indeed, when Co/TiO<sub>2</sub>-ox and Co/TiO<sub>2</sub>-red were additionally tested under FTS conditions (**Figure 4.14**), we found that the olefin/paraffin ratios for Co/TiO<sub>2</sub>-ox were around 10 for C<sub>2</sub>-C<sub>4</sub> products, whereas the ratios were only between 0.3 and 3.6 for Co/TiO<sub>2</sub>-red. Co-feeding CO increased the olefin/paraffin ratios drastically for Co/TiO<sub>2</sub>-ox and Co/TiO<sub>2</sub>-red started producing some olefins as well (**Figure 4.14b**). The calculated thermodynamic stability of the different cobalt phases metallic Co, CoO, Co<sub>3</sub>O<sub>4</sub>, and Co<sub>2</sub>C under reaction conditions can be found in **Figure 4.15**. During CO<sub>2</sub> hydrogenation, co-feeding CO<sub>2</sub> and CO, and FTS (**Figure 4.15a-c**), metallic Co and CoO were both thermodynamically feasible. Co<sub>3</sub>O<sub>4</sub> and Co<sub>2</sub>C, however, were not present in significant amounts during the simulation at 250°C while varying the pressure between 1 and 20 bar. Additionally, under FTS conditions we varied the H<sub>2</sub>/CO ratio between 0 and 4 at constant temperature (250°C) and pressure (20 bar) (**Figure 4.15d**). We found that the formation of Co<sub>2</sub>C was only thermodynamically feasible at H<sub>2</sub>/CO < 1. Though, at typical cobalt-based FTS conditions (H<sub>2</sub>/CO = 2) metallic Co and CoO were the dominant phases. Co<sub>3</sub>O<sub>4</sub> was again not significantly present during the simulation.

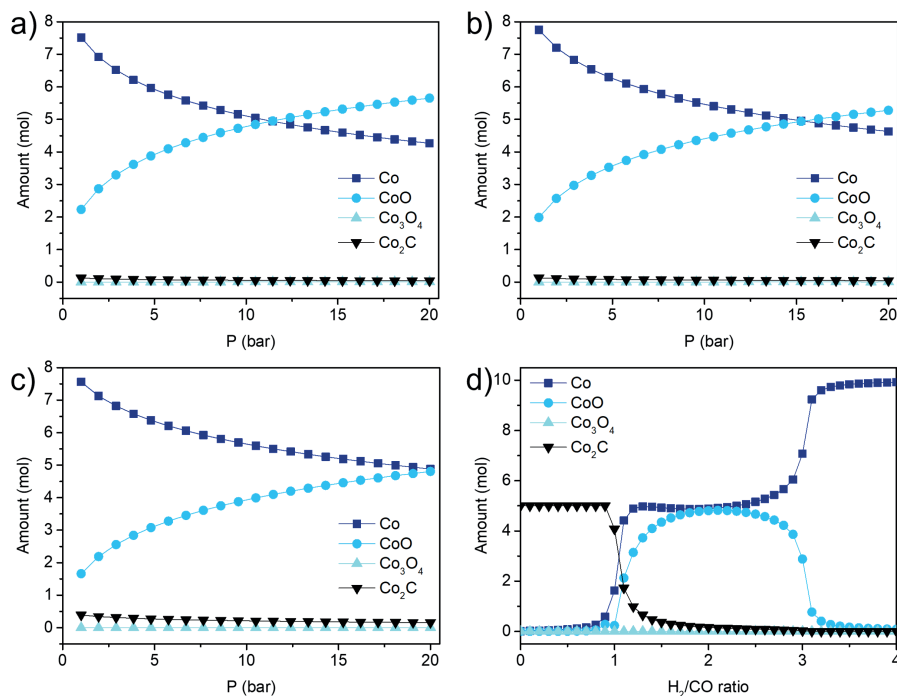


**Figure 4.15. Thermodynamic stability of different cobalt phases under relevant reaction conditions.** **a)** CO<sub>2</sub> hydrogenation at T=250°C and H<sub>2</sub>/CO<sub>2</sub>=3 while varying the pressure. **b)** T=250°C and H<sub>2</sub>/CO<sub>2</sub>/CO=9/2/1 while varying the pressure. **c)** Fischer-Tropsch Synthesis (FTS) at T=250°C and H<sub>2</sub>/CO=2 while varying the pressure. **d)** Varying the H<sub>2</sub>/CO ratio during FTS at T=250°C and P=20 bar.

Co-feeding CO/CO<sub>2</sub> mixtures may thus be a profitable method to directly produce long-chain hydrocarbons from CO<sub>2</sub> at industrial scale. To assess the long-term stability of the Co/TiO<sub>2</sub>-ox catalyst, it was tested at 250°C and 20 bar for 150 h in total: first for 50 h under CO/CO<sub>2</sub> co-feeding conditions (CO<sub>2</sub>/CO=2) and then for 100 h under CO<sub>2</sub> hydrogenation conditions (H<sub>2</sub>/CO<sub>2</sub>=3) (**Figure 4.12cd**). For the 50 h of co-feeding, the total carbon conversion started at ~18% and stabilized after about 10 h to ~16%, while the C<sub>2+</sub> selectivity started at ~40% and stabilized at ~35%. For the following 100 h of CO<sub>2</sub> conversion only, the conversion started at ~7.0% and remained ~4.5% after 100 h, while the C<sub>2+</sub> selectivity increased from ~10% in the first few h to ~20% after 100 h, indicating that the activity loss over time was mostly related to a decrease in methane production. The long-term stability of Co/TiO<sub>2</sub>-red over 150 h time-on-stream can be found in **Figure 4.14**. During the 50 h of co-feeding, the total carbon conversion started at ~18% and decreased to ~16% after 50 h, while the C<sub>2+</sub> selectivity started at ~10% and increased to ~13%. For the following 100 h of CO<sub>2</sub> conversion only, the conversion remained stable at ~5.0% during the 100 h, while the C<sub>2+</sub> selectivity remained stable

around ~5.0% during the 100 h. After 150 h time-on-stream, we verified with XRD that Co/TiO<sub>2</sub>-ox contained CoO and Co/TiO<sub>2</sub>-red contained metallic cobalt (face-centered cubic (FCC) (Figure 4.15).

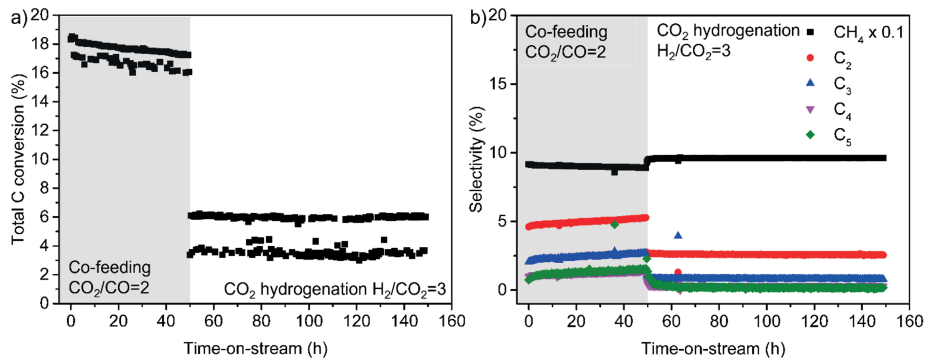


**Figure 4.16. Long-term stability test of the Co-TiO<sub>2</sub>-red catalyst material.** The reactor was operated for 150 h ( $T=250^{\circ}\text{C}$ ,  $P=20$  bar,  $\text{GHSV}=3000\text{ h}^{-1}$ ) **a)** is displaying conversion and **b)** selectivity first while co-feeding CO/CO<sub>2</sub> ( $\text{H}_2/\text{CO}_2/\text{CO}=9/2/1$ ) for 50 h and then during CO<sub>2</sub> hydrogenation only ( $\text{H}_2/\text{CO}_2=3$ ) for 100 h. The sample was treated at  $450^{\circ}\text{C}$  in  $\text{N}_2/\text{H}_2=2$  prior to the reaction.

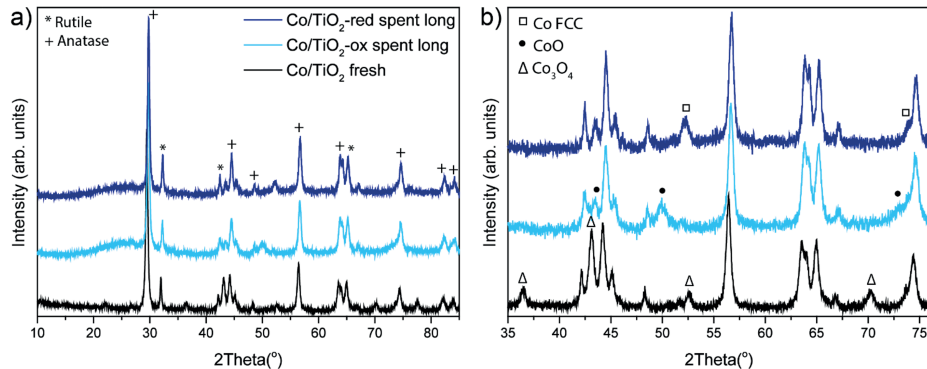


**Figure 4.17. X-ray diffraction (XRD) patterns of the Co/TiO<sub>2</sub> material after 150 h of catalytic testing.** XRD patterns **(a)** of Co/TiO<sub>2</sub> fresh (black), Co/TiO<sub>2</sub>-ox spent (pre-treated at  $250^{\circ}\text{C}$  in  $\text{N}_2/\text{H}_2=2$ ), and Co/TiO<sub>2</sub>-red spent (pre-treated at  $450^{\circ}\text{C}$  in  $\text{N}_2/\text{H}_2=2$ ). The diffraction lines of rutile and anatase are indicated with stars and plusses. The zoom-in **(b)** indicated Co<sub>3</sub>O<sub>4</sub> (triangles) in the fresh catalyst, while Co/TiO<sub>2</sub>-ox spent contained CoO (circles) and Co/TiO<sub>2</sub>-red spent face-centered cubic (FCC) metallic cobalt (squares). Note that the spent catalysts were passivated in 1 vol.% O<sub>2</sub>/Ar for 2 h at room temperature before they were taken out of the reactor.

## 4.4 Conclusions

In this **Chapter**, it was established that both metallic Co and CoO are active phases in the catalytic hydrogenation of CO and CO<sub>2</sub>. To investigate the influence of the support oxide, we have prepared a set of cobalt-based catalyst materials with both non-reducible supports (*i.e.*, SiO<sub>2</sub> and Al<sub>2</sub>O<sub>3</sub>) and reducible supports (*i.e.*, TiO<sub>2</sub> and CeO<sub>2</sub>). We have performed catalytic testing at industrially relevant conditions (*i.e.*, T=250°C and P=20 bar) and explained the observed phenomena by identifying active species using *operando* modulation excitation diffuse reflectance infrared Fourier-transform spectroscopy (ME DRIFTS). The TiO<sub>2</sub> support provided the optimum reducibility for weakening C-O bonds and resulted in the highest CO<sub>2</sub> hydrogenation activity. For most catalyst materials under study, metallic cobalt was more active than cobalt oxide, which is in accordance with the classical view of metallic cobalt as active phase. However, all catalyst materials with cobalt oxide were active as well. For Co/TiO<sub>2</sub>, the catalyst containing CoO was even more active than the catalyst containing only metallic Co. We have found that the catalyst materials with metallic Co mainly followed the direct dissociation pathway with adsorbed CO as a key surface intermediate. On the other hand, the catalyst materials with CoO mainly followed the H-assisted pathway *via* surface carbonate, formate, and formyl species. Although the direct dissociation was kinetically faster compared to the H-assisted pathway, the latter seemed more beneficial for the production of C<sub>2+</sub> hydrocarbons. The fundamental insights obtained here provide a paradigm shift in the classical view of the catalytically active phase. This has implications for the catalytic industry, as reductive pre-treatments at elevated temperature may not always be necessary. For the best catalyst in this **Chapter**, CoO/TiO<sub>2</sub>, we have managed to double the CO<sub>2</sub> conversion and to shift the selectivity to C<sub>2+</sub> hydrocarbons from 11% to 39% by co-feeding CO and CO<sub>2</sub> at a ratio of 1:2. This led to a high overall C<sub>2+</sub> yield of 104 mmol h<sup>-1</sup> g<sub>cat</sub><sup>-1</sup> at T=250°C, P=20 bar, and a gas hourly space velocity (GHSV) of 3000 h<sup>-1</sup>. This can thus be a promising way for industrial applications to directly produce long-chain hydrocarbons, instead of methane, from CO<sub>2</sub>.

## 4.5. Author Contributions and Acknowledgments

This Chapter is based on the manuscript "ten Have, I. C., Kromwijk, J. J.G., Monai, M., Ferri, D., Sterk, E. B., Meirer, F., Weckhuysen B. M. (2022). Uncovering the Reaction Mechanism behind CoO as Active Phase in CO<sub>2</sub> Hydrogenation, *Nature Communications* 13, 324."

Iris ten Have and Joyce Kromwijk synthesized the catalysts and performed catalytic testing. Joyce Kromwijk performed the XRD measurements and Raman experiments. Iris ten Have and Matteo Monai performed the ME DRIFTS measurements. Davide Ferri

facilitated the ME DRIFTS measurements and Florian Meirer facilitated the ME DRIFTS data analysis. Ellen Sterk performed DFT calculations. Bert Weckhuysen directed the research. Iris ten Have wrote the manuscript with input from all co-authors.

Ramon Oord (Utrecht University, UU) is gratefully acknowledged for technical support regarding the catalytic testing set-up. Mark J. Meijerink (UU) and Nienke L. Visser (UU) are acknowledged for the TEM measurements. Jelle Kranenburg (UU) is thanked for help with the ME DRIFTS experiments. Maarten Nachtegaal (Paul Scherrer Institute) is thanked for providing access to the offline laboratory of the SuperXAS beamline for the ME DRIFTS experiments. Sander van Bavel (Shell Global Solutions International B.V.) is thanked for the fruitful discussions on the topic. Jaap Louwen (UU) is gratefully acknowledged for his input on and assistance with the DFT calculations.

## 4.6 References

1. Aziz, M. A. A., Jalil, A. A., Triwahyono, S. & Ahmad, A. CO<sub>2</sub> methanation over heterogeneous catalysts: recent progress and future prospects. *Green Chemistry* **17**, 2647–2663 (2015).
2. Ronda-Lloret, M., Rothenberg, G. & Shiju, N. R. A Critical Look at Direct Catalytic Hydrogenation of Carbon Dioxide to Olefins. *ChemSusChem* **12**, 3896–3914 (2019).
3. Stavitski, E. *et al.* Complexity behind CO<sub>2</sub> capture on NH<sub>2</sub>-MIL-53(Al). *Langmuir* **27**, 3970–3976 (2011).
4. Chen, W. Y., Suzuki, T. & Lackner, M. *Handbook of climate change mitigation and adaptation. Springer International Publishing 9783319144092*, (Berlin, 2017).
5. Wang, W., Wang, S., Ma, X. & Gong, J. Recent advances in catalytic hydrogenation of carbon dioxide. *Chemical Society Reviews* **40**, 3703–3727 (2011).
6. Li, W. *et al.* A short review of recent advances in CO<sub>2</sub> hydrogenation to hydrocarbons over heterogeneous catalysts. *RSC Advances* **8**, 7651–7669 (2018).
7. Luk, H. T., Mondelli, C., Ferre, C., Stewart, J. A. & Pe, J. Status and prospects in higher alcohols synthesis from syngas. *Chemical Society Reviews* **46**, 1358–1426 (2016).
8. Martin, O. *et al.* Heterogeneous Catalysis Operando Synchrotron X-ray Powder Diffraction and Modulated-Excitation Infrared Spectroscopy Elucidate the CO<sub>2</sub> Promotion on a Commercial Methanol Synthesis Catalyst. *Angewandte Chemie International Edition* **55**, 11031–11036 (2016).
9. Tu, W., Zhou, Y. & Zou, Z. Photocatalytic conversion of CO<sub>2</sub> into renewable hydrocarbon fuels: State-of-the-art accomplishment, challenges, and prospects. *Advanced Materials* **26**, 4607–4626 (2014).
10. Nitopi, S. *et al.* Progress and Perspectives of Electrochemical CO<sub>2</sub> Reduction on Copper in Aqueous Electrolyte. *Chemical Reviews* **119**, 7610–7672 (2019).
11. Timoshenko, J. & Roldan Cuenya, B. In Situ/Operando Electrocatalyst Characterization by X-ray Absorption Spectroscopy. *Chemical Reviews* **121**, 882–961 (2021).
12. Gao, D., Arán-Ais, R. M., Jeon, H. S. & Roldan Cuenya, B. Rational catalyst and electrolyte design for CO<sub>2</sub> electroreduction towards multicarbon products. *Nature Catalysis* **2**, 198–210 (2019).
13. Dorner, R. W., Hardy, D. R., Williams, F. W. & Willauer, H. D. Heterogeneous catalytic CO<sub>2</sub> conversion to value-added hydrocarbons. *Energy and Environmental Science* **3**, 884–890 (2010).
14. Ye, R. P. *et al.* CO<sub>2</sub> hydrogenation to high-value products via heterogeneous catalysis. *Nature Communications* **10**, 5698 (2019).
15. Yao, B. *et al.* Transforming carbon dioxide into jet fuel using an organic combustion-synthesized Fe-Mn-K catalyst. *Nature Communications* **11**, 6395 (2020).
16. Luna, M. L. *et al.* Role of the Oxide Support on the Structural and Chemical Evolution of Fe Catalysts during the Hydrogenation of CO<sub>2</sub>. *ACS Catalysis* **11**, 6175–6185 (2021).
17. Álvarez, A. *et al.* Challenges in the Greener Production of Formates/Formic Acid, Methanol, and DME by Heterogeneously Catalyzed CO<sub>2</sub> Hydrogenation Processes. *Chemical Reviews* **117**, 9804–9838 (2017).
18. Hahn, C. *et al.* Engineering Cu surfaces for the electrocatalytic conversion of CO<sub>2</sub>: Controlling selectivity toward oxygenates and hydrocarbons. *Proceedings of the National Academy of Sciences of the United States of America* **114**, 5918–5923 (2017).
19. Dinh, C. T. *et al.* CO<sub>2</sub> electroreduction to ethylene via hydroxide-mediated copper catalysis at an abrupt interface. *Science* **360**, 783–787 (2018).



20. Vogt, C., Monai, M., Kramer, G. J. & Weckhuysen, B. M. The renaissance of the Sabatier reaction and its applications on Earth and in space. *Nature Catalysis* **2**, 188-197 (2019).
21. Vogt, C. *et al.* Unravelling structure sensitivity in CO<sub>2</sub> hydrogenation over nickel. *Nature Catalysis* **1**, 127-134 (2018).
22. Stangeland, K., Kalai, D., Li, H. & Yu, Z. CO<sub>2</sub> Methanation: The Effect of Catalysts and Reaction Conditions. *Energy Procedia* **105**, 2022-2027 (2017).
23. Vogt, C. *et al.* Understanding carbon dioxide activation and carbon-carbon coupling over nickel. *Nature Communications* **10**, 5330 (2019).
24. Bushuyev, O. S. *et al.* What Should We Make with CO<sub>2</sub> and How Can We Make It? *Joule* **2**, 825-832 (2018).
25. van de Loosdrecht, J. *et al.* Fischer-Tropsch Synthesis: Catalysts and Chemistry. in *Comprehensive Inorganic Chemistry II: from elements to applications* vol. 7 525-557 (Elsevier, Amsterdam, 2013).
26. Bezemer, G. L. *et al.* Cobalt particle size effects in the Fischer-Tropsch reaction studied with carbon nanofiber supported catalysts. *Journal of the American Chemical Society* **128**, 3956-3964 (2006).
27. Melaet, G., Lindeman, A. E. & Somorjai, G. A. Cobalt particle size effects in the Fischer-Tropsch synthesis and in the hydrogenation of CO<sub>2</sub> studied with nanoparticle model catalysts on silica. *Topics in Catalysis* **57**, 500-507 (2014).
28. Prieto, G., Martínez, A., Concepción, P. & Moreno-Tost, R. Cobalt particle size effects in Fischer-Tropsch synthesis: structural and in situ spectroscopic characterisation on reverse micelle-synthesised Co/ITQ-2 model catalysts. *Journal of Catalysis* **266**, 129-144 (2009).
29. Iablokov, V. *et al.* Size-controlled model Co nanoparticle catalysts for CO<sub>2</sub> hydrogenation: Synthesis, characterization, and catalytic reactions. *Nano Letters* **12**, 3091-3096 (2012).
30. Ravenhorst, van Ravenhorst, I.K. *et al.* Capturing the Genesis of an Active Fischer-Tropsch Synthesis Catalyst with Operando X-ray Nano-Spectroscopy. *Angewandte Chemie International Edition* **57**, 11957-11962 (2018).
31. van Ravenhorst, I. K. *et al.* On the Cobalt Carbide Formation in a Co/TiO<sub>2</sub> Fischer-Tropsch Synthesis Catalyst as Studied by High-Pressure, Long-Term Operando X-ray Absorption and Diffraction. *ACS Catalysis* **11**, 2956-2967 (2021).
32. Melaet, G. *et al.* Evidence of highly active cobalt oxide catalyst for the Fischer-Tropsch synthesis and CO<sub>2</sub> hydrogenation. *Journal of the American Chemical Society* **136**, 2260-2263 (2014).
33. Li, C. S. *et al.* High-performance hybrid oxide catalyst of manganese and cobalt for low-pressure methanol synthesis. *Nature Communications* **6**, 6538 (2015).
34. He, Z. H. *et al.* Photothermal CO<sub>2</sub> hydrogenation to methanol over a CoO/Co/TiO<sub>2</sub> catalyst in aqueous media under atmospheric pressure. *Catalysis Today* **356**, 579-588 (2020).
35. Wang, L. *et al.* Selective hydrogenation of CO<sub>2</sub> into ethanol over cobalt catalysts. *Angewandte Chemie International Edition* **130**, 6212-6216 (2018).
36. Wang, L. *et al.* Silica accelerates the selective hydrogenation of CO<sub>2</sub> to methanol on cobalt catalysts. *Nature Communications* **11**, 1033 (2020).
37. Parastaev, A. *et al.* Boosting CO<sub>2</sub> hydrogenation via size-dependent metal-support interactions in cobalt/ceria-based catalysts. *Nature Catalysis* **3**, 526-533 (2020).
38. Saeidi, S. *et al.* Mechanisms and kinetics of CO<sub>2</sub> hydrogenation to value-added products: A detailed review on current status and future trends. *Renewable and Sustainable Energy Reviews* **80**, 1292-1311 (2017).

39. Ojelade, O. A. & Zaman, S. F. A review on CO<sub>2</sub> hydrogenation to lower olefins: Understanding the structure-property relationships in heterogeneous catalytic systems. *Journal of CO<sub>2</sub> Utilization* **47**, 101506 (2021).
40. Wang, L. *et al.* Cobalt-Nickel Catalysts for Selective Hydrogenation of Carbon Dioxide into Ethanol. *ACS Catalysis* **9**, 11335-11340 (2019).
41. Blöchl, P. E. Projector augmented-wave method. *Physical Review B* **50**, 17953-17979 (1994).
42. Joubert, D. From ultrasoft pseudopotentials to the projector augmented-wave method. *Physical Review B - Condensed Matter and Materials Physics* **59**, 1758-1775 (1999).
43. Perdew, J. P., Burke, K. & Ernzerhof, M. Generalized gradient approximation made simple. *Physical Review Letters* **77**, 3865-3868 (1996).
44. Kresse, G. & Furthmüller, J. Efficient iterative schemes for ab initio total-energy calculations using a plane-wave basis set. *Physical Review B - Condensed Matter and Materials Physics* **54**, 11169-11186 (1996).
45. Kresse, G. & Hafner, J. Ab initio molecular-dynamics simulation of the liquid-metal-amorphous-semiconductor transition in germanium. *Physical Review B* **49**, 14251-14269 (1994).
46. Häglund, J., Fernández Guillermet, A., Grimvall, G. & Körling, M. Theory of bonding in transition-metal carbides and nitrides. *Physical Review B* **48**, 11685-11691 (1993).
47. Jauch, W., Reehuis, M., Bleif, H. J., Kubanek, F. & Pattison, P. Crystallographic symmetry and magnetic structure of CoO. *Physical Review B - Condensed Matter and Materials Physics* **64**, 2-4 (2001).
48. Monkhorst, H. J. M. & Pack, J. D. Special points for Brillouin-zone integrations. *Journal of Materials Chemistry A* **13**, 5188-5192 (1976).
49. Methfessel, M. & Paxton, A. T. High-precision sampling for Brillouin-zone integration in metals. *Physical Review B* **40**, 3616-3621 (1989).
50. Zhou, C. *et al.* Highly Active ZnO-ZrO<sub>2</sub> Aerogels Integrated with H-ZSM-5 for Aromatics Synthesis from Carbon Dioxide. *ACS Catalysis* **10**, 302-310 (2020).
51. Chiarello, G. L., Nachttegaal, M., Marchionni, V., Quaroni, L. & Ferri, D. Adding diffuse reflectance infrared Fourier transform spectroscopy capability to extended X-ray-absorption fine structure in a new cell to study solid catalysts in combination with a modulation approach. *Review of Scientific Instruments* **85**, 074102 (2014).
52. Baurecht, D. & Fringeli, U. P. Quantitative modulated excitation Fourier transform infrared spectroscopy. *Review of Scientific Instruments* **72**, 3782-3792 (2001).
53. Zhang, M., Wang, M., Xu, B. & Ma, D. How to Measure the Reaction Performance of Heterogeneous Catalytic Reactions Reliably. *Joule* **3**, 2876-2883 (2019).
54. White, W. B., Johnson, S. M. & Dantzig, G. B. Chemical equilibrium in complex mixtures. *The Journal of Chemical Physics* **28**, 751-755 (1958).
55. Khodakov, A. Y., Chu, W. & Fongarland, P. Advances in the development of novel cobalt Fischer-Tropsch catalysts for synthesis of long-chain hydrocarbons and clean fuels. *Chemical Reviews* **107**, 1692-1744 (2007).
56. Ernst, B., Libs, S., Chaumette, P. & Kiennemann, A. Preparation and characterization of Fischer-Tropsch active Co/SiO<sub>2</sub> catalysts. *Applied Catalysis A: General* **186**, 145-168 (1999).
57. Quindimil, A. *et al.* Effect of metal loading on the CO<sub>2</sub> methanation: A comparison between alumina supported Ni and Ru catalysts. *Catalysis Today* **356**, 419-432 (2020).

58. Koo, K. Y., Lee, S. H., Jung, U. H., Roh, H. S. & Yoon, W. L. Syngas production via combined steam and carbon dioxide reforming of methane over Ni-Ce/MgAl<sub>2</sub>O<sub>4</sub> catalysts with enhanced coke resistance. *Fuel Processing Technology* **119**, 151–157 (2014).
59. Kriesel, J. W. & Tilley, T. D. A new molecular precursor for magnesia-silica materials. *Journal of Materials Chemistry* **11**, 1081–1085 (2001).
60. Prymak, I., Kalevaru, V. N., Wohlrab, S. & Martin, A. Continuous synthesis of diethyl carbonate from ethanol and CO<sub>2</sub> over Ce-Zr-O catalysts. *Catalysis Science and Technology* **5**, 2322–2331 (2015).
61. Martin, D. & Duprez, D. Mobility of Surface Species on Oxides. 1. Isotopic Exchange of <sup>18</sup>O<sub>2</sub> with <sup>16</sup>O of SiO<sub>2</sub>, Al<sub>2</sub>O<sub>3</sub>, ZrO<sub>2</sub>, MgO, CeO<sub>2</sub>, and CeO<sub>2</sub>-Al<sub>2</sub>O<sub>3</sub>. *Journal of Physical Chemistry* **100**, 9429–9438 (1996).
62. Kydd, R., Teoh, W. Y., Scott, J., Ferri, D. & Amal, R. Probing surface properties and reaction intermediates during heterogeneous catalytic oxidation of acetaldehyde. *ChemCatChem* **1**, 286–294 (2009).
63. Lavalley, J. C. Infrared spectrometric studies of the surface basicity of metal oxides and zeolites using adsorbed probe molecules. *Catalysis Today* **27**, 377–401 (1996).
64. Tomishige, K. *et al.* Catalytic performance and properties of ceria based catalysts for cyclic carbonate synthesis from glycol and carbon dioxide. *Green Chemistry* **6**, 206–214 (2004).
65. Ferri, D., Newton, M. A. & Nachtegaal, M. Modulation Excitation X-Ray Absorption Spectroscopy to Probe Surface Species on Heterogeneous Catalysts. *Topics in Catalysis* **54**, 1070–1078 (2011).
66. Müller, P. & Hermans, I. Applications of Modulation Excitation Spectroscopy in Heterogeneous Catalysis. *Industrial & Engineering Chemistry Research* **56**, 1123–1136 (2017).
67. Bürgi, T. & Baiker, A. In situ infrared spectroscopy of catalytic solid-liquid interfaces using phase-sensitive detection: Enantioselective hydrogenation of a pyrone over Pd/TiO<sub>2</sub>. *Journal of Physical Chemistry B* **106**, 10649–10658 (2002).
68. Urakawa, A., Wirz, R., Bu, T. & Baiker, A. ATR-IR Flow-Through Cell for Concentration Modulation Excitation Spectroscopy : Diffusion Experiments and Simulations. *Journal of Physical Chemistry B* **107**, 13061–13068 (2003).
69. Rehr, J. J., Kas, J. J., Vila, F. D., Prange, M. P. & Jorissen, K. Parameter-free calculations of X-ray spectra with FEFF9. *Physical Chemistry Chemical Physics* **12**, 5503–5513 (2010).
70. Szanyi, J. & Kwak, J. H. Dissecting the steps of CO<sub>2</sub> reduction: 1. The interaction of CO and CO<sub>2</sub> with γ-Al<sub>2</sub>O<sub>3</sub>: An in situ FTIR study. *Physical Chemistry Chemical Physics* **16**, 15117–15125 (2014).
71. Karim, W. *et al.* Catalyst support effects on hydrogen spillover. *Nature* **541**, 68–71 (2017).
72. Hartman, T., Geitenbeek, R. G., Whiting, G. T. & Weckhuysen, B. M. Operando monitoring of temperature and active species at the single catalyst particle level. *Nature Catalysis* **2**, 986–996 (2019).
73. Srinivasan, P. D., Patil, B. S., Zhu, H. & Bravo-Suárez, J. J. Application of modulation excitation-phase sensitive detection-DRIFTS for: In situ /operando characterization of heterogeneous catalysts. *Reaction Chemistry and Engineering* **4**, 862–883 (2019).
74. Kantcheva, M., Kucukkal, M. U. & Suzer, S. Spectroscopic investigation of species arising from CO chemisorption on titania-supported manganese. *Journal of Catalysis* **190**, 144–156 (2000).
75. Aguirre, A. & Collins, S. E. Selective detection of reaction intermediates using concentration-modulation excitation DRIFT spectroscopy. *Catalysis Today* **205**, 34–40 (2013).
76. Vrijburg, W. L. *et al.* Efficient Base-Metal NiMn/TiO<sub>2</sub> Catalyst for CO<sub>2</sub> Methanation. *ACS Catalysis* **9**, 7823–7839 (2019).

77. Li, M. R. & Wang, G. C. The mechanism of ethanol steam reforming on the Co<sup>0</sup> and Co<sup>2+</sup> sites: A DFT study. *Journal of Catalysis* **365**, 391-404 (2018).
78. de la Peña O'Shea, V. A., González, S., Illas, F. & Fierro, J. L. G. Evidence for spontaneous CO<sub>2</sub> activation on cobalt surfaces. *Chemical Physics Letters* **454**, 262-268 (2008).
79. Pang, X. Y., Liu, C., Li, D. C., Lv, C. Q. & Wang, G. C. Structure sensitivity of CO oxidation on Co<sub>3</sub>O<sub>4</sub>: A DFT study. *ChemPhysChem* **14**, 204-212 (2013).
80. Nie, X. *et al.* DFT insight into the support effect on the adsorption and activation of key species over Co catalysts for CO<sub>2</sub> methanation. *Journal of CO<sub>2</sub> Utilization* **24**, 99-111 (2018).
81. Marchionni, V., Ferri, D., Kröcher, O. & Wokaun, A. Increasing the Sensitivity to Short-Lived Species in a Modulated Excitation Experiment. *Analytical Chemistry* **89**, 5801-5809 (2017).
82. Guo, Y. *et al.* Low-Temperature CO<sub>2</sub> Methanation over CeO<sub>2</sub>-Supported Ru Single Atoms, Nanoclusters, and Nanoparticles Competitively Tuned by Strong Metal-Support Interactions and H-Spillover Effect. *ACS Catalysis* **8**, 6203-6215 (2018).
83. Mutschler, R., Moiola, E. & Züttel, A. Modelling the CO<sub>2</sub> hydrogenation reaction over Co, Ni and Ru/Al<sub>2</sub>O<sub>3</sub>. *Journal of Catalysis* **375**, 193-201 (2019).
84. Owen, R. E. *et al.* Cobalt catalysts for the conversion of CO<sub>2</sub> to light hydrocarbons at atmospheric pressure. *Chemical Communications* **49**, 11683-11685 (2013).
85. Owen, R. E. *et al.* Effect of support of Co-Na-Mo catalysts on the direct conversion of CO<sub>2</sub> to hydrocarbons. *Journal of CO<sub>2</sub> Utilization* **16**, 97-103 (2016).
86. He, Z. *et al.* Synthesis of liquid fuel via direct hydrogenation of CO<sub>2</sub>. *Proceedings of the National Academy of Sciences of the United States of America* **116**, 12654-12659 (2019).
87. Dorner, R. W., Hardy, D. R., Williams, F. W., Davis, B. H. & Willauer, H. D. Influence of Gas Feed Composition and Pressure on the Catalytic Conversion of CO<sub>2</sub> to Hydrocarbons Using a Traditional Cobalt-Based Fischer-Tropsch Catalyst. *Energy and Fuels* **23**, 4190-4195 (2009).
88. Choi, Y. H. *et al.* Carbon dioxide Fischer-Tropsch synthesis: A new path to carbon-neutral fuels. *Applied Catalysis B: Environmental* **202**, 605-610 (2017).
89. Iloy, R. A. & Jalama, K. Effect of Operating Temperature, Pressure and Silica-Supported Cobalt Catalyst in CO<sub>2</sub> Hydrogenation to Hydrocarbon Fuel. *Catalysts* **9**, 807 (2019).
90. Shi, Z. *et al.* Direct conversion of CO<sub>2</sub> to long-chain hydrocarbon fuels over K-promoted CoCu/TiO<sub>2</sub> catalysts. *Catalysis Today* **311**, 65-73 (2018).
91. Yao, Y., Hildebrandt, D., Glasser, D. & Liu, X. Fischer-Tropsch Synthesis Using H<sub>2</sub>/CO/CO<sub>2</sub> Syngas Mixtures over a Cobalt Catalyst. *Industrial and Engineering Chemistry Research* **49**, 11061-11066 (2010).
92. Numpilai, T. *et al.* Structure-activity relationships of Fe-Co/K-Al<sub>2</sub>O<sub>3</sub> catalysts calcined at different temperatures for CO<sub>2</sub> hydrogenation to light olefins. *Applied Catalysis A: General* **547**, 219-229 (2017).
93. Dong, Z., Zhao, J., Tian, Y., Zhang, B. & Wu, Y. Preparation and performances of ZIF-67-derived FeCo bimetallic catalysts for CO<sub>2</sub> hydrogenation to light olefins. *Catalysts* **10**, 455 (2020).
94. Sathawong, R., Koizumi, N., Song, C. & Prasassarakich, P. Bimetallic Fe-Co catalysts for CO<sub>2</sub> hydrogenation to higher hydrocarbons. *Journal of CO<sub>2</sub> Utilization* **3-4**, 102-106 (2013).
95. Díaz, J. A., De La Osa, A. R., Sánchez, P., Romero, A. & Valverde, J. L. Influence of CO<sub>2</sub> co-feeding on Fischer-Tropsch fuels production over carbon nanofibers supported cobalt catalyst. *Catalysis Communications* **44**, 57-61 (2014).
96. Lu, J. *et al.* Promotion effects of nitrogen doping into carbon nanotubes on supported iron Fischer-Tropsch catalysts for lower olefins. *ACS Catalysis* **4**, 613-621 (2014).

97. Li, Z. *et al.* Mechanism of the Mn Promoter via CoMn Spinel for Morphology Control: Formation of Co<sub>2</sub>C Nanoprisms for Fischer-Tropsch to Olefins Reaction. *ACS Catalysis* **7**, 8023-8032 (2017).
98. Morales, F. & Weckhuysen, B. M. Promotion Effects in Co-based Fischer-Tropsch Catalysis. *Catalysis* **19**, 1-40 (2006).
99. Athariboroujeny, M. *et al.* Competing Mechanisms in CO Hydrogenation over Co-MnO<sub>x</sub> Catalysts. *ACS Catalysis* **9**, 5603-5612 (2019).
100. Morales, F., de Smit, E., de Groot, F. M. F., Visser, T. & Weckhuysen, B. M. Effects of manganese oxide promoter on the CO and H<sub>2</sub> adsorption properties of titania-supported cobalt Fischer-Tropsch catalysts. *Journal of Catalysis* **246**, 91-99 (2007).
101. Morales, F. *et al.* In Situ X-ray Absorption of Co/Mn/TiO<sub>2</sub> Catalysts for Fischer-Tropsch Synthesis. *The Journal of Physical Chemistry B* **108**, 16201-16207 (2004).
102. Zhao, Z. *et al.* Tuning the Fischer-Tropsch reaction over Co<sub>x</sub>Mn<sub>y</sub>La/AC catalysts toward alcohols: Effects of La promotion. *Journal of Catalysis* **361**, 156-167 (2018).



# **CHAPTER 5**

## **POTASSIUM PROMOTER EFFECTS IN COBALT-BASED CATALYTIC HYDROGENATION OF CO AND CO<sub>2</sub>**



**Abstract**

Promoters are used in heterogeneous catalysis to enhance or suppress specific catalytic properties. Promoter elements are typically added in small quantities to the default catalyst formulation of metal (oxide) nanoparticles on a stabilizing support material. Alkali metals, like potassium, are used in many commercial catalyst formulations, including iron-based Fischer-Tropsch Synthesis (FTS) catalyst materials to enhance the hydrocarbon product chain length, diminish unwanted methane formation, and increase the olefin to paraffin ratio. While some interesting effects have been reported in the academic literature, alkali metals are to the best of our knowledge currently not added to commercial cobalt-based FTS catalyst formulations. Although commercialization of CO<sub>2</sub> hydrogenation processes is still in its infancy, promising results have been reported for potassium-promoted iron-based CO<sub>2</sub> hydrogenation in the literature. The number of studies on potassium promoter effects on cobalt-based CO<sub>2</sub> hydrogenation is, however, limited. In this **Chapter**, potassium promoter effects in the cobalt-based CO and CO<sub>2</sub> hydrogenation will be investigated and discussed. The addition of K as promoter element to Co/TiO<sub>2</sub> had a detrimental effect on the CO hydrogenation performance, as the overall CO conversion rate and C-C coupling rate decreased. For CO<sub>2</sub> hydrogenation, however, K appeared beneficial as the C<sub>2+</sub> hydrocarbons yield increased.



## 5.1 Introduction

In **Chapter 1**, we have concluded that most researchers hold metallic cobalt (Co) responsible as the catalytically active phase in the Fischer-Tropsch Synthesis (FTS) reaction towards linear paraffins.<sup>1</sup> However, we have also briefly mentioned that Co<sub>2</sub>C has been reported as a highly active phase in the cobalt-based FTS towards olefins<sup>2-5</sup> or oxygenates.<sup>3,6-10</sup> All these studies mentioned that Co<sub>2</sub>C was stabilized by and in synergy with an oxidic compound, like MnO<sup>2-5,9,11-15</sup> or La<sub>2</sub>O<sub>3</sub>,<sup>7,16</sup> and/or an alkali promoter.<sup>3,6,17</sup> For iron-based catalyst materials, it is well-established that alkali promoters, such as sodium (Na)<sup>18,19</sup> and potassium (K)<sup>20,21</sup>, act as structural stabilizers for the formation of iron carbides<sup>18-21</sup> and improve overall catalyst performance<sup>22</sup>. As cobalt carbides are intrinsically less stable than iron carbides,<sup>23</sup> the presence of an alkali metal may even be more essential for stabilization of the cobalt carbide phase.

Even though interesting effects have been reported in the academic literature,<sup>3,6,17</sup> alkali promoters are typically not used in cobalt-based catalyst formulations, as can be noted in various patents filed by several industrial FTS companies.<sup>24</sup> Possible reasons for this could be that alkali metals increase the cobalt reduction temperature<sup>25</sup> or that the addition of alkali metals decreases the FTS reaction rate.<sup>22</sup> For CO<sub>2</sub> hydrogenation, on the other hand, it has been reported that addition of K to a cobalt-based catalyst material drastically decreases the selectivity towards the unwanted product methane, while producing more desired long-chain hydrocarbons.<sup>26</sup>

This Chapter investigates the effects of K as promoter element on the cobalt-catalyzed CO and CO<sub>2</sub> hydrogenation. We demonstrate that K addition could be particularly interesting for sustainable industrial processes that aim to convert CO<sub>2</sub> into long-chain hydrocarbons. The effects of the K promoter are also compared to the effects of MnO as promoter, which is currently used in industrial cobalt-based catalyst formulations,<sup>24</sup> and to the effects induced by CoO instead of metallic Co as catalytically active phase.

## 5.2 Materials and Methods

### 5.2.1 Catalyst Synthesis

A 10 wt.% Co/TiO<sub>2</sub> catalyst with 14.6 nm average Co<sub>3</sub>O<sub>4</sub> crystallite size (**Chapter 4**) was synthesized via incipient wetness impregnation (IWI), as described in **Chapters 3** and **4**. This starting catalyst material was then impregnated with a KNO<sub>3</sub> solution and calcined at 250°C in flowing N<sub>2</sub> for 1 h to create a 0.4 wt.% K loading. Another set of unpromoted, Mn-promoted, and K-promoted 10 wt.% Co/TiO<sub>2</sub> catalyst materials was prepared via deposition precipitation (DP), indicated with suffix -DP throughout this

**Chapter.** An aqueous solution of  $\text{Co}(\text{NO}_3)_2 \cdot 6\text{H}_2\text{O}$  (1.01 g), urea (2.68 g) and  $\text{TiO}_2$  support (1.81 g) was added to a double-walled vessel. The vessel was heated to a temperature of  $94^\circ\text{C}$  via the double walls. In this way, the temperature within the vessel could reach  $90^\circ\text{C}$ , the decomposition temperature of urea. As a consequence, the pH of the mixture slowly increased under continuous stirring with a mechanical stirrer at 500 rpm for 20 h. Subsequently, the suspension was poured in a centrifuge tube. The suspension was washed with water and centrifuged twice at 4000 rpm for 5 min. The remaining powder was dried overnight at  $60^\circ\text{C}$ . After drying, the solid was crushed with a mortar to obtain a powder. The powder was calcined at  $400^\circ\text{C}$  for 4 h (heating ramp of  $5^\circ\text{C min}^{-1}$ ) in a tubular furnace in a  $100 \text{ mL min}^{-1} \text{ N}_2$  flow. To prepare the Mn-Co/ $\text{TiO}_2$ -DP (Mn/Co=0.2 molar ratio, 1.8 wt.% Mn) and K-Co/ $\text{TiO}_2$ -DP (K/Co=0.2 molar ratio, 1.3 wt.% K) catalyst materials, the sample was subsequently impregnated to incipient wetness with a  $\text{Mn}(\text{NO}_3)_2 \cdot 6\text{H}_2\text{O}$  solution or a  $\text{KNO}_3$  solution, respectively. The samples were calcined again at  $400^\circ\text{C}$  for 4 h (heating ramp of  $5^\circ\text{C min}^{-1}$ ) in a tubular furnace in a  $100 \text{ mL min}^{-1} \text{ N}_2$  flow.

### 5.2.2 Catalyst Characterization

X-ray diffraction (XRD) patterns were recorded using a Bruker D2 phaser instrument equipped with a Co radiation source ( $\lambda = 1.789 \text{ \AA}$ ). XRD patterns were recorded between  $5$  and  $85^\circ 2\theta$  with an increment of  $0.05^\circ$  and 1 s per step. The average Co crystallite size was calculated with the  $43^\circ$  XRD peak using the Bruker EVA software.

Transmission electron microscopy (TEM) was performed with a FEI Talos F200X instrument. The TEM samples were prepared suspending the catalyst materials in absolute ethanol using sonication. Consequently, the suspension was drop-casted on a carbon/formvar-coated Cu grid (200 mesh). The microscope was operated at 200 kV and equipped with a high-brightness field emission gun (X-FEG) and a Super-X G2 energy dispersive X-ray (EDX) detector. The samples were analyzed with scanning (S) TEM combined with high-angle annular dark-field (HAADF-STEM). To determine the average cobalt particle size, the STEM images were analyzed using the ImageJ software.

$\text{H}_2$  chemisorption was measured using a Micrometrics ASAP 2020 C.  $\sim 100$  mg of catalyst was either heated to  $250^\circ\text{C}$  to create CoO or to  $450^\circ\text{C}$  to create metallic Co (both with  $5^\circ\text{C min}^{-1}$  ramps) in pure  $\text{H}_2$  and held there for 1 h. The samples were cooled down to  $150^\circ\text{C}$  ( $10^\circ\text{C min}^{-1}$  ramp). At this temperature, the samples were evacuated for 1 h in He. After evacuation, the samples were exposed to  $\text{H}_2$  at increasing pressures up to 680 mbar to analyze the chemisorption of  $\text{H}_2$ .

### 5.2.3 Catalyst Testing

Catalyst testing was performed using a stainless-steel fixed bed reactor. Typically, 200 mg of catalyst was mixed with 200 mg SiC (Alpha Aesar, no. A14470, 300-425  $\mu\text{m}$ ) and positioned in between two quartz wool plugs. Prior to catalytic testing, the samples were reduced for 1 h in  $\text{N}_2/\text{H}_2=2$  at 250°C to create the CoO (suffix: -ox) phase or at 450°C to create metallic Co (suffix: -red). CO<sub>2</sub> hydrogenation was carried out at 250°C and 20 bar with  $\text{H}_2/\text{CO}_2=3$ , while CO hydrogenation was performed at 220°C and 20 bar with  $\text{H}_2/\text{CO}=2$ . The catalytic performance was assessed using gas chromatography (GC) with one injection per 23 min as described in **Chapter 4**. The activation energies were determined by varying between 220 and 280°C at  $P=20$  bar and  $\text{H}_2/\text{CO}_2=3$  for CO<sub>2</sub> hydrogenation and between 180 and 220°C at  $P=20$  bar and  $\text{H}_2/\text{CO}=2$  for FTS. The measured intrinsic rates were used to calculate the apparent activation energy ( $E_a$ ) according to the Arrhenius equation (**Equation (5.1)**)<sup>27</sup>, where  $k$  is the rate constant,  $A$  is the pre-exponential factor,  $R$  the universal gas constant, and  $T$  the absolute temperature in Kelvin.

$$k = Ae^{-E_a/RT} \quad (\text{Equation 5.1})$$

## 5.3 Results and Discussion

### 5.3.1 Catalytic Performance

The catalytic activities and product distributions during CO<sub>2</sub> hydrogenation, co-feeding of CO<sub>2</sub>/CO=2, and CO hydrogenation were assessed for the K-Co/TiO<sub>2</sub> (0.4 wt.% K, 10 wt.% Co) material and compared to the results obtained with its unpromoted Co/TiO<sub>2</sub> counterpart (**Figure 5.1** and **Table 5.1**). The catalysts, prepared using the IWI method, had an average cobalt crystallite size of 14.6 nm, as determined with XRD, and an average cobalt nanoparticle size of 17 nm, as determined with STEM-EDX (**Chapter 4**). For the CO<sub>2</sub> hydrogenation reaction, the addition of K appeared to have a beneficial effect. The CO<sub>2</sub> conversion increased from 4.12% to 6.01%, while the C<sub>2+</sub> selectivity increased from 4.80% to 11.1% (**Figure 5.1a**). The addition of K also caused a decrease of the paraffin to olefin ratio. The C<sub>2</sub>-C<sub>5</sub> products consisted primarily of olefins (**Figure 5.1b**), suggesting that a lower hydrogenation capability was induced by K. For co-feeding CO<sub>2</sub>/CO=2, a beneficial effect was particularly observed in terms of C<sub>2+</sub> selectivity. While the conversion only increased marginally from 14.1% to 14.3%, the C<sub>2+</sub> selectivity improved from 13.0% to 58.1% (**Figure 5.1a**) and the amount of olefins increased (**Figure 5.1b**).

For CO hydrogenation, the addition of K as promoter appeared to have a detrimental effect (Figure 5.1a and Table 5.1). The CO conversion decreased from 7.97% to 5.11%, while the  $C_{2+}$  selectivity decreased from 78.0% to 35.5%. Besides, the K-promoted Co/TiO<sub>2</sub> catalyst material produced more olefins compared to the unpromoted Co/TiO<sub>2</sub> counterpart (Figure 5.1b). It has been reported previously that the addition of K to cobalt-based catalyst materials decreases the CO conversion as well as the paraffin to olefin ratio during CO hydrogenation.<sup>28,29</sup> In general, the addition of K appeared to lower the hydrogenation capability of the Co/TiO<sub>2</sub> catalyst, as indicated by the centroid in Figure 5.1b shifting from the paraffin regime (positive Log(paraffin/olefin)) to the olefin regime (negative Log(paraffin/olefin)).

In terms of overall catalytic performance, the addition of K was thus only beneficial for the CO<sub>2</sub> hydrogenation reaction and for co-feeding CO<sub>2</sub>/CO=2, while for the CO hydrogenation reaction the addition of K seemed to be detrimental. The  $C_{2+}$  yield improved from 0.20 to 0.67% for CO<sub>2</sub> hydrogenation and from 1.83 to 8.31% for co-feeding CO<sub>2</sub>/CO=2 upon the addition of K to a Co/TiO<sub>2</sub> catalyst material.

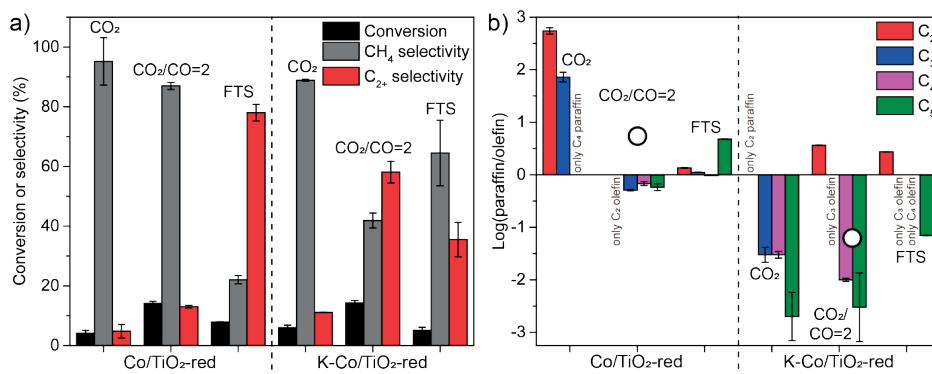


**Figure 5.1. Catalytic performance during CO<sub>2</sub> hydrogenation, co-feeding, and CO hydrogenation with Co/TiO<sub>2</sub> and K-Co/TiO<sub>2</sub>.** a) Conversion and selectivity and b) paraffin to olefin ratios of Co/TiO<sub>2</sub> and K-Co/TiO<sub>2</sub> during CO<sub>2</sub> hydrogenation (250°C, 20 bar, H<sub>2</sub>/CO<sub>2</sub>=3, and gas hourly space velocity (GHSV)=3200 h<sup>-1</sup>), co-feeding CO<sub>2</sub>/CO=2 (250°C, 20 bar, H<sub>2</sub>/C=3, and GHSV=3200 h<sup>-1</sup>) and CO hydrogenation (220°C, 20 bar, H<sub>2</sub>/CO=2, and GHSV=3200 h<sup>-1</sup>). The white dots in b) represent the centroid of all paraffin to olefin ratios for Co/TiO<sub>2</sub> (left side of b) and K-Co/TiO<sub>2</sub> (right side of b) The whiskers represent the standard deviation in the 26 on-line gas chromatography (GC) injections, which were sampled during the 10 h time-on-stream.

**Table 5.1. Average hydrocarbon distribution over 10 h catalytic testing during CO<sub>2</sub> hydrogenation, co-feeding, and CO hydrogenation with Co/TiO<sub>2</sub> and K-Co/TiO<sub>2</sub> prepared via incipient wetness impregnation (IWI).** The reaction conditions for CO<sub>2</sub> hydrogenation were 250°C, 20 bar, H<sub>2</sub>/CO<sub>2</sub>=3, and gas hourly space velocity (GHSV)=3200 h<sup>-1</sup>. Co-feeding was performed at the same reaction conditions as CO<sub>2</sub> hydrogenation with CO<sub>2</sub>/CO=2. The reaction conditions for CO hydrogenation were 220°C, 20 bar, H<sub>2</sub>/CO=2, and GHSV=3200 h<sup>-1</sup>. Every entry consists of averages of 26 on-line gas chromatography (GC) injections. The samples were pre-reduced at 450°C in N<sub>2</sub>/H<sub>2</sub>=2 for 1 h (suffix: -red).

Catalyst	Reaction	Carbon conversion	CH <sub>4</sub> <sup>a</sup>	C <sub>2</sub>	C <sub>3</sub>	C <sub>4</sub>	C <sub>5+</sub>
Co/TiO <sub>2</sub> -red	CO <sub>2</sub>	%	4.12	2.19	2.14	0.11	n.a.
		P/O <sup>b</sup>		5.47	72.7	P <sup>c</sup>	n.a.
Co/TiO <sub>2</sub> -red	Co-feed	%	14.1	6.97	3.87	1.69	0.43
		P/O <sup>b</sup>		O <sup>c</sup>	0.51	0.68	0.58 <sup>d</sup>
Co/TiO <sub>2</sub> -red	FTS	%	7.97	3.34	9.06	9.20	55.0
		P/O <sup>b</sup>		1.35	1.11	0.96	4.78 <sup>d</sup>
K-Co/TiO <sub>2</sub> -red	CO <sub>2</sub>	%	6.01	6.02	2.99	1.25	0.79
		P/O <sup>b</sup>		P <sup>c</sup>	0.03	0.03	0.002 <sup>d</sup>
K-Co/TiO <sub>2</sub> -red	Co-feed	%	14.3	6.92	12.8	12.3	33.1
		P/O <sup>b</sup>		3.65	O <sup>c</sup>	0.01	0.003 <sup>d</sup>
K-Co/TiO <sub>2</sub> -red	FTS	%	5.11	1.83	14.2	11.3	8.43
		P/O <sup>b</sup>		2.74	O <sup>c</sup>	O <sup>c</sup>	0.07 <sup>d</sup>

<sup>a</sup> CO and CO<sub>2</sub> free selectivities are reported for CO<sub>2</sub> hydrogenation and FTS, respectively.

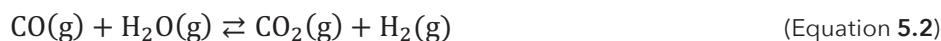
<sup>b</sup> P/O = Paraffin/olefin.

<sup>c</sup> P = Paraffin only, O = Olefin only.

<sup>d</sup> C<sub>5</sub>: paraffin/olefin.

### 5.3.2 Deriving Kinetic Parameters

To obtain a better understanding of the kinetic principles behind the either beneficial or detrimental effects induced by K as promoter element for Co-based CO and CO<sub>2</sub> hydrogenation catalysts, the activation energies for K-promoted Co/TiO<sub>2</sub> were calculated from Arrhenius plots for the CO and CO<sub>2</sub> hydrogenation reactions (**Figure 5.2** and **Table 5.2**). For CO<sub>2</sub> hydrogenation, the activation energy  $E_a$  was found to be  $103 \pm 1$  kJ mol<sup>-1</sup> for the promoted Co/TiO<sub>2</sub> catalyst, while a value of  $122 \pm 5$  kJ mol<sup>-1</sup> was obtained for the unpromoted Co/TiO<sub>2</sub> catalyst (as calculated in **Chapter 4**). An interesting parameter to look at here is the CO selectivity, as K is known to catalyze the (reverse) water-gas shift reaction ((R)WGS)<sup>30</sup> (**Equation (5.2)**).



The CO selectivity for the K-promoted Co/TiO<sub>2</sub> was 1.75%, while only 0.20% was obtained for Co/TiO<sub>2</sub>. Besides, the  $E_a$  for CO formation was  $\sim 70$  kJ mol<sup>-1</sup> lower for the K-Co/TiO<sub>2</sub> catalyst compared to the unpromoted Co/TiO<sub>2</sub> counterpart (**Table 5.2**, **Figures 5.2-5.4**). Though the  $E_a$  values for C<sub>2+</sub> formation were fairly similar for the K-promoted ( $126 \pm 1$  kJ mol<sup>-1</sup>) and unpromoted ( $115 \pm 5$  kJ mol<sup>-1</sup>) catalysts, the improved C<sub>2+</sub> yield can be explained by the fact that K catalyzed the RWGS reaction.

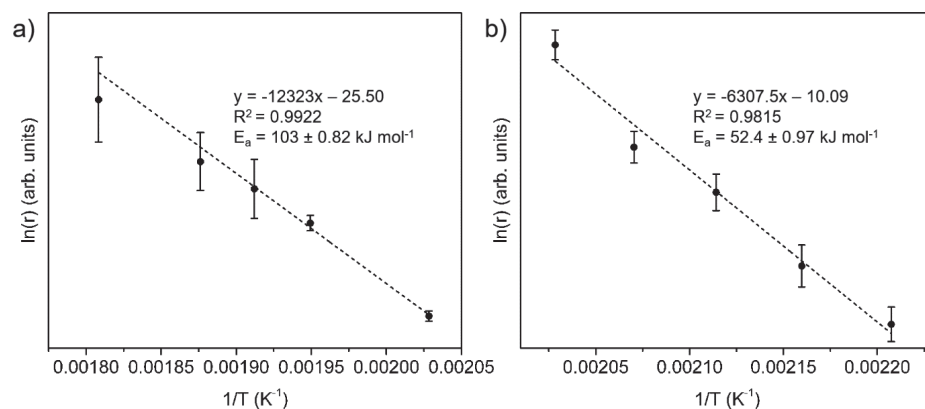


**Figure 5.2. Arrhenius plots for K-Co/TiO<sub>2</sub> during CO and CO<sub>2</sub> hydrogenation.** Arrhenius plots during a) CO<sub>2</sub> hydrogenation at 20 bar and H<sub>2</sub>/CO<sub>2</sub>=3 at temperatures between 220 and 280°C and b) CO hydrogenation at 20 bar and H<sub>2</sub>/CO=2 at temperatures between 180 and 220°C. Every point is an average of 6 on-line gas chromatography (GC) injections and the whiskers indicate the standard deviation.

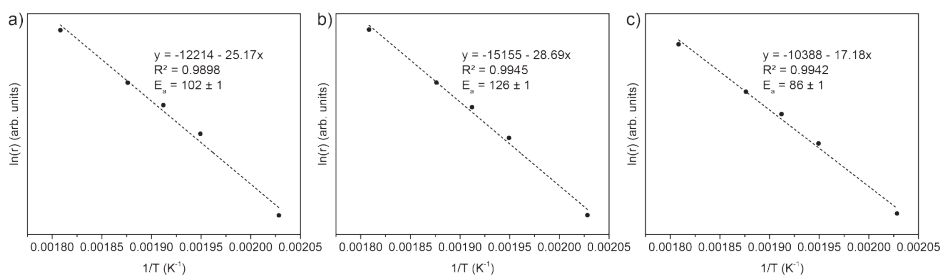


**Figure 5.3. Arrhenius plots for K-Co/TiO<sub>2</sub> during CO<sub>2</sub> hydrogenation.** Arrhenius plots for the reaction products **a)** methane, **b)** C<sub>2+</sub> hydrocarbons, and **c)** CO during CO<sub>2</sub> hydrogenation at 20 bar and H<sub>2</sub>/CO<sub>2</sub>=3 at temperatures between 220 and 280°C. The sample was pre-treated for 1 h at 450°C in N<sub>2</sub>/H<sub>2</sub>=2. Every point is an average of 6 on-line gas chromatography (GC) injections and the whiskers indicate the standard deviation.

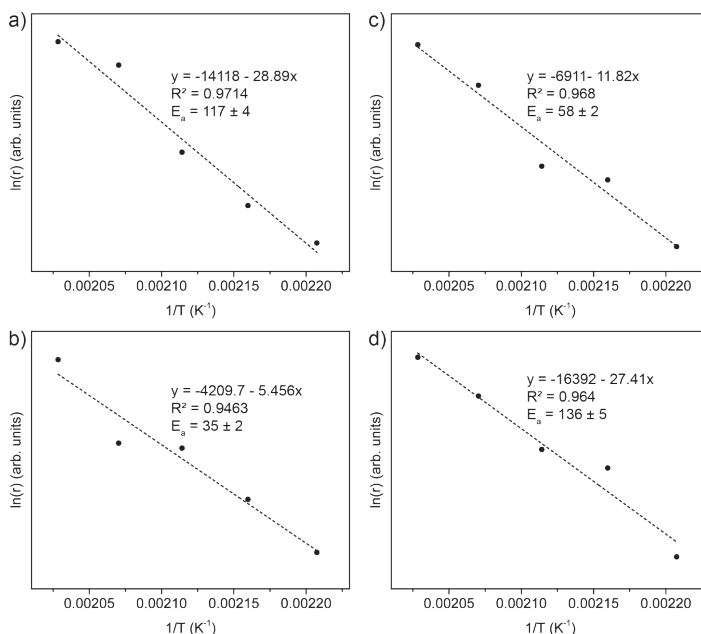


**Figure 5.4. Arrhenius plots for Co/TiO<sub>2</sub> and K-Co/TiO<sub>2</sub> during CO hydrogenation.** Arrhenius plots for the reaction products **a, b)** methane and **c, d)** C<sub>2+</sub> hydrocarbons during CO hydrogenation between 180 and 220°C at 20 bar and H<sub>2</sub>/CO=2. The top row displays the plots for Co/TiO<sub>2</sub> (pre-treated for 1 h at 450°C in N<sub>2</sub>/H<sub>2</sub>=2) and the bottom row displays the plots for K-Co/TiO<sub>2</sub>-red (pre-treated for 1 h at 450°C in N<sub>2</sub>/H<sub>2</sub>=2). Every point is an average of 4-6 on-line gas chromatography (GC) injections and the whiskers indicate the standard deviation.

For the CO hydrogenation reaction, the K-promoted Co/TiO<sub>2</sub> catalyst had an  $E_a$  value of  $52.4 \pm 1.0$  kJ mol<sup>-1</sup>, while for the unpromoted Co/TiO<sub>2</sub> catalyst  $83.3 \pm 1.1$  kJ mol<sup>-1</sup> was obtained (Calculated in **Chapter 3**). The addition of K thus appeared to lower the  $E_a$  significantly for CO hydrogenation as well. Relatively low activation energies have been reported previously for K-promoted cobalt-based catalyst materials.<sup>26,31</sup> Although K lowered the activation energy in both CO and CO<sub>2</sub> hydrogenation, its addition seemed only beneficial in terms of catalytic performance for the CO<sub>2</sub> hydrogenation reaction.

The exponential pre-factor  $A$ , which is calculated via the y-intercept of the Arrhenius plot, may offer further explanation for these differences. This kinetic factor describes the activation temperature of the catalyzed reaction. For example, from a set of catalyst materials with similar activation energies, the catalyst with the highest pre-factor  $A$  activates at the lowest temperature.<sup>32</sup> The calculated pre-factors for the CO<sub>2</sub> hydrogenation reaction over Co/TiO<sub>2</sub> and K-Co/TiO<sub>2</sub> were in the same order of magnitude ( $10^{11}$ ) (**Table 5.2**). For the CO reaction, on the other hand, the pre-factor for K-Co/TiO<sub>2</sub> was 5 orders of magnitude lower ( $10^4$ ) compared to unpromoted Co/TiO<sub>2</sub> ( $10^9$ ). This large difference may offer an explanation for the drastically lower reaction rate observed for K-Co/TiO<sub>2</sub> compared to Co/TiO<sub>2</sub> during the CO hydrogenation reaction (5% vs. 8% CO conversion) (**Table 5.1**). To explain the higher methane selectivity and lower C<sub>2+</sub> selectivity upon K promotion (**Table 5.1**), we turn to the  $E_a$  values for methane and C<sub>2+</sub>. The  $E_a$  for methane formation was  $\sim 80$  kJ mol<sup>-1</sup> lower, while the  $E_a$  for C<sub>2+</sub> formation was  $\sim 80$  kJ mol<sup>-1</sup> higher for the K-promoted compared to the unpromoted catalyst (**Table 5.2**). However, it remains important to compare our values with that of other work in the literature. It was found that for cobalt supported on carbon nanotubes (*i.e.*, Co/CNT), a pre-factor of  $\sim 10^8$  s<sup>-1</sup> has been reported,<sup>33</sup> while for the highly active Co(110) step sites the pre-factor can go up to  $\sim 10^{17}$  s<sup>-1</sup>.<sup>34</sup> For Co/TiO<sub>2</sub>, a pre-factor of  $2.40 \cdot 10^7$  s<sup>-1</sup> ( $\log(A)=7.38$ ) during CO hydrogenation has been determined in another study at  $P=12$  bar and GHSV=5000 h<sup>-1</sup>.<sup>35</sup> In our work, the kinetic parameters were determined at  $P=20$  bar and GHSV=3200 h<sup>-1</sup>. We therefore observed a higher pre-factor of  $2.36 \cdot 10^9$  s<sup>-1</sup> for Co/TiO<sub>2</sub>, as higher pressure and lower GHSV led to higher reaction rates and activation at lower temperatures.



**Table 5.2. Activation energies  $E_a$  and exponential pre-factors  $A$  for the CO and CO<sub>2</sub> hydrogenation reactions with Co/TiO<sub>2</sub> and K-Co/TiO<sub>2</sub>.** The reaction conditions for CO<sub>2</sub> hydrogenation were 220-280°C, 20 bar, H<sub>2</sub>/CO<sub>2</sub>=3, and gas hourly space velocity (GHSV)=3200 h<sup>-1</sup>. The reaction conditions for CO hydrogenation were 180-220°C, 20 bar, H<sub>2</sub>/CO=2, and GHSV=3200 h<sup>-1</sup>. The samples were pre-reduced at 450°C in N<sub>2</sub>/H<sub>2</sub>=2 for 1 h (suffix: -red).

Catalyst	Reaction	Product	Activation energy $E_a$ (kJ mol <sup>-1</sup> )	Exponential pre-factor $A$ (s <sup>-1</sup> )
Co/TiO <sub>2</sub> -red	CO <sub>2</sub>	Total	122 ± 5	(6.96 ± 0.31) *10 <sup>11</sup>
		CH <sub>4</sub>	121 ± 4	(3.62 ± 0.16) *10 <sup>12</sup>
		C <sub>2+</sub>	115 ± 5	(1.27 ± 0.07) *10 <sup>10</sup>
		CO	156 ± 8	(1.18 ± 0.09) *10 <sup>14</sup>
Co/TiO <sub>2</sub> -red	FTS	Total	83.3 ± 1.1	(2.36 ± 0.25) *10 <sup>9</sup>
		CH <sub>4</sub>	117 ± 4	(3.51 ± 0.42) *10 <sup>12</sup>
		C <sub>2+</sub>	57.5 ± 1.8	(1.35 ± 0.03) *10 <sup>5</sup>
K-Co/TiO <sub>2</sub> -red	CO <sub>2</sub>	Total	103 ± 1	(1.19 ± 0.17) *10 <sup>11</sup>
		CH <sub>4</sub>	102 ± 1	(8.54 ± 1.32) *10 <sup>10</sup>
		C <sub>2+</sub>	126 ± 1	(8.89 ± 0.48) *10 <sup>12</sup>
		CO	86.3 ± 0.5	(2.89 ± 0.48) *10 <sup>7</sup>
K-Co/TiO <sub>2</sub> -red	FTS	Total	52.4 ± 1.0	(2.40 ± 0.54) *10 <sup>4</sup>
		CH <sub>4</sub>	35.0 ± 1.9	(2.34 ± 0.59) *10 <sup>2</sup>
		C <sub>2+</sub>	136 ± 5	(8.08 ± 1.43) *10 <sup>11</sup>

The so-called compensation effect describes a linear relation between  $\ln(A)$  and  $E_a$  for a set of catalyst materials or for a set of reactions, which typically caused by a common reaction mechanism.<sup>36,37</sup> Hence, plotting  $\ln(A)$  versus  $E_a$ , a compensation plot, can give insights into the similarities or differences in reaction mechanisms at play. A better linear correlation between  $\ln(A)$  and  $E_a$  for a set of catalysts or reactions would thus indicate more similarities in reaction mechanisms and/or catalytically active centers.<sup>37</sup> Compensation plots for the CO and CO<sub>2</sub> hydrogenation reactions with unpromoted and K-promoted Co/TiO<sub>2</sub> can be found in **Figure 5.5**. From **Figure 5.5a** it appeared that unpromoted and K-promoted Co/TiO<sub>2</sub> had slight differences in reaction mechanism or active centers<sup>37</sup> for both CO and CO<sub>2</sub> hydrogenation, as they were not on the same compensation line. However, the points related to methane formation (**Figure 5.5b**) were on the same compensation line ( $R^2=0.99$ ), implying that methane formation occurred via a common mechanism for the unpromoted and K-promoted catalysts in both CO and CO<sub>2</sub> hydrogenation.

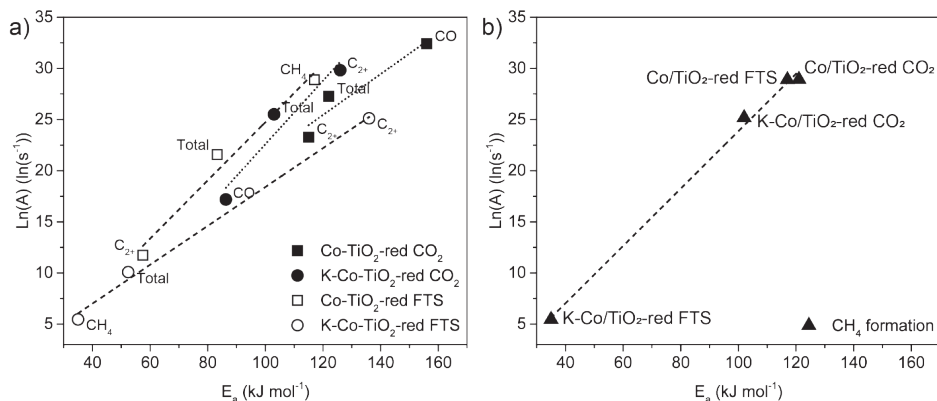


**Figure 5.5. Compensation plots for the CO and CO<sub>2</sub> hydrogenation reactions with unpromoted and K-promoted Co/TiO<sub>2</sub>.** a) Plot with all calculated activation energies ( $E_a$ ) and pre-exponential factors ( $A$ ). The dotted compensation lines describe CO<sub>2</sub> hydrogenation and the dashed compensation lines describe CO hydrogenation. b) Plot for methane formation. All compensation lines had  $R^2$  values between 0.85 and 0.99.

### 5.3.3 Comparison between Potassium and Manganese Oxide as Promoter

It is known that manganese oxide (MnO) is added to Co/TiO<sub>2</sub> systems in industrial FTS catalyst formulations<sup>24</sup> mainly as a structural promoter as it is considered that MnO affects the formation and stability of the cobalt active phase. The addition of MnO to cobalt-based FTS catalysts has been reported to also hamper the reduction of CoO into metallic Co.<sup>38</sup> Besides, MnO is known to increase C<sub>5+</sub> selectivity, decrease methane selectivity, and decrease the paraffin to olefin ratio in FTS.<sup>39</sup> Apart from a structural and synergistic (e.g., water-gas shift (WGS) reaction) promoter,<sup>39</sup> MnO is also an electronic promoter. Mn<sup>2+</sup> withdraws electron density from metallic Co, causing a partial positive charge as Co<sup>δ+</sup>.<sup>38</sup>

In this **Chapter**, we have compared the effects of K promotion with the effects of Mn promotion and the effects of CoO as active phase instead of metallic Co. We will first image the distribution of the promoter elements Mn and K with X-ray elemental mapping (EDX) and investigate the influence of the promoter elements and the CoO versus metallic Co active phase on H<sub>2</sub> adsorption. Then, we will test these catalyst materials for their performance in the CO<sub>2</sub> hydrogenation reaction.

The way that promoter elements are distributed over the catalyst strongly influences the resulting effects on catalysis.<sup>38,39,42</sup> Homogeneous distribution and fine dispersion typically lead to a more pronounced promoter effect, such as a lower or higher reducibility of the cobalt phase.<sup>38,42</sup> In our case, X-ray elemental mapping results showed that

both the promoter elements Mn and K were homogeneously distributed over the Co/TiO<sub>2</sub>-DP catalyst after calcination (**Figure 5.6**).

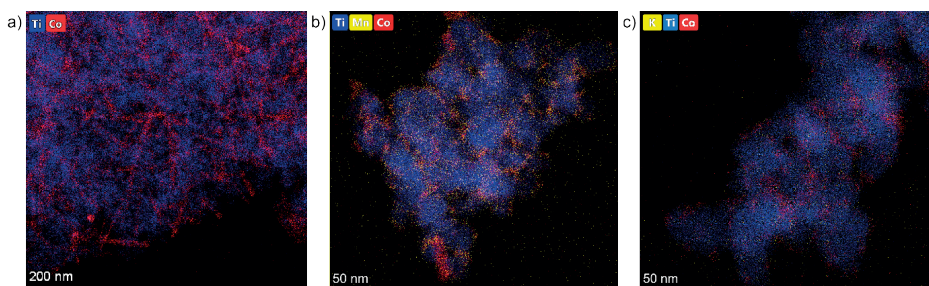


**Figure 5.6. X-ray elemental mapping to investigate the distribution of promoter elements Mn and K on Co/TiO<sub>2</sub>.** Energy dispersive X-ray (EDX) spectroscopy mapping of the calcined catalyst materials (250°C in N<sub>2</sub>) **a**) Co/TiO<sub>2</sub>-DP, **b**) Mn-Co/TiO<sub>2</sub>-DP, and **c**) K-Co/TiO<sub>2</sub>-DP. Cobalt (Co) is indicated in red, titanium (Ti) in blue, and manganese (Mn) or potassium (K) in yellow.

H<sub>2</sub> chemisorption measurements were carried out to investigate the influence of Mn and K on H<sub>2</sub> adsorption by Co/TiO<sub>2</sub>-DP (**Table 5.3**). Co/TiO<sub>2</sub>-DP had an average Co<sub>3</sub>O<sub>4</sub> crystallite size of 27.2 nm, as measured with XRD after calcination. Addition of Mn (1.8 wt.%) did not have a significant influence on the Co<sub>3</sub>O<sub>4</sub> crystallite size (27.8 nm), while addition of K (1.3 wt.%) yielded slightly smaller Co<sub>3</sub>O<sub>4</sub> crystallites of 22.0 nm. The chemisorption of H<sub>2</sub> was measured for all samples after pre-treatment at 250°C in H<sub>2</sub> to yield the CoO phase (suffix: -ox) and at 450°C in H<sub>2</sub> to yield the metallic Co phase (suffix: -red). Generally, the measured H<sub>2</sub> uptake was about 4-7 times higher for the -ox catalysts compared to the -red catalysts. Decreased H<sub>2</sub> chemisorption has been reported previously for TiO<sub>2</sub> supported catalysts treated at elevated temperatures in H<sub>2</sub>.<sup>38,40</sup> This effect has been ascribed to formation and migration of TiO<sub>x</sub> overlayers, which mask the cobalt surface and thereby decrease the measured H<sub>2</sub> uptake.<sup>38</sup> The addition of promoter elements Mn and K both decreased the H<sub>2</sub> uptake in the order of unpromoted>Mn>K. Both Mn and K could block cobalt sites, making them unavailable for H<sub>2</sub> adsorption. Moreover, Mn and K could act as electronic promoters by withdrawing electron density from cobalt<sup>39</sup> and thereby limiting the H<sub>2</sub> uptake.<sup>41</sup>

**Table 5.3. Physicochemical properties of the unpromoted, Mn-promoted, and K-promoted Co/TiO<sub>2</sub> catalysts prepared via deposition precipitation (DP).** Suffix -ox indicates pre-treated at 250°C in H<sub>2</sub> and suffix -red indicates pre-treated at 450°C in H<sub>2</sub>.

Catalyst	Promoter/Co	Co <sub>3</sub> O <sub>4</sub> XRD (nm)	H <sub>2</sub> uptake (μmol g <sup>-1</sup> )	Co dispersion (%)
Co/TiO <sub>2</sub> -DP-ox	n.a.	27.2	81.7	9.63
Mn-Co/TiO <sub>2</sub> -DP-ox	0.2	27.8	72.8	8.58
K-Co/TiO <sub>2</sub> -DP-ox	0.2	22.0	53.3	6.28
Co/TiO <sub>2</sub> -DP-red	n.a.	27.2	22.2	2.61
Mn-Co/TiO <sub>2</sub> -DP-red	0.2	27.8	19.3	2.27
K-Co/TiO <sub>2</sub> -DP-red	0.2	22.0	7.89	0.93

Unpromoted, Mn-promoted, and K-promoted Co/TiO<sub>2</sub>-DP catalysts were tested for CO<sub>2</sub> hydrogenation activity at 250°C, 20 bar, and H<sub>2</sub>/CO<sub>2</sub>=3 in both CoO (suffix: -ox) and metallic Co (suffix: -red) state (**Figure 5.6** and **Table 5.4**). For this set of catalyst materials, the CO<sub>2</sub> conversion was generally higher for the metallic Co compared to the CoO variant. Except for the unpromoted Co/TiO<sub>2</sub>-DP, where the CO<sub>2</sub> conversion was slightly higher for the CoO variant. Though, this effect was more pronounced for the Co/TiO<sub>2</sub> catalyst prepared via the IWI method, as observed in **Chapter 4**. Methane was the main reaction product formed by Co/TiO<sub>2</sub>-DP-ox and Co/TiO<sub>2</sub>-DP-red with respectively 98.2 and 98.5% selectivity (**Figure 5.6a**). Of the C<sub>2</sub>-C<sub>4</sub> products, the metallic Co catalyst had a higher paraffin to olefin ratio compared to the CoO catalyst (**Figure 5.6b**).

Although Mn-Co/TiO<sub>2</sub>-DP-red displayed a higher CO<sub>2</sub> conversion compared to unpromoted Co/TiO<sub>2</sub>-DP, the Mn-promoted catalysts had a similarly high selectivity towards methane (**Figure 5.6** and **Table 5.4**). The Mn-promoted Co/TiO<sub>2</sub> catalyst materials possessed a lower hydrogenation capability compared to the unpromoted catalysts, as indicated by the lower paraffin to olefin ratio in the C<sub>2</sub>-C<sub>4</sub> products. The centroid of the Log(paraffin/olefin) shifted from 1.80 for the unpromoted to 1.37 for the Mn-promoted catalysts (**Figure 5.6b**).

The K-promoted catalyst materials had a slightly lower CO<sub>2</sub> conversion compared to the unpromoted and Mn-promoted catalyst materials. However, the methane selectivity shifted down to 79.0 and 78.6% for K-Co/TiO<sub>2</sub>-DP-ox and K-Co/TiO<sub>2</sub>-DP-red, respectively (**Figure 5.6** and **Table 5.4**). The addition of K also appeared to promote the RWGS reaction (**Equation (5.2)**), as the selectivity towards CO increased to 2.44 and 0.42% for the CoO and metallic Co variants, respectively. Alkali metals are known to accelerate the decomposition of formate intermediates via electronic effects and there-

by enhance the (R)WGS reaction rate.<sup>30</sup> The K-promoted catalysts possessed an even lower hydrogenation capability compared to the Mn-promoted catalysts. The centroid of the Log(paraffin/olefin) shifted down to 1.24 for the K-promoted catalysts, indicating a lower paraffin to olefin ratio in the C<sub>2</sub>-C<sub>4</sub> products compared to the unpromoted and Mn-promoted catalysts.

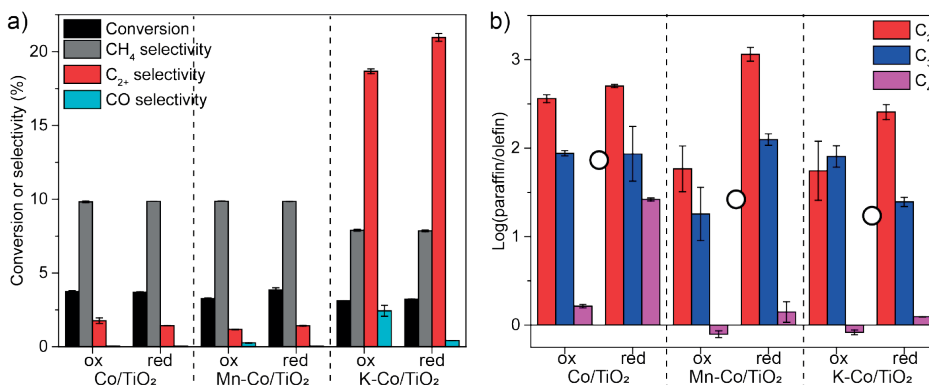


**Figure 5.7. Catalytic performance during CO<sub>2</sub> hydrogenation with the Co/TiO<sub>2</sub>-DP, Mn-Co/TiO<sub>2</sub>-DP, and K-Co/TiO<sub>2</sub>-DP catalyst materials.** a) Conversion and selectivity and b) paraffin to olefin ratios of Co/TiO<sub>2</sub>-DP, Mn-Co/TiO<sub>2</sub>-DP, and K-Co/TiO<sub>2</sub>-DP in both CoO (ox) and metallic Co (red) state during CO<sub>2</sub> hydrogenation (250°C, 20 bar, H<sub>2</sub>/CO<sub>2</sub>=3, and GHSV=3200 h<sup>-1</sup>). The white dots in b) represent the centroid of all paraffin to olefin ratios for Co/TiO<sub>2</sub>-DP (left side of b), Mn-Co/TiO<sub>2</sub>-DP (middle of b), and K-Co/TiO<sub>2</sub>-DP (right side of b). The whiskers represent the standard deviation in the 26 on-line gas chromatography (GC) injections, which were sampled during the 10 h time-on-stream.

**Table 5.4. Average catalytic performance over 10 h catalytic testing during CO<sub>2</sub> hydrogenation with the Co/TiO<sub>2</sub>-DP, Mn-Co/TiO<sub>2</sub>-DP, and K-Co/TiO<sub>2</sub>-DP catalyst materials.**

The reaction conditions for CO<sub>2</sub> hydrogenation were 250°C, 20 bar, H<sub>2</sub>/CO<sub>2</sub>=3, and GHSV=3200 h<sup>-1</sup>. Every entry consists of averages of 26 on-line gas chromatography (GC) injections. The samples were pre-reduced either at 250°C (suffix: -ox) or at 450°C (suffix: -red) in N<sub>2</sub>/H<sub>2</sub>=2 for 1 h.

Catalyst		CO <sub>2</sub> conversion	CH <sub>4</sub>	CO	C <sub>2</sub>	C <sub>3</sub>	C <sub>4</sub>
Co/TiO <sub>2</sub> -DP-ox	%	3.75	98.2	0.05	1.42	0.28	0.06
	P/O <sup>a</sup>				363	87.3	1.64
Co/TiO <sub>2</sub> -DP-red	%	3.70	98.5	0.05	1.20	0.23	0.001
	P/O <sup>a</sup>				504	86.2	26.4
Mn-Co/TiO <sub>2</sub> -DP-ox	%	3.26	98.6	0.26	1.03	0.15	0.003
	P/O <sup>a</sup>				58.5	18.1	0.78

**Table 5.4.** (Continued)

Catalyst		CO <sub>2</sub> conversion	CH <sub>4</sub>	CO	C <sub>2</sub>	C <sub>3</sub>	C <sub>4</sub>
Mn-Co/TiO <sub>2</sub> -DP-red	%	3.85	98.5	0.05	1.26	0.17	0.001
	P/O <sup>a</sup>				1149	125	1.41
K-Co/TiO <sub>2</sub> -DP-ox	%	3.11	79.0	2.44	12.2	6.41	0.03
	P/O <sup>a</sup>				55.6	80.5	0.83
K-Co/TiO <sub>2</sub> -DP-red	%	3.22	78.6	0.42	12.1	8.84	0.02
	P/O <sup>a</sup>				256	24.7	1.25

<sup>a</sup> P/O = Paraffin/olefin

In the CO<sub>2</sub> hydrogenation reaction, Co/TiO<sub>2</sub> performed better in terms of CO<sub>2</sub> conversion and C<sub>2+</sub> selectivity when prepared via the IWI method versus the DP method. The K-Co/TiO<sub>2</sub> catalyst system performed better in terms of CO<sub>2</sub> conversion when prepared via IWI, while the C<sub>2+</sub> selectivity was higher for the catalyst system prepared via the DP method. Though it must also be noted that K-Co/TiO<sub>2</sub> had 0.4 wt.% K, while K-Co/TiO<sub>2</sub>-DP had a higher K loading of 1.3 wt.%. It has been reported previously for Mn-promoted Co/TiO<sub>2</sub> catalysts that the DP preparation method enhanced the association of the cobalt and the manganese phases compared to the IWI method.<sup>42</sup> Closer contact of the promoter element with the cobalt phase may explain the increased C<sub>2+</sub> selectivity of K-Co/TiO<sub>2</sub>-DP.

## 5.4 Conclusions

In this **Chapter**, we have investigated the K promoter effects on cobalt-based CO and CO<sub>2</sub> hydrogenation. Although alkali promoter elements, such as K and Na, are widely in commercial applications of iron-based CO hydrogenation to improve catalyst performance, the addition of K to a cobalt-based CO hydrogenation catalyst appeared detrimental. When K was added to the Co/TiO<sub>2</sub> catalyst formulation, the CO conversion rate as well as the C-C coupling rate and the overall hydrogenation activity deteriorated compared to the unpromoted Co/TiO<sub>2</sub> catalyst. However, the addition of K as promoter element appeared interesting for renewable energy applications that aim to convert CO<sub>2</sub> into valuable C<sub>2+</sub> hydrocarbons. By increasing the RWGS activity via electronic effects and decreasing the amount of hydrogen atoms on the surface, the C-C coupling activity was enhanced. Consequently, the addition of K led to a selectivity shift away from undesired methane and towards more valuable C<sub>2+</sub> hydrocarbons. For co-feeding CO and CO<sub>2</sub> (CO<sub>2</sub>/CO=2), K-Co/TiO<sub>2</sub>-red yielded 149 mmol h<sup>-1</sup> g<sub>cat</sub><sup>-1</sup> C<sub>2+</sub> hydrocarbons, which was a 43% improvement compared to the 104 mmol h<sup>-1</sup> g<sub>cat</sub><sup>-1</sup> C<sub>2+</sub> hydrocarbons

yielded by Co/TiO<sub>2</sub>-ox in **Chapter 4**. The addition of cheap and abundant alkali metal K to heterogeneous catalysts may thus bring us a step closer to the commercialization of CO<sub>2</sub> hydrogenation processes. For commercialization purposes, using Na instead of K could be of interest, as Na is easier to obtain and more affordable than K. Future scientific research on this topic should then systematically investigate the addition of different alkali metals in varying quantities to cobalt-based catalyst materials to find an optimum. Exploring multiple combinations of alkali elements, next to cobalt and a suitable support, should ultimately lead to the discovery of a highly active catalyst formulation for industrial CO<sub>2</sub> valorization processes.

### **5.5 Author Contributions and Acknowledgements**

The research ideas in this Chapter were conceptualized by Iris ten Have, Florian Meirer, and Bert Weckhuysen. The experimental work in this Chapter was performed by Joyce Kromwijk and Iris ten Have. Nienke Visser is gratefully acknowledged for the STEM-EDX measurements.

## 5.6 References

1. ten Have, I. C. & Weckhuysen, B. M. The active phase in cobalt-based Fischer-Tropsch synthesis. *Chem Catalysis* **1**, 339-363 (2021).
2. Lin, T., Gong, K., Wang, C., An, Y., Wang, X., Qi, X., Li, S., Lu, Y., Zhong, L. & Sun, Y. Fischer-Tropsch Synthesis to Olefins: Catalytic Performance and Structure Evolution of Co<sub>2</sub>C-Based Catalysts under a CO<sub>2</sub> Environment. *ACS Catalysis* **9**, 9554-9567 (2019).
3. Xiang, Y. & Kruse, N. Tuning the catalytic CO hydrogenation to straight-and long-chain aldehydes/alcohols and olefins/paraffins. *Nature Communications* **7**, 13058 (2016).
4. Zhong, L., Yu, F., An, Y., Zhao, Y., Sun, Y., Li, Z., Lin, T., Lin, Y., Qi, X., Dai, Y., Gu, L., Hu, J., Jin, S., Shen, Q. & Wang, H. Cobalt carbide nanoprisms for direct production of lower olefins from syngas. *Nature* **538**, 84-87 (2016).
5. Yang, R., Xia, Z., Zhao, Z., Sun, F., Du, X., Yu, H., Gu, S., Zhong, L., Zhao, J., Ding, Y. & Jiang, Z. Characterization of CoMn catalyst by in situ X-ray absorption spectroscopy and wavelet analysis for Fischer-Tropsch to olefins reaction. *Journal of Energy Chemistry* **32**, 118-123 (2019).
6. Zhang, S., Liu, X., Shao, Z., Wang, H. & Sun, Y. Direct CO<sub>2</sub> hydrogenation to ethanol over supported Co<sub>2</sub>C catalysts: Studies on support effects and mechanism. *Journal of Catalysis* **382**, 86-96 (2020).
7. Lebarbier, V. M., Mei, D., Kim, D. H., Andersen, A., Male, J. L., Holladay, J. E., Rousseau, R. & Wang, Y. Effects of La<sub>2</sub>O<sub>3</sub> on the mixed higher alcohols synthesis from syngas over Co catalysts: A combined theoretical and experimental study. *Journal of Physical Chemistry C* **115**, 17440-17451 (2011).
8. Pei, Y. P., Liu, J. X., Zhao, Y. H., Ding, Y. J., Liu, T., Dong, W. Da, Zhu, H. J., Su, H. Y., Yan, L., Li, J. L. & Li, W. X. High alcohols synthesis via Fischer-Tropsch reaction at cobalt metal/carbide interface. *ACS Catalysis* **5**, 3620-3624 (2015).
9. Gnanamani, M. K., Jacobs, G., Graham, U. M., Ribeiro, M. C., Noronha, F. B., Shafer, W. D. & Davis, B. H. Influence of carbide formation on oxygenates selectivity during Fischer-Tropsch synthesis over Ce-containing Co catalysts. *Catalysis Today* **261**, 40-47 (2016).
10. Chen, P. P., Liu, J. X. & Li, W. X. Carbon Monoxide Activation on Cobalt Carbide for Fischer-Tropsch Synthesis from First-Principles Theory. *ACS Catalysis* **9**, 8093-8103 (2019).
11. Wang, X., Chen, W., Lin, T., Li, J., Yu, F., An, Y., Dai, Y., Wang, H., Zhong, L. & Sun, Y. Effect of the support on cobalt carbide catalysts for sustainable production of olefins from syngas. *Chinese Journal of Catalysis* **39**, 1869-1880 (2018).
12. Zhao, Z., Lu, W., Yang, R., Zhu, H., Dong, W., Sun, F., Jiang, Z., Lyu, Y., Liu, T., Du, H. & Ding, Y. Insight into the Formation of Co@Co<sub>2</sub>C Catalysts for Direct Synthesis of Higher Alcohols and Olefins from Syngas. *ACS Catalysis* **8**, 228-241 (2018).
13. Athariboroujeny, M., Raub, A., Iablokov, V., Chenakin, S., Kovarik, L. & Kruse, N. Competing Mechanisms in CO Hydrogenation over Co-MnO<sub>x</sub> Catalysts. *ACS Catalysis* **9**, 5603-5612 (2019).
14. An, Y., Zhao, Y., Yu, F., Lin, T., Lu, Y., Li, S., Li, Z., Dai, Y., Wang, X., Wang, H., Zhong, L. & Sun, Y. Morphology control of Co<sub>2</sub>C nanostructures via the reduction process for direct production of lower olefins from syngas. *Journal of Catalysis* **366**, 289-299 (2018).
15. Paterson, J., Peacock, M., Purves, R., Partington, R., Sullivan, K., Sunley, G. & Wilson, J. Manipulation of Fischer-Tropsch Synthesis for Production of Higher Alcohols Using Manganese Promoters. *ChemCatChem* **10**, 5154-5163 (2018).



16. Wang, Z., Kumar, N. & Spivey, J. J. Preparation and characterization of lanthanum-promoted cobalt-copper catalysts for the conversion of syngas to higher oxygenates: Formation of cobalt carbide. *Journal of Catalysis* **339**, 1-8 (2016).
17. Li, Z., Zhong, L., Yu, F., An, Y., Dai, Y., Yang, Y., Lin, T., Li, S., Wang, H., Gao, P., Sun, Y. & He, M. Effects of Sodium on the Catalytic Performance of CoMn Catalysts for Fischer-Tropsch to Olefin Reactions. *ACS Catalysis* **7**, 3622-3631 (2017).
18. Paalanen, P. P., van Vreeswijk, S. H. & Weckhuysen, B. M. Combined in Situ X-ray Powder Diffraction/Raman Spectroscopy of Iron Carbide and Carbon Species Evolution in Fe(-Na-S)/ $\alpha$ -Al<sub>2</sub>O<sub>3</sub> Catalysts during Fischer-Tropsch Synthesis. *ACS Catalysis* **10**, 9837-9855 (2020).
19. Paalanen, P. P., van Vreeswijk, S. H., Dugulan, A. I. & Weckhuysen, B. M. Identification of Iron Carbides in Fe(-Na-S)/ $\alpha$ -Al<sub>2</sub>O<sub>3</sub> Fischer-Tropsch Synthesis Catalysts with X-ray Powder Diffraction and Mössbauer Absorption Spectroscopy. *ChemCatChem* **12**, 5121-5139 (2020).
20. Han, Y., Fang, C., Ji, X., Wei, J., Ge, Q. & Sun, J. Interfacing with Carbonaceous Potassium Promoters Boosts Catalytic CO<sub>2</sub> Hydrogenation of Iron. *ACS Catalysis* **10**, 12098-12108 (2020).
21. Huo, C.-F., Wu, B.-S., Gao, P., Yang, Y., Li, Y.-W. & Jiao, H. The Mechanism of Potassium Promoter: Enhancing the Stability of Active Surfaces. *Angew. Chem. Int. Ed.* **123**, 7541-7544 (2011).
22. Gaube, J. & Klein, H. F. The promoter effect of alkali in Fischer-Tropsch iron and cobalt catalysts. *Applied Catalysis A: General* **350**, 126-132 (2008).
23. Mohandas, J. C., Gnanamani, M. K., Jacobs, G., Ma, W., Ji, Y., Khalid, S. & Davis, B. H. Fischer-tropsch synthesis: Characterization and reaction testing of cobalt carbide. *ACS Catalysis* **1**, 1581-1588 (2011).
24. van de Loosdrecht, J., Botes, F. G., Ciobica, I. M., Ferreira, A., Gibson, P., Moodley, D. J., Saib, A. M., Visagie, J. L., Weststrate, C. J. & Niemantsverdriet, J. W. in *Comprehensive Inorganic Chemistry II: from elements to applications* **7**, 525-557 (Elsevier, Amsterdam, 2013).
25. Jacobs, G., Das, T. K., Zhang, Y., Li, J., Racoillet, G. & Davis, B. H. Fischer-Tropsch synthesis: Support, loading, and promoter effects on the reducibility of cobalt catalysts. *Applied Catalysis A: General* **233**, 263-281 (2002).
26. Khangale, P. R. Hydrogenation of CO<sub>2</sub> to Hydrocarbons over Zirconia-Supported Cobalt Catalyst Promoted with Potassium. *Catalysis Letters* **152**, 2745-2755 (2022).
27. Zhang, M., Wang, M., Xu, B. & Ma, D. How to Measure the Reaction Performance of Heterogeneous Catalytic Reactions Reliably. *Joule* **3**, 2876-2883 (2019).
28. Xiang, Y. & Kruse, N. Tuning the catalytic CO hydrogenation to straight-and long-chain aldehydes/alcohols and olefins/paraffins. *Nature Communications* **7**, 13058 (2016).
29. Gaube, J. & Klein, H. F. The promoter effect of alkali in Fischer-Tropsch iron and cobalt catalysts. *Applied Catalysis A: General* **350**, 126-132 (2008).
30. Ratnasamy, C. & Wagner, J. Water gas shift catalysis. *Catalysis Reviews - Science and Engineering* **51**, 325-440 (2009).
31. Khangale, P. R., Meijboom, R. & Jalama, K. CO<sub>2</sub> hydrogenation to liquid hydrocarbons via modified Fischer-Tropsch over alumina-supported cobalt catalysts: Effect of operating temperature, pressure and potassium loading. *Journal of CO<sub>2</sub> Utilization* **41**, 101268 (2020).
32. Mutschler, R., Moioli, E., Luo, W., Gallandat, N. & Züttel, A. CO<sub>2</sub> hydrogenation reaction over pristine Fe, Co, Ni, Cu and Al<sub>2</sub>O<sub>3</sub> supported Ru: Comparison and determination of the activation energies. *Journal of Catalysis* **366**, 139-149 (2018).

33. Thiessen, J., Rose, A., Meyer, J., Jess, A. & Curulla-Ferré, D. Effects of manganese and reduction promoters on carbon nanotube supported cobalt catalysts in Fischer-Tropsch synthesis. *Microporous and Mesoporous Materials* **164**, 199-206 (2012).
34. Liao, K., Fiorin, V., Gunn, D. S. D., Jenkins, S. J. & King, D. A. Single-crystal adsorption calorimetry and density functional theory of CO chemisorption on fcc Co{110}. *Physical Chemistry Chemical Physics* **15**, 4059-4065 (2013).
35. Zennaro, R., Tagliabue, M. & Bartholomew, C. H. Kinetics of Fischer - Tropsch synthesis on titania-supported cobalt. *Catalysis Today* **58**, 309-319 (2000).
36. Biloen, P. & Sachtler, W. M. H. Mechanism of Hydrocarbon Synthesis over Fischer-Tropsch Catalysts. *Advances in Catalysis* **30**, 165-216 (1981).
37. Bond, G. C., Keane, M. A., Kral, H. & Lercher, J. A. Compensation Phenomena in Heterogeneous Catalysis: General Principles and a Possible Explanation. *Catalysis Reviews - Science and Engineering* **42**, 323-383 (2000).
38. Morales, F., de Smit, E., de Groot, F. M. F., Visser, T. & Weckhuysen, B. M. Effects of manganese oxide promoter on the CO and H<sub>2</sub> adsorption properties of titania-supported cobalt Fischer-Tropsch catalysts. *Journal of Catalysis* **246**, 91-99 (2007).
39. Morales, F. & Weckhuysen, B. M. Promotion Effects in Co-based Fischer-Tropsch Catalysis. *Catalysis* **19**, 1-40 (2006).
40. Tauster, S. J., Fung, S. C., Baker, R. T. & Horsley, J. A. Strong interactions in supported-metal catalysts. *Science (1979)* **211**, 1121-1125 (1981).
41. Shi, Z., Yang, H., Gao, P., Li, X., Zhong, L., Wang, H., Liu, H., Wei, W. & Sun, Y. Direct conversion of CO<sub>2</sub> to long-chain hydrocarbon fuels over K-promoted CoCu/TiO<sub>2</sub> catalysts. *Catalysis Today* **311**, 65-73 (2018).
42. Morales, F., Grandjean, D., Mens, A., De Groot, F. M. F. & Weckhuysen, B. M. X-ray absorption spectroscopy of Mn/Co/TiO<sub>2</sub> Fischer-Tropsch catalysts: Relationships between preparation method, molecular structure, and catalyst performance. *Journal of Physical Chemistry B* **110**, 8626-8639 (2006).



This Chapter is based on the following scientific article:

ten Have, I. C., van den Brink, R. Y., Marie-Rose, S. C., Meirer, F., Weckhuysen, B. M. (2022). Using Biomass Gasification Mineral Residue as Catalyst to Produce Light Olefins from CO, CO<sub>2</sub>, and H<sub>2</sub> Mixtures. *ChemSusChem*, e202200436.

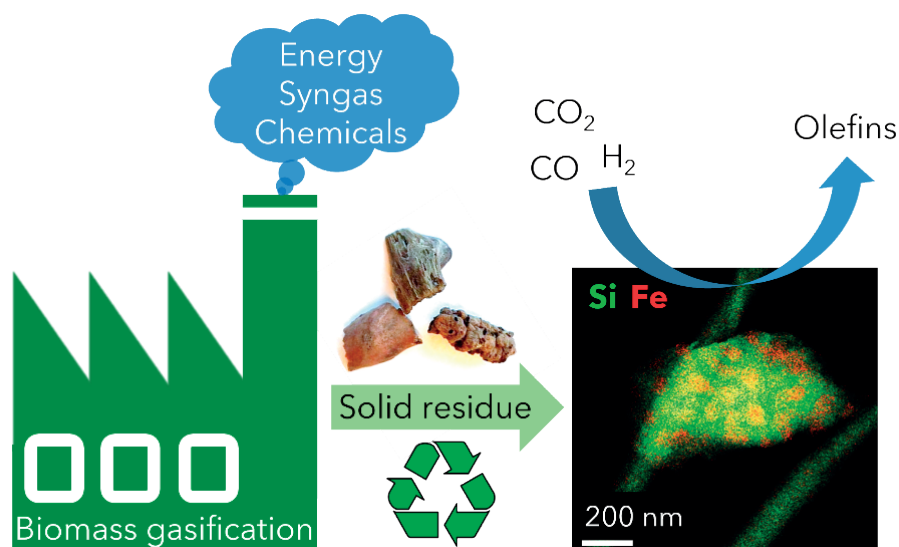
# CHAPTER 6

USING BIOMASS GASIFICATION MINERAL  
RESIDUE AS HYDROGENATION CATALYST  
TO PRODUCE LIGHT OLEFINS FROM CO,  
CO<sub>2</sub>, AND H<sub>2</sub> MIXTURES



## Abstract

Gasification is a process to transform solids, such as agricultural and municipal waste, into gaseous feedstock for making chemicals and fuels. The so-called coarse solid residue (CSR) that remains after this conversion process is currently discarded as a process solid residue. In the context of transitioning from a linear to a circular society, the feasibility of using the solid process residue from waste gasification as a solid catalyst for light olefin production from CO, CO<sub>2</sub>, and H<sub>2</sub> mixtures was investigated in this **Chapter**. This CSR-derived catalyst material converted biomass-derived syngas, a H<sub>2</sub>-poor mixture of CO, CO<sub>2</sub>, H<sub>2</sub>, and N<sub>2</sub>, into methane (57%) and C<sub>2</sub>-C<sub>4</sub> olefins (43%) at 450°C and 20 bar. The main active ingredient of CSR was Fe, and it was discovered with *operando* X-ray diffraction that metallic Fe, present after pre-reduction in H<sub>2</sub>, transformed into an Fe carbide phase under reaction conditions. The increased formation of Fe carbides correlated with an increase in CO conversion and olefin selectivity. The presence of alkali elements, such as Na and K, in CSR-derived catalyst increased the production of light olefins as well.



## 6.1 Introduction

Ceaselessly increasing both global greenhouse gas emissions and energy demand, while depleting fossil resources constitutes a major issue for today's society. To solve this, radical changes in awareness, mindset, and behavior of both the consumer and industry are inevitable. Currently, we are living in a mostly linear economy; resources are converted to products and disposed after usage. Efforts are being made to transition from a linear economy to a circular economy, where resources and products are fully recycled.<sup>1</sup> It is thus indispensable to explore potential solutions and set off in new directions. On the one hand, we need to find efficient ways to mitigate anthropogenic emissions of greenhouse gases, such as CO<sub>2</sub>, and reverse global warming effects.<sup>2</sup> On the other hand, alternative feedstocks, including waste, are required to meet the needs of the further increasing energy demand.<sup>3-5</sup> During the last years, the awareness of proceeding climate change and the urgent need to act grew, which forced the implementation of several climate change mitigation policies.<sup>2</sup> Nevertheless, the global CO<sub>2</sub> emissions are predicted to continuously increase. To solve this issue, carbon capture and storage (CCS) and carbon capture and utilization (CCU) are promising options. Especially the efficient conversion of captured CO<sub>2</sub> into value-added products, including chemicals and fuels, could be a significant breakthrough.<sup>6,7</sup> In this context, thermochemical CO<sub>2</sub> hydrogenation towards value-added products gained attention, as the broad range of possible output comprises not only hydrocarbons, but also higher alcohols and oxygenates.<sup>8-11</sup> In the past decade, many research efforts were made to revive the more than 100 years old Sabatier reaction, which is the catalytic hydrogenation of CO<sub>2</sub> towards methane.<sup>12</sup> Ni-based catalysts are typically used in this process because of their high activity and selectivity, while being inexpensive compared to noble metal-based catalysts, such as Rh, Ru, Au, and Pt.<sup>12-20</sup> However, converting CO<sub>2</sub> towards value-added products other than methane, using relatively cheap, abundant, and non-toxic transition metal catalysts, *i.e.*, Fe, Co, Cu, would be a major advance.

Moreover, using waste residues as solid catalysts for CO<sub>2</sub> conversion towards value-added products would be of particular interest for the industrial sector. Hereby, on the one hand, high costs for waste handling could be minimized, while on the other hand, industrial CO<sub>2</sub> emissions could be directly converted into value-added products in a circular fashion. Ideally, gaseous industrial waste streams could be directly used as reactant over the solid process waste products, which then act as solid catalyst materials for producing value-added products. To this end, the "recycled process residue catalyst" should be able to convert the waste stream, generally consisting of a mixture of various gases. For example, waste streams from biomass char gasification consist of CO, CO<sub>2</sub>, H<sub>2</sub>, and inert gases.<sup>21-25</sup> The solid residue that remains after this process may contain many different elements in various phases and oxidation states. Typically, the main components are

Si, Al, Ca, Mg, Fe, K, and Na,<sup>22,24</sup> but *i.e.*, Ti, S, and P have also been reported.<sup>23</sup> It has already been documented that iron-containing char from biomass gasification catalyzes hydrocarbon cracking reactions.<sup>26</sup> Although, the ideal solid residue would possess both CO<sub>2</sub> hydrogenation and Fischer-Tropsch Synthesis (FTS) activity, as the gaseous stream from gasification consists mainly of CO, CO<sub>2</sub>, and H<sub>2</sub>.

For the FTS process, an industrial process to convert CO and H<sub>2</sub> into synthetic fuels, Co and Fe are the most widely used for the synthesis of the required catalyst materials.<sup>27-29</sup> Cobalt operates at 200-250°C and mainly yields linear C<sub>5+</sub> paraffins. Iron, on the other hand, is able to operate in a broader temperature range (200-350°C) and typically produces more olefins and oxygenates, particularly at higher reaction temperatures (320-350°C).<sup>25,30-32</sup> Fischer-Tropsch-to-Olefins (FTO), a subclass of the FTS process, is particularly interesting for the direct conversion of alternative carbon resources to lower olefins.<sup>33</sup> For this sustainable process, iron-based catalysts are preferred over cobalt-based catalysts because of their high olefin selectivity, low cost, and high water gas shift (WGS) activity. The latter enables the catalyst to alter the H<sub>2</sub>/CO ratio of the synthesis gas or syngas,<sup>32,33</sup> which is essential when *e.g.*, biomass is used as feedstock and the H<sub>2</sub>/CO ratio of the resulting syngas is below 1.<sup>25,34,35</sup> Biomass-derived syngas may additionally contain CO<sub>2</sub> and N<sub>2</sub> since air is typically used as oxidation agent in the biomass gasification process.<sup>36</sup> The specifications of biomass-derived syngas may lead to low conversion efficiency and worse catalyst performance.<sup>35</sup> Apart from the traditional FTS process, CO<sub>2</sub> hydrogenation to fuels, also referred to as modified (M)FTS, gained attraction in terms of CO<sub>2</sub> mitigation strategies.<sup>37-40</sup> Fe-based FTO catalysts yielded a very stable product selectivity when changing the gas feed from traditional CO and H<sub>2</sub> mixture towards CO<sub>2</sub>, CO, and H<sub>2</sub>.<sup>11,41,42</sup> Besides, the addition of alkali metals, such as K and Na, to Fe-based catalysts has been reported to improve long-chain hydrocarbon and olefin production from CO<sub>2</sub>.<sup>11,43,44</sup> Accordingly, solid residue containing Fe and alkali metals might represent a promising candidate for industrial waste stream conversion.

In this **Chapter**, we have investigated the applicability of a Coarse Solid Residue (CSR) in CO<sub>2</sub>/CO/H<sub>2</sub> conversion. The CSR catalyst material was generated during a solid waste gasification process at Enerkem (Westbury, Canada). Hereby, we aimed to employ the CSR sample without further modification, potentially enabling the direct usage of industrial solid waste as a suitable solid catalyst to convert gaseous industrial waste streams into valuable products. To evaluate the potential of this CSR sample for CO/CO<sub>2</sub> hydrogenation, an Fe/SiO<sub>2</sub> reference catalyst with comparable iron oxide nanoparticle sizes was used, hereby mimicking the main active ingredients of the CSR sample. We show that CSR catalyst materials make methane and olefins from a CO, CO<sub>2</sub>, H<sub>2</sub>, and N<sub>2</sub> gas feed, thereby mimicking the composition of biomass-derived syngas. Alkali



promoter effects on the CO<sub>2</sub> and CO hydrogenation performances were investigated using a K-Fe/SiO<sub>2</sub> reference catalyst. The presence of K enhanced the (reverse) (R)WGS activity and led to an increase in olefin production. Besides catalytic testing, *operando* X-ray diffraction (XRD) and Raman spectroscopy studies were performed to gain insights into the catalytically active phase and deducing a fundamental understanding of structure-performance correlations in the CSR samples. It was found that the increased presence of the iron carbide phase in the catalyst materials coincided with an increase in olefin selectivity.

## 6.2 Materials and Methods

### 6.2.1. Catalyst Preparation

The industrial waste sample, a coarse solid residue (CSR) sample, also called “slag” was generated during solid waste residue gasification process at Enerkem (Westbury, Canada). The CSR sample was used without further treatment. The Fe/SiO<sub>2</sub> (7.7 wt.% Fe) and the K-Fe/SiO<sub>2</sub> (0.71 wt.% K and 7.6 wt.% Fe) reference catalysts were prepared by the incipient wetness impregnation (IWI) technique. To this purpose, commercially available high-purity grade silica gel (Davisil Grade 643, pore size 150 Å, 200-425 mesh, Sigma Aldrich) was used as support material. The synthesis procedure was conducted as follows. Initially, the required amount of FeCl<sub>3</sub>·6 H<sub>2</sub>O (Sigma Aldrich, ≥ 99%) was dissolved in water, whereby the volume of water was adjusted to that of the pore volume of the silica support. After impregnation and drying at 60°C for 24 h, calcination of the impregnated catalyst was conducted under flowing N<sub>2</sub> (100 mL min<sup>-1</sup>) in a tubular furnace at 450°C for 5 h (5°C min<sup>-1</sup> ramp). The K-promoted Fe/SiO<sub>2</sub> catalyst was prepared by consecutive impregnation with an aqueous solution of K<sub>2</sub>CO<sub>3</sub> (Sigma Aldrich, ≥ 99%), drying, and calcination as described above.

### 6.2.2. Catalyst Characterization

The metal concentrations were determined *via* optical emission spectroscopy using inductively coupled plasma (ICP-OES) with a PerkinElmer Avio® 500 ICP Optical Emission Spectrometer. Here, the CSR and Fe/SiO<sub>2</sub> samples were prepared by iron extraction in aqua regia. Additionally, the chemical composition of the CSR sample was analyzed by X-ray fluorescence (XRF) spectrometry (Panalytical, Axios Advanced instrument).

Electron microscopy investigations were performed in scanning mode (SEM) with energy dispersive X-ray (EDX) spectroscopy using a FEI Helios Nanolab.G3 instrument operating at 5-30 keV. Electron microscopy investigations were performed in trans-

mission mode (TEM) and high-angle annular dark-field (HAADF) mode using a FEI Talos F200X microscope operating at 200 kV. Elemental mapping was performed using energy dispersive X-ray (EDX) spectroscopy. For the TEM measurements, the samples were suspended in ethanol under ultrasonic vibrations. Subsequently, a drop of the suspension was deposited onto a Carbon-type B copper 200 mesh grid. For determining the particle size distribution of the supported nanoparticles from TEM images, the software ImageJ was used for manually fitting the particle diameters (> 100 particles).

*Ex situ* X-ray diffraction (XRD) patterns of the fresh and spent catalysts were recorded on a Bruker D2 Phaser X-ray diffractometer using Co K $\alpha_{1,2}$  radiation ( $\lambda = 1.790 \text{ \AA}$ ) in the range of  $2\theta = 20\text{--}80^\circ$  with a scan step size of  $0.01^\circ$  and scan time 1 s/step. The Fe<sub>2</sub>O<sub>3</sub> average crystallite sizes were estimated by applying the Scherrer equation (k-factor of 0.9) to the (0 1 2) diffraction of Fe<sub>2</sub>O<sub>3</sub> ( $2\theta=28.0^\circ$ ).

Temperature-programmed reduction (TPR) measurements were performed using a Micromeritics AutoChem II 2920 instrument. Samples were placed on quartz wool into a U-tube quartz reactor. The gas mixture consisted of 5% H<sub>2</sub> in Ar with a total gas flow of 40 ml/min. H<sub>2</sub> TPR was carried out by heating with  $5^\circ\text{C}/\text{min}$  up to  $800^\circ\text{C}$  for Fe/SiO<sub>2</sub> catalysts and the coarse solid residue (CSR) sample and held for 30 min at this temperature. A constant initial sample weight of 0.05 g was used and H<sub>2</sub> consumption was continuously monitored by a thermal conductivity detector.

*Operando* XRD patterns were recorded on a Bruker D8 Discover X-ray diffractometer in Debye-Scherrer transmission (capillary) geometry with a Mo (K $\alpha_1 = 0.709 \text{ \AA}$ ) source. At the beginning of each *operando* reaction run, the capillary was moved to the focus of the X-ray beam (beam  $\approx 600 \times 15\,000 \text{ \mu m}$ , height  $\times$  width) for maximum diffraction. The XRD patterns were collected over a  $2\theta$  range of  $7\text{--}25^\circ$  with a scan step size of  $0.015^\circ$ . Data were collected of the fresh sample, during reduction at  $450^\circ\text{C}$  in pure H<sub>2</sub> ( $3 \text{ mL min}^{-1}$ ), after reduction, and during CO hydrogenation (CO/H<sub>2</sub>/He=2.25/1.5/1). The products were analyzed with on-line gas chromatography (GC) (Thermo Fischer Scientific).

Raman spectra were recorded using a Horiba Xplora with a 532 nm laser and 1200 grating for 30 s with 5 accumulations. For performing *operando* experiments, a Raman high temperature reaction chamber from Harrick Scientific, suitable for high pressures and temperatures, was used. To monitor the iron phase during the reduction procedure, the CSR sample was heated to  $450^\circ\text{C}$  with  $10^\circ\text{C min}^{-1}$  in  $3 \text{ mL min}^{-1}$  H<sub>2</sub> and  $3 \text{ mL min}^{-1}$  Ar. Then, the sample was exposed to  $2.2 \text{ mL min}^{-1}$  CO,  $1.2 \text{ mL min}^{-1}$  CO<sub>2</sub>,  $1.5 \text{ mL min}^{-1}$  H<sub>2</sub>, and  $0.2 \text{ mL min}^{-1}$  Ar at  $P=20 \text{ bar}$  and  $T=450^\circ\text{C}$ . Meanwhile, Raman spectra were recorded

to monitor the iron phase and carbonaceous species under reaction conditions. The gaseous products were analyzed with on-line mass spectrometry (MS) (Pfeiffer Vacuum).

### 6.2.3. Catalyst Testing

Catalyst performance was tested in a fixed-bed reactor. The steel reactor was typically filled with 200-250 mg of catalyst sample sieved to a grain size of 150-425  $\mu\text{m}$ . The sample was plugged between two quartz wool plugs. The reactor was placed in an oven and was connected to the gas inlet and outlet. A back pressure controller (BPC) was incorporated in the gas line connected to the outlet to maintain a defined pressure. An on-line gas Thermo Fischer Trace 1300 gas chromatograph was used for product analysis. The catalyst was reduced in 20 mL  $\text{min}^{-1}$   $\text{H}_2$  and 40 mL  $\text{min}^{-1}$   $\text{N}_2$  at 450°C for 1 h (10°C  $\text{min}^{-1}$  ramp). Then, the reactor was cooled down to 250°C with a 10°C  $\text{min}^{-1}$  ramp in the same atmosphere. At 250°C the gas flow was switched to 22.5 mL  $\text{min}^{-1}$   $\text{CO}$ , 12.5 mL  $\text{min}^{-1}$   $\text{CO}_2$ , 15 mL  $\text{min}^{-1}$   $\text{H}_2$ , 5 mL  $\text{min}^{-1}$   $\text{N}_2$ , and 1.2 mL  $\text{min}^{-1}$  Ar. The pressure was built up with 1 bar  $\text{min}^{-1}$  to 5 bar or 20 bar. For 12-24 h the products of the reaction were analyzed with an on-line GC (injection every 23 min). This was repeated at 300-450°C. The conversion and selectivities were calculated from the obtained GC data. The amounts of converted CO or  $\text{CO}_2$  were calculated using **Equation 6.1**.

$$X_{\text{CO}} (\%) = \left(1 - \frac{A_{\text{CO}}/A_{\text{Ar}}}{A_{\text{CO}}^0/A_{\text{Ar}}^0}\right) * 100\% \quad (\text{Equation 6.1})$$

$A_{\text{CO}}$  and  $A_{\text{Ar}}$  represent the thermal conductivity detector (TCD) peak area of CO and Ar during the reaction.  $A_{\text{CO}}^0$  and  $A_{\text{Ar}}^0$  are the TCD peak areas of CO and Ar recorded during a blank measurement. The selectivity was calculated using **Equation 6.2**.

$$S_i (\%) = \left(\frac{A_i * F_i}{\sum A_i * F_i}\right) * 100\% \quad (\text{Equation 6.2})$$

In this equation,  $A_i$  corresponds to the peak area of product  $i$  and  $F_i$  represents the response factor of the analyte.<sup>45</sup>

### 6.3 Results and Discussion

#### 6.3.1 Chemical Composition

The mineral composition of the coarse solid residue (CSR) material obtained during solid waste gasification, as determined with X-ray fluorescence (XRF) and inductively coupled plasma-optical emission spectroscopy (ICP-OES), can be found in **Table 6.1**.

**Table 6.1.** Coarse Solid Residue (CSR) composition from various solid waste feedstocks obtained by X-ray fluorescence (XRF) spectrometry and inductively coupled plasma-optical emission spectroscopy (ICP-OES)<sup>[a]</sup> analysis of the specific CSR batch used in this study, as well as the Fe/SiO<sub>2</sub> reference catalyst.

CSR Compound	Min. (wt.%) XRF	Max. (wt.%) XRF	Element	CSR ICP-OES (wt.%)	Fe/SiO <sub>2</sub> ICP-OES (wt.%)
SiO <sub>2</sub>	38.9	59.2	n.a.	n.a. <sup>[a]</sup>	n.a. <sup>[a]</sup>
CaO	13.0	24.3	Ca	9.5	
Al <sub>2</sub> O <sub>3</sub>	7.7	36.1	Al	5.1	
MgO	1.4	3.1	Mg	0.7	
Na <sub>2</sub> O	1.6	4.2	Na	2.5	
K <sub>2</sub> O	0.5	1.6	K	1.9	
MnO	0.1	1.6	Mn	0.04	
ZrO <sub>2</sub>	0.1	3.0	n.a.	n.a.	
TiO <sub>2</sub>	0.8	1.5	Ti	0.7	
Cr <sub>2</sub> O <sub>3</sub>	0	0.1	Cr	0.03	
Fe <sub>2</sub> O <sub>3</sub>	1.2	4.8	Fe	1.9	7.7
BaO	0	0.1	Ba	0.05	
SO <sub>3</sub>	0	0.4	S	0.01	
P <sub>2</sub> O <sub>5</sub>	0	3.0	P	0.7	
LOI	0	0.2	n.a.	n.a.	
			Cu	0.2	

<sup>[a]</sup> The Si concentration could not be determined quantitatively with ICP-OES.

The main components were the metal oxides SiO<sub>2</sub>, CaO, and Al<sub>2</sub>O<sub>3</sub>, which in heterogeneous catalysis generally function as support or binder material and stabilize the catalytically active metal nanoparticles. Another important component in the CSR sample was Fe<sub>2</sub>O<sub>3</sub>. Fe is believed to be the catalytically active component in solid residues from gasification processes<sup>26</sup> and also the active ingredient in FTO-based catalyst materials.<sup>46,47</sup>

Then, the alkali metals Na and K in CSR can act as a promoter or a poison, depending on their concentration and interplay with the active metal phase.<sup>47-49</sup> As promoters, the alkali metals both increase the reducibility of iron oxides and the carbon deposition rate. The latter is beneficial for FTO, as the active phase is considered an Fe carbide phase.<sup>46</sup> In the CO<sub>2</sub> hydrogenation reaction, the addition of alkali metals to Fe-based catalysts has been reported to increase the selectivity towards high-valued olefins due to reverse water-gas shift (RWGS) activity.<sup>43,49</sup> Moreover, Mg and Ca that are present in CSR have been reported to increase the deactivation rate and the methane formation rate compared to unpromoted and K-promoted iron-based FTO catalysts.<sup>50</sup> Besides, CSR contained Cr and Cu, which are known to promote the (R)WGS reaction as well.<sup>51</sup>

### 6.3.2 Morphology of the Coarse Solid Residue Sample

The morphology of the CSR sample and spatial distribution of the elements were investigated with electron microscopy (EM) and energy-dispersive X-ray spectroscopy (EDX). The CSR morphology resembled a typical Fe/SiO<sub>2</sub> heterogeneous catalyst: Fe nanoparticles supported by a SiO<sub>2</sub> matrix (Figure 6.1).

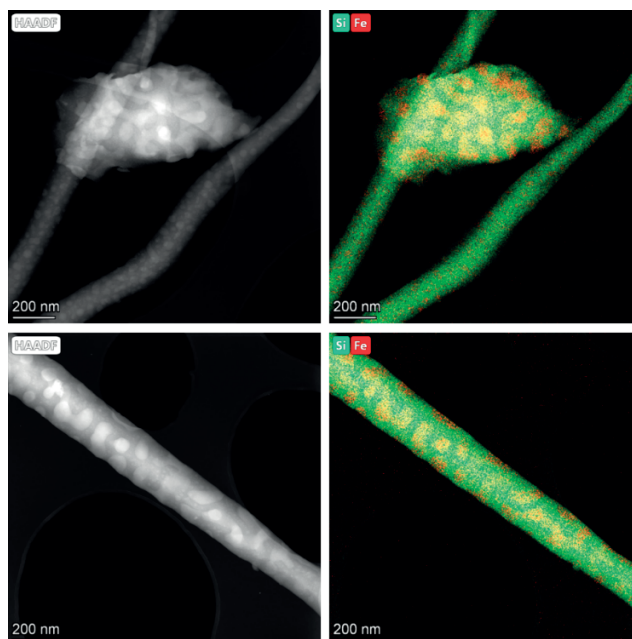


**Figure 6.1.** High-angle annular dark-field (HAADF)-scanning transmission electron microscopy (STEM) images of the fresh coarse solid residue (CSR) sample (left) and energy-dispersive X-ray (EDX) spectroscopy chemical mapping (right). Fe is shown in red and Si is shown in green.

However, CSR contained more elements than just Fe and Si. For example, Al appeared to be in the same location as Si, whereas Ca and Ti appeared to be in close vicinity of the Fe nanoparticles (**Figures 6.2** and **6.3**). The average  $\text{Fe}_2\text{O}_3$  nanoparticle size was  $64 \pm 16$  nm from the high-angle annular dark-field (HAADF)-scanning transmission electron microscopy (STEM) images (**Figure 6.4**).

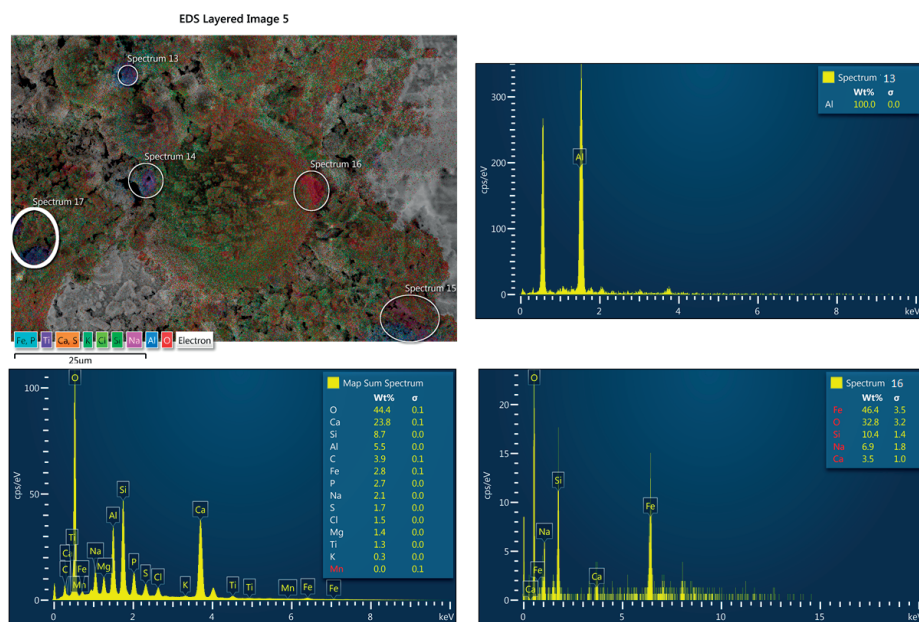


**Figure 6.2.** Scanning electron microscopy (SEM) with energy-dispersive X-ray (EDX) spectroscopy image (top left) and the corresponding map sum spectrum (bottom left). Spectrum 13 (top right) was exclusively aluminum oxide, while spectrum 16 contained mostly iron oxide (bottom right).

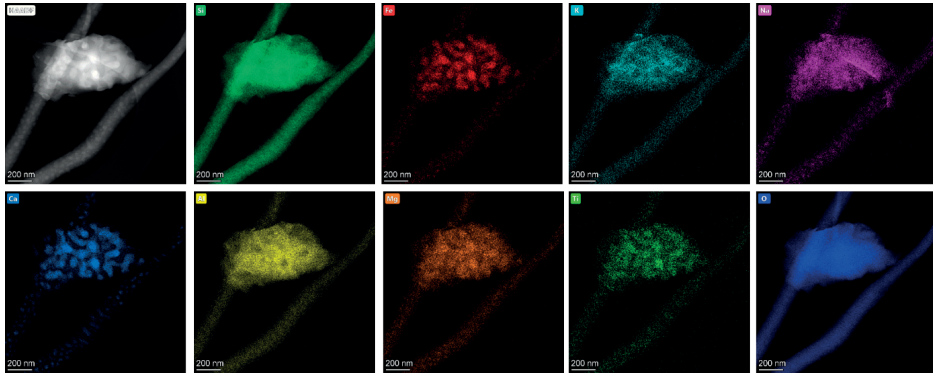


**Figure 6.3.** High-angle annular dark-field (HAADF)-scanning transmission electron microscopy (STEM) image (top left) and energy dispersive X-ray spectroscopy (EDX) chemical mapping of Si, Fe, K, Na, Ca, Al, Mg, Ti, and O.

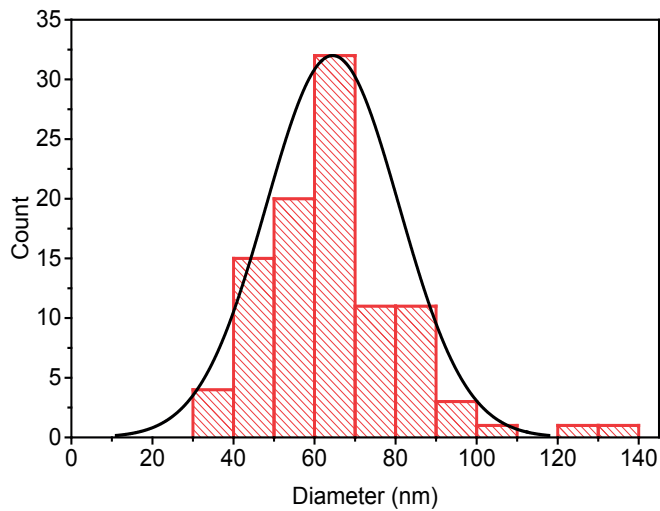


**Figure 6.4.** Particle size distribution of the Fe<sub>2</sub>O<sub>3</sub> nanoparticles in the coarse solid residue (CSR) sample. The average Fe<sub>2</sub>O<sub>3</sub> nanoparticle size was 64 ± 16 nm and in total 100 particles were counted from the high-angle annular dark-field (HAADF)-scanning transmission electron microscopy (STEM) images.

### 6.3.3 Determination of the Iron Crystalline Phases and Crystallite Sizes

The crystalline phases and Fe crystallite sizes in the CSR sample and Fe/SiO<sub>2</sub> reference catalyst were analyzed with X-ray diffraction (XRD) (Figure 6.5 and 6.6). The diffraction peaks of the CSR sample matched with the mineral gehlenite (*i.e.*, Ca<sub>2</sub>Al<sub>2</sub>SiO<sub>7</sub>) and with hematite (*i.e.*, Fe<sub>2</sub>O<sub>3</sub>). For the Fe/SiO<sub>2</sub> reference catalyst only hematite (*i.e.*, Fe<sub>2</sub>O<sub>3</sub>) was detected as crystalline phase. The average Fe<sub>2</sub>O<sub>3</sub> crystallite size was 63 nm for the CSR sample and 53 nm for the Fe/SiO<sub>2</sub> reference catalyst.

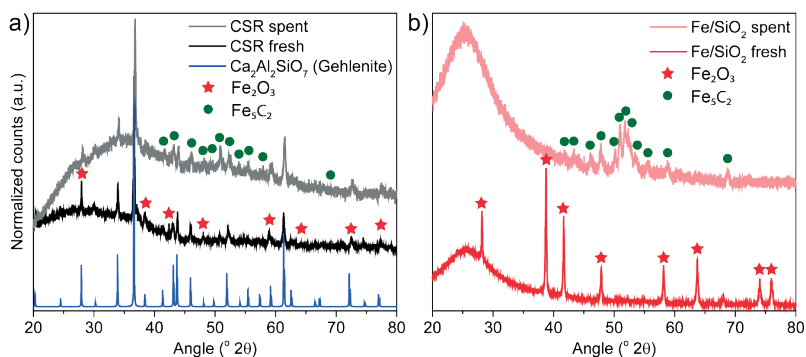


**Figure 6.5.** Characterization of the crystalline phases in the coarse solid residue (CSR) sample and a reference Fe/SiO<sub>2</sub> catalyst material with X-ray diffraction (XRD). **a)** XRD patterns of the fresh and spent ( $T=450^{\circ}\text{C}$ ,  $P=5$  bar, and  $\text{CO}:\text{CO}_2:\text{H}_2:\text{N}_2=4.5:2.5:3:1$ ) CSR sample. XRD pattern of the mineral gehlenite from the PDF-4+ XRD database is added as a reference. **b)** Fe/SiO<sub>2</sub> (7.7 wt.%) fresh and spent ( $T=450^{\circ}\text{C}$ ,  $P=5$  bar, and  $\text{CO}:\text{CO}_2:\text{H}_2:\text{N}_2=4.5:2.5:3:1$ ).

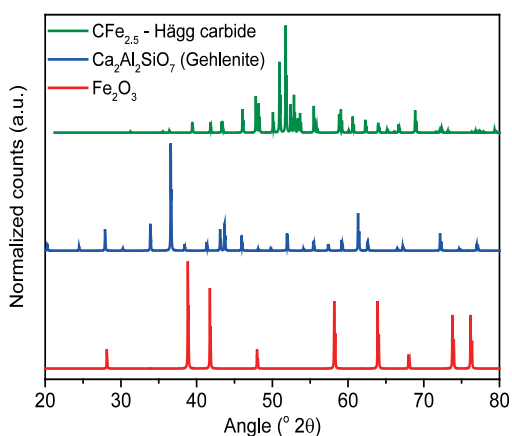


**Figure 6.6.** X-ray diffraction (XRD) patterns from the PDF-4+ XRD database.



### 6.3.4 Hydrocarbon Production from Reactant Mixtures

The CSR sample and the Fe/SiO<sub>2</sub> reference catalyst were catalytically tested in CO:CO<sub>2</sub>:H<sub>2</sub>:N<sub>2</sub>=4.5:2.5:3:1 and at 5 bar pressure (**Figure 6.7**). This particular gas feed composition was chosen with renewable energy resources in mind, as biomass-derived syngas typically has a gas composition with H<sub>2</sub>/CO < 1 and may contain CO<sub>2</sub> and N<sub>2</sub>.<sup>25,34</sup> Prior to the reaction, the sample was heated in H<sub>2</sub> at 450°C to transform Fe<sub>2</sub>O<sub>3</sub> into metallic Fe. The reduction profiles of CSR and Fe/SiO<sub>2</sub> can be found in **Figure 6.8**. First, we explored the influence of reaction temperature by performing multiple tests at 250, 350, and 450°C (**Figures 6.7a and 6.7c**). We found 450°C as the optimum operating temperature for the CSR sample (**Figure 6.7a**), as the total carbon conversion increased with temperature. Besides, the very exothermic methane formation reactions from CO ( $\Delta H = -220 \text{ kJ mol}^{-1}$  @450°C) and CO<sub>2</sub> ( $\Delta H = -183 \text{ kJ mol}^{-1}$  @450°C) are thermodynamically more favorable at relatively low temperatures (see also thermodynamic calculations in **Figure 6.9**) and in high H<sub>2</sub> concentrations. This was indeed reflected by the methane selectivity, which was the lowest at 450°C. From CO and H<sub>2</sub> the C<sub>2</sub> and C<sub>3</sub> olefin formation reactions are exothermic, while from CO<sub>2</sub> and H<sub>2</sub> these reactions are endothermic.<sup>52</sup> In our study, higher temperature appeared favorable for the lower olefin yield (**Tables 6.2 and 6.3**) from the CO:CO<sub>2</sub>:H<sub>2</sub>:N<sub>2</sub>=4.5:2.5:3:1 gas feed; propene was only formed at 350 and 450°C and not at lower temperatures. Compared to the total carbon conversion of the Fe/SiO<sub>2</sub> reference catalyst (24.9% @450°C), CSR had a lower overall carbon conversion (16.0% @450°C) (**Tables 6.2-6.5**). The lower carbon conversion of CSR compared to the Fe/SiO<sub>2</sub> reference catalyst is explained by the lower content of the active ingredient Fe in CSR (1.9 wt.%) compared to Fe/SiO<sub>2</sub> (7.7 wt.%), as displayed in **Table 6.1**. Besides, the high content of K (1.9 wt.%) and Na (2.5 wt.%) in CSR could have a detrimental effect on catalytic performance.<sup>48</sup> Moreover, Mg and Ca in CSR could increase the deactivation rate and the methane formation rate during the FTO reaction.<sup>50</sup>

The stabilities of the CSR sample and Fe/SiO<sub>2</sub> were evaluated in CO:CO<sub>2</sub>:H<sub>2</sub>:N<sub>2</sub>=4.5:2.5:3:1, P=5 bar, and T=450°C (see **Figure 6.7b,d** and **Tables 6.3 and 6.5**). For CSR, the methane (59.3%), C<sub>2</sub> (28.6%), and C<sub>3</sub> (11.6%) selectivities remained stable over the course of 24 h. In some of the gas chromatography (GC) injections, C<sub>4</sub> products were detected as well (**Figure 6.7b** and **Table 6.3**; 0.5% average selectivity). However, the total carbon conversion decreased over time. Considering the high CO/CO<sub>2</sub> ratio (CO/CO<sub>2</sub>=1.8) in the gas feed, the occurrence of the WGS reaction ( $\text{CO} + \text{H}_2\text{O} \rightarrow \text{CO}_2 + \text{H}_2$ ;  $\Delta H = -37.8 \text{ kJ mol}^{-1}$  @450°C) could provide a potential explanation for the decrease in carbon conversion. Fe-based catalysts are known to promote this reaction at moderately high temperatures (350-500°C).<sup>51</sup> Besides, CSR contains Cr, Cu, K, and Na, which are known to promote the WGS reaction as well.<sup>51</sup> CO and the inevitably formed H<sub>2</sub>O then produce CO<sub>2</sub>, which is less reactive than CO and

consequently lowers the total carbon conversion. Besides, Mg and Ca, also present in CSR, have been reported to increase the deactivation rate during the FTO reaction.<sup>50</sup> An alternative explanation for the lower carbon conversion could be the oxidation of iron phases on the catalyst surface. CO<sub>2</sub> and H<sub>2</sub>O are known to have an oxidizing effect and thereby deactivate conventional iron-based catalysts.<sup>25,32,53</sup>

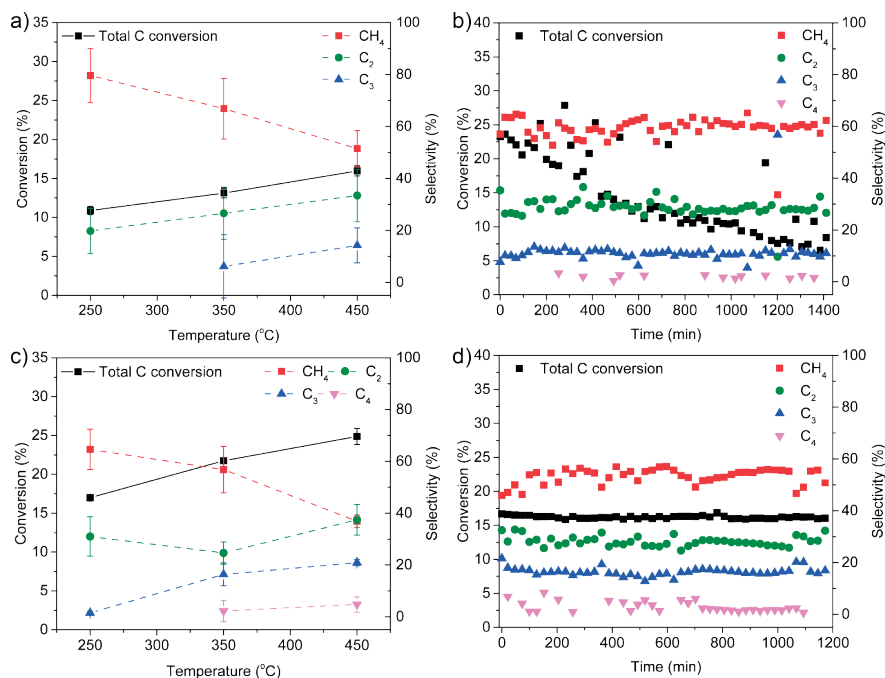


**Figure 6.7.** Catalytic performance of the coarse solid residue (CSR) sample and the Fe/SiO<sub>2</sub> reference catalyst material. Catalytic testing of **a)** CSR and **c)** Fe/SiO<sub>2</sub> in CO:CO<sub>2</sub>:H<sub>2</sub>:N<sub>2</sub>=4.5:2.5:3:1 at  $P=5$  bar,  $T=250, 350, 450^{\circ}\text{C}$ , and gas hourly space velocity (GHSV)=3400 h<sup>-1</sup> (12 h per temperature). Stability testing of **b)** CSR and **d)** Fe/SiO<sub>2</sub> at 450°C for 24 h and 20 h, respectively, under the same gases and pressure as (a).

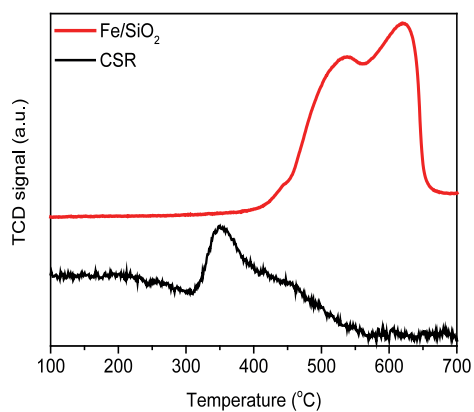


**Figure 6.8.** H<sub>2</sub>-temperature-programmed reduction (TPR) profiles for the Fe/SiO<sub>2</sub> reference catalyst and for the coarse solid residue (CSR) sample.

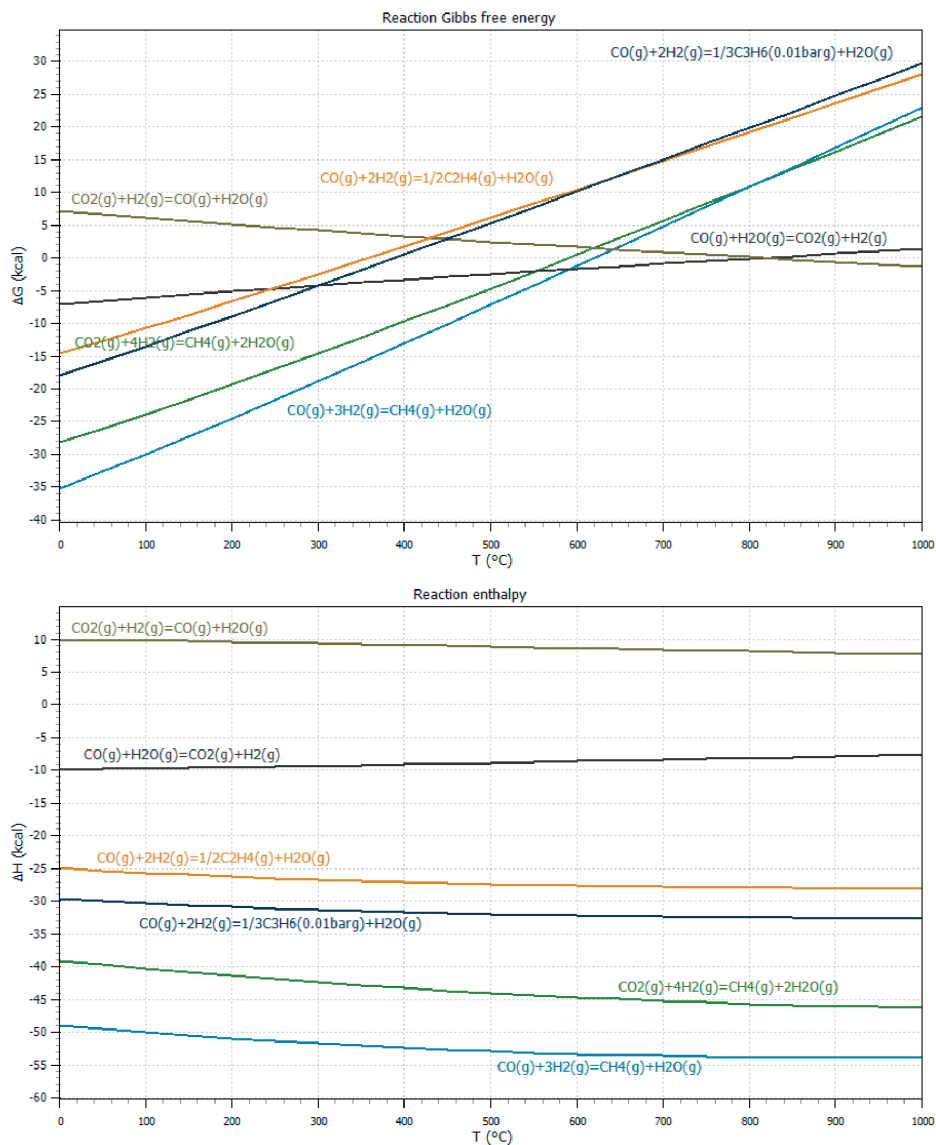


**Figure 6.9.** Thermodynamic calculations for the possible reactions taking place during  $\text{CO}/\text{CO}_2$  hydrogenation using the coarse solid residue (CSR) sample. The top panel displays the Gibbs free energy and the bottom panel the reaction enthalpy.

**Table 6.2.** Catalytic performance of coarse solid residue (CSR) at various temperatures,  $P=5$  bar,  $\text{CO}:\text{CO}_2:\text{H}_2:\text{N}_2=4.5:2.5:3:1$ , and gas hourly space velocity (GHSV)=3400  $\text{h}^{-1}$ . Per temperature step, 12 h of catalytic testing was performed with 1 gas chromatography (GC) injection per 23 min.

Temperature ( $^{\circ}\text{C}$ )	Total C conversion (%)	$\text{CH}_4$ (%)	$\text{C}_2$ (%)	$\text{C}_2$ O/P <sup>[a]</sup>	$\text{C}_2$ olefin yield (%)	$\text{C}_3$ (%)	$\text{C}_3$ O/P <sup>[a]</sup>	$\text{C}_3$ olefin yield (%)
250	$10.9 \pm 0.5$	$79.6 \pm 10.4$	$19.8 \pm 8.7$	$1.18 \pm 0.26$	2.55			
350	$13.1 \pm 0.6$	$66.9 \pm 11.7$	$26.6 \pm 10.0$	$1.29 \pm 0.24$	4.48	$6.14 \pm 12.2$	$0.87 \pm 0.19$	0.70
450	$16.0 \pm 0.7$	$51.5 \pm 6.9$	$33.4 \pm 10.2$	$1.57 \pm 0.29$	8.37	$14.2 \pm 6.7$	$0.82 \pm 0.13$	1.87

[a] O/P stands for olefin/paraffin ratio

**Table 6.3.** Average catalytic performance of coarse solid residue (CSR) over 24 h time-on-stream at  $T=450^{\circ}\text{C}$ ,  $P=5$  bar,  $\text{CO}:\text{CO}_2:\text{H}_2:\text{N}_2=4.5:2.5:3:1$ , and gas hourly space velocity (GHSV)=3400  $\text{h}^{-1}$ . A gas chromatography (GC) injection was performed every 23 min.

Total C conversion (%)	$\text{CH}_4$ (%)	$\text{C}_2$ (%)	$\text{C}_2$ O/P <sup>[a]</sup>	$\text{C}_3$ (%)	$\text{C}_3$ O/P <sup>[a]</sup>	$\text{C}_4$ (%)	$\text{C}_4$ O/P <sup>[a]</sup>
$14.7 \pm 5.9$	$59.3 \pm 4.5$	$28.6 \pm 3.5$	$1.15 \pm 0.42$	$11.6 \pm 3.4$	$0.80 \pm 0.23$	$0.48 \pm 0.94$	$3.87 \pm 1.56$

[a] O/P stands for olefin/paraffin ratio

**Table 6.4.** Catalytic performance of Fe/SiO<sub>2</sub> at various temperatures,  $P=5$  bar,  $\text{CO}:\text{CO}_2:\text{H}_2:\text{N}_2=4.5:2.5:3:1$ , and gas hourly space velocity (GHSV)=3400  $\text{h}^{-1}$ . Per temperature step, 12 h of catalytic testing was performed with 1 gas chromatography (GC) injection per 23 min.

Temperature ( $^{\circ}\text{C}$ )	Total C conversion (%)	$\text{CH}_4$ (%)	$\text{C}_2$ (%)	$\text{C}_2$ O/P <sup>[a]</sup>	$\text{C}_3$ (%)	$\text{C}_3$ O/P <sup>[a]</sup>	$\text{C}_4$ (%)	$\text{C}_4$ O/P <sup>[a]</sup>
250	$17.0 \pm 0.2$	$64.6 \pm 7.8$	$31.0 \pm 7.6$	$1.18 \pm 0.56$	$1.48 \pm 0.68$	$1.87 \pm 0.27$		
350	$21.7 \pm 0.1$	$56.8 \pm 9.0$	$24.6 \pm 4.3$	$1.05 \pm 0.10$	$16.4 \pm 4.4$	$1.7 \pm 0.458$	$2.20 \pm 4.12$	$2.63 \pm 1.20$
450	$24.9 \pm 1.0$	$36.9 \pm 2.4$	$37.4 \pm 5.9$	$0.87 \pm 0.29$	$20.9 \pm 1.2$	$1.43 \pm 0.14$	$4.77 \pm 0.95$	$0.70 \pm 0.08$

[a] O/P stands for olefin/paraffin ratio

**Table 6.5.** Average catalytic performance of Fe/SiO<sub>2</sub> over 20 h time-on-stream at T=450°C, P=5 bar, CO:CO<sub>2</sub>:H<sub>2</sub>:N<sub>2</sub>=4.5:2.5:3:1, and gas hourly space velocity (GHSV)=3400 h<sup>-1</sup>. A gas chromatography (GC) injection was performed every 23 min.

Total C conversion (%)	Methane (%)	C <sub>2</sub> (%)	C <sub>2</sub> O/P <sup>[a]</sup>	C <sub>3</sub> (%)	C <sub>3</sub> O/P <sup>[a]</sup>	C <sub>4</sub> (%)	C <sub>4</sub> O/P <sup>[a]</sup>
16.2 ± 0.2	53.3 ± 3.0	28.2 ± 2.0	0.87 ± 0.49	16.4 ± 1.6	1.37 ± 0.36	2.09 ± 2.20	1.15 ± 0.68

<sup>[a]</sup> O/P stands for olefin/paraffin ratio

### 6.3.5 Fe Carbides in the Spent Catalyst Materials

The spent CSR sample as well as the Fe/SiO<sub>2</sub> reference catalyst material contained Fe carbides as determined with XRD (**Figure 6.5**). The Hägg carbide (Fe<sub>5</sub>C<sub>2</sub>) is known to be the most stable Fe carbide phase under FTO reaction conditions<sup>46</sup> and this was the only Fe carbide phase observed herein. Fe<sub>5</sub>C<sub>2</sub> has also been proposed as main active phase in the FTO reaction and postulated as responsible phase for hydrocarbon chain growth.<sup>54</sup> To further investigate the correlations between alkali promoter elements, (reverse) WGS ((R)WGS) activity, Fe carbide formation, and catalytic performance, CSR, Fe/SiO<sub>2</sub>, and K-Fe/SiO<sub>2</sub> were tested consecutively for CO<sub>2</sub> hydrogenation, FTO, and again CO<sub>2</sub> hydrogenation to assess whether iron carbide formation affected the RWGS activity.

### 6.3.6 Reverse Water Gas Shift Activity Promoted by Alkali Elements

To examine the occurrence of the RWGS reaction, we tested the CSR sample, the Fe/SiO<sub>2</sub> reference catalyst material, and a K-promoted Fe/SiO<sub>2</sub> reference catalyst material (0.71 wt.% K and 7.6 wt.% Fe (ICP-OES)) for CO<sub>2</sub> hydrogenation. Alkali elements, like K, are known to promote the (R)WGS reaction,<sup>51</sup> leading to an increased CO selectivity during CO<sub>2</sub> hydrogenation, which could boost the overall catalyst performance. First, the samples were pre-reduced at 450°C in N<sub>2</sub>/H<sub>2</sub>=2 for 1 h. Then, the CO<sub>2</sub> hydrogenation performance was tested for at  $T=250^{\circ}\text{C}$ ,  $P=5$  bar, and H<sub>2</sub>/CO<sub>2</sub>=3. Subsequently, the FTO performance was tested at  $T=350^{\circ}\text{C}$ ,  $P=5$  bar, and H<sub>2</sub>/CO=0.7. Thereafter, the samples were again tested for CO<sub>2</sub> hydrogenation performance to investigate whether iron carbide formation, known to occur in the presence of H<sub>2</sub>-poor syngas,<sup>46,47</sup> affected RWGS activity. As can be seen in **Figure 6.10**, relatively low CO<sub>2</sub> conversions were observed at 250°C for all samples (~2%). Interestingly, CSR displayed high RWGS activity and produced 91.9% CO during the first CO<sub>2</sub> hydrogenation step (**Figures 6.10a** and **6.10b**). The Fe/SiO<sub>2</sub> catalyst did not produce any CO and appeared thus inactive for the RWGS reaction (**Figures 6.10c** and **6.10d**). However, the presence of the alkali element K promoted the RWGS activity drastically, as the K-Fe/SiO<sub>2</sub> catalyst produced 30.4% CO (**Figures 6.10e** and **6.10f**). The RWGS activity induced by K was beneficial for C<sub>2+</sub> production, as the C<sub>2+</sub> selectivity increased from 12.9% with Fe/SiO<sub>2</sub> to 28.2% with K-Fe/SiO<sub>2</sub> (CO-free selectivities). Besides, the C<sub>2</sub>-C<sub>4</sub> hydrocarbons produced by K-Fe/SiO<sub>2</sub> contained more olefins compared to unpromoted Fe/SiO<sub>2</sub>. The complete product distribution as well as olefin/paraffin ratios can be found in **Tables 6.6** and **6.7**. Increased C<sub>2+</sub> production and olefin selectivity by iron-based catalysts upon K promotion has been reported previously for CO<sub>2</sub> hydrogenation.<sup>25,43</sup>

During the FTO step, the initial apparent CO conversions were high (~11-25%) for all samples (**Figure 6.10**), likely due to CO consumption for iron carbide formation. Under

FTO conditions, carbon diffusion into iron has a lower activation barrier than the FTO reaction.<sup>31</sup> Hence, CO will mostly be used for iron carbide formation until a saturated metal carbide is formed. For Fe/SiO<sub>2</sub>, the catalyst performance deteriorated slightly over time, as more methane and CO<sub>2</sub> were produced (**Figures 6.10c** and **6.10d**). K-Fe/SiO<sub>2</sub> (**Figures 6.10e** and **6.10f**), on the other hand, produced less methane and CO<sub>2</sub>, while more C<sub>2+</sub> was formed over time. For CSR (**Figures 6.10a** and **6.10b**), the CO<sub>2</sub> selectivity went down, the methane selectivity became slightly higher, and the C<sub>2+</sub> selectivity slightly lower over time (**Tables 6.6** and **6.7**). Alkali elements thus appeared to limit catalyst deactivation during the FTO reaction. Besides, alkali promoters clearly enhanced the WGS activity, as average CO<sub>2</sub> selectivities of 14.6%, 27.5%, and 73.1% were observed for Fe/SiO<sub>2</sub>, K-Fe/SiO<sub>2</sub>, and CSR, respectively. The C<sub>2+</sub> selectivity again seemed to benefit from K promotion: On average Fe/SiO<sub>2</sub> produced 34.5% C<sub>2+</sub> (**Figure 6.10d**), while K-Fe/SiO<sub>2</sub> displayed 40.1% C<sub>2+</sub> hydrocarbons (**Figure 6.10f**), and CSR 60.5% (C<sub>2+</sub> CO<sub>2</sub>-free selectivities). The C<sub>2+</sub> hydrocarbons produced by K-Fe/SiO<sub>2</sub> and CSR contained more olefins compared to unpromoted Fe/SiO<sub>2</sub>.

In the second, consecutive, CO<sub>2</sub> hydrogenation step, higher methane and CO selectivities were observed compared to the first CO<sub>2</sub> hydrogenation step for all samples. For CSR, 99.4% CO was observed (**Figure 6.10b**), while Fe/SiO<sub>2</sub> displayed 48.0% (**Figure 6.10d**) and K-Fe/SiO<sub>2</sub> 58.1% (**Figure 6.10f**). The iron carbide phase, as formed under FTO conditions (**Figures 6.5** and **6.11**), thus appeared to have a higher RWGS activity compared to the metallic iron phase present after reduction.



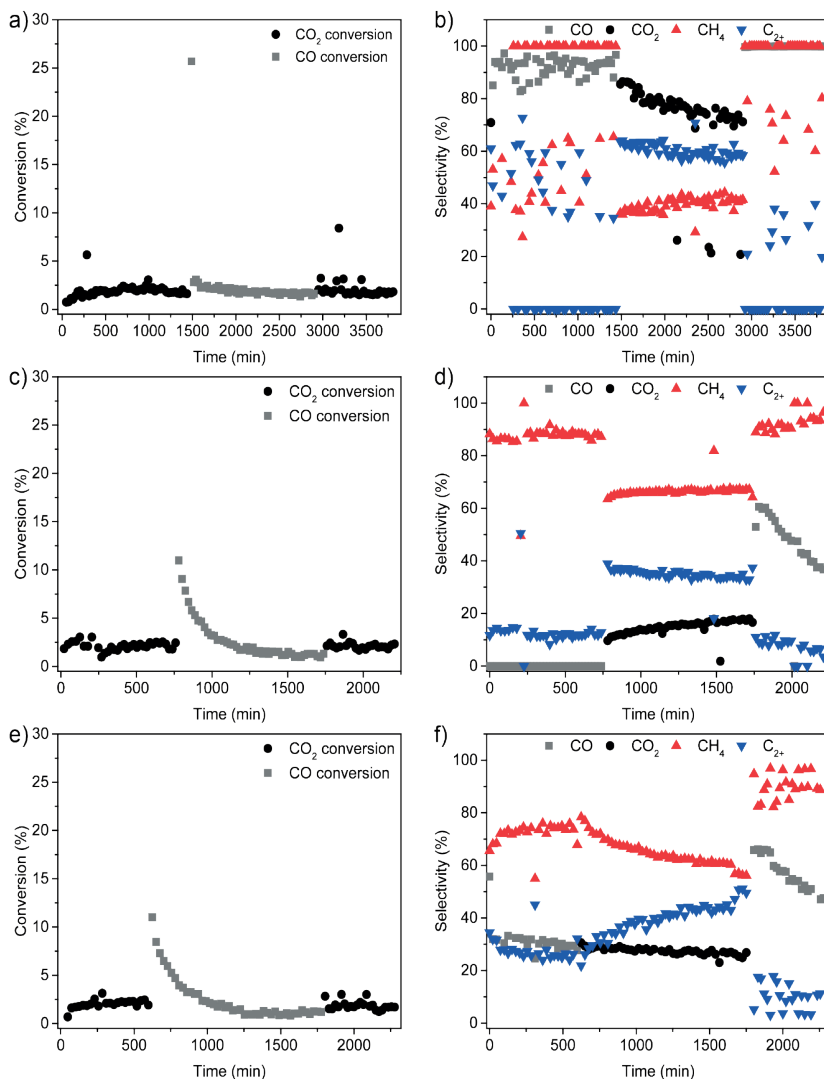


**Figure 6.10.** Catalytic performance in (consecutively) the CO<sub>2</sub> hydrogenation reaction, the Fischer-Tropsch-to-Olefins (FTO) reaction, and the subsequent CO<sub>2</sub> hydrogenation reaction of **a, b**) coarse solid residue (CSR), **c, d**) Fe/SiO<sub>2</sub>, and **e, f**) K-Fe/SiO<sub>2</sub>. The CO<sub>2</sub> hydrogenation steps were carried out at T=250°C, P=5 bar, H<sub>2</sub>/CO<sub>2</sub>=3, and gas hourly space velocity (GHSV)=3070 h<sup>-1</sup>, while the FTO step was carried out at T=350°C, P=5 bar, H<sub>2</sub>/CO =0.7, and GHSV=2425 h<sup>-1</sup>. The hydrocarbon (CH<sub>4</sub> and C<sub>2+</sub>) selectivities displayed are CO and/or CO<sub>2</sub>-free. Prior to the first CO<sub>2</sub> hydrogenation step, the samples were pre-reduced at 450°C in N<sub>2</sub>/H<sub>2</sub>=2 for 1 h.

**Table 6.6.** Average catalytic performance in (consecutively) the CO<sub>2</sub> hydrogenation reaction, the Fischer-Tropsch to-Olefins (FTO) reaction, and the CO<sub>2</sub> hydrogenation reaction of the coarse solid residue (CSR) sample, Fe/SiO<sub>2</sub> catalyst, and the K-Fe/SiO<sub>2</sub> catalyst. The CO<sub>2</sub> hydrogenation steps were carried out at T=250°C, P=5 bar, H<sub>2</sub>/CO<sub>2</sub>=3, and gas hourly space velocity (GHSV)=3070 h<sup>-1</sup>, while the FTO step was carried out at T=350°C, P=5 bar, CO/H<sub>2</sub>=1.5, and GHSV=2425 h<sup>-1</sup>. The hydrocarbon selectivities displayed are CO and/or CO<sub>2</sub>-free. Prior to the first CO<sub>2</sub> hydrogenation step, the samples were pre-reduced at 450°C in N<sub>2</sub>/H<sub>2</sub>=2 for 1 h. The complete set of measurement points (recorded with gas chromatography (GC) with 1 injection per 23 min) can be found in **Figure 6.10**.

Reaction	Catalyst	Conversion (%)	CO or CO <sub>2</sub> (%)	CH <sub>4</sub> (%)	C <sub>2</sub> (%)	C <sub>3</sub> (%)	C <sub>4</sub> (%)	C <sub>5</sub> (%)
CO <sub>2</sub> hydrogenation	CSR	1.91	91.9	79.4	20.6			
	Fe/SiO <sub>2</sub>	2.13	0	87.3	7.59	4.92	0.24	
	K-Fe/SiO <sub>2</sub>	2.04	30.4	71.9	17.1	10.4	1.48	
FTO	CSR	2.11	73.1	39.6	36.0	20.9	3.56	
	Fe/SiO <sub>2</sub>	2.69	14.6	66.7	14.0	12.7	6.69	1.15
	K-Fe/SiO <sub>2</sub>	2.49	27.5	64.3	11.0	14.8	9.85	4.09
CO <sub>2</sub> hydrogenation	CSR	1.90	99.4	92.7	7.29			
	Fe/SiO <sub>2</sub>	2.26	48.0	92.2	7.12	0.71		
	K-Fe/SiO <sub>2</sub>	1.89	58.1	89.9	9.39	0.73		

**Table 6.7.** Average olefin/paraffin (O/P) ratios during (consecutively) the CO<sub>2</sub> hydrogenation reaction, the Fischer-Tropsch-to-Olefins (FTO) reaction, and the CO<sub>2</sub> hydrogenation reaction of the coarse solid residue (CSR) sample, the Fe/SiO<sub>2</sub> sample, and the K-Fe/SiO<sub>2</sub> sample. The CO<sub>2</sub> hydrogenation steps were carried out at T=250°C, P=5 bar, H<sub>2</sub>/CO<sub>2</sub>=3, and gas hourly space velocity (GHSV)=3070 h<sup>-1</sup>, while the FTO step was carried out at T=350°C, P=5 bar, CO/H<sub>2</sub>=1.5, and GHSV=2425 h<sup>-1</sup>. Prior to the first CO<sub>2</sub> hydrogenation step, the samples were pre-reduced at 450°C in N<sub>2</sub>/H<sub>2</sub>=2 for 1 h. The complete set of measurement points (recorded with gas chromatography (GC) with 1 injection per 23 min) can be found in **Figure 6.10**.

Reaction	Catalyst	O/P C <sub>2</sub> <sup>[a]</sup>	O/P C <sub>3</sub> <sup>[a]</sup>	O/P C <sub>4</sub> <sup>[a]</sup>	O/P C <sub>5</sub> <sup>[a]</sup>
CO <sub>2</sub> hydrogenation	CSR	2.07 ± 0.44			
	Fe/SiO <sub>2</sub>	2.09 ± 0.43	2.31 ± 0.58	2.63 ± 1.10	
	K-Fe/SiO <sub>2</sub>	3.98 ± 0.50	2.52 ± 0.30	4.68 ± 0.86	
FTO	CSR	10.8 ± 1.4	15.3 ± 2.6	25.9 ± 7.7	
	Fe/SiO <sub>2</sub>	13.0 ± 3.7	13.9 ± 3.3	20.7 ± 5.9	6.67 ± 4.59
	K-Fe/SiO <sub>2</sub>	18.8 ± 4.0	18.0 ± 3.3	36.2 ± 6.8	8.50 ± 3.90
CO <sub>2</sub> hydrogenation	CSR	1.40 ± 0.45			
	Fe/SiO <sub>2</sub>	1.72 ± 0.54	0.71 ± 0.38		
	K-Fe/SiO <sub>2</sub>	3.23 ± 2.04	1.23 ± 0.40		

<sup>[a]</sup> O/P stands for olefin/paraffin ratio

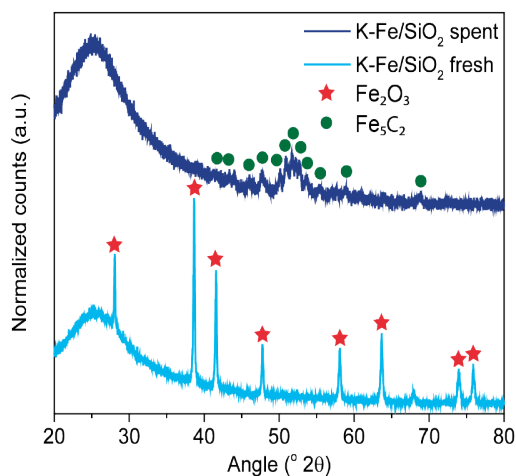


**Figure 6.11.** X-ray diffraction (XRD) patterns of the K-Fe/SiO<sub>2</sub> (0.71 wt.% K and 7.6 wt.% Fe) sample after calcination (fresh) containing Fe<sub>2</sub>O<sub>3</sub> and after consecutive CO<sub>2</sub> hydrogenation, Fischer-Tropsch-to-Olefins (FTO), and CO<sub>2</sub> hydrogenation containing the Hägg carbide (Fe<sub>5</sub>C<sub>2</sub>).

### 6.3.7 Fe Carbides Evolved as Active Phase in the Coarse Solid Residue Sample under Reaction Conditions

To further investigate the formation of iron carbides, *operando* XRD was performed under FTO conditions. *Operando* XRD patterns of the CSR sample were recorded after reduction at 450°C in H<sub>2</sub>, and during CO hydrogenation (H<sub>2</sub>/CO=0.7) for 70 h at 450°C and 5 bar (see **Figure 6.12**). After the reduction procedure, the CSR sample contained a mixture of Fe<sub>3</sub>O<sub>4</sub> and metallic Fe (**Figure 6.12a and 6.12b**). Under H<sub>2</sub>-poor FTO reaction conditions this slowly transformed into the Hägg carbide phase (Fe<sub>5</sub>C<sub>2</sub>) (**Figure 6.12b**), which correlated with an increase in CO conversion and an increase in C<sub>2+</sub> selectivity (**Figure 6.12** and **6.12d**). C<sub>5</sub> products were only detected after ~30 h time-on-stream. Both the CO conversion and the C<sub>2+</sub> selectivity reached a stable level after about 55 h time-on-stream. The olefin/paraffin ratio in the C<sub>2</sub>-C<sub>4</sub> products increased with increasing reaction time, suggesting that the Fe<sub>5</sub>C<sub>2</sub> phase is more selective to olefins compared to metallic Fe. A complete overview of all the products detected, including all isomers, can be found in **Table 6.8**. At 40-60 h time-on-stream (green XRD pattern in **Figure 6.12b**), CSR solely contained the Hägg carbide phase (Fe<sub>5</sub>C<sub>2</sub>), while Fe<sub>3</sub>O<sub>4</sub> and metallic Fe were not observed. We can thus conclude that Hägg carbide is the (most) active phase for C<sub>2+</sub> production, as its emergence was correlated with enhanced catalytic performance.

This is in accordance with an earlier study that ascribed the increase in  $C_{2+}$  selectivity to the transition of metallic iron to iron carbides.<sup>55</sup>

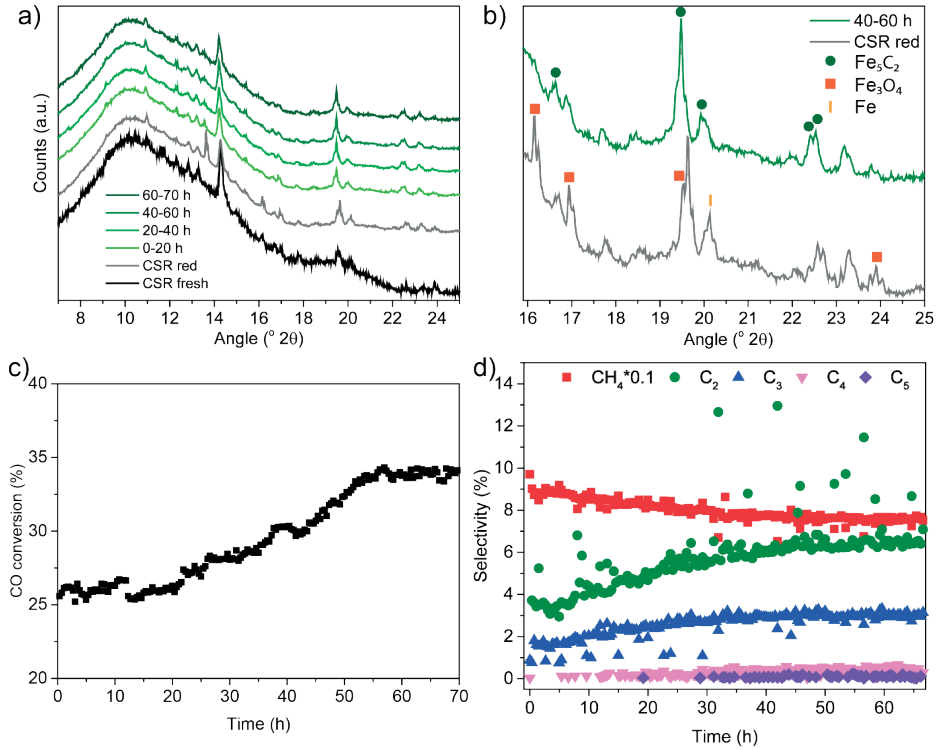


**Figure 6.12.** Operando X-ray diffraction (XRD) of the coarse solid residue (CSR) sample. **a)** CSR fresh, after reduction at  $450^{\circ}C$  in  $H_2$ , and during CO hydrogenation ( $H_2/CO=0.7$ ) for 70 h at  $450^{\circ}C$  and 5 bar. **b)** Zoom in of  $16-25^{\circ} 2\theta$ , showing CSR contained a mixture of  $Fe_3O_4$  and metallic Fe after reduction. Under reaction conditions ( $Fe_3C_2$ ), Hägg carbide, evolved as active phase in the CSR sample. **c)** CO conversion (%) and **d)** product selectivities over time.

**Table 6.8.** Catalytic performance as measured with gas chromatography (GC), with one injection per 23 min, during the *operando* X-ray diffraction (XRD) experiment with a coarse solid residue (CSR) material. The sample was pre-treated in pure H<sub>2</sub> for 1 h at 450°C prior to the reaction. Fischer-Tropsch-to-Olefins (FTO) reaction conditions were  $T=450^{\circ}\text{C}$ ,  $P=5$  bar, and  $\text{CO:H}_2:\text{He}=2.25:1.5:1$  for a total of 70 h time-on-stream (TOS). The averages of 0-10 h TOS are compared to the averages of 60-70 h TOS.

Product	Conversion or selectivity at 0-10 h (%)	Conversion or selectivity at 60-70 h (%)
CO conversion	25.9 ± 0.3	33.9 ± 0.3
Methane	87.9 ± 2.27	75.8 ± 1.2
Ethane	2.94 ± 0.81	4.62 ± 0.53
Ethene	0.79 ± 0.13	2.01 ± 0.09
Propane	0.80 ± 0.20	0.93 ± 0.04
Propene	0.73 ± 0.31	2.08 ± 0.08
iso-Butane	0	0
n-Butane	0.02 ± 0.04	0.15 ± 0.06
Acetylene	0	0
trans-2-butene	0	0.03 ± 0.04
1-butene	0	0.18 ± 0.13
iso-butene	0	0.04 ± 0.05
cis-2-butene	0	0.01 ± 0.02
isopentane / 2-methyl-butane	0	0
pentane	0	0.06 ± 0.05
1,3-butadiene	0	0
neopentane / 2,2-dimethylpropane	0	0
3-methyl-1-butene	0	0
trans-2-pentene	0	0
2-methyl-2-butene	0	0.01 ± 0.03
1-pentene	0	0
2-methyl-1-butene	0	0

### 6.3.8 Improving C<sub>2+</sub> Selectivity with Increased Reaction Pressure

To improve the selectivity to lower olefins, we increased the pressure to 20 bar and tested the CSR sample at different temperatures (250-450°C) (Figure 6.13). Again, 450°C appeared to be the optimum temperature for CO/CO<sub>2</sub> conversion (total C con-

version=45.9%) and  $C_{2+}$  production. At 20 bar the methane selectivity went down to 57.1% and the  $C_2$ - $C_4$  olefin/paraffin selectivity increased up to 42.9%. The olefin/paraffin ratio increased with pressure as well (Table 6.9). Even though the CSR sample may not outperform commercial Fe-based FTO catalysts ( $CH_4$  selectivity=3-42%<sup>30</sup>) or Fe-based catalysts developed for  $CO_2$  to fuels ( $CH_4$  selectivity=3-16%<sup>11,43</sup>), our results present an attractive strategy in the field of renewables.<sup>25,56</sup> Fe-containing CSR catalyzes the conversion of  $CO/CO_2$  to valuable olefins and would otherwise have been discarded as an industrial waste product. Repurposing the waste product as a  $CO/CO_2$  conversion catalyst represents an example of a strategy to reuse and thus minimize industrial waste streams.

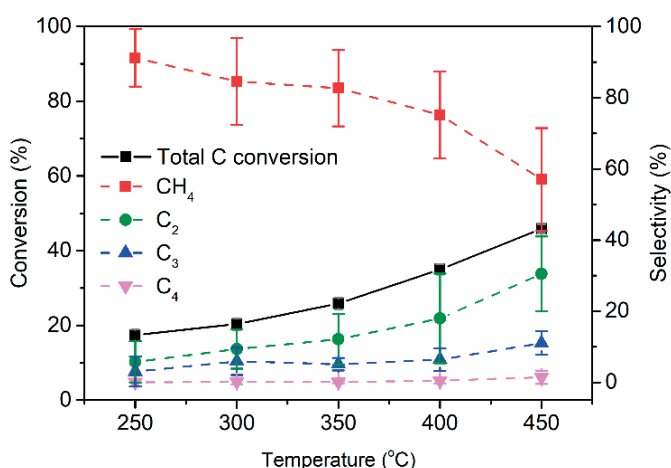


**Figure 6.13.** Catalytic performance of the coarse solid residue (CSR) sample in  $CO:CO_2:H_2:N_2=4.5:2.5:3:1$  at  $P=20$  bar,  $T=250$ - $450^\circ C$ , and gas hourly space velocity (GHSV)= $3400\text{ h}^{-1}$  (6 h per temperature).

**Table 6.9.** Average olefin/paraffin (O/P) ratio in the hydrocarbon products made by coarse solid residue (CSR) at varying temperatures (6 h per temperature),  $P=20$  bar,  $CO:CO_2:H_2:N_2=4.5:2.5:3:1$ , and gas hourly space velocity (GHSV)= $3400\text{ h}^{-1}$ . A gas chromatography (GC) injection was performed every 23 min.

Temperature ( $^\circ C$ )	O/P $C_2$ <sup>[a]</sup>	O/P $C_3$ <sup>[a]</sup>	O/P $C_4$ <sup>[a]</sup>
250	$1.75 \pm 1.75$	$2.34 \pm 2.28$	
300	$2.61 \pm 2.13$	$2.44 \pm 2.24$	$1.65 \pm 0.17$
350	$6.52 \pm 3.89$	$3.43 \pm 3.63$	$1.61 \pm 0.93$
400	$8.72 \pm 6.82$	$5.06 \pm 2.34$	$2.44 \pm 1.22$
450	$13.3 \pm 2.7$	$14.0 \pm 3.4$	$7.41 \pm 3.64$

<sup>[a]</sup> O/P stands for olefin/paraffin ratio

### 6.3.9 Carbonaceous Deposits Evolved under Optimized Reaction Conditions

To investigate whether or not carbon deposits were formed under reaction conditions, we have performed *operando* Raman micro-spectroscopy studies (**Figure 6.14a** and **6.14b**). While X-ray diffraction techniques, like XRD, are usually the method of choice for crystalline solid materials (*i.e.*, long-range order), Raman spectroscopy is more promising to analyze carbon deposits with a highly disordered structure.<sup>57,58</sup> Raman spectroscopy probes molecular structures (short-range order) and is sensitive to the degree of structural disorder. We compared the fresh CSR sample with an Fe<sub>2</sub>O<sub>3</sub> (hematite) reference. CSR indeed displayed the characteristic Fe<sub>2</sub>O<sub>3</sub> peaks at 222, 242, 291, 408, 490, 608, 662, and 1309 cm<sup>-1</sup> (**Figure 6.14a**).<sup>59</sup> Structural changes were not yet observed at 150°C in H<sub>2</sub>. However, at 350°C line broadening was visible, indicating that Fe<sub>2</sub>O<sub>3</sub> was transformed into Fe<sub>3</sub>O<sub>4</sub> (magnetite). At 450°C, the iron oxide peaks had disappeared, indicating the presence of the Raman-inactive metallic iron. Then, CO/CO<sub>2</sub> hydrogenation was carried out at 20 bar and 450°C. After 1-3 h of reaction, bands at 1340 and 1580 cm<sup>-1</sup> appeared, indicating the formation of carbonaceous species.<sup>55,59</sup> This is in line with earlier studies on Fe-based FTO catalysts, where carbonaceous species were observed during CO hydrogenation.<sup>46</sup> Inactive carbon species could play a role in catalyst deactivation,<sup>32</sup> but carbonaceous species have also been reported as intermediates in CO hydrogenation processes.<sup>55,59</sup> While carbonaceous species evolved during our experiments, the total carbon conversion, as measured (semi-quantitatively) with mass spectrometry (MS) and compared to a blank measurement, decreased. Besides, the MS response of CH<sub>4</sub> increased, while the C<sub>2</sub>-C<sub>4</sub> olefins MS response (**Figure 6.14c**) decreased over time. Although the deposition of carbonaceous species coincided with deteriorating catalytic performance, the apparent catalyst deactivation could also be assigned to other causes. For example, the presence of Mg and Ca has previously been reported to increase catalyst deactivation and methane formation.<sup>50</sup> Moreover, the presence of K, Na, Cr, and Cu in CSR promote the WGS reaction,<sup>51</sup> which could increase the amount of CO<sub>2</sub> in the gas feed and consequently decrease the catalytic performance. Re-oxidation of iron (carbide) nanoparticles was, however, not observed in the Raman spectra.



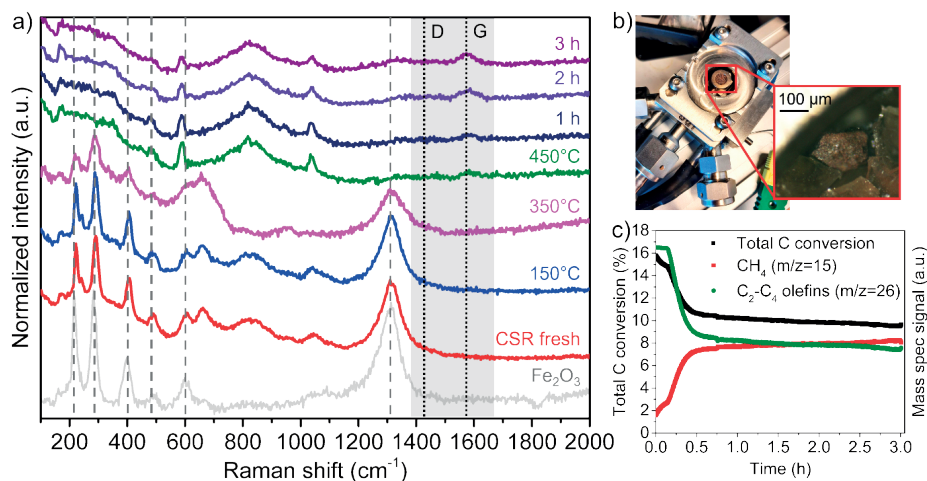


**Figure 6.14.** *Operando* Raman micro-spectroscopy on the coarse solid residue (CSR) sample **a)** during the reduction procedure in  $H_2/Ar=1$  and during catalytic  $CO/CO_2$  hydrogenation ( $CO/CO_2/H_2=2.2/1.2/1.5$ ) at  $P=20$  bar and  $T=450^\circ C$ . The  $Fe_2O_3$  peaks are indicated with a gray dashed lines and the carbon D and G bands with black dotted lines. **b)** Photograph of the high-pressure Raman cell and microscopy image of a CSR particle. **c)** mass spectrometry (MS) signals for  $CH_4$  ( $m/z=15$ ) and  $C_2-C_4$  olefins ( $m/z=26$ ).

## 6.4 Conclusions

A coarse solid residue (CSR) material, which is a waste product obtained from solid waste gasification, was tested as a potential solid catalyst material for the hydrogenation of  $CO$  and  $CO_2$ . Fe carbides were identified as the active phase during  $CO/CO_2$  conversion with *operando* X-ray diffraction (XRD) and their presence were linked to an increase in  $CO/CO_2$  conversion and the desired light olefin selectivity. More specifically, the CSR material produced 57% methane and 43%  $C_2-C_4$  olefins from a  $CO/CO_2/H_2$  mixture with a total C conversion of 46% at  $T=450^\circ C$  and  $P=20$  bar. The alkali elements in the CSR material appeared responsible for the (R)WGS activity and for an increased  $C_{2+}$  olefin production. With these new insights, the gasification process conditions could be optimized to obtain a catalytically superior CSR material, for example with a higher Fe content. Strategies to reuse waste streams, like the one presented in this **Chapter**, should be widely employed to minimize industrial waste output. Besides, recycling waste streams will decrease the usage of valuable raw materials required for e.g., catalyst synthesis. Considering that the CSR material used catalyzes the conversion of  $CO/CO_2$  mixtures into valuable olefins and would otherwise have been discarded as industrial waste, our findings offer a new perspective on how waste streams can be utilized. In this manner, it adds to the concept of materials circularity and related metal scarcity abatement.

### **6.5 Author Contributions and Acknowledgements**

This Chapter is based on the manuscript “ten Have, I. C., van den Brink, R. Y., Marie-Rose, S. C., Meirer, F., & Weckhuysen, B. M. (2022). Using Biomass Gasification Mineral Residue as Catalyst to Produce Light Olefins from CO, CO<sub>2</sub>, and H<sub>2</sub> Mixtures. *ChemSusChem*, e202200436.”.

Bert Weckhuysen, Florian Meirer, Stephane Marie-Rose, and Iris ten Have conceptualized the research ideas. Robin van den Brink helped with catalyst synthesis and characterization. The work was written by Iris ten Have under the supervision of Bert Weckhuysen and Florian Meirer and all co-authors contributed to the written text with scientific input.

Peter J. Nieuwenhuizen (European Circular Bioeconomy Fund) is acknowledged for his support to the project. Dr. R. Oord (Utrecht University) is acknowledged for technical support. Savannah J. Turner (Utrecht University) is thanked for performing the STEM-EDX measurements. Nina S. Genz (Utrecht University) is thanked for performing X-ray characterization measurements.

## 6.6 References

1. Puga, A. V. On the nature of active phases and sites in CO or CO<sub>2</sub> hydrogenation catalysts. *Catalysis Science & Technology* **8**, 5681-5707 (2018).
2. United Nations. *Paris Agreement*. (2015).
3. Hashimoto, K., Yamasaki, M., Fujimura, K., Matsui, T., Izumiya, K., Komori, M., El-Moneim, A. A., Akiyama, E., Habazaki, H., Kumagai, N., Kawashima, A. & Asami, K. Global CO<sub>2</sub> recycling - Novel materials and prospect for prevention of global warming and abundant energy supply. *Materials Science and Engineering A* **267**, 200-206 (1999).
4. Davis, S. J., Caldeira, K. & Matthews, H. D. Future CO<sub>2</sub> Emissions and Climate Change from Existing Energy Infrastructure. *Science* **329**, 1330-1333 (2010).
5. Ye, R. P., Ding, J., Gong, W., Argyle, M. D., Zhong, Q., Wang, Y., Russell, C. K., Xu, Z., Russell, A. G., Li, Q., Fan, M. & Yao, Y. G. CO<sub>2</sub> hydrogenation to high-value products via heterogeneous catalysis. *Nature Communications* **10**, 5698 (2019).
6. Hepburn, C., Adlen, E., Beddington, J., Carter, E. A., Fuss, S., Mac Dowell, N., Minx, J. C., Smith, P. & Williams, C. K. The technological and economic prospects for CO<sub>2</sub> utilization and removal. *Nature* **575**, 87-97 (2019).
7. Mac Dowell, N., Fennell, P. S., Shah, N. & Maitland, G. C. The role of CO<sub>2</sub> capture and utilization in mitigating climate change. *Nature Climate Change* **7**, 243-249 (2017).
8. Luk, H. T., Novak, G., Safonova, O. V., Siol, S., Stewart, J. A., Curulla Ferré, D., Mondelli, C. & Pérez-Ramírez, J. CO<sub>2</sub>-Promoted Catalytic Process Forming Higher Alcohols with Tunable Nature at Record Productivity. *ChemCatChem* **12**, 2732-2744 (2020).
9. Wang, W., Wang, S., Ma, X. & Gong, J. Recent advances in catalytic hydrogenation of carbon dioxide. *Chemical Society Reviews* **40**, 3703-3727 (2011).
10. Rodemerck, U., Holeňa, M., Wagner, E., Smejkal, Q., Barkschat, A. & Baerns, M. Catalyst development for CO<sub>2</sub> hydrogenation to fuels. *ChemCatChem* **5**, 1948-1955 (2013).
11. Yao, B., Xiao, T., Makgae, O. A., Jie, X., Gonzalez-cortes, S., Guan, S., Kirkland, A. I., Dilworth, J. R., Al-megren, H. A., Alshihri, S. M., Dobson, P. J., Owen, G. P., Thomas, J. M. & Edwards, P. P. Transforming carbon dioxide into jet fuel using an organic combustion-synthesized Fe-Mn-K catalyst. *Nature Communications* **11**, 6395 (2020).
12. Vogt, C., Monai, M., Kramer, G. J. & Weckhuysen, B. M. The renaissance of the Sabatier reaction and its applications on Earth and in space. *Nature Catalysis* **2**, 188-197 (2019).
13. Vogt, C., Groeneveld, E., Kamsma, G., Nachtegaal, M., Lu, L., Kiely, C. J., Berben, P. H., Meirer, F. & Weckhuysen, B. M. Unravelling structure sensitivity in CO<sub>2</sub> hydrogenation over nickel. *Nature Catalysis* **1**, 127-134 (2018).
14. Vrijburg, W. L., Muioli, E., Chen, W., Zhang, M., Terlingen, B. J. P., Zijlstra, B., Pilot, I. A. W., Züttel, A., Pidko, E. A. & Hensen, E. J. M. Efficient Base-Metal NiMn/TiO<sub>2</sub> Catalyst for CO<sub>2</sub> Methanation. *ACS Catalysis* **9**, 7823-7839 (2019).
15. Vrijburg, W. L., Garbarino, G., Chen, W., Parastaev, A., Longo, A., Pidko, E. A. & Hensen, E. J. M. Ni-Mn catalysts on silica-modified alumina for CO<sub>2</sub> methanation. *Journal of Catalysis* **382**, 358-371 (2020).
16. Zhang, Z., Zhang, L., Yao, S., Song, X., Huang, W., Hülsey, M. J. & Yan, N. Support-dependent rate-determining step of CO<sub>2</sub> hydrogenation to formic acid on metal oxide supported Pd catalysts. *Journal of Catalysis* **376**, 57-67 (2019).

17. Martin, N. M., Velin, P., Skoglundh, M., Bauer, M. & Carlsson, P. A. Catalytic hydrogenation of CO<sub>2</sub> to methane over supported Pd, Rh and Ni catalysts. *Catalysis Science and Technology* **7**, 1086-1094 (2017).
18. Dreyer, J. A. H., Li, P., Zhang, L., Beh, G. K., Zhang, R., Sit, P. H. L. & Teoh, W. Y. Influence of the oxide support reducibility on the CO<sub>2</sub> methanation over Ru-based catalysts. *Applied Catalysis B: Environmental* **219**, 715-726 (2017).
19. Hartadi, Y., Widmann, D. & Behm, R. J. CO<sub>2</sub> hydrogenation to methanol on supported Au catalysts under moderate reaction conditions: Support and particle size effects. *ChemSusChem* **8**, 456-465 (2015).
20. Aziz, M. A. A., Jalil, A. A., Triwahyono, S. & Ahmad, A. CO<sub>2</sub> methanation over heterogeneous catalysts: Recent progress and future prospects. *Green Chemistry* **17**, 2647-2663 (2015).
21. Nzihou, A., Stanmore, B. & Sharrock, P. A review of catalysts for the gasification of biomass char, with some reference to coal. *Energy* **58**, 305-317 (2013).
22. Dupont, C., Nocquet, T., Da Costa, J. A. & Verne-Tournon, C. Kinetic modelling of steam gasification of various woody biomass chars: Influence of inorganic elements. *Bioresource Technology* **102**, 9743-9748 (2011).
23. Habibi, R., Kopyscinski, J., Masnadi, M. S., Lam, J., Grace, J. R., Mims, C. A. & Hill, J. M. Co-gasification of biomass and non-biomass feedstocks: Synergistic and inhibition effects of switchgrass mixed with sub-bituminous coal and fluid coke during CO<sub>2</sub> gasification. *Energy and Fuels* **27**, 494-500 (2013).
24. Assima, G. P., Marie-Rose, S. & Lavoie, J. M. Role of fixed carbon and metal oxides in char during the catalytic conversion of tar from RDF gasification. *Fuel* **218**, 406-416 (2018).
25. Abelló, S. & Montané, D. Exploring Iron-based Multifunctional Catalysts for Fischer-Tropsch Synthesis: A Review. *ChemSusChem* **4**, 1538-1556 (2011).
26. Klinghoffer, N. B., Castaldi, M. J. & Nzihou, A. Catalyst properties and catalytic performance of char from biomass gasification. *Industrial and Engineering Chemistry Research* **51**, 13113-13122 (2012).
27. Khodakov, A. Y., Chu, W. & Fongarland, P. Advances in the development of novel cobalt Fischer-Tropsch catalysts for synthesis of long-chain hydrocarbons and clean fuels. *Chemical Reviews* **107**, 1692-1744 (2007).
28. Ismail, A. S. M., Casavola, M., Liu, B., Gloter, A., Van Deelen, T. W., Versluijs, M., Meeldijk, J. D., Stéphan, O., De Jong, K. P. & De Groot, F. M. F. Atomic-Scale Investigation of the Structural and Electronic Properties of Cobalt-Iron Bimetallic Fischer-Tropsch Catalysts. *ACS Catalysis* **9**, 7998-8011 (2019).
29. van Deelen, T. W., Yoshida, H., Oord, R., Zečević, J., Weckhuysen, B. M. & de Jong, K. P. Cobalt nanocrystals on carbon nanotubes in the Fischer-Tropsch synthesis: Impact of support oxidation. *Applied Catalysis A: General* **593**, 117441 (2020).
30. van de Loosdrecht, J., Botes, F. G., Ciobica, I. M., Ferreira, A., Gibson, P., Moodley, D. J., Saib, A. M., Visagie, J. L., Weststrate, C. J. & Niemantsverdriet, J. W. in *Comprehensive Inorganic Chemistry II: from elements to applications* **7**, 525-557 (Elsevier, Amsterdam, 2013).
31. ten Have, I. C. & Weckhuysen, B. M. The active phase in cobalt-based Fischer-Tropsch synthesis. *Chem Catalysis* **1**, 339-363 (2021).
32. de Smit, E. & Weckhuysen, B. M. The renaissance of iron-based Fischer-Tropsch synthesis: On the multifaceted catalyst deactivation behaviour. *Chemical Society Reviews* **37**, 2758-2781 (2008).

33. Gu, B., Ordonsky, V. V., Bahri, M., Ersen, O., Chernavskii, P. A., Filimonov, D. & Khodakov, A. Y. Effects of the promotion with bismuth and lead on direct synthesis of light olefins from syngas over carbon nanotube supported iron catalysts. *Applied Catalysis B: Environmental* **234**, 153-166 (2018).
34. Yung, M. M., Jablonski, W. S. & Magrini-Bair, K. A. Review of catalytic conditioning of biomass-derived syngas. *Energy and Fuels* **23**, 1874-1887 (2009).
35. Lu, Y., Yan, Q., Han, J., Cao, B., Street, J. & Yu, F. Fischer-Tropsch synthesis of olefin-rich liquid hydrocarbons from biomass-derived syngas over carbon-encapsulated iron carbide/iron nanoparticles catalyst. *Fuel* **193**, 369-384 (2017).
36. Yan, Q., Yu, F., Liu, J., Street, J., Gao, J., Cai, Z. & Zhang, J. Catalytic conversion wood syngas to synthetic aviation turbine fuels over a multifunctional catalyst. *Bioresource Technology* **127**, 281-290 (2013).
37. Visconti, C. G., Martinelli, M., Falbo, L., Fratolocchi, L. & Lietti, L. CO<sub>2</sub> hydrogenation to hydrocarbons over Co and Fe-based Fischer-Tropsch catalysts. *Catalysis Today* **277**, 161-170 (2016).
38. Lin, T., Gong, K., Wang, C., An, Y., Wang, X., Qi, X., Li, S., Lu, Y., Zhong, L. & Sun, Y. Fischer-Tropsch Synthesis to Olefins: Catalytic Performance and Structure Evolution of Co<sub>2</sub>C-Based Catalysts under a CO<sub>2</sub> Environment. *ACS Catalysis* **9**, 9554-9567 (2019).
39. Saeidi, S., Najari, S., Fazlollahi, F., Nikoo, M. K., Sefidkon, F., Klemeš, J. J. & Baxter, L. L. Mechanisms and kinetics of CO<sub>2</sub> hydrogenation to value-added products: A detailed review on current status and future trends. *Renewable and Sustainable Energy Reviews* **80**, 1292-1311 (2017).
40. Ojelade, O. A. & Zaman, S. F. A review on CO<sub>2</sub> hydrogenation to lower olefins: Understanding the structure-property relationships in heterogeneous catalytic systems. *Journal of CO<sub>2</sub> Utilization* **47**, 101506 (2021).
41. Gnanamani, M. K., Shafer, W. D., Sparks, D. E. & Davis, B. H. Fischer-Tropsch synthesis: Effect of CO<sub>2</sub> containing syngas over Pt promoted Co/ $\gamma$ -Al<sub>2</sub>O<sub>3</sub> and K-promoted Fe catalysts. *Catalysis Communications* **12**, 936-939 (2011).
42. Lin, T., Gong, K., Wang, C., An, Y., Wang, X., Qi, X., Li, S., Lu, Y., Zhong, L. & Sun, Y. Fischer-Tropsch Synthesis to Olefins: Catalytic Performance and Structure Evolution of Co<sub>2</sub>C-Based Catalysts under a CO<sub>2</sub> Environment. *ACS Catalysis* **9**, 9554-9567 (2019).
43. Han, Y., Fang, C., Ji, X., Wei, J., Ge, Q. & Sun, J. Interfacing with Carbonaceous Potassium Promoters Boosts Catalytic CO<sub>2</sub> Hydrogenation of Iron. *ACS Catalysis* **10**, 12098-12108 (2020).
44. Xu, Y., Zhai, P., Deng, Y., Xie, J., Liu, X., Wang, S. & Ma, D. Highly Selective Olefin Production from CO<sub>2</sub> Hydrogenation on Iron Catalysts: A Subtle Synergy between Manganese and Sodium Additives. *Angewandte Chemie International Edition* **59**, 21736-21744 (2020).
45. Zhou, C., Shi, J., Zhou, W., Cheng, K., Zhang, Q., Kang, J. & Wang, Y. Highly Active ZnO-ZrO<sub>2</sub> Aerogels Integrated with HZSM5 for Aromatics Synthesis from Carbon Dioxide. *ACS Catalysis* **10**, 302-310 (2020).
46. Paalanen, P. P., van Vreeswijk, S. H. & Weckhuysen, B. M. Combined in Situ X-ray Powder Diffractometry/Raman Spectroscopy of Iron Carbide and Carbon Species Evolution in Fe(-Na-S)/ $\alpha$ -Al<sub>2</sub>O<sub>3</sub> Catalysts during Fischer-Tropsch Synthesis. *ACS Catalysis* **10**, 9837-9855 (2020).
47. Paalanen, P. P., van Vreeswijk, S. H., Dugulan, A. I. & Weckhuysen, B. M. Identification of Iron Carbides in Fe(-Na-S)/ $\alpha$ -Al<sub>2</sub>O<sub>3</sub> Fischer-Tropsch Synthesis Catalysts with X-ray Powder Diffractometry and Mössbauer Absorption Spectroscopy. *ChemCatChem* **12**, 5121-5139 (2020).
48. Dorner, R. W., Hardy, D. R., Williams, F. W. & Willauer, H. D. K and Mn doped iron-based CO<sub>2</sub> hydrogenation catalysts: Detection of KAlH<sub>4</sub> as part of the catalyst's active phase. *Applied Catalysis A: General* **373**, 112-121 (2010).

49. Liang, B., Duan, H., Sun, T., Ma, J., Liu, X., Xu, J., Su, X., Huang, Y. & Zhang, T. Effect of Na Promoter on Fe-Based Catalyst for CO<sub>2</sub> Hydrogenation to Alkenes. *ACS Sustainable Chemistry and Engineering* **7**, 925-932 (2019).
50. Luo, M. & Davis, B. H. Fischer-Tropsch synthesis: Group II alkali-earth metal promoted catalysts. *Applied Catalysis A: General* **246**, 171-181 (2003).
51. Ratnasamy, C. & Wagner, J. Water gas shift catalysis. *Catalysis Reviews - Science and Engineering* **51**, 325-440 (2009).
52. Yao, B., Ma, W., Gonzalez-Cortes, S., Xiao, T. & Edwards, P. P. Thermodynamic study of hydrocarbon synthesis from carbon dioxide and hydrogen. *Greenhouse Gases: Science and Technology* **7**, 942-957 (2017).
53. Zhang, Y., Cao, C., Zhang, C., Zhang, Z., Liu, X., Yang, Z., Zhu, M., Meng, B., Xu, J. & Han, Y. F. The study of structure-performance relationship of iron catalyst during a full life cycle for CO<sub>2</sub> hydrogenation. *Journal of Catalysis* **378**, 51-62 (2019).
54. Zhang, Q., Cheng, K., Kang, J., Deng, W. & Wang, Y. Fischer-Tropsch Catalysts for the Production of Hydrocarbon Fuels with High Selectivity. *ChemSusChem* **7**, 1251-1264 (2014).
55. Zhang, Y., Fu, D., Liu, X., Zhang, Z., Zhang, C., Shi, B., Xu, J. & Han, Y. F. *Operando* Spectroscopic Study of Dynamic Structure of Iron Oxide Catalysts during CO<sub>2</sub> Hydrogenation. *ChemCatChem* **10**, 1272-1276 (2018).
56. Choi, Y. H., Jang, Y. J., Park, H., Kim, W. Y., Lee, Y. H., Choi, S. H. & Lee, J. S. Carbon dioxide Fischer-Tropsch synthesis: A new path to carbon-neutral fuels. *Applied Catalysis B: Environmental* **202**, 605-610 (2017).
57. Sadezky, A., Muckenhuber, H., Grothe, H., Niessner, R. & Pöschl, U. Raman microspectroscopy of soot and related carbonaceous materials: Spectral analysis and structural information. *Carbon* **43**, 1731-1742 (2005).
58. Ferrari, A. C. & Basko, D. M. Raman spectroscopy as a versatile tool for studying the properties of graphene. *Nature Nanotechnology* **8**, 235-246 (2013).
59. Fu, D., Dai, W., Xu, X., Mao, W., Su, J., Zhang, Z., Shi, B., Smith, J., Li, P., Xu, J. & Han, Y. F. Probing the structure evolution of iron-based Fischer-Tropsch to produce olefins by *operando* Raman spectroscopy. *ChemCatChem* **7**, 752-756 (2015).







# **CHAPTER 7**

## **SUMMARY, CONCLUSIONS, AND FUTURE PERSPECTIVES**





## 7.1 Summary

This PhD Thesis described surface-sensitive spectroscopy as a promising analytical tool for the better understanding of reaction and deactivation mechanisms in heterogeneous catalysis. **Chapter 1** introduced the basic principles of spectroscopy and catalysis, as well as the Fischer-Tropsch Synthesis reaction (*i.e.*, CO hydrogenation) and how fundamental insights are obtained through spectroscopic characterization under realistic reaction conditions. Although the drive to establish structure-composition-performance relationships existed since the beginning of the science of catalysis, the spectroscopic tools to realize this dream were unfortunately lacking. While spectroscopy has been a prominent analytical tool since the beginning of the 20<sup>th</sup> century, a concerted research effort to apply spectroscopy under relevant reaction conditions with clear proof of catalytic performance only began in earnest in the 21<sup>st</sup> century. The origins of this thorough methodology, coined *operando* spectroscopy, were reviewed in **Chapter 1**. Then, we set the stage for investigating the cobalt-catalyzed CO and CO<sub>2</sub> hydrogenation reactions. We formulated a two-pronged approach: firstly, we aimed to provide new or improved insights into the active phase of cobalt-based catalysts for CO and CO<sub>2</sub> hydrogenation. Secondly, we targeted to uncover the reaction mechanisms at play during the formation of (un)desired reaction products and the related phenomena of catalyst deactivation. To achieve these two goals, the capabilities and limitations of a range of analytical techniques were explored and utilized.

Nanoscale spectroscopy techniques are promising tools to achieve the goals formulated above. Photo-induced force microscopy, which combines infrared spectroscopy with a very sharp tip to record infrared spectra with 10-20 nm spatial resolution, was introduced in **Chapter 2**. This nanoscale spectroscopy technique was first demonstrated successfully by its inventors in the polymer science field; various nanoscale polymer domains could easily be distinguished from each other. Additionally, we highlighted some recent applications of this tip-based spectroscopy methodology, including the detection of nanometer-sized plastic particles that arise from plastic waste degradation in the environment and structural analysis of catalytic materials with special emphasis on olefin polymerization catalysts. Some of the analytical tools required to achieve the goals of this PhD Thesis function best under vacuum or low pressure and with rather simplified model-based catalyst systems. However, industrial processes are typically catalyzed by complex, multi-component and hierarchically structured materials, while the reaction are conducted at elevated temperatures and pressures. Although the academic world strives to understand the fundamental phenomena that occur on the catalysts' surfaces, the most sensitive analytical tools are often unable to operate under the harsh reaction conditions that industrial catalysis requires. This chasm between industrial catalysis and academic research was discussed in **Chapter 2**. It was demonstrated that the gap

between commercial catalysis and academic research should be bridged with more advanced analytical tools as well as with the design and use of more realistic model systems. At the end of **Chapter 2**, we introduced a more realistic model system consisting of cobalt nanoparticles stabilized by ordered mesoporous titania islands. While the cobalt-based CO hydrogenation catalysts were well-represented by this system, its relatively flat surface structure enabled analysis with photo-induced force microscopy.

In **Chapter 3**, a multitude of advanced spectroscopic techniques were used to decipher the reaction mechanisms involved in hydrocarbon product formation and carbon deposition onto the catalyst surface during the CO hydrogenation reaction with cobalt-titania catalysts. By modulating the concentration of the reactant CO, infrared spectroscopy was turned into a surface-sensitive method and consequently active species could be observed during the reaction. Hydrogen-containing oxygenated species, such as formates and carboxylates, responded to the CO stimulus and thus provided evidence for the occurrence of hydrogen-assisted C-O bond scission. Besides, the performance-enhancing role of the titania support material appeared related to supplying essential building blocks to cobalt during the reaction. Then, gold nanoparticles were used to enhance the Raman spectroscopy signal and observe surface species at elevated temperatures and pressures during the reaction. The improved catalytic performance at elevated pressure appeared to be caused by longer hydrocarbon chains on the surface. Moreover, evidence was observed for the occurrence of the direct C-O bond scission mechanism. Carbon deposition onto the catalyst surface was found to occur *via* unsaturated bonds by means of photo-induced force microscopy.

The idea of modulating a reactant to make a spectroscopy technique surface-sensitive recurred in **Chapter 4**. This time, we have investigated the catalytically active phase and reaction mechanisms at play during CO<sub>2</sub> hydrogenation with cobalt-based catalysts. From the various support materials used to stabilize the cobalt (oxide) nanoparticles, titania support did the best job in terms of CO<sub>2</sub> conversion. **Chapter 4** also refutes the general consensus that metallic cobalt is the only active phase in heterogeneous catalysis, as cobalt oxide nanoparticles on titania support performed better in terms of long-chain hydrocarbon yield compared to the metallic cobalt variant. Modulating the CO<sub>2</sub> reactant concentration during infrared spectroscopy measurements enabled us to see that cobalt oxide and metallic cobalt followed different reaction pathways. While metallic cobalt was capable of dissociating CO<sub>2</sub> into CO directly, cobalt oxide required the assistance of hydrogen atoms to split the C-O bonds. Co-feeding CO to the CO<sub>2</sub> and H<sub>2</sub> gas stream increased the long-chain hydrocarbon yield of Co/TiO<sub>2</sub> and thus represented a promising future direction for CO<sub>2</sub> valorization.

In **Chapter 5**, we have explored the effects of a particular promoter element, namely potassium, in both the CO and CO<sub>2</sub> hydrogenation reactions with cobalt-titania catalysts. Although oxidic promoter elements, such as manganese, have been widely applied in industrial cobalt-catalyzed CO hydrogenation processes, alkali promoters have only been applied in iron-catalyzed processes and yet almost unexplored in combination with cobalt. The addition potassium to the cobalt-titania catalyst formulation appeared particularly interesting for renewable energy applications that aim to convert CO<sub>2</sub> into long-chain hydrocarbons. Potassium made the cobalt surface slightly positively charged and enabled the conversion of CO<sub>2</sub> into the more reactive CO molecule via the reverse water gas shift reaction. Besides, the amount of hydrogen on the catalyst surface diminished upon the addition of potassium. These effects shifted the reaction product composition away from undesired methane and towards more valuable long-chain hydrocarbons.

In **Chapter 6**, a solid mineral residue from industrial biomass gasification was repurposed as a solid catalyst material. The residue contained around 15 different elements, of which iron was the most important one. Iron enabled the conversion of a gas feed mixture of CO, CO<sub>2</sub>, H<sub>2</sub>, and N<sub>2</sub> into methane (57%) and C<sub>2</sub>-C<sub>5</sub> olefins (43%). By means of *operando* X-ray diffraction, the transformation of metallic iron into an iron carbide phase was associated with an increase in total carbon conversion and an improved selectivity towards the desired lower olefins. The alkali elements potassium and sodium present in the residue catalyzed the reverse water gas shift reaction. These elements enabled the conversion of CO<sub>2</sub> into the more reactive CO molecule and led to a higher yield of valuable long-chain reaction products.

This Chapter will still provide concluding remarks, where we aim to connect the dots between the different Chapters presented in this PhD Thesis, as well as propose some future perspectives and directions for future research.

## 7.2 Concluding Remarks

Surface-sensitive spectroscopy techniques proved fruitful in terms of physicochemical insights obtained. Conventional spectroscopy techniques are typically not surface-sensitive. However, the surface sensitivity can often be boosted by combining spectroscopy with creative methodologies. Examples of such methodologies are modulating a reactant during spectroscopy measurements, employing signal enhancing shell-isolated (gold) nanoparticles, and using a narrow (metal) tip as a nanometer-scale detector.

Knowing which exact roles are fulfilled by separate components in (commercial) catalyst formulations, is essential for developing a tailored catalyst composition that precisely fits the process needs. In **Chapter 3**, for example, we have found that the chain length of hydrocarbon products formed by cobalt-titania during CO hydrogenation increased with reaction pressure. For this insight, we used Raman signal enhancing shell-isolated (gold) nanoparticles. The role of performance-enhancing titania support appeared to supply essential building blocks to cobalt during the CO hydrogenation reaction. This revelation was obtained through modulation of the reactant CO, making conventional infrared spectroscopy a surface-sensitive method.

The modulation method also featured in **Chapter 4**, where we demonstrated that cobalt oxide nanoparticles follow a different reaction mechanism than metallic cobalt nanoparticles during CO<sub>2</sub> hydrogenation. When stabilized on titania support material, cobalt oxide nanoparticles are more efficient in terms of long-chain hydrocarbon production from CO<sub>2</sub> compared to the metallic variant. This observation, which refutes the general consensus that metallic cobalt is the only active phase, was backed up by the kinetic parameters activation energy and reaction order. We concluded that it takes cobalt oxide on titania less effort than metallic cobalt on titania to create long-chain hydrocarbons from CO<sub>2</sub>.

Curious to see if the beneficial effects from the cobalt oxide phase could be recreated in other ways, we investigated the element potassium as promoter for the CO and CO<sub>2</sub> hydrogenation reactions in **Chapter 5**. Generally, the addition of potassium lowered the hydrogenation capabilities of the cobalt-titania catalyst and consequently led to longer hydrocarbon chains with more unsaturated bonds; olefins rather than paraffins. Kinetic parameters revealed that potassium additionally catalyzes the conversion of CO<sub>2</sub> into the more reactive CO molecule, which led to enhanced performance. The addition of potassium to the catalyst formulation seemed promising for the development of renewable processes that aim to create long-chain hydrocarbons from CO<sub>2</sub>.

Alkali promoter elements were a recurring theme in **Chapter 6**, where we repurposed mineral residue from industrial biomass gasification as CO and CO<sub>2</sub> conversion catalyst. Although iron was the main active ingredient in the mineral residue, alkali elements potassium and sodium enabled the conversion of CO<sub>2</sub> into the more reactive CO molecule, leading to enhanced performance.

### 7.2.1 Connecting the Dots

The catalytic hydrogenation of CO into hydrocarbon fuels, as outlined in **Chapter 1**, has been invented more than a century ago. Although it is a well-established and also industrially applied process, the catalytically active phases and reaction mechanisms at play are complex due to the wide variety of possible reaction products and thus still topics of debate. This PhD Thesis utilized surface-sensitive spectroscopy techniques and explored (combinations of) unconventional methods to obtain new physicochemical insights into the CO and CO<sub>2</sub> conversion reactions with cobalt-based catalysts. The industrial CO hydrogenation process offers a solid foundation to develop renewable processes that convert deleterious greenhouse gas CO<sub>2</sub> into valuable products. CO<sub>2</sub> is chemically speaking much more inert compared to the reactive CO molecule and consequently more difficult to break apart. It is, however, important to realize that CO and CO<sub>2</sub> only differ one oxygen atom from each other and that the reaction mechanisms postulated for both reactions on metal (oxide) surfaces are fairly similar (**Figure 7.1**). The terms direct dissociation mechanism and the hydrogen-assisted mechanism featured therefore in both **Chapters 3** and **4**, which investigated CO and CO<sub>2</sub> hydrogenation, respectively.

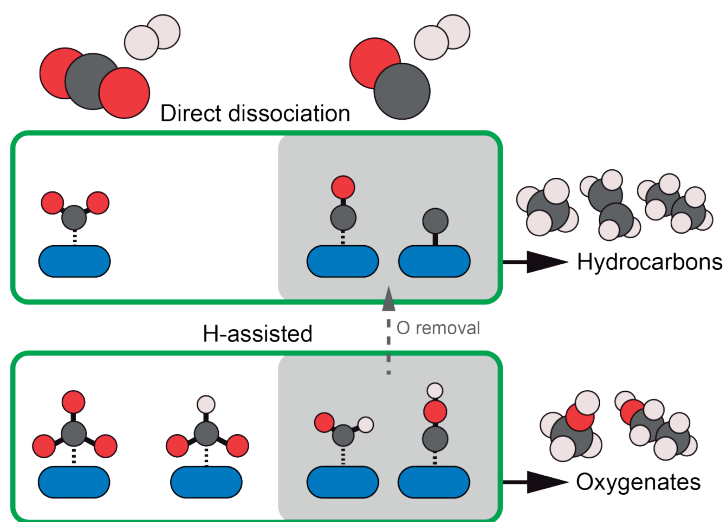


**Figure 7.1. Connecting the dots between catalytic CO and CO<sub>2</sub> hydrogenation.** CO and CO<sub>2</sub> only differ one oxygen atom from each other and therefore the reaction mechanisms at play on catalytically active metal (oxide) surface can generally be depicted in a similar way. While the left side of the figure begins with CO<sub>2</sub> as input molecule, the right side of the figure (shaded in gray) represents both CO and CO<sub>2</sub> hydrogenation. The terms direct dissociation (top) and hydrogen(H)-assisted (bottom) pathway can thus be used for both reactions.

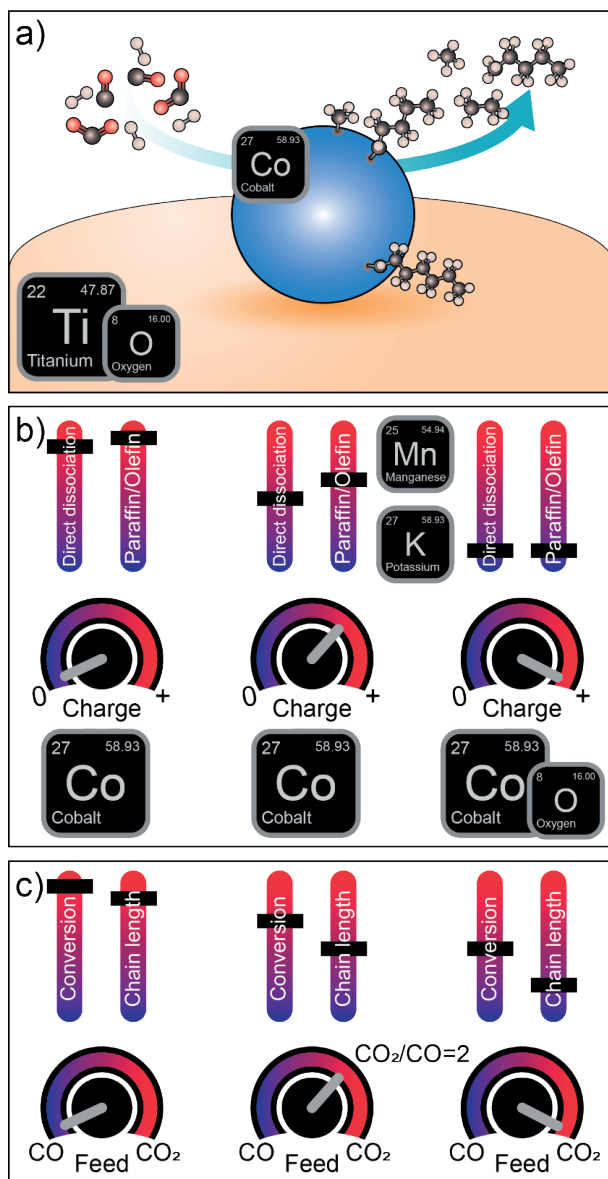


**Figure 7.2. Schematic overview of the factors controlling CO and CO<sub>2</sub> hydrogenation with cobalt-based catalyst materials.** (a) The CO/CO<sub>2</sub> hydrogenation reactions to hydrocarbons over titania-supported cobalt nanoparticles. (b) The catalyst's surface charge control panel, which influences, amongst others, the reaction mechanism and the paraffin/olefin ratio of the reaction products. Metallic cobalt has a low surface charge, resulting in more direct CO/CO<sub>2</sub> dissociation and a higher paraffin/olefin ratio. Cobalt oxide, as well as the addition of promoter elements manganese and potassium, causes a higher surface charge. (c) The gas feed control panel, which influences the, amongst others, the CO/CO<sub>2</sub> conversion and reaction product chain length.



The cobalt atoms in cobalt oxide, which is featured in **Chapter 4**, have a net positive ( $\text{Co}^{2+}\text{O}^{2-}$ ) charge, whereas metallic cobalt comprises cobalt atoms with a net zero charge ( $\text{Co}^0$ ). The addition of promoter element potassium (K), as explained in **Chapter 5**, induced an electronic effect that is reminiscent of the cobalt oxide phase.  $\text{K}^+$  withdraws electron density from  $\text{Co}^0$ , resulting in a slight positive charge ( $\text{Co}^{\delta+}$ ). This electronic effect has also been reported for promoter element manganese (Mn).<sup>1</sup> Together with the decreased amount of hydrogen on the catalyst surface, the electronic effect induced by potassium led to a higher yield of long-chain hydrocarbons with more unsaturated bonds. A schematic overview of the factors controlling the CO and  $\text{CO}_2$  hydrogenation reactions over cobalt-based catalysts is provided in **Figure 7.2**. Although potassium is part of the commercial catalyst formulation in iron-based CO hydrogenation processes,<sup>2</sup> the element is in our view somewhat underappreciated in cobalt-based processes.<sup>3</sup> Especially for renewable purposes that aim to convert  $\text{CO}_2$ , the addition of the cheap and abundant element potassium may offer an advantageous outcome.

CO and  $\text{CO}_2$  hydrogenation to hydrocarbons can be envisioned as a series of events where  $\text{CH}_x$  monomers are concatenated into hydrocarbon chains of various lengths. Coupling together a lot of units would eventually yield a polymer. For example, polyethylene, a commonly used plastic, is structurally identical to a saturated long-chain hydrocarbon (paraffin); only longer. One may now start wondering where the boundary lies between a long-chain hydrocarbon and polymer: What is the minimum amount of units that a polymer should have? The prefix “poly” originates from the Greek word πολλύ, which literally means “many”. This, however, blurs the lines and makes it difficult to define where a long-chain hydrocarbon ends and a polymer starts.

In practice, olefin polymerization is conducted with different catalysts than CO and  $\text{CO}_2$  hydrogenation, which can also be considered as either  $\text{CO}_x$ ,  $\text{CO}_x\text{H}_y$  or  $\text{CH}_x$  polymerization. Olefins, such as ethylene and propylene, are commercially polymerized with, for example, metallocene-based catalysts.<sup>4</sup> Though the initial monomer may be different compared to CO and  $\text{CO}_2$  hydrogenation, these catalysts also enable the concatenation of multiple units. What catalysts generally have in common is that they function as scissors and/or glue: they make and/or break bonds (**Figure 7.3**). It is thus not unthinkable that ideas or concepts from one catalytic process may also (partially) apply to other processes. This is not only relevant within the field of heterogeneous catalysis, but also beyond that. For example, resemblances between heterogeneous and homogeneous CO conversion, e.g., hydroformylation, have been highlighted before.<sup>5</sup> General concepts can sometimes be applicable in multiple different fields and interdisciplinary communication is thus vital.

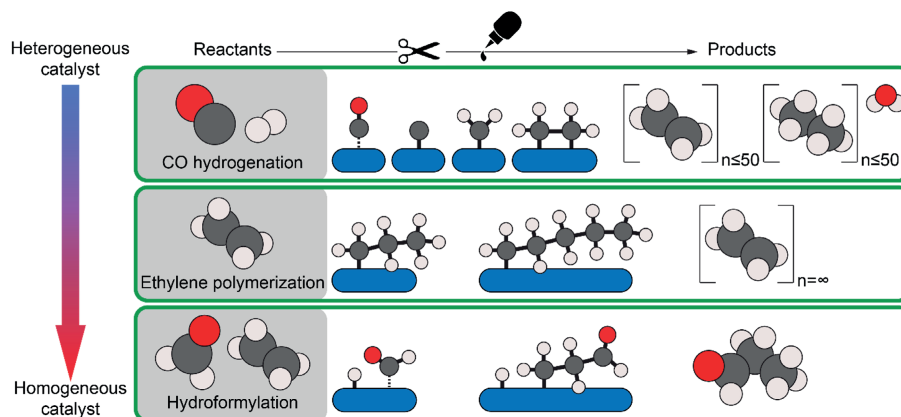


**Figure 7.3. Comparison between hydrogenation, polymerization, and hydroformylation catalysis.** Although CO and CO<sub>2</sub> hydrogenation (top panel) may have different initial monomers (reactants) than olefin polymerization (middle panel) or hydroformylation (bottom panel), the concept of breaking bonds and consequently linking units together is similar. Olefin polymerization can be compared to the direct dissociation mechanism and consequent insertion of CH<sub>x</sub> units in hydrogenation catalysis. In terms of catalyst classification, olefin polymerization operates with a hybrid between hetero- and homogeneous, e.g., metallocene complexes anchored onto a support oxide, such as silica. Metallocene complexes are activated using methylaluminoxane (MAO) as co-catalyst, which then provides the -CH<sub>3</sub> end group for the polymer chain. Hydroformylation with homogeneous catalysts (*i.e.*, organometallic complexes) has been postulated as a mechanistic analogue to the hydrogen (H)-assisted mechanism in CO and CO<sub>2</sub> hydrogenation with heterogeneous catalysts.

### 7.3 Future Perspectives

Future endeavors should pursue a multitude of things in various subbranches of science related, but not limited to heterogeneous catalysis, renewable energy, and sustainability. They are summarized below.

#### 7.3.1 Towards New Catalyst Formulations

In **Chapter 5** we have investigated the effects of adding alkali promoter element potassium to the cobalt-based catalyst formulation for the CO and CO<sub>2</sub> hydrogenation reactions. This appeared particularly interesting for the CO<sub>2</sub> hydrogenation reaction and for co-feeding CO<sub>2</sub>/CO with a ratio of 2. We recommend that future studies systematically investigate the optimum potassium loading in terms of long-chain hydrocarbon yield. It would also be worthwhile to explore other alkali metals, like sodium or lithium, as promoter elements. Moreover, combinations of multiple promoter elements in a catalyst formulation will be interesting. For example, alkali metals together with oxidic compounds, such as manganese oxide, could enable the production of oxygenated

hydrocarbons, such as alcohols and aldehydes.<sup>3</sup> Apart from cobalt, iron-based systems should also be investigated for renewable processes.<sup>6</sup>

### 7.3.2 Towards more Powerful Analytical Techniques

As formulated nicely and accurately by Vladimir Ipatieff at the end of his 1940 article in *Science*: "*I wish to state that for a thorough investigation of the mechanism of catalytic reaction it will be necessary to apply all the chemical and physical tools at our disposal*".<sup>7</sup> In his era, petroleum was one of the main focus points of many great chemists. Nowadays, we are slowly shifting towards more renewable resources, such as biomass, CO<sub>2</sub>, and plastic waste. Obtaining energy from these renewable resources will require new or adapted catalyst formulations and thus thorough investigations with the analytical tools at hand. Thermally-driven catalytic processes, heterogeneous catalysis, will be essential for the transition towards renewable energy. The identification of (short-lived) active species will require analytical techniques with enhanced sensitivity,<sup>8</sup> better time resolution,<sup>9</sup> and advanced data analysis.<sup>10</sup> Apart from thermal processes, electrocatalysis, which is conducted with electrodes in aqueous media, will play an important role. However, electrocatalytic processes have a few additional factors, such as the aqueous medium, that complicates the use of spectroscopic techniques.<sup>11</sup> To enable thorough investigation of such processes under realistic reaction conditions, the analytical tools will require attention and modification. Exciting techniques to investigate electrocatalytic processes include X-ray absorption spectroscopy<sup>11</sup> and surface-sensitive Raman spectroscopy.<sup>12</sup>

### 7.3.3 Exploring New Research Approaches

Photo-induced force microscopy was successfully demonstrated as an infrared spectroscopy method with 10-20 nm spatial resolution in **Chapters 2** and **3**. Although not a high-throughput method, the approach can be applied to virtually any polymer or catalyst material. We recommend that tip-based infrared spectroscopy tools will be equipped with lasers that can operate in a broad wavenumber range (100-4000 cm<sup>-1</sup>) to yield complete spectral fingerprints in the future. In **Chapter 2**, the pressing societal matter of nanometer-sized plastic particles in the environment, arising from plastic waste degradation, was highlighted. We recommend that future efforts in this research field are directed towards a broad range of environmental samples, such as ocean, river, and drinking water. Besides, the potential presence of nanometer-sized plastic particles in biological samples, such as tissue, blood, and serum, should be assessed with this method. The endeavors should be complemented with more quantitative methods, such as proton transfer reaction - mass spectrometry (PTR-MS).<sup>17,18</sup>

The methodology of modulating the reactants CO and CO<sub>2</sub> has been applied to increase surface-sensitivity during infrared spectroscopy measurements in **Chapters 3** and **4**. Future catalyst development studies regarding alkali promoter effects in the CO<sub>2</sub> hydrogenation reaction would greatly benefit from this approach. The so-called modulation excitation approach could be combined with virtually any spectroscopy technique where increased surface sensitivity is required. Future endeavors should particularly explore modulation excitation combined with Raman spectroscopy, X-ray diffraction,<sup>13</sup> and X-ray absorption spectroscopy.<sup>14</sup> To facilitate modulation excitation, solenoid valves, which enable fast switching of gas feeds, should be installed at the reactor cell inlet. Besides, future cell designs should aim to minimize the dead volume of the reactor cells.<sup>15</sup> In the case that unidentified species appear in the infrared or Raman spectra, isotopically labeled gases should be used to clarify the species' structure.

Shell-isolated (gold) nanoparticles<sup>16</sup> were used to enhance the sensitivity of Raman spectroscopy measurements during the CO hydrogenation reaction (**Chapter 3**). While modulation excitation can typically be applied only up to a maximum pressure of ~4 bar, the shell-isolated nanoparticles were able to withstand up to 20 bar pressure and temperatures of 450°C. This is particularly exciting for understanding industrially-relevant catalytic processes, as most of them are conducted at elevated temperatures and pressures. We recommend that future studies utilize shell-isolated nanoparticles as a diagnostic tool in their mechanistic investigations. For example, to explore alkali promoter effects in CO and CO<sub>2</sub> hydrogenation reactions.

### 7.3.4 Towards an Interdisciplinary Research Attitude

Although working in an academic environment can sometimes feel like a rather individual task, communication and collaborations are essential for a broader impact of scientific results. Working together with scientists from multiple fields of science and technology can lead to creative solutions, as they view problems from different angles. An open and interdisciplinary attitude is what sets a great scientist apart from a good scientist. Besides, academics should aim to collaborate closely with industrial partners, as this will enable application of scientific concepts in the real world. An example of an issue where collaborations can have a major impact is the improvement of analytical tools. Continuous progress, as desired for thermal heterogeneous and electrocatalyst characterization under realistic reaction conditions, requires - at least - the collaborations between chemists and physicists. Another example is the risk analysis of nanoplastics on the environment, animals, and humans. This complex assessment requires interdisciplinary collaborations between chemists, biologists, medical personnel, and toxicologists. Even beyond all the Science, Technology, Engineering, and Math (STEM) subjects,

chemists can and should collaborate with psychologists and economists to strategize how to make sustainability and environmental awareness desirable for consumers.

### 7.3.5 Renewable and Circular Should be the New Normal

The Industrial Revolution, which began in the early 18<sup>th</sup> century, required investments from wealthy entrepreneurs, who were guided by the profit motive. This has led to the rise of capitalism in many societies.<sup>19</sup> Ceaseless consumption has been and still is central to the emergence and support of capitalism all over the world.<sup>20</sup> Capitalism glorifies a linear way of thinking (**Figure 7.4**), as required by the capitalist economic system to maintain consumerism. Since the Industrial Revolution, the rate of fossil fuel utilization has grown eleven-fold.<sup>21</sup> While the warming effects of carbon dioxide that arise from burning fossil fuels were already mentioned in 1896 by Svante Arrhenius,<sup>22</sup> the abundance of fossil fuels simply impeded its reduction throughout the whole 20<sup>th</sup> century.<sup>23</sup> However, over the past two decades humanity has slowly started to realize that fossil fuels are not an inexhaustible source and awareness has grown amongst scientists regarding the potentially devastating climate change effects. Consumers, industries, and policy makers are all responsible for preventing and reversing the adverse effects of climate change. The consumer mindset should change from linear to circular thinking; recycling rather than discarding. Industries are responsible for recycling too and they should strategize on how to repurpose e.g., waste material and residual heat. To set an example, we repurposed an iron-containing mineral residue from industrial biomass gasification as a catalyst to produce lower olefins from CO, CO<sub>2</sub>, and H<sub>2</sub> in **Chapter 6**. To balance environmentalism and consumerism in a capitalist society, interventions and transformational strategies should be explored by industries, policy makers, and scientists.<sup>19</sup>

The same concept applies to plastic. Although plastic was invented halfway through the 19<sup>th</sup> century, it was only around the 1950s that its popularity skyrocketed.<sup>24</sup> The mass production of cheap plastic products started in the 1960s-1970s and has led to a single-use culture.<sup>25</sup> While plastic products play an important role in our current society and will continue to do so in the future, the general mindset has to change from linear to circular to limit the detrimental effects of mismanaged plastic waste.

**Figure 7.4** depicts a conceptual overview of our current society (left, in red) as well as the desired net zero scenario (right, in green). Our current society is based on linear thinking, while the desired net zero scenario adopts a more circular mindset and would valorize captured CO<sub>2</sub> emissions into fuels, chemicals, and plastics. Additionally, the resulting CO<sub>2</sub> emissions would ideally be captured again and recycled. Upgrading of

CO<sub>2</sub> can either be done directly or via a two-step process, where it is first converted into the more reactive CO molecule. Examples of the one-step process include thermal catalytic processes, such as direct CO<sub>2</sub> hydrogenation to fuels or methanol.<sup>6</sup> While CO<sub>2</sub> electrolysis into C<sub>2+</sub> hydrocarbons, for example with Cu-based catalysts, certainly presents an interesting concept, it is not yet ready for commercial applications at its current state-of-the-art performance.<sup>26</sup> Photocatalytic conversion of CO<sub>2</sub> into C<sub>1</sub> and C<sub>2</sub> hydrocarbons with heterogeneous catalysts has also been reported.<sup>27</sup> Due to the UV-light responsiveness, TiO<sub>2</sub>-based materials are in my view amongst the most interesting and are without doubt the most widely studied for photocatalytic CO<sub>2</sub> conversion applications.<sup>27,28</sup> The two-step process could be beneficial to increase the overall process efficiency. CO<sub>2</sub> would first be converted to the more reactive CO molecule either *via* the reverse water-gas shift (RWGS) reaction,<sup>29</sup> *i.e.*, thermal catalysis, or *via* electrocatalytic reduction.<sup>26,30</sup> In the second step, CO can be upgraded either *via* thermal catalysis, electrocatalysis, or photocatalysis depending on the specific needs. In this case, the thermal catalytic route is currently the most established one in terms of commercial applications.<sup>29</sup>

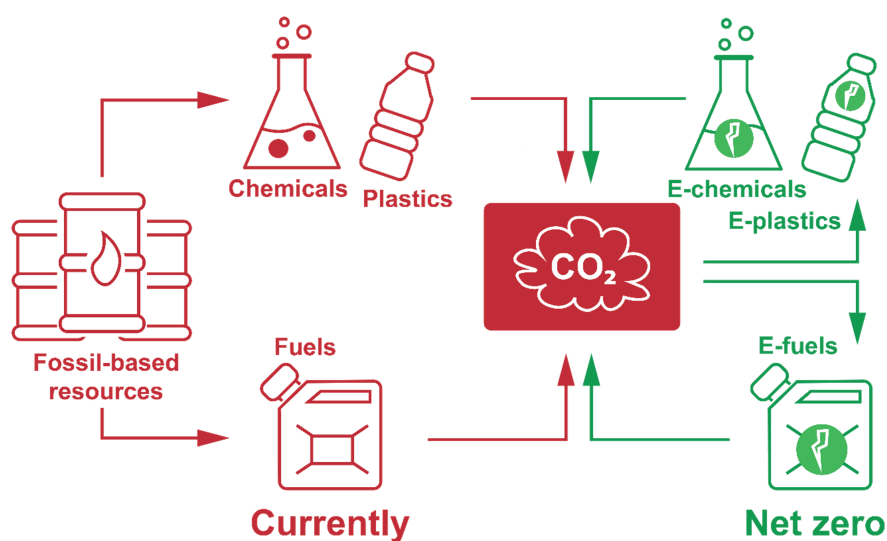


**Figure 7.4. Conceptual overview of the current scenario to create fuels and chemicals and the desired net zero scenario.** In our current society, fuels, chemicals, and plastics are produced from fossil-based resources and emit CO<sub>2</sub>. In the desired net zero scenario, renewable fuels, chemicals, and plastics (prefix: E-) are produced from captured CO<sub>2</sub> emissions using, for example, thermal catalytic routes, photocatalysis, or electrocatalysis. Ideally, the resulting emissions are then again recycled and valorized.

## 7.4 References

1. Morales, F., de Smit, E., de Groot, F. M. F., Visser, T. & Weckhuysen, B. M. Effects of manganese oxide promoter on the CO and H<sub>2</sub> adsorption properties of titania-supported cobalt Fischer-Tropsch catalysts. *Journal of Catalysis* **246**, 91–99 (2007).
2. van de Loosdrecht, J., Botes, F. G., Ciobica, I. M., Ferreira, A. C., Gibson, P., Moodley, D. J., Saib, A. M., Visagie, J. L., Weststrate, C. J. & Niemantsverdriet, J. W. in *Comprehensive Inorganic Chemistry II: from elements to applications* **7**, 525–557 (Elsevier, Amsterdam, 2013).
3. Xiang, Y. & Kruse, N. Tuning the catalytic CO hydrogenation to straight-and long-chain aldehydes/alcohols and olefins/paraffins. *Nature Communications* **7**, 13058 (2016).
4. Werny, M. J., Zarupski, J., ten Have, I. C., Piovano, A., Hendriksen, C., Friederichs, N. H., Meirer, F., Groppo, E. & Weckhuysen, B. M. Correlating the Morphological Evolution of Individual Catalyst Particles to the Kinetic Behavior of Metallocene-Based Ethylene Polymerization Catalysts. *JACS Au* **1**, 1996–2008 (2021).
5. Schulz, H. Confinements on growth sites of Fischer-Tropsch synthesis, manifesting in hydrocarbon-chain branching. *Applied Catalysis A: General* **602**, 117695 (2020).
6. Yao, B., Xiao, T., Makgae, O. A., Jie, X., Gonzalez-cortes, S., Guan, S., Kirkland, A. I., Dilworth, J. R., Al-megren, H. A., Alshihri, S. M., Dobson, P. J., Owen, G. P., Thomas, J. M. & Edwards, P. P. Transforming carbon dioxide into jet fuel using an organic combustion-synthesized Fe-Mn-K catalyst. *Nature Communications* **11**, 6395 (2020).
7. Ipatieff, V. N. Mixed Catalysts. *Science* **91**, 605–608 (1940).
8. Marchionni, V., Ferri, D., Kröcher, O. & Wokaun, A. Increasing the Sensitivity to Short-Lived Species in a Modulated Excitation Experiment. *Analytical Chemistry* **89**, 5801–5809 (2017).
9. Meirer, F. & Weckhuysen, B. M. Spatial and temporal exploration of heterogeneous catalysts with synchrotron radiation. *Nature Reviews Materials* **3**, 324–340 (2018).
10. Alcaraz, M. R., Aguirre, A., Goicoechea, H. C., Culzoni, M. J. & Collins, S. E. Resolution of intermediate surface species by combining modulated infrared spectroscopy and chemometrics. *Analytica Chimica Acta* **1049**, 38–46 (2019).
11. Timoshenko, J. & Roldan Cuenya, B. In Situ/Operando Electrocatalyst Characterization by X-ray Absorption Spectroscopy. *Chemical Reviews* **121**, 882–961 (2021).
12. An, H., Wu, L., Mandemaker, L. D. B., Yang, S., de Ruiter, J., Wijten, J. H. J., Janssens, J. C. L., Hartman, T., van der Stam, W. & Weckhuysen, B. M. Sub-Second Time-Resolved Surface-Enhanced Raman Spectroscopy Reveals Dynamic CO Intermediates during Electrochemical CO<sub>2</sub> Reduction on Copper. *Angewandte Chemie International Edition* **60**, 16576–16584 (2021).
13. Müller, P. & Hermans, I. Applications of Modulation Excitation Spectroscopy in Heterogeneous Catalysis. *Industrial & Engineering Chemistry Research* **56**, 1123–1136 (2017).
14. Vogt, C., Groeneveld, E., Kamsma, G., Nachtegaal, M., Lu, L., Kiely, C. J., Berben, P. H., Meirer, F. & Weckhuysen, B. M. Unravelling structure sensitivity in CO<sub>2</sub> hydrogenation over nickel. *Nature Catalysis* **1**, 127–134 (2018).
15. Chiarello, G. L., Nachtegaal, M., Marchionni, V., Quaroni, L. & Ferri, D. Adding diffuse reflectance infrared Fourier transform spectroscopy capability to extended x-ray-absorption fine structure in a new cell to study solid catalysts in combination with a modulation approach. *Review of Scientific Instruments* **85**, 074102 (2014).
16. Hartman, T., Geitenbeek, R. G., Whiting, G. T. & Weckhuysen, B. M. Operando monitoring of temperature and active species at the single catalyst particle level. *Nature Catalysis* **2**, 986–996 (2019).

17. Materić, D., Kasper-Giebl, A., Kau, D., Anten, M., Greiling, M., Ludewig, E., Van Seville, E., Röckmann, T. & Holzinger, R. Micro-and Nanoplastics in Alpine Snow: A New Method for Chemical Identification and (Semi)Quantification in the Nanogram Range. *Environmental Science and Technology* **54**, 2353–2359 (2020).
18. Holzinger, R., Ludewig, E., Brunner, D. & Thomas, R. Nanoplastics transport to the remote, high-altitude Alps. *Environmental Pollution* **288**, 117697 (2021).
19. Panizzut, N., Rafi-ul-Shan, P. M., Amar, H., Sher, F., Mazhar, M. U. & Klemeš, J. J. Exploring relationship between environmentalism and consumerism in a market economy society: A structured systematic literature review. *Cleaner Engineering and Technology* **2**, 100047 (2021).
20. Trentmann, F. Beyond consumerism: New historical perspectives on consumption. *Journal of Contemporary History* **39**, 373–401 (2004).
21. Ross, M. B., De Luna, P., Li, Y., Dinh, C. T., Kim, D., Yang, P. & Sargent, E. H. Designing materials for electrochemical carbon dioxide recycling. *Nature Catalysis* **2**, 648–658 (2019).
22. Arrhenius, S. XXXI. On the Influence of Carbonic Acid in the Air upon the Temperature of the Ground. *The London, Edinburgh, and Dublin Philosophical Magazine and Journal of Science* **41**, 237–276 (1896).
23. Kaempffert, W. Science in Review. *New York Times* 191 (1956).
24. Jubinville, D., Esmizadeh, E., Saikrishnan, S., Tzoganakis, C. & Mekonnen, T. A comprehensive review of global production and recycling methods of polyolefin (PO) based products and their post-recycling applications. *Sustainable Materials and Technologies* **25**, (2020).
25. The Age of Plastic: From Parkesine to Pollution. <https://www.sciencemuseum.org.uk/objects-and-stories/chemistry/age-plastic-parkesine-pollution> (2019).
26. Wakerley, D., Lamaison, S., Wicks, J., Clemens, A., Feaster, J., Corral, D., Jaffer, S.A., Sarkar, A., Fontecave, M., Duoss, E.B. & Baker, S. Gas diffusion electrodes, reactor designs and key metrics of low-temperature CO<sub>2</sub> electrolyzers. *Nature Energy* **7**, 130–143 (2022).
27. Li, K., Peng, B., & Peng, T. Recent advances in heterogeneous photocatalytic CO<sub>2</sub> conversion to solar fuels. *ACS Catalysis* **6**, 7485–7527 (2016).
28. He, Z. H., Jiang, C. S., Wang, K., Wang, Z. Y., Li, N., Wang, W. T., & Liu, Z. T. Photothermal CO<sub>2</sub> hydrogenation to methanol over a CoO/Co/TiO<sub>2</sub> catalyst in aqueous media under atmospheric pressure. *Catalysis Today* **356**, 579–588 (2020).
29. Daza, Y. A., & Kuhn, J. N. CO<sub>2</sub> conversion by reverse water gas shift catalysis: comparison of catalysts, mechanisms and their consequences for CO<sub>2</sub> conversion to liquid fuels. *RSC advances* **6**, 49675–49691 (2016).
30. Nitopi, S., Bertheussen, E., Scott, S.B., Liu, X., Engstfeld, A.K., Horch, S., Seger, B., Stephens, I.E., Chan, K., Hahn, C. and Nørskov, J.K. Progress and perspectives of electrochemical CO<sub>2</sub> reduction on copper in aqueous electrolyte. *Chemical reviews* **119**, 7610–7672 (2019).







# **CHAPTER 8**

**SUMMARY IN DUTCH, LIST OF  
ABBREVIATIONS, ACKNOWLEDGEMENTS,  
AND INFORMATION ABOUT THE AUTHOR**





## 8.1 Nederlandse Samenvatting

Dit proefschrift besprak het gebruik van oppervlaktegevoelige spectroscopie als een veelbelovende methodologie om de werking van heterogene katalysatoren te ontrafelen. **Hoofdstuk 1** introduceerde de basisprincipes van spectroscopie en katalyse. Ook werd het Fischer-Tropsch Synthese proces (d.w.z., de hydrogenatiereactie van koolstofmonoxide) geïntroduceerd en de geschiedenis van dit proces werd besproken. Daarna werd er uitgelegd hoe fundamentele inzichten verkregen kunnen worden in dit proces met spectroscopische karakterisering onder realistische reactie condities zoals gebruikt in de industrie (hoge temperaturen en drukken). Hoewel de wens om verbanden te leggen tussen katalysatorstructuur, katalysatorsamenstelling, en katalytische effectiviteit al bestond sinds de ontdekking van het concept van katalyse, ontbraken de spectroscopische instrumenten om deze droom te realiseren. Ondanks dat spectroscopie al sinds het begin van de 20<sup>ste</sup> eeuw een prominent analytisch hulpmiddel was, begon een gezamenlijke onderzoeksinspanning om spectroscopie toe te passen onder relevante reactieomstandigheden met bewijs van katalytische prestaties pas echt aan het begin van de 21<sup>ste</sup> eeuw. De oorsprong van deze grondige methodologie, genaamd *operando* spectroscopie, werd besproken in **Hoofdstuk 1**. Daarna baanden we de weg voor het onderzoeken van de door kobalt-gekatalyseerde hydrogenatie van koolstofmonoxide (CO) en koolstofdioxide (CO<sub>2</sub>). We formuleerden hierbij een tweeledig doel. Het eerste doel was om fundamenteel inzicht verkrijgen in de actieve fase van op kobalt-gebaseerde katalysatoren tijdens de hydrogenatie van CO en CO<sub>2</sub>. Het tweede doel was om de reactiemechanismen bloot te leggen, die een rol spelen tijdens de vorming van (on)gewenste reactieproducten en het deactiveren van het katalysatormateriaal. Om deze twee doelen te bereiken, werden de mogelijkheden en beperkingen van moderne spectroscopietechnieken verder verkend en benut.

Spectroscopietechnieken, die op nanometerschaal werken, zijn veelbelovende hulpmiddelen om de hierboven geformuleerde doelen te bereiken. Foto-geïnduceerde krachtmicroscopie, waarbij infraroodspectroscopie gecombineerd wordt met een zeer scherpe punt om infraroodspectra met een resolutie van 10-20 nanometers (nm) op te nemen, werd geïntroduceerd in **Hoofdstuk 2**. Deze nanoschaal spectroscopietechniek werd door de uitvinders voor het eerst succesvol gedemonstreerd in de polymeerwetenschap waarbij gemakkelijk onderscheid gemaakt kon worden tussen verschillende nanoschaal polymeerdomeinen. Daarnaast hebben we enkele recente toepassingen van deze tip-gebaseerde spectroscopiemethodologie uitgelicht, waaronder de detectie van plastic nanodeeltjes, die ontstaan door de afbraak van plastic afval in het milieu, en de structurele analyse van katalytische materialen, waaronder polymerisatiekatalysatoren en CO<sub>2</sub> hydrogenatiekatalysatoren. Sommige van de analytische instrumenten die nodig waren om de doelen van dit proefschrift te bereiken, functioneren normaal-

gesproken het best onder een vacuüm of lagedruk atmosfeer en met vereenvoudigde modelkatalysatoren. Industriële processen worden echter typisch gekatalyseerd door complexere materialen met meerdere componenten en uitgevoerd bij hoge temperaturen en drukken. Hoewel de academische wereld ernaar streeft de fundamentele fenomenen die zich voordoen op de oppervlakken van de katalysatoren te begrijpen, zijn de meest gevoelige analytische instrumenten vaak niet in staat om naar behoren te functioneren onder deze zware omstandigheden. Deze kloof tussen industriële katalyse en academisch onderzoek werd besproken in **Hoofdstuk 2**. Het verschil tussen commerciële heterogene katalyse en academisch onderzoek zou overbrugd kunnen worden door gebruik te maken van geavanceerde analytische instrumenten en door de inzet van realistischere modelsystemen. Voor dit laatste hebben we een modelsysteem geïntroduceerd dat bestond uit kobaltnanodeeltjes gestabiliseerd door mesoporeuze titania-eilanden. Terwijl het modelsysteem dat de op kobalt-gebaseerde katalysatoren voor de hydrogenatie van CO nabootst realistischer is dan simpele kristalstructuren, maakte de relatief vlakke oppervlaktestructuur een geavanceerde analyse mogelijk met foto-geïnduceerde krachtmicroscopie.

In **Hoofdstuk 3** werd een groot aantal onconventionele spectroscopietechnieken gebruikt om de reactiemechanismen te ontcijferen die betrokken zijn bij de vorming van koolwaterstofproducten en koolstofafzetting op het katalysatoroppervlak tijdens de hydrogenatie van CO met kobalt-titania katalysatoren. Door de concentratie van het reactant CO te moduleren, werd infraroodspectroscopie getransformeerd in een oppervlaktegevoelige methode en vervolgens konden reactieve tussenproducten spectroscopisch worden waargenomen tijdens de reactie. Waterstof- en zuurstofbevattende reactieve tussenproducten, zoals formaten en carboxylaten, reageerden op de CO-stimulus en leverden daarmee bewijs dat de door waterstof ondersteunde splitsing van CO-bindingen plaatsvond. Daarnaast bleek de efficiëntie-verbeterende rol van het titania dragermateriaal gerelateerd aan het leveren van essentiële bouwstenen aan kobalt tijdens de reactie. Vervolgens werden gouden nanodeeltjes gebruikt om het Raman spectroscopiesignaal te versterken en tussenproducten te observeren tijdens de reactie bij hoge temperaturen en drukken. De verbeterde katalytische efficiëntie bij verhoogde druk bleek te worden veroorzaakt door langere koolwaterstofketens aan het oppervlak. Bovendien werd er bewijs gevonden voor het optreden van het directe C-O-bindingssplitsingsmechanisme. Verder namen we waar met behulp van foto-geïnduceerde krachtmicroscopie dat koolstofafzetting op het katalysatoroppervlak plaatsvond *via* de vorming van onverzadigde koolstof-koolstof bindingen en/of carbonylfunctionaliteiten.

Het idee om een reactant te moduleren om een spectroscopietechniek oppervlaktegevoelig te maken werd verder uitgewerkt in **Hoofdstuk 4**. Deze keer onderzochten we de katalytisch actieve componenten en reactiemechanismen die een rol spelen tijdens de hydrogenatie van  $\text{CO}_2$  met op kobalt-gebaseerde katalysatoren. Van de verschillende dragermaterialen die werden gebruikt om de kobalt(oxide) nanodeeltjes te stabiliseren, zette de katalysator met dragermateriaal titania de meeste  $\text{CO}_2$  om. **Hoofdstuk 4** weerlegde ook de algemene consensus dat metallisch kobalt de enige actieve component is, aangezien kobaltoxide-nanodeeltjes op titania dragermateriaal meer koolwaterstoffen met lange ketens oprachten in vergelijking met de metallische kobaltvariant. Dit is gunstig, aangezien langere koolwaterstofketens meer energie opslaan dan kortere ketens. Door de  $\text{CO}_2$ -reactantconcentratie tijdens infraroodspectroscopiemetingen te moduleren, konden we zien dat kobaltoxide en metallisch kobalt verschillende reactiepaden volgden. Terwijl metallisch kobalt  $\text{CO}_2$  direct in CO kon dissociëren, had kobaltoxide de hulp van waterstofatomen nodig om de CO-bindingen te splitsen. Toevoer van CO aan de  $\text{CO}_2$ - en  $\text{H}_2$ -gasstroom verhoogde de lange-keten koolwaterstofopbrengst van de kobalt-titania katalysator en resulteerde in een veelbelovende richting voor commerciële  $\text{CO}_2$ -valorisatie toepassingen.

In **Hoofdstuk 5** onderzochten we de effecten van het promotor element kalium in de hydrogenatiereactie van CO en  $\text{CO}_2$  met kobalt-titania katalysatoren. Hoewel oxidische promotorelementen, zoals mangaan, op grote schaal worden toegepast in industriële CO-hydrogenatieprocessen, die door kobalt gekatalyseerd worden, worden alkalische promotorelementen alleen op grote schaal toegepast in processen die door ijzer gekatalyseerd worden. Alkalische promotorelementen waren nog niet grondig onderzocht in combinatie met kobalt. Voor de hydrogenatie van CO bleek de toevoeging van kalium aan de kobalt katalysator een negatief effect te hebben: de CO conversie nam af en er werden minder koolwaterstoffen met lange ketens gevormd. De toevoeging van kalium aan de katalysatorformulering bleek echter wel interessant voor duurzame energietoepassingen die als doel hebben  $\text{CO}_2$  om te zetten in koolwaterstoffen met lange ketens. Kalium maakte het kobaltoppervlak licht elektropositief en maakte de omzetting van  $\text{CO}_2$  naar het reactievere CO-molecuul mogelijk *via* de omgekeerde watergasverschuivingsreactie. Bovendien nam de hoeveelheid waterstof op het katalysatoroppervlak af door de toevoeging van kalium. Door deze effecten verschoof de samenstelling van de reactieproducten van het ongewenste methaan naar waardevollere koolwaterstoffen met lange ketens.

In **Hoofdstuk 6** werd een residu van industriële biomassavergassing hergebruikt als katalysator. Het residu bevatte zo'n 15 verschillende elementen, waarvan ijzer de belangrijkste was. IJzer maakte de omzetting mogelijk van een gastoevoermengsel van

CO, CO<sub>2</sub>, H<sub>2</sub>, en N<sub>2</sub> in methaan (57%) en C<sub>2</sub>-C<sub>5</sub>-olefinen (43%). Door middel van *operando*-röntgendiffractie ontdekten we dat de omzetting van metallisch ijzer in een ijzer-carbidefase gepaard ging met een toename van de totale CO en CO<sub>2</sub> omzetting en een verbeterde selectiviteit naar de gewenste olefinen. De alkali-elementen kalium en natrium in het residu katalyseerden de omgekeerde watergasverschuivingsreactie. Deze elementen maakten de omzetting van CO<sub>2</sub> in het reactievere CO-molecuul mogelijk en leidden tot een hogere opbrengst aan waardevolle koolwaterstoffen met lange ketens als reactieproducten.

Tot slot verschaft **Hoofdstuk 7** een Engelse samenvatting van dit proefschrift en werden enkele toekomstperspectieven gepresenteerd. In de voorgestelde onderzoeken zal de nadruk moeten worden gelegd op het optimaliseren van katalysatorformuleringen, gevoeliger analysetechnieken, ingenieuze methodologieën en protocollen, en een interdisciplinaire aanpak waarbij duurzaamheid en circulariteit centraal staan.



## 8.2 List of Abbreviations

AA	Acetic Aldehyde
AFM	Atomic Force Microscopy
AIP	Aluminum IsoPropoxide
AP	Ambient Pressure
ASF	Anderson-Schulz-Flory
ATR-IR	Attenuated Total Reflectance - InfraRed
BA	BenzAldehyde
BCC	Body-Centered Cubic
BET	Brunauer-Emmett-Teller
BPC	Back-Pressure Controller
BPE	Perdew-Becke-Ernzerhof
BSE	BackScattered Electron
CCS	Carbon Capture and Storage
CCU	Carbon Capture and Utilization
CP	Cubic Primitive
CTD	Conductivity, Temperature, and Depth
CTY	Cobalt-Time-Yield
DFT	Density Functional Theory
DLS	Dynamic Light Scattering
DP	Deposition Precipitation
DRIFTS	Diffuse Reflectance Infrared Fourier-Transform Spectroscopy
DRS	Diffuse Reflectance Spectroscopy
EDX	Energy Dispersive X-ray spectroscopy
EELS	Electron Energy Loss Spectroscopy
EPR	Electron Paramagnetic Resonance
EXAFS	Extended X-ray Absorption Fine Structure
FA	FormAldehyde
FCC	Face-Centered Cubic
FEG	Field Emission Gun
FIB	Focused Ion Beam
FTS	Fischer-Tropsch Synthesis
FWHM	Full Width at Half Maximum
GC	Gas Chromatography
GHSV	Gas Hourly Space Velocity
GI	Grazing Incidence
HAADF	High-Angle Annular Dark-Field
HCP	Hexagonal Closest Packed
HP	High Pressure

<b>IR</b>	<b>I</b> nfra <b>R</b> ed
<b>IWI</b>	<b>I</b> ncipient <b>W</b> etness <b>I</b> mpregnation
<b>MAO</b>	<b>M</b> etal <b>A</b> lumin <b>O</b> xane
<b>MCM</b>	<b>M</b> obil <b>C</b> rystalline <b>M</b> aterials
<b>MCT</b>	<b>M</b> ercury <b>C</b> admium <b>T</b> elluride
<b>ME</b>	<b>M</b> odulation <b>E</b> xcitation
<b>MRI</b>	<b>M</b> agnetic <b>R</b> esonance <b>I</b> maging
<b>MRS</b>	<b>M</b> agnetic <b>R</b> esonance <b>S</b> pectroscopy
<b>MS</b>	<b>M</b> ass <b>S</b> pectrometry
<b>MSI</b>	<b>M</b> etal- <b>S</b> upport <b>I</b> nteraction
<b>NA</b>	<b>N</b> aph <b>A</b> ldehyde
<b>NEXAFS</b>	<b>N</b> ear <b>E</b> dge <b>X</b> -ray <b>A</b> bsorption <b>F</b> ine <b>S</b> tructure
<b>NMR</b>	<b>N</b> uclear <b>M</b> agnetic <b>R</b> esonance
<b>ODTS</b>	<b>O</b> cta <b>D</b> ecyl <b>T</b> richloro <b>S</b> ilane
<b>OPO</b>	<b>O</b> ptical <b>P</b> arametric <b>O</b> scillator
<b>P123</b>	<b>P</b> oly(ethylene glycol)- <i>block</i> -poly(propylene glycol)- <i>block</i> -poly(ethylene glycol)
<b>PAW</b>	<b>P</b> rojector- <b>A</b> ugmented <b>W</b> ave
<b>PCA</b>	<b>P</b> rincipal <b>C</b> omponent <b>A</b> nalysis
<b>PE</b>	<b>P</b> oly <b>E</b> thylene
<b>PES</b>	<b>P</b> otential <b>E</b> nergy (hyper-) <b>S</b> urface
<b>PET</b>	<b>P</b> oly <b>E</b> thylene <b>T</b> erephthalate
<b>PiFM</b>	<b>P</b> hoto- <b>I</b> nduced <b>F</b> orce <b>M</b> icroscopy
<b>PM-IRRAS</b>	<b>P</b> olarization <b>M</b> odulation- <b>I</b> nfrared <b>R</b> eflection- <b>A</b> bsorption <b>S</b> pectroscopy
<b>PP</b>	<b>P</b> oly <b>P</b> ropylene
<b>PS</b>	<b>P</b> oly <b>S</b> tylene
<b>PSD</b>	<b>P</b> hase <b>S</b> ensitive <b>D</b> etection
<b>PSDs</b>	<b>P</b> article <b>S</b> ize <b>D</b> istributions
<b>PtM</b>	<b>P</b> ower- <b>t</b> o- <b>M</b> ethane
<b>PTR-MS</b>	<b>P</b> roton <b>T</b> ransfer <b>R</b> eaction - <b>M</b> ass <b>S</b> pectrometry
<b>QCL</b>	<b>Q</b> uantum <b>C</b> ascade <b>L</b> aser
<b>RIXS</b>	<b>R</b> esonant <b>I</b> nelastic <b>X</b> -ray <b>S</b> cattering
<b>RWGS</b>	<b>R</b> everse <b>W</b> ater- <b>G</b> as <b>S</b> hift
<b>SAXS</b>	<b>S</b> mall <b>A</b> ngle <b>X</b> -ray <b>S</b> cattering
<b>SBA</b>	<b>S</b> anta <b>B</b> arbara <b>A</b> morphous
<b>SEIRAS</b>	<b>S</b> urface- <b>E</b> nhanced <b>I</b> nfra <b>R</b> ed <b>A</b> bsorption <b>S</b> pectroscopy
<b>SEM</b>	<b>S</b> canning <b>E</b> lectron <b>M</b> icroscopy
<b>SERS</b>	<b>S</b> urface- <b>E</b> nhanced <b>R</b> aman <b>S</b> pectroscopy
<b>SHIN</b>	<b>S</b> hell- <b>I</b> solated <b>N</b> anoparticle

<b>SHINERS</b>	<b>S</b> Hell-Isolated <b>N</b> anoparticle- <b>E</b> nhanced <b>R</b> aman <b>S</b> pectroscopy
<b>SMSI</b>	<b>S</b> trong <b>M</b> etal- <b>S</b> upport <b>I</b> nteraction
<b>SNOM</b>	<b>S</b> canning <b>N</b> ear-field <b>O</b> ptical <b>M</b> icroscopy
<b>SPM</b>	<b>S</b> canning <b>P</b> robe <b>M</b> icroscopy
<b>STEM</b>	<b>S</b> canning <b>T</b> ransmission <b>E</b> lectron <b>M</b> icroscopy
<b>STEM</b>	<b>S</b> cience, <b>T</b> echnology, <b>E</b> ngineering, and <b>M</b> ath
<b>STM</b>	<b>S</b> canning <b>T</b> unneling <b>M</b> icroscopy
<b>STS</b>	<b>S</b> canning <b>T</b> unneling <b>S</b> pectroscopy
<b>STXM</b>	<b>S</b> canning <b>T</b> ransmission <b>X</b> -ray <b>M</b> icroscopy
<b>TCD</b>	<b>T</b> hermal <b>C</b> onductivity <b>D</b> etector
<b>TEOS</b>	<b>T</b> etra <b>E</b> thyl <b>O</b> rtho <b>S</b> ilicate
<b>TERS</b>	<b>T</b> ip- <b>E</b> nhanced <b>R</b> aman <b>S</b> pectroscopy
<b>TIP</b>	<b>T</b> itanium <b>I</b> so <b>P</b> ropoxide
<b>TLD</b>	<b>T</b> hrough the <b>L</b> ens <b>D</b> etector
<b>TOF</b>	<b>T</b> urn <b>O</b> ver <b>F</b> requency
<b>TOS</b>	<b>T</b> ime- <b>O</b> n- <b>S</b> tream
<b>TPD</b>	<b>T</b> emperature- <b>P</b> rogrammed <b>D</b> esorption
<b>TPR</b>	<b>T</b> emperature <b>P</b> rogrammed <b>R</b> eduction
<b>TXM</b>	<b>T</b> ransmission <b>X</b> -ray <b>M</b> icroscopy
<b>UHV</b>	<b>U</b> ltra- <b>H</b> igh <b>V</b> acuum
<b>UPW</b>	<b>U</b> ltra- <b>P</b> ure <b>W</b> ater
<b>UV-Vis</b>	<b>U</b> ltra <b>V</b> iolet <b>V</b> isible
<b>VASP</b>	<b>V</b> ienna <b>A</b> b-initio <b>S</b> imulation <b>P</b> ackage
<b>WAXS</b>	<b>W</b> ide <b>A</b> ngle <b>X</b> -ray <b>S</b> cattering
<b>WGS</b>	<b>W</b> ater- <b>G</b> as <b>S</b> hift
<b>XANES</b>	<b>X</b> -ray <b>A</b> bsorption <b>N</b> ear <b>E</b> dge <b>S</b> pectroscopy
<b>XAS</b>	<b>X</b> -ray <b>A</b> bsorption <b>S</b> pectroscopy
<b>XES</b>	<b>X</b> -ray <b>E</b> mission <b>S</b> pectroscopy
<b>XPS</b>	<b>X</b> -ray <b>P</b> hotoelectron <b>S</b> pectroscopy
<b>XRD</b>	<b>X</b> - <b>R</b> ay <b>D</b> iffraction
<b>XRF</b>	<b>X</b> -ray <b>F</b> luorescence
<b>XRS</b>	<b>X</b> -ray <b>R</b> aman <b>S</b> cattering

### 8.3 List of Scientific Publications, Conference Contributions, and Awards

#### A. List of Publications Appearing in this PhD Thesis

**ten Have, I. C.**, Weckhuysen, B. M. (2021). The Active Phase in Cobalt-based Fischer-Tropsch Synthesis. *Chem Catalysis*, *1*, 339-363.

**ten Have, I. C.**, Hartman, T., van Bavel, A.P., Bezemer, G. L., Ferri, D., Geitner, R., Huang, T., Kupfer, S., Gräfe, S., Meirer, F., Weckhuysen, B. M. (2022). Through the Lens of *Operando* Spectroscopy: Mechanistic Insights in the Fischer-Tropsch Synthesis. *Submitted for publication*.

**ten Have, I. C.**, Kromwijk, J. J. G., Monai, M., Ferri, D., Meirer, F., & Weckhuysen, B. M. (2022). Uncovering the Reaction Mechanism behind CoO as Active Phase in CO<sub>2</sub> Hydrogenation. *Nature Communications*, *13*, 324.

Werny, M. J.<sup>§</sup>, Zarupski, J.<sup>§</sup>, **ten Have, I. C.**, Piovano, A., Hendriksen, C., Friederichs, N. H., Groppo, E., Meirer, F. & Weckhuysen, B. M. (2021). Correlating the Morphological Evolution of Individual Catalyst Particles to the Kinetic Behavior of Metallocene-Based Ethylene Polymerization Catalysts. *JACS Au*, *1*, 1996-2008.

<sup>§</sup> These authors have contributed equally.

**ten Have, I. C.**, van den Brink, R. Y., Marie-Rose, S. C., Meirer, F. & Weckhuysen, B. M. (2022) Using Biomass Gasification Mineral Residue as Catalyst to Produce Light Olefins from CO, CO<sub>2</sub>, and H<sub>2</sub> Mixtures. *ChemSusChem*, *15*, e202200436

**ten Have, I. C.**, Duijndam, A. J. A., Oord, R., van Berlo-van den Broek, H. J., Vollmer, I., Weckhuysen, B. M., & Meirer, F. (2021). Photoinduced Force Microscopy as an Efficient Method Towards the Detection of Nanoplastics. *Chemistry-Methods*, *1*, 205-209.

Meirer, F.<sup>§</sup>, **ten Have, I. C.**<sup>§</sup>, Oord, R., Zettler, E., van Sebille, E., Amaral-Zettler, L., & Weckhuysen, B. M. (2021). Nanoscale Infrared Spectroscopy Reveals Nanoplastics at 5000 m Depth in the South Atlantic Ocean. *Submitted for publication*. *Pre-print available at* <https://doi.org/10.21203/rs.3.rs-955379/v1>.

<sup>§</sup> These authors have contributed equally.

## B. List of Other Publications by the Author

Oord, R., **ten Have, I. C.**, Arends, J. M., Hendriks, F. C., Schmidt, J., Lezcano-Gonzalez, I., & Weckhuysen, B. M. (2017). Enhanced activity of desilicated Cu-SSZ-13 for the selective catalytic reduction of NO<sub>x</sub> and its comparison with steamed Cu-SSZ-13. *Catalysis Science & Technology*, *7*, 3851-3862.

**ten Have, I. C.**, Valle, E., Gallo, A., Snider, J. L., Duyar, M. S., & Jaramillo, T. F. (2019). Development of Molybdenum Phosphide Catalysts for Higher Alcohol Synthesis from Syngas by Exploiting Support and Promoter Effects. *Energy Technology*, *7*, 1801102.

Jongkind, M. K., Meirer, F., Bossers, K. W., **ten Have, I. C.**, Ohldag, H., Watts, B., van Kessel, T., Friedrichs, N. & Weckhuysen, B. M. (2021). Influence of Metal-Alkyls on Early-Stage Ethylene Polymerization over a Cr/SiO<sub>2</sub> Phillips Catalyst: A Bulk Characterization and X-ray Chemical Imaging Study. *Chemistry-A European Journal*, *27*, 1688-1699.

Moya-Cancino, J. G., Honkanen, A. P., van der Eerden, A. M., Oord, R., Monai, M., **ten Have, I. C.**, Sahle, C. J., Meirer, F., Weckhuysen, B. M., de Groot, F. M. F. & Huotari, S. (2021). In Situ X-ray Raman Scattering Spectroscopy of the Formation of Cobalt Carbides in a Co/TiO<sub>2</sub> Fischer-Tropsch Synthesis Catalyst. *ACS Catalysis*, *11*, 809-819.

## C. List of Cover Features

**ten Have, I. C.**, van den Brink, R. Y., Marie-Rose, S. C., Meirer, F. & Weckhuysen, B. M. (2022) Using Biomass Gasification Mineral Residue as Catalyst to Produce Light Olefins from CO, CO<sub>2</sub>, and H<sub>2</sub> Mixtures. *ChemSusChem*, *15*, e202200436

**ten Have, I. C.**, Duijndam, A. J. A., Oord, R., van Berlo-van den Broek, H. J., Vollmer, I., Weckhuysen, B. M., & Meirer, F. (2021). Photoinduced Force Microscopy as an Efficient Method Towards the Detection of Nanoplastics. *Chemistry-Methods*, *1*, 205-209.

## D. List of Oral Presentations at Scientific Conferences

ten Have, I. C., Bossers, K. W., Weckhuysen, B. M. "Bridging the Material Gap with Micro-island Model Catalysts: The Co/TiO<sub>2</sub> Fischer-Tropsch Showcase." 20<sup>th</sup> Netherlands Catalysis and Chemistry Conference, Noordwijkerhout, The Netherlands, March 2019.

ten Have, I. C., Bossers, K. W., Weckhuysen, B. M. "Bridging the Material Gap with Micro-island Model Catalysts: The Co/TiO<sub>2</sub> Fischer-Tropsch Showcase." 26<sup>th</sup> North American Catalysis Society Meeting, Chicago, Illinois, United States of America, June 2019.

ten Have, I. C., van Bavel, A. P., Duijndam, A. J. A., Geitner, R., Huang, T., Kupfer, S., Gräfe, S., Bossers, K. W., Meirer, F., Weckhuysen, B. M. "Identifying Aldehyde Functionalities as a Source for Polyaromatics during Fischer-Tropsch Synthesis." 22<sup>nd</sup> Netherlands Catalysis and Chemistry Conference, Noordwijkerhout, The Netherlands, March 2021.

ten Have, I. C., Kromwijk, J. J. G., Monai, M., Ferri, D., Meirer, F., & Weckhuysen, B. M. "Uncovering Key Intermediates and Active Phases in the Cobalt-based CO<sub>2</sub> Hydrogenation." American Chemical Society Spring Meeting, Online, April 2021.

ten Have, I. C., van Bavel, A. P., Duijndam, A. J. A., Geitner, R., Huang, T., Kupfer, S., Gräfe, S., Bossers, K. W., Meirer, F., Weckhuysen, B. M. "Identifying Aldehyde Functionalities as a Source for Polyaromatics during Fischer-Tropsch Synthesis." American Chemical Society Spring Meeting, Online, April 2021.

ten Have, I. C., Kromwijk, J. J. G., Monai, M., Ferri, D., Meirer, F., & Weckhuysen, B. M. "Uncovering Key Intermediates and Active Phases in the Cobalt-based CO<sub>2</sub> Hydrogenation." International Seminar on Transient Kinetics, Online, April 2021.

### **E. Lecture Award**

2021 NIOK Lecture Award for the best presentation at the 22<sup>nd</sup> Netherlands Catalysis and Chemistry Conference.

### **F. List of Outreach Activities**

- In one of the editions of *Zapp Your Planet* on Dutch National Television ([https://www.zapp.nl/programmas/zapp-your-planet/filmpjes/1075-lab-leven/clips/WO\\_NTR\\_16328121](https://www.zapp.nl/programmas/zapp-your-planet/filmpjes/1075-lab-leven/clips/WO_NTR_16328121)) professor Bert Weckhuysen and I explained how greenhouse gas CO<sub>2</sub> can be used to make sustainable fuels.
- News article on the *Nature Communications* article on the Utrecht University website: <https://www.uu.nl/en/news/what-if-we-could-turn-co2-into-something-useful>. This article was further noted and highlighted by *Chemisch2Weekblad*: <https://www.sciencelink.net/nieuws-and-verdieping/katalysatormodel-op-de-schop/20420.article>.
- In the Magazine *LabInsights* (<https://www.labinsights.nl/magazine/2020/LB2020-8p28.pdf>) we explained catalysis research at the micro- and nanoscale.

- Together with the company VSPARTICLE, we have explained the design of catalyst materials in a video ([https://www.linkedin.com/posts/vsparticle-b-v\\_learn-more-about-their-experience-in-the-activity-6760124978458361857-hKY3/](https://www.linkedin.com/posts/vsparticle-b-v_learn-more-about-their-experience-in-the-activity-6760124978458361857-hKY3/)).

## 8.4 Acknowledgements

First of all, I would like to thank my supervisors Bert Weckhuysen and Florian Meirer for all their feedback and support. Bert, thank you for believing in me and for all the great opportunities that you have created in my life. I am grateful for the fiery and fruitful scientific discussions we had, which made the scientific work stronger. Florian, thank you for supporting me, for listening to me when I needed it, and for involving me in your great ideas around nanoplastics. You have been a great mentor and contributed tremendously to my understanding of complex spectroscopy concepts, such as modulation excitation. Bert and Florian, you have both been invaluable in the process of shaping me into a better scientist and teacher.

Furthermore, I would like to thank all of the students that have worked under my supervision; in particular the MSc. students Tessa Brouwer, Joyce Kromwijk, and Adriaan Duijndam, who have worked closely together with me for about a year. Your presence was a fun experience that motivated me to become a better teacher. I am looking forward to seeing all of you flourish during the next steps in your professional careers as well as personal lives. Another thanks goes out to the BSc./MSc. students that have worked with me for shorter time periods: Robin van den Brink, Florine Kooij, Juliëtte Verschoor, Arjan Hijlkema, Max Sebes, and Ruben van der Loo.

The technical personnel of the Inorganic Chemistry and Catalysis (ICC) group at Utrecht University have been invaluable during the process. Especially in the last year of my PhD, where they were often involved in discussions and preparations for challenging experiments, such as isotopic labeling experiments. Ramon, Oscar, Jochem, Joris, Pascal, Fouad, Dennie, Jan-Willem, and Herrick many thanks that you were ready to help out every day and for facilitating all the great science that is performed in the ICC group. Keep up the great work! Chris, Hans, and Sergei, many thanks for training, help, and advice with electron microscopy.

A big thanks goes out to the administrative staff of the ICC group, as well as the permanent staff at Utrecht University. Dymph, Iris, Monique, Belen, and Sandra our management and coordination skills have been essential for keeping the group up and running throughout the years. I am especially grateful for your assistance with deadlines. I really appreciate these stressful moments where you responded swiftly and took actions assertively. Anita and Jane, many thanks for your advice on projects and finances. Another special thank you goes out to Inge from the mailroom for making sure that all my parcels arrived safely at their destinations.



Then, I would like express my gratitude for meeting many great colleagues during my time at the ICC group. I am especially grateful for the colleagues that turned into good friends, whom I shared many fun moments with. Michael and Joris, many thanks for the eventful running sessions we had on Wednesday evenings during the COVID-19 pandemic. These running sessions kept my mind sane during these difficult times. Francesco, Rafael, and Laura, thanks for hosting many great evenings at the caliphate. All the fun and insightful conversations would not have been possible without you. Kordula and Florian, I am glad that you guys were always up for doing something fun. Thanks for joining in on many different activities. This really provided some stress relief and relaxation during difficult times. Max, I am definitely most grateful for meeting you during my time in the group. I cannot even express with words how much your presence and mental support has meant to me. I am very excited to see what the future holds for us. Please don't ever stop being your great self!

I am very grateful to have worked together with many other great people both within ICC group and outside of it. A big thanks goes out to all of the co-authors that appear on the scientific publications mentioned in this final **Chapter** of my PhD Thesis. None of the work would have been possible without your input. A special thanks goes out to Davide Ferri from the Paul Scherrer Institute (SLS, Villigen, Switzerland). Davide, your help has facilitated some of the most essential experiments during my PhD. Thomas, your graphical artworks have tremendously improved the way I communicated some of the scientific results in papers and during presentations. Thanks a lot and please keep doing this great work.

All the intense and unforgettable beamtrips to many different synchrotron facilities I went on with some great colleagues from the ICC group have a special place in my memory. Ramon, none of these beamtrips would have been possible without your technical support. Ilse and Maarten, many thanks for the great times that we've had during our beamtrips at the Advanced Light Source (ALS) in Berkeley (USA). Ilse, these trips to Berkeley wouldn't have been half as much fun without you. A special thanks goes out to all the hard-working beamline scientists that I've met during beamtrips. Hendrik Ohldag, Doug Taube, and David Shapiro from ALS, Simon Bare and Adam Hoffman from the Stanford Synchrotron Radiation Lightsource (SSRL, Menlo Park, USA), Maarten Nachtegaal and Benjamin Watts from the Swiss Light Source (SLS), thank you all for your invaluable technical assistance. Matteo, Charlotte, Silvia, Koen, Max, Jelle, Angela, Adriaan, Kordula, Florian, Yannick, Joyce, Nina, Nicolette thanks to all of you for these tough, but interesting times.

Finally, I would like to thank the sponsors and collaborators within Technology Area grant (no. 731016201) of the Innovation Fund Chemistry supplied by the Netherlands Research Council (NWO). From Shell Global Solutions International B.V., I would particularly like to thank Sander van Bavel and Leendert Bezemer. Your input and scientific discussions have been of great value to the work in this PhD Thesis.

Iris ten Have

## 8.5 Curriculum Vitae

Iris Chloe ten Have was born on the 5<sup>th</sup> of November 1993 in Amsterdam, the Netherlands. She enrolled in an undergraduate program with a Major in Chemistry and a Minor in Business and Entrepreneurship at Utrecht University (The Netherlands) in 2012. She obtained a Bachelor of Science degree in 2015 after writing a Bachelor's thesis on NO<sub>x</sub> selective catalytic reduction with copper zeolites under the supervision of Prof. dr. ir. Bert M. Weckhuysen at Utrecht University. In 2015, she started the Master's program Nanomaterials: Chemistry and Physics at Utrecht University. During the master's, she carried out two research projects. The first project was related to engineering porous carbon materials *via* hard-templating to produce performance-enhancing support materials for the conversion of CO and H<sub>2</sub> to fuels under the supervision of Prof. dr. ir. Krijn P. de Jong at Utrecht University. The second project investigated molybdenum phosphide catalysts for higher alcohol production from CO and H<sub>2</sub> under the supervision of Prof. dr. Thomas F. Jaramillo at Stanford University (USA). After obtaining a Master of Science, Iris started her PhD work in the group of Prof. dr. ir. Bert M. Weckhuysen at Utrecht University. The results of her PhD research are described within this PhD Thesis, published in peer-reviewed scientific journals, and presented at multiple national and international scientific conferences.



